# Robustness estimation of self-sensing active magnetic bearings via system identification

**Thesis submitted for the degree *Philosophiae Doctor***

**at the Potchefstroom campus of the North-West University**

**P.A. van Vuuren**

**Promoter: Prof. G. van Schoor**
**Co-promoter: Prof. W.C. Venter**
**December 2009**

# Acknowledgements

I want to thank You Lord for giving me a second chance and providing me with everything I need. Truly, Your presence is a subtle magic.

Helen, you are one in a trillion. Thank you for your love, support and encouragement.

The rest of my family also deserves a heartfelt word of thanks. To both my sets of parents I want to say that your help and support have meant a lot to me.

Thank you prof. George and prof. Willie for your attentive ears and critical remarks that have shaped this study during its long and arduous journey.

Lastly I want to thank M-Tech Industrial (Pty) Ltd for their financial support during the past three years.

# Abstract

Due to their frictionless operation active magnetic bearings (AMBs) are essential components in high-speed rotating machinery. Active magnetic control of a high speed rotating rotor requires precise knowledge of its position. Self-sensing endeavours to eliminate the required position sensors by deducing the rotor's position from the voltages and currents with which it is levitated. For self-sensing AMBs to be of practical worth, they have to be robust. Robustness analysis aims to quantify a control system's tolerance for uncertainty. In this study the stability margin of a two degree-of-freedom self-sensing AMB is estimated by means of $\mu$-analysis. Detailed black-box models are developed for the main subsystems in the AMB by means of discrete-time system identification. Suitable excitation signals are generated for system identification in cognisance of frequency induced nonlinear behaviour of the AMB. Novel graphs that characterize an AMB's behaviour for input signals of different amplitudes and frequency content are quite useful in this regard. In order to obtain models for dynamic uncertainty in the various subsystems (namely the power amplifier, self-sensing module and AMB plant), the identified models are combined to form a closed-loop model for the self-sensing AMB. The response of this closed-loop model is compared to the original AMB's response and models for the dynamic uncertainty are empirically deduced. Finally, the system's stability margin for the modelled uncertainty is estimated by means of $\mu$-analysis. The potentially destabilizing effects of parametric uncertainty in the controller coefficients as well as dynamic uncertainty in the AMB plant and self-sensing module are examined. The resultant $\mu$-analyses show that self-sensing AMBs are much less robust for parametric uncertainty in the controller than AMBs equipped with sensors. The $\mu$-analyses for dynamic uncertainty confirm that self-sensing AMBs are rather sensitive for variations in the plant or the self-sensing algorithm. Validation of the stability margins estimated by $\mu$-analysis reveal that $\mu$-analysis is overoptimistic for parametric uncertainty on the controller and conservative for dynamic uncertainty. (Validation is performed by means of Monte Carlo simulations.) The accuracy of $\mu$-analysis is critically dependent on the accuracy of the uncertainty model and the degree to which the system is linear or not. If either of these conditions are violated, $\mu$-analysis is essentially worthless.

*Keywords: robustness analysis, $\mu$-analysis, system identification, self-sensing active magnetic bearings*

# Opsomming

Aktiewe magneetlaers word gekenmerk deur wrywinglose werking. 'n Magneetlaer se beheerstelsel benodig deurentyd akkurate kennis van die rotor se posisie. Self-waarnemende magneetlaers poog om vanuit die magneetlaer se spannings en strome die posisie van die rotor af te lei. Praktiese self-waarnemende magneetlaers moet robuust wees. Dit is nodig om 'n magneetlaer se mate van robuustheid te kwantifiseer m.b.v. 'n robuustheid beramer. In hierdie studie word $\mu$-analise ingespan om die stabiliteitsgrens van 'n twee-vryheidsgraad self-waarnemende magneetlaer te beraam. Diskrete-tyd stelselidentifikasie word gebruik om modelle vir die vernaamste onderdele van 'n magneetlaer te bou. Geskikte opwekkingseine word vir stelselidentifikasie gegenereer met inagneming van frekwensie-geïndusseerde nielineêre gedrag in die magneetlaer. Unieke grafieke waarmee 'n magneetlaer se gedrag as 'n funksie van die frekwensie en amplitude van sy inset sein uitgedruk word, is behulpsaam in hierdie verband. Afsonderlike modelle is geïdentifiseer vir die drywingsversterker, magneetlaer aanleg en self-waarneming module. 'n Geslote-lus model is vanuit hierdie komponentmodelle gevorm en die gedrag vergelyk met die oorspronklike magneetlaer stelsel. Empiriese modelle vir die dinamiese onsekerheid waarmee die magneetlaer te kampe het, is vanuit die response van die oorspronklike magneetlaer en sy model afgelei. Uiteindelik is die stabiliteitsgrens van die magneetlaer vir die gemodelleerde dinamiese onsekerheid m.b.v. $\mu$-analise beraam. Die stabiliteitsgrens van die magneetlaer vir onsekerheid in sy beheerder koëffisiënte, sowel as vir dinamiese onsekerheid in die magneetlaer aanleg en self-waarneming module is ondersoek. Daar is bevind dat self-waarnemende magneetlaers meer sensitief is vir variasies in hul beheerder parameters as gewone magneetlaers. Self-waarnemende magneetlaers is ook sensitief vir ongemodelleerde effekte in beide die aanleg en die self-waarneming module. Die beraamde stabiliteitsgrense van $\mu$-analise is vergelyk met resultate bekom deur Monte Carlo simulasies. Hieruit blyk dat $\mu$-analise oor-optimisties is in die geval van parametriese onsekerheid in die beheerder parameters, terwyl $\mu$-analise konserwatief is vir dinamiese onsekerhede. Die akkuraatheid van $\mu$-analise is krities afhanklik van die akkuraatheid van die onsekerheidsmodelle, asook die mate waartoe die stelsel lineêr is of nie. Indien hierdie voorwaardes nie bevredig word nie, is $\mu$-analise nie 'n geskikte robuustheid beramer nie.

*Sleutelterme: robuustheid analise, $\mu$-analise, stelselidentifikasie, self-waarnemende magneetlaers*

# CONTENTS

# LIST OF FIGURES

# LIST OF TABLES

# List of symbols and abbreviations

## Roman symbols

| Symbol | Description |
|---|---|
| $A$ | Pole face area |
| $\mathbf{A}$ | State matrix of an LTI state-space model |
| $\hat{B}$ | Estimated magnetic flux density |
| $\mathbf{B}$ | Input matrix of an LTI state-space model |
| $\mathbf{C}$ | Output matrix of an LTI state-space model |
| $\mathcal{C}$ | Set of complex-valued numbers |
| $\mathbf{D}$ | Feedthrough matrix of an LTI state-space model |
| $E(s)$ | Laplace transform of $e(t)$ |
| $e(t)$ | Error signal applied to the controller input |
| $e_x$ | $X$-axis component of the error signal $e(t)$ |
| $e_y$ | $Y$-axis component of the error signal $e(t)$ |
| $f_m(t)$ | Electromagnetic force exerted by an AMB on its rotor |
| $\boldsymbol{G}(s)$ | Transfer function matrix |
| $G_{AMB}$ | AMB plant transfer function |
| $G_{AMB(n,m)}(s)$ | SISO AMB plant transfer function from input $m$ through to output $n$ |
| $\bar{G}(s)$ | Nominal LTI transfer function of the system $G(s)$ |
| $\bar{G}_{AMB(n,m)}(s)$ | Nominal AMB plant transfer function from input $m$ through to output $n$ |
| $G_C(s)$ | Controller transfer function |
| $G_{CL}(s)$ | Closed-loop transfer function |
| $G_{noise}(s)$ | Filter responsible for transforming general white noise into the specific noise which impacts a particular plant |
| $G_P(s)$ | Plant transfer function |
| $G_{PA}$ | Power amplifier module transfer function |

*Continued on next page*

| Symbol | Description |
|---|---|
| $G_{SS}$ | Self-sensing module transfer function |
| $\bar{G}_{SS}(s)$ | Nominal LTI transfer function of the self-sensing module |
| $\mathbf{I}$ | Identity matrix (a diagonal matrix with ones on the main diagonal) |
| $i(t)$ | Current flowing in an AMB stator coil |
| $i_0$ | Bias current used in the AMB power amplifiers |
| $i_{\max}$ | Peak ripple current during one switching cycle |
| $i_y$ | Current reference signal produced by the controller for the top and bottom power amplifiers |
| $I_1(s)$ | Laplace transform of $i_1(t)$ |
| $i_1$ | Current in the top pair of coils in an 8-pole heteropolar AMB stator |
| $I_2(s)$ | Laplace transform of $i_2(t)$ |
| $i_2$ | Current in the right hand pair of coils in an 8-pole heteropolar AMB stator |
| $I_3(s)$ | Laplace transform of $i_3(t)$ |
| $i_3$ | Current in the bottom pair of coils in an 8-pole heteropolar AMB stator |
| $I_4(s)$ | Laplace transform of $i_4(t)$ |
| $i_4$ | Current in the left hand pair of coils in an 8-pole heteropolar AMB stator |
| $\mathbf{K}$ | Controller in the generalized control configuration |
| $K_D$ | Derivative coefficient in a PID controller |
| $k_{DCM}$ | Conversion constant between current and position |
| $K_{DC}$ | DC value of a transfer function |
| $K_I$ | Integral coefficient in a PID controller |
| $k_i$ | Current stiffness constant |
| $K_P$ | Proportional coefficient in a PID controller |
| $k_s$ | Position stiffness constant |
| $l_c$ | Total length of the magnetic path (excluding the airgap) |
| $m$ | Mass of the AMB rotor |
| $N$ | Number of windings in any one of the AMB stator coils |
| $\mathbf{N}$ | Transfer function matrix representing the combination of the generalized plant $\mathbf{P}$ and the controller $\mathbf{K}$ |
| $\mathbf{N}_{ij}$ | Component matrix of the block-matrix $\mathbf{N}$ |
| $\mathbf{P}$ | Generalized plant (excluding the controller and structured uncertainty matrix) |
| $\mathbf{P}_{ij}$ | Component matrix of the block-matrix $\mathbf{P}$ |
| $R$ | Electrical resistance of a coil wire |
| $\mathcal{R}$ | Set of real-valued numbers |
| $R(s)$ | Laplace transform of $r(t)$ |
| $\bar{R}(s)$ | Laplace transform of the nominal value of $r(t)$ |
| $r(t)$ | Reference signal applied at a closed-loop system's input |
| $r_c$ | Stator back-iron inner radius |

*Continued on next page*

| Symbol | Description |
|---|---|
| $r_j$ | Journal outer radius |
| $r_p$ | Stator pole radius |
| $r_r$ | Journal inner radius |
| $r_s$ | Stator outer radius |
| $r_w$ | Pole width |
| $r_x(t)$ | $X$-axis position reference input to the AMB |
| $r_y(t)$ | $Y$-axis position reference input to the AMB |
| $S(s)$ | SISO sensitivity function |
| $S_{peak}(s)$ | Peak value of the sensitivity function |
| $s$ | Laplace domain complex-valued variable |
| $s_w$ | The approximated s-plane variable obtained by the bilinear transform |
| $T$ | Sampling period |
| $T_{PA}$ | Switching period of the power amplifier |
| $\mathbf{U}^+$ | Moore-Penrose pseudo-inverse of the matrix $\mathbf{U}$ |
| $U(s)$ | Laplace transform of $u(t)$ |
| $\bar{U}(s)$ | Laplace transform of the nominal value of $u(t)$ |
| $u(t)$ | Controller output signal applied to the input of the plant |
| $u_x$ | $X$-axis component of the controller output signal $u(t)$ |
| $u_y$ | $Y$-axis component of the controller output signal $u(t)$ |
| $v(t)$ | Coil voltage |
| $W(s)$ | General uncertainty weight transfer function for dynamic uncertainty |
| $W_{AMB(n,m)}(s)$ | Uncertainty weight transfer function from the $m^{\text{th}}$ input to the AMB plant to its $n^{\text{th}}$ output |
| $W_{SS}(s)$ | Uncertainty weight transfer function for self-sensing |
| $x_g(t)$ | Airgap distance (between the AMB stator and rotor) |
| $y_0$ | Bias $y$-axis position of the AMB rotor |
| $Y(s)$ | Laplace transform of $y(t)$ |
| $\bar{Y}(s)$ | Laplace transform of the nominal value of $y(t)$ |
| $y(t)$ | Output of a closed-loop control system |
| $y_{linear}$ | Uncompensated estimated position |
| $y_{nonlinear}$ | Empirically determined nonlinear compensation term for the estimated position |
| $Y_x(s)$ | Laplace transform of the $x$-axis position of the AMB rotor |
| $y_x$ | $X$-axis position of the AMB rotor |
| $Y_y(s)$ | Laplace transform of the $y$-axis position of the AMB rotor |
| $y_y$ | $Y$-axis position of the AMB rotor |
| $\hat{y}_y$ | Estimated $y$-axis position of the AMB rotor |
| $\lvert y(j\omega)\rvert_{dB}$ | Measured gain frequency response (expressed in decibels) |
| $\lvert \hat{y}(j\omega)\rvert_{dB}$ | Approximated gain frequency response (expressed in decibels) |
| $\mathcal{Z}$ | Z-transform |
| $z$ | Z-plane complex-valued variable |

# Greek symbols

| Symbol | Description |
|---|---|
| $\alpha$ | Scaling constant used during rescaling of data as part of decimation (downsampling) |
| $\Delta$ | General norm-bounded uncertainty (either for parametric uncertainty or dynamic uncertainty |
| $\mathbf{\Delta}$ | Structured uncertainty matrix in the generalized control configuration |
| $\mathbf{\Delta}_u$ | Unstructured uncertainty matrix |
| $\Delta(s)$ | LTI norm-bounded uncertainty (i.e. any transfer function whose magnitude is less than 1 for all frequencies) |
| $\epsilon(t)$ | Time domain residuals of a model |
| $\epsilon(j\omega)$ | Decibel difference between two different gain frequency responses at a specific frequency |
| $\theta$ | Pole face angle (the angle between the vertical axis of the stator and the normal line to the pole face) |
| $\mu$ | Structured singular value |
| $\mu_0$ | Magnetic permeability of free space (vacuum) ($\mu_0 = 4\pi \times 10^{-7}$Vs/Am |
| $\mu_{\mathbf{\Delta}}$ | Extended representation of the structured singular value $\mu$ accentuating the fact that $\mu$ is a function of both the nominal model as well as the structured uncertainty matrix $\mathbf{\Delta}$ |
| $\Xi(s)$ | Laplace transform of the excitation signal |
| $\xi$ | Adjustable parameter in the frequency-amplitude interrogation algorithm of section 3.2.3 |
| $\sigma$ | Singular value |
| $\sigma_{\max}$ | Maximum singular value |
| $\omega$ | Frequency |

# Abbreviations

| | |
|---|---|
| AM | Amplitude modulation |
| AMB | Active magnetic bearing |
| ARMAX | Autoregressive moving average with external input |
| ARX | Autoregressive with external input |
| DC | Direct current |
| DCM | Direct current measurement |
| DOF | Degree-of-freedom |
| ETFE | Empirical transfer function estimate |
| FM | Frequency modulation |
| IQR | Interquartile range |
| LFT | Linear fractional transformation |

*Continued on next page*

| | |
|---|---|
| LTI | Linear time-invariant |
| MIMO | Multiple-input, multiple-output |
| OE | Output error |
| PD | Proportional derivative |
| PEM | Prediction-error method |
| PID | Proportional integral derivative |
| PWM | Pulse-width modulation |
| SISO | Single-input, single-output |

CHAPTER 1

# Introduction

## 1.1 The heart of control systems

Robustness. A common term that is frequently used in colloquial and technical language, yet, what does it mean precisely?

In terms of the performance of a natural (or man-made) system, robustness can be defined as: "...a relative insensitivity to perturbations; it is the persistence of a system's characteristic behavior under perturbations or conditions of uncertainty." [1]. Robustness is therefore the specific property of a system that determines how it reacts to messy, unconstrained, and unpredictable real life.

Engineers and scientists would prefer a neat and tidy world with everything in its place and accounted for. Scientists use axioms and engineers resort to design assumptions to reign in the wildness of nature, to pacify the unpredictable, to placate the uncontrollable, to give mankind some measure of understanding and control over our all-encompassing environment. We develop theories on paper and optimize designs in the laboratory, yet outside the circle of our scientific campfires lurk chaotic and nonlinear behaviour which is simply beyond our ken.

This has been dramatically put, I must confess, but the fact remains that even with our best theories we "...see but a poor reflection as in a mirror ..." [2]. It is essential that we endow our engineering designs with the ability to fulfill their objectives in the presence of inexactly described disturbances and dynamics that often wander beyond the limits of our understanding. In a nutshell, engineering designs have to be robust.

Nowhere is this more true than in control systems. In fact, feedback control systems were originally developed with robustness in mind [3]. Today still, stability and performance problems in a control system are often due to a mismatch between the mathematical model of the plant and the real hardware [4]. One could therefore be forgiven for saying that the quest for robustness stands at the heart of control systems theory.

Since uncertainty in a control system is ever-present, controllers have to be designed to take uncertainty into account and still deliver acceptable system performance. These controllers are called robust controllers [5]. As could be expected, there are a plethora of different approaches to robust control. Choosing the best robust controller for a particular application obviously requires comparing the different options amongst other things on the basis of their *robustness* [6]. This leads to the requirement for accurately measuring (or at least estimating) a system's degree of robustness.

Robustness estimation is important, because measuring a system's robustness paves the way to using this knowledge as a design tool with which controllers can be designed to optimize their robustness [7]. Furthermore, certification of a control system's safety and reliability also presupposes a tool with which to measure the system's robustness.

Robustness analysis is therefore concerned with assessing the level of a system's insensitivity for uncertainty in the system parameters, dynamics and possible external disturbances. Obviously, robustness analysis also includes pinpointing the causes of sensitive behaviour and gaining the necessary understanding to rectify the situation.

## 1.2 The focus of the study: active magnetic bearings

This study isn't concerned with robustness analysis in general, but rather robustness estimation applied to active magnetic bearings (AMBs).

Conventional bearings use lubricated contact surfaces to support a rotating axle. As such, bearings are as old as the wheel itself. Despite centuries of development, friction remains a fact of life for conventional bearings. Friction causes loss of power and energy as well as limited component lifetime due to wear and tear. These problems can be avoided by employing magnets to support the rotating shaft by magnetic forces thereby realising contactless and consequently frictionless rotation. Such bearings are known as magnetic bearings [8].

Magnetic bearings most frequently operate on the principle of an attracting magnetic force which suspends an object against gravity. Such magnetic bearings exhibit negative stiffness[1] [9], and have to be actively controlled to ensure contactless levitation (a notion supported by everyday experience with fridge magnets). Such bearings are called active magnetic bearings.

As seen in figure 1.2, the basic construction of a typical active magnetic bearing consists of a stationary stator enclosing the shaft. The stator contains several electromagnets that exert reluctance magnetic forces on the rotor thereby suspending it against the force of gravity and preventing contact with the stator surface. Sensors mounted on the stator continually monitor the position of the rotor. These position signals are used by a controller to adjust the power amplifier that supplies each pole with the necessary current to suspend the rotor.

[1] Conventional elastic springs possess the property of positive stiffness, namely that any deformation of the spring is opposed by the spring. In contrast, if the distance between a magnet and a ferrous object is decreased, this displacement is met with an increasing attractive force from the magnet. The latter property is known as negative stiffness [8].

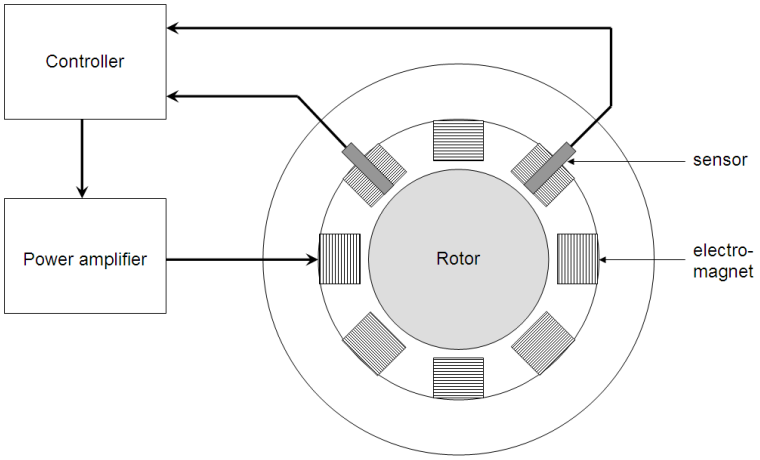


Figure 1.1: General structure of an AMB

The primary advantages of AMBs revolve around their ability to suspend a rotating shaft without any contact at all [10]. Consequently, lubrication is unnecessary and maintenance requirements significantly reduced. High speed rotation is possible, as well as active vibration control. Even their required complicated control system technology can be turned into an advantage, since this opens the door for online condition monitoring and all the benefits of predictive maintenance.

With respect to their place in the greater systems theory, AMBs are multivariable nonlinear systems. A typical AMB employs between six and eight electromagnets that are differentially controlled [8]. At least two orthogonally positioned sensors are necessary to monitor the position of the rotor. Although the controllers responsible for controlling the shaft in the $x$- and $y$-axes are often decoupled in practical AMBs, significant electromagnetic cross-coupling does exist between the various magnetic poles in the stator [11]. Consequently, an AMB is a true multiple input, multiple output (MIMO) plant.

Concerning their linearity magnetic bearings are nonlinear systems, since material magnetization is a nonlinear phenomenon [11]. This is easily seen in the hysteresis and saturation that characterises any magnetic material's magnetization curve.

As could be imagined, accurate and reliable position sensors form a critical component of a functioning AMB system. These sensors are however expensive. If they could be eliminated from the design it would reduce the cost and complexity of the whole system [12]. Furthermore, noncollocation of sensors and actuators in an AMB results in a loss of dynamic performance [13].

These disadvantages could be eliminated by employing self-sensing techniques for estimating the rotor's position. Hanson and Levesley define self-sensing in general as "...the technique of using a transducer to both actuate and sense concurrently" [12]. In the context of AMBs, self-sensing entails the estimation of the rotor position by monitoring the electrical impedance of the actuator (in this case the stator electromagnet coils) [14].

In this study the spotlight falls on estimating the robustness of self-sensing active magnetic

bearings.

## 1.3 Self-sensing techniques and the analysis thereof

Self-sensing techniques can be dichotomized into two main camps, namely the state-estimation approach and the modulation approach [11]. In the state-estimation approach to self-sensing, the AMB is modelled by means of an analytically derived state-space model where one of the state variables is the position of the shaft. Classical state-estimators can then be used to estimate the position of the shaft from the model with only the coil currents as measured variables [15]. This approach has however been shown to be sensitive for model parameters due to poor observability at higher frequencies [16].

One useful byproduct of the switching power amplifiers (the *de facto* standard in AMBs these days), is that the position information of the rotor is modulated onto the current waveform [11]. This forms the basis of the modulation approach to self-sensing where demodulation techniques are used to extract the position information from the current signals.

Most modulation self-sensing techniques suffer from small stability margins due to the phase lag introduced by the filters that are essential for the demodulation process [17]. This problem was circumvented by Niemann's direct current measurement method (DCM) where the peak value of the current ripple is directly measured and manipulated to obtain a duty-cycle invariant position estimate with little additional phase lag [17].

Accurate robustness analysis of self-sensing techniques is very important. It is especially important that the model upon which the subsequent analyses are based is an accurate representation of the underlying principles of self-sensing. This danger was clearly illustrated in the results obtained by Morse *et al.* who found that self-sensing AMBs are fundamentally more sensitive to parameter variations than normal AMBs operating with explicit position sensors[2] [18]. Subsequent laboratory results of demodulation-based self-sensing techniques seemed to contradict these theoretical predictions [11]. As Maslen *et al.* however pointed out [13], it is essential to include the switching ripple present in the coil currents into the AMB model, since it is the current ripple that improves the robustness of demodulation-based self-sensing techniques.

Accurate robustness estimates for self-sensing AMBs are therefore based upon detailed models of all of the components in the control system that include all of the essential dynamics that help them to attain stable levitation. This is however not the whole story, since an accurate model of the system has to be married to an equally accurate robustness estimation technique in order to obtain true and trustworthy robustness estimates.

[2]Hereafter denoted as sensed AMBs.

## 1.4 Robustness estimation technique: $\mu$-analysis

The robustness analysis literature makes distinction between stability robustness and performance robustness [6]. Whilst *stability robustness* focusses on system stability in the face of uncertainty, *performance robustness* is a measure of a system's ability to maintain a certain level of specified performance irrespective of uncertainty. Since stability is an essential requirement of any control system, this study focusses on the estimation of stability robustness.

In stability robustness estimation the literature distinguishes between the "stability check problem" and the "stability margin problem" [5]. The former basically entails answering the question: "is the system stable or not?". Calculating the stability margin of a control system boils down to finding the minimum perturbation that will destabilize it (under the assumption that it is stable). Obviously a robustness estimate that includes a stability margin is much more informative and useful than a mere stability check.

It comes as no surprise that stability robustness, being such a fundamental property of control systems, can be estimated by means of an abundance of different methods. Lyapunov theory is suitable for the stability analysis of nonlinear systems, but is limited by the difficulty in finding a suitable Lyapunov function. Furthermore, Lyapunov theorems provide necessary, but not sufficient conditions for stability [19]. Lyapunov techniques are also by and large restricted to the stability check problem.

Classical techniques such as the gain- and phase margin give intuitive stability margins. They are however unsuitable for the analysis of multivariable systems, since these techniques require that each feedback loop has to be broken individually (under the tacit assumption that the feedback loops are decoupled) [20][3].

Another option for estimating the stability margin is to use the peak of the sensitivity function. This measure forms the basis of the proposed ISO standard for AMBs [9]. But, as so eloquently argued in [22], the output sensitivity function may in some instances result in conservative robustness estimates even though it is a MIMO analysis technique.

At this point it is necessary to clarify the concept of a conservative robustness estimate. An *accurate* measuring instrument provides a "precise, exact, [and] correct" measurement [23]. In the context of robustness estimation, accuracy means steering clear from two possible errors. One possibility is that the robustness estimator overestimates a system's robustness and misses a potential unstable situation. On the other end of the scale, a robustness estimator can be too cautious and underestimate a system's robustness (i.e. it regards the system as being less robust than what it in fact is). When a robustness measure is erring on the safe side of caution, it is called *conservative* [24].

At present, $\mu$-analysis (based on the structured singular value [3]) is one of the best options for accurate estimation of the stability margin of a multivariable system. It is one of the least conservative robustness estimates based on singular values [25] and can be easily calculated by means of existing software packages (e.g. [26]). Another advantage of $\mu$-analysis is that it

[3] Although some results indicate that the gain- and phase margin can give accurate stability margins for AMBs [21], most authorities on robust control advise against its use [3].

expresses the stability margin of a control system as a scalar-valued function of frequency. This feature gives the designer an indication of specific problematic frequency intervals where the plant is more sensitive for uncertainty than at others (e.g. [27]).

The main disadvantage of $\mu$-analysis is that it assumes that the plant is linear time-invariant (LTI). In many applications, this assumption is quite reasonable (even if the plant is slightly nonlinear). Although AMBs exhibit nonlinear dynamics they are operated in so-called differential mode with the express purpose of increasing their region of linear operation [8]. Consequently, it seems as if $\mu$-analysis is a sensible choice for a robustness estimation technique.

Inherent to any robustness analysis is a specific uncertainty or variability for which the control system must be insensitive. Control systems must for example be robust for ageing components or changing operating environments. The fundamental principle is that every robustness analysis is inextricably bound to a specific uncertainty that also has to be modelled. Not only should the nominal system[4] be accurately modelled, but also the expected uncertainties that will be encountered. Accurate models for both the nominal system and the expected uncertainties surrounding it are essential for accurate robustness analysis.

## 1.5 Modelling via system identification

Most robustness estimation techniques require some sort of model of the plant to be controlled. Broadly speaking, these models can be obtained via inductive or deductive methods. Inductive models are obtained from the laws of physics and have the advantage of giving the designer a deeper understanding of the underlying dynamics of the plant [28][5]. In contrast, empirical models follow a deductive approach inferring models from experimental input/output measurements. System identification is the field of study devoted to the derivation of mathematical models solely from experimental measurements [28].

Although empirical models are less illuminating than models obtained via first principles, the mathematics that is required to obtain a specific analytical model may simply be intractable. This is the case when attempting to include electromagnetic cross-coupling that occurs within the stator of an AMB. The cross-talk between the different coils in an AMB stator has a noticeable effect on the response of a self-sensing AMB [17]. Consequently it is important to include this behaviour in the analytical model that is required for $\mu$-analysis. Unfortunately the typical eight-pole heteropolar AMB stator is an underdetermined system with only four input currents but eight pole fluxes influencing each other (i.e. there are more variables than equations). Deriving an analytical model for an AMB that includes the electromagnetic cross-coupling between the various poles is a challenging task to say the least.

[4] The nominal system model refers to the ideal system without any uncertainties included in the model.

[5] Inductive models can be divided into analytical models and simulation models. For MIMO plants *analytical models* can be either in state-space or transfer function matrix form. *Simulation models* however require the solution of successive differential and/or algebraic equations in order to obtain the response of the system as a function of time.

The only alternative is therefore to model self-sensing active magnetic bearings by means of system identification.

## 1.6 Research problem

Our journey thus far has narrowed the focus of this study down to the robustness analysis of DCM self-sensing AMBs. To date $\mu$-analysis hasn't been applied to the robustness analysis of self-sensing techniques. This is despite the fact that $\mu$-analysis is uniquely suited to the analysis of multivariable systems and theoretically capable of delivering stability margin estimates of minimal conservatism.

As noted previously, the accuracy of robustness estimates for self-sensing AMBs is critically dependent on a detailed and accurate model of both the nominal system and the expected uncertainties. System identification holds the most promise to deliver precisely such models.

In summary, this study entails using system identification to obtain the required models with which to estimate the stability margin of DCM self-sensing AMBs by means of $\mu$-analysis.

## 1.7 Methodology

The scientific method is the quest for knowledge that is amongst other things characterised by being true and objective in the sense that it repeatable and verifiable by the rest of the scientific community [29]. Validation therefore forms one of the central pillars of any scientific study. It is worrisome that the robustness analysis literature sometimes neglects this cardinal aspect of science in that the accuracy of robustness estimates are rarely validated against some other measure.

The accuracy of a robustness estimate is to a large extent determined by the validity of the models for the nominal system as well as the expected uncertainties which have to be catered for. This study will therefore be approached from a bottom-up perspective first focussing on the models and then culminating in the application of $\mu$-analysis. After each step (whether deriving models or estimating the final stability margin) all claims will be validated by comparison with the true, nonlinear AMB system.

## 1.8 Thesis overview and contributions

The above mentioned methodology also forms the basis for the structure of this thesis.

As a prelude to the development of models for the various components in a typical self-sensing AMB system, the next chapter describes all of the important aspects of two-degree of freedom AMBs, in particular DCM self-sensing. Chapter two furthermore gives an overview

of the relevant theory and practices of system identification that are used to obtain models for AMBs and their associated uncertainties. The chapter also places $\mu$-analysis in the context of robustness analysis in general and thoroughly motivates its use in this study.

Chapter three is devoted to the issues that arise when system identification is applied to self-sensing AMBs. More specifically a lot of effort is expended in ensuring that the eventual nominal models are indeed accurate linear time invariant models for the system components (as required by $\mu$-analysis). A new perspective on the boundary between linear and nonlinear behaviour in AMBs is also presented in this chapter.

The fourth chapter focusses on the application of $\mu$-analysis on the nominal models obtained by means of system identification. As previously noted, robustness analysis is impossible without an uncertainty description. Consequently, a significant portion of this chapter is devoted to the modelling of the uncertainties that can be represented when using a black-box approach (such as system identification). This chapter closes with the development of procedures to validate the stability margins estimated by $\mu$-analysis.

In chapter five everything is put together. All of the techniques described in the previous chapters are applied to obtain the required nominal and uncertainty models, as well as the final robustness estimates for various forms of uncertainty in the different components of a typical self-sensing AMB.

The last chapter (chapter six) makes closing arguments supporting the case for the following contributions made by this study:

- Successful application of $\mu$-analysis to DCM self-sensing AMBs.
- A new perspective on the boundary between linear and nonlinear behaviour in AMBs.
- Black-box modelling of DCM self-sensing via system identification.

# CHAPTER 2

# Setting the scene

*This study rests on three areas of expertise namely: self-sensing AMBs, system identification and robustness analysis. First of all, the component subsystems of both sensed and self-sensing 2-DOF AMB systems are discussed. To ensure repeatable results, the simulation platforms that form the basis of this study are also described. The basic principles upon which DCM self-sensing is based are given special attention, since this influences the subsequent system identification phase. Secondly, the vast field of system identification is concisely presented from the viewpoint of using system identification to find accurate nominal models for inherently unstable multivariable plants (namely AMBs). The final step of robustness analysis entails applying a suitable robustness estimation technique to obtain an estimate of the system's stability margin. Different robustness estimation techniques are therefore contrasted with the aim of finding the most suitable one for the analysis of 2-DOF self-sensing AMBs. The chapter finally closes with a section which makes the case for the uniqueness of this study.*

## 2.1 Summary of active magnetic bearings

### 2.1.1 Sensed AMBs

The focus of this study falls on an eight pole heteropolar two-degree of freedom (2-DOF) active magnetic bearing (AMB)[1]. In contrast with homopolar AMBs the magnetic flux moves perpendicular to the rotor axis [8]. This can be clearly seen from the schematic representation (figure 2.1) of the AMB that will be the subject for the rest of this study. Four electromagnets are arranged on the circumference of the stator. Each electromagnet is supplied with its own current from a power amplifier. Also shown in this figure is the pattern according to which the poles of the four electromagnets are winded. This gives rise to the north-south-south-north

[1]This choice was influenced by the existing software models and hardware implementation of self-sensing AMBs at our laboratory.

distribution of poles as one proceeds around the stator. (This winding scheme mimimizes the occurrence of electromagnetic cross-coupling [30].)

Not shown in figure 2.1 is the position of the backup bearings. Backup bearings are also known as retainer bearings and are situated in the airgap between the rotor surface and the stator poles. Retainer bearings are specialized conventional bearings with the sole purpose of preventing the rotor from physically touching the AMB stator. These bearings are only in use when the AMB is switched off (i.e. the rotor is resting on the retainer bearings) or during an AMB failure condition [8]. AMB failure can occur either due to a power failure, or mechanical overloading of the AMB, or in the event of a failure of some critical component inside the AMB control system. In this study, the inner diameter of the retainer bearing is 250 μm. Any excursion of the rotor beyond this perimeter signals delevitation or instability.

A simplified representation of the control system of a general AMB is shown in figure 2.2. The AMB plant consists of the stator, coils and rotor shown in figure 2.1. The position of the rotor is measured by two perpendicularly arranged position-sensors and subtracted from the reference position signal applied to the system input. The resulting error in position is converted by a compensator (typically a PID controller) into a reference current, which in turn is amplified by the power amplifier to the correct current value. In the AMB plant this current exerts an electromagnetic force on the rotor thereby closing the control loop.

Active magnetic suspension (for a single magnet 1-DOF AMB) entails that an attractive magnetic force be exerted by an electromagnet that will counteract the gravitational force exerted by the earth. The attractive electromagnetic force exerted by a current-carrying coil on a

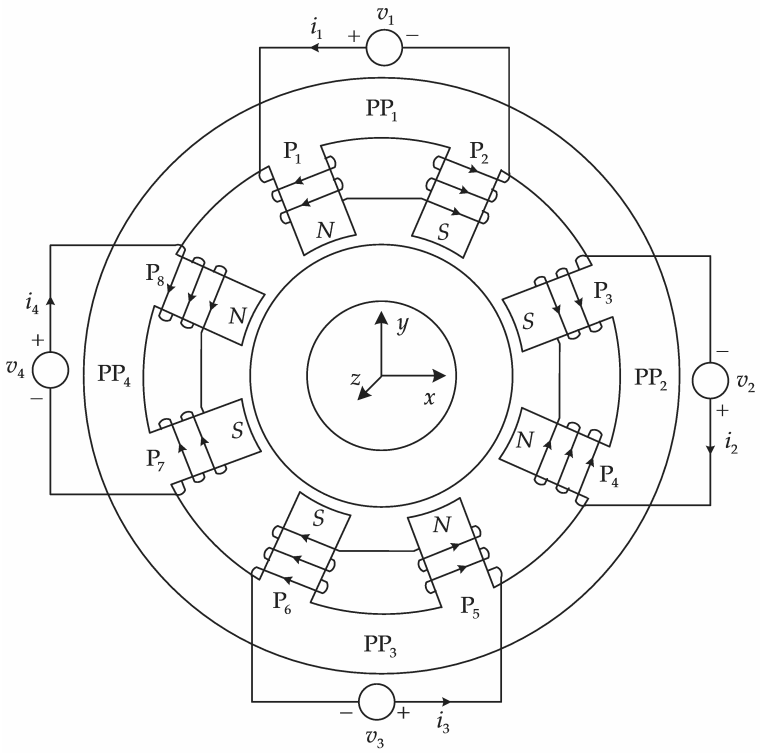


Figure 2.1: Stator of an 8-pole heteropolar AMB (with permission from [31])

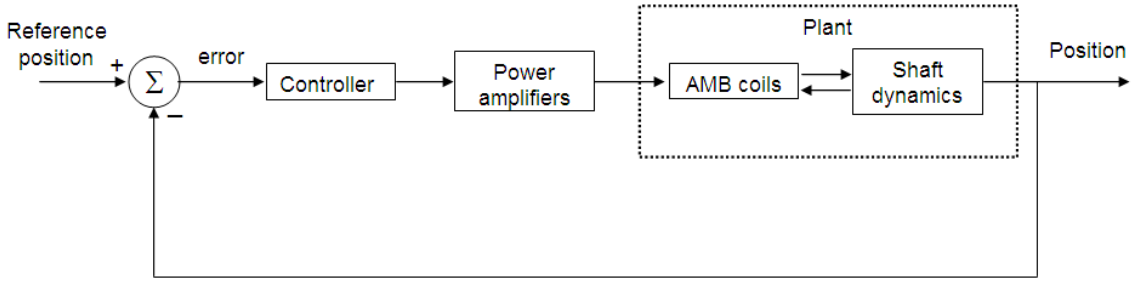


Figure 2.2: Block-diagram of an AMB

ferromagnetic material is also known as a reluctance force [8]. This force is derived from the energy stored in the magnetic field. Any small change in the volume of the airgap would result in an increase in the energy stored in the field. This increase in energy must be supplied by an external force (which explains why fridge magnets generally don't fall off on their own).

If only the top coil in figure 2.1 is allowed to carry a current and electromagnetic cross-coupling is ignored, the force exerted by the resulting 1-DOF [2] can be modelled by the following equation [8]:

$$f_m = \mu_0 \left( \frac{Ni}{l_c/\mu_r + 2x_g} \right)^2 A \cos(\theta) \tag{2.1}$$

where $l_c$ is the length of the magnetic path (excluding the airgap);
$\mu_0$ is the permeability of free space;
$\mu_r$ is the relative permeability of the AMB stator;
$x_g$ is the distance of the airgap between the stator and rotor;
$N$ is the number of windings in the coil;
$i$ is the current flowing in the coil;
$A$ is the pole-face area; and
$\theta$ is the angle between the vertical axis and the normal line to the pole face.

The force equation for a 1-DOF AMB given in (2.1) shows the relationship between the applied current in the coil, the position of the shaft within the airgap and the electromagnetic force exerted on the rotor by the stator pole. Clearly, the force is proportional to the square of the current as well as inversely proportional to the square of the airgap between the stator and rotor. This equation disregards the effects of fringing and leakage of magnetic flux and is only valid under the following assumptions [8]:

- permeablity of the iron is constant;
- only small variations in the airgap are allowed; and

[2] A *one degree-of-freedom* (1-DOF) AMB allows movement in only one dimension (e.g. the vertical axis in figure 2.1), while a *two degree-of-freedom* (2-DOF) AMB allows movement along both the horizontal and vertical axes of figure 2.1.

- uniform flux in the airgap (i.e. a homogeneous field).

Even when the effects of magnetic saturation and hysteresis have been disregarded, AMBs are still nonlinear devices, as can be seen from equation (2.1). To take advantage of the existing body of knowledge on linear systems, most AMB designers opt for linearising the AMB around a setpoint and controlling it as if it were a linear system. The range over which a linear approximation is valid, can be increased by driving opposing electromagnets in the AMB stator with mirror images of the same current signal. This is known as differential driving mode and is exhibited in figure 2.3 [8].

The schematic drawing in figure 2.3 only illustrates differential driving mode for the top and bottom electromagnets of the AMB in figure 2.1, but the same principle also holds for the other two electromagnets. The output of the controller is a current reference signal which is added to and subtracted from a bias current level. (The latter bias current is typically chosen somewhere in the centre of the linear region in the magnetic material's hysteresis curve.) The end result is that the forces exerted by respectively the top and bottom electromagnets are symmetrical about some bias force level. In the absence of gravity, the nett electromagnetic force applied to the point mass is consequently given by:

$$f_m = k\left[\frac{(i_0 + i_y)^2}{(x_g)^2} - \frac{(i_0 - i_y)^2}{(x_g)^2}\right] \tag{2.2}$$

where the constants $\mu_0$, $N$, $A$ and $\cos(\theta)$ have been subsumed into the constant $k$.

After linearizing (2.2) for small position deviations $(\delta_y)$ around some bias position $(y_0)$, the force exerted by an AMB in the vertical degree of freedom can be modelled as follows:

$$f_m = k_i i_y + k_s \delta_y \tag{2.3}$$

where the current- and position stiffness constants are respectively given by [32]:

$$k_i = 2\frac{\mu_0 N^2 i_0 A}{y_0^2}\cos(\theta) \qquad k_s = -2\frac{\mu_0 N^2 i_0^2 A}{y_0^3}\cos(\theta) \tag{2.4}$$

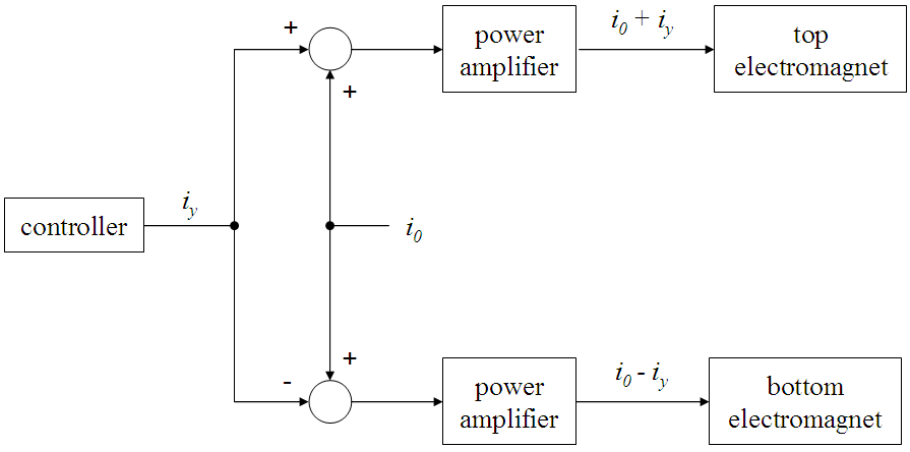


Figure 2.3: Schematic diagram of differential driving mode

### 2.1.2 Simulation model for a sensed 2-DOF AMB

This study's results are based on simulation studies performed with accurate simulation models of both sensed and self-sensing AMBs. (In a simulation model each component in the system is modelled by means of one or more differential and/or algebraic equations. These equations may be linear or nonlinear. The simulation model then entails that these equations are solved in succession for each component of the control system at each specific sampling instant.) The accuracy of these simulation models have been established in previous studies ([31] and [17]) by comparison with experimental results. (It must be noted that the simulation model for the self-sensing AMB is not as accurate as the simulation model for the sensed AMB. The inaccuracies of the self-sensing AMB simulation model can be attributed to unmodelled behaviour in the electronic circuitry of the hardware implementation [17].)

From figure 2.2 the simulation model for the sensed 2-DOF AMB consists of a controller, four power amplifiers, a magnetic circuit model, point mass and ideal position sensors. This simulation model forms the core of the self-sensing simulation model (which is characterised in section 2.1.4). (With the exception that the $y$-axis position sensor in the sensed AMB is replaced by a self-sensing algorithm.)

Although AMBs are multivariable systems, they are in practice often controlled with decoupled PID controllers, each responsible for a single axis of movement. This is the case in the sensed 2-DOF AMB simulation model where each axis is controlled separately with identical PD controllers.

Power amplifiers are responsible for controlling the amount of energy stored in the total AMB magnetic circuit (comprising the electromagnets, stator, rotor and airgap) [33]. Two-state switching power amplifiers are implemented in the sensed AMB simulation model. Switching amplifiers are noisy, but more efficient than linear amplifiers. In most applications of switching amplifiers, the unwanted switching ripple in the output signal is filtered out by means of a low-pass filter. For demodulation-based self-sensing algorithms, the switching ripple is an essential byproduct of the power amplifier, since the current ripple contains information on the position of the rotor [33]. In the sensed 2-DOF AMB simulation each of the four stator electromagnets is powered by its own power amplifier. The duty cycle of each of these amplifiers is constrained to remain within the interval of 25 % to 75 % and is controlled with a PI controller.

The remainder of the sensed-AMB simulation model is concerned with the AMB plant, which is dominated by the electromagnetic calculations required to model the force exerted on the point mass. The flux distribution in the AMB magnetic circuit is modelled by means of a reluctance network model [34]. This lumped parameter model entails that each section of the AMB magnetic circuit (e.g. the airgap between a particular pole and the rotor or the stator back-iron between two specific poles) is modelled by means of an equivalent electrical circuit. The latter network of reluctances is solved algebraically to obtain the magnetic flux in each section of the AMB [31]. The response of the reluctance network model is enriched with two additional models: one responsible for predicting eddy currents and the other for modelling magnetic hysteresis and saturation.

Eddy currents are induced in the laminated iron of the stator and rotor due to the switching

current flowing in the electromagnet coils. Eddy currents are modelled in the AMB simulation model by means of another equivalent circuit model consisting of an imaginary single coil surrounding the magnetic material under scrutiny. This single coil then acts as a source to a ladder network of resistors and inductors [34]. In this simulation the ladder network is truncated to a single resistor without significant loss in accuracy.

Numerous models are available for magnetic saturation and hysteresis. Few are however suitable for an AMB simulation model due to computational constraints. In the AMB simulation model hysteresis and saturation are modelled with a parameterized analytical model [31]. This model mathematically mimics the form of the hysteresis curve without replicating the underlying physical causes of the phenomenon.

The combination of the reluctance network model, with the eddy current and hysteresis models makes it possible to accurately calculate the flux density in the airgap of each of the eight poles in the AMB. The final electromagnetic force exerted by the AMB on the point mass is proportional to the square of the magnetic flux density [8], [31]. Finally, the physical movement of the point mass is determined by means of the well-known Newton laws.

The specific AMB modelled in the nonlinear simulation model is characterized in table 2.1. (Some of the physical measurements of the AMB are clarified in figure 2.4. The particular quantities are identified in table 2.1 by means of symbols.)

Table 2.1: Summary of the simulated sensed AMB

| Description | Value |
|---|---|
| Proportional constant (position PD controller) | 20,000 |
| Derivative constant (position PD controller) | 38 |
| Proportional constant (power amplifier PI controller) | 1 |
| Integral constant (power amplifier PI controller) | 0.01 |
| Relative magnetic permeability | 4,000 |
| Power amplifier switching frequency | 20 kHz |
| Lower bound on power amplifier duty cycle | 25 % |
| Upper bound on power amplifier duty cycle | 75 % |
| Supply voltage | 50 V |
| Bias current | 3 A |
| Resistance of coil wires | 0.2 Ω |
| Coil turns | 50 |
| Mass of the point mass | 3 kg |
| Axial bearing length | $49.15 \times 10^{-3}$ m |
| Journal inner radius $(r_r)$ | $15.88 \times 10^{-3}$ m |
| Journal outer radius $(r_j)$ | $34.95 \times 10^{-3}$ m |
| Stator pole radius $(r_p)$ | $35.60 \times 10^{-3}$ m |
| Stator back-iron inner radius $(r_c)$ | $60.00 \times 10^{-3}$ m |
| Stator outer radius $(r_s)$ | $75.00 \times 10^{-3}$ m |
| Pole width $(r_w)$ | $13.89 \times 10^{-3}$ m |

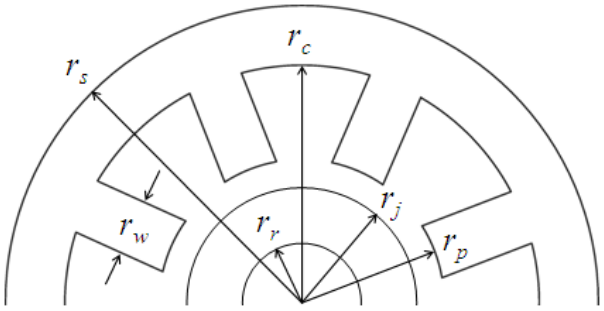


Figure 2.4: Physical measurements of an AMB

### 2.1.3 Principles of self-sensing

" Self-sensing bearings detect the position of the supported object by monitoring the electrical impedance of the actuator." This definition by Eric Maslen ([14]) emphasizes the fact that self-sensing capitalizes on the principle that the inductance of an AMB stator coil is influenced by the airgap.

To see how the impedance of an AMB coil is influenced by the airgap take for example the magnetic circuit in figure 2.5 [11]. This well-known circuit also functions as a simplified model for a 1-DOF AMB. To simplify the analysis eddy current effects are neglected (as well as magnetic leakage and fringing). Furthermore, it is assumed that the magnetic flux has a uniform distribution throughout the magnetic circuit. By making use of the laws of Faraday, Ohm and Ampere, the relationship between the coil voltage $(v(t))$ and current $(i(t))$ is given by equation (2.5) [35]. Clearly, the relationship between the coil voltage and current is influenced by the instantaneous position of the rotor within the airgap.

$$v(t) = \left(\frac{\mu_0 N^2 A}{2x_g(t) + l_c/\mu_r}\right)\frac{di(t)}{dt} - 2\left(\frac{\mu_0 N^2 A i(t)}{\left(2x_g(t) + l_c/\mu_r\right)^2}\right)\frac{dx_g(t)}{dt} + i(t)R \tag{2.5}$$

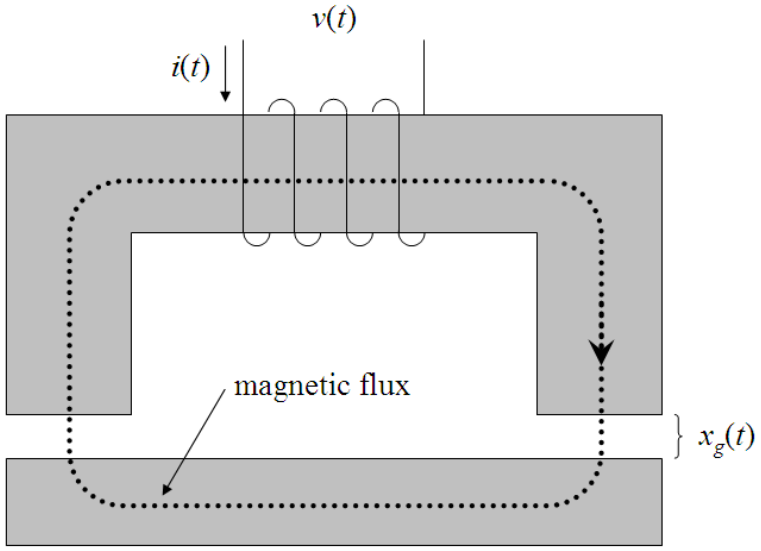


Figure 2.5: Magnetic circuit of a 1-DOF AMB

where $R$ denotes the electrical resistance of the coil wire.

The self-sensing problem therefore entails deducing the position of the AMB rotor from the measured coil current and voltage.

Different approaches have been taken in the literature to solve the self-sensing problem. Modulation based self-sensing techniques have proven themselves to be more robust than the state-estimation approach ([16], [11]). Modulation based self-sensing techniques can in turn be classified into frequency modulation and amplitude modulation techniques [11]. Frequency modulation techniques require hysteresis power amplifiers which are uncommon in typical AMB applications [17]. Consequently, the broad focus of this study is on amplitude modulation self-sensing techniques.

The high efficiency of switching power amplifiers has made them ubiquitous in modern AMB systems. From the perspective of self-sensing, the switching ripple in the coil current signal caused by these power amplifiers is an added benefit, since this current ripple is directly related to the position of the AMB rotor. The reason for this is that class D amplifiers perform pulse-width modulation. In the absence of an output lowpass filter the output spectrum of a switching power amplifier contains the intended low frequency current signal as well as numerous modulated components[3] [36]. Consequently, the position of the rotor can be derived via amplitude demodulation of one of these modulated components (typically the component situated at the switching frequency) [11].

Amplitude demodulation invariably involves the use of bandpass and lowpass filters. The additional phase lag introduced by these filters result in poor stability margins for self-sensing techniques based on amplitude demodulation [17]. More robust self-sensing can be attained by directly measuring the current ripple at the switching frequency and converting the measured ripple into a position estimate [17]. This technique is known as the direct current measurement (DCM) method and is the specific focus of this study.

### 2.1.4 DCM selfsensing

DCM self-sensing stems from the fact that the rotor position is directly related to the peak value of the ripple current during a switching cycle. This becomes obvious when (2.5) is simplified further to its bare essentials. By neglecting the coil resistance, as well as nonlinear magnetic effects and assuming that the AMB rotor moves very slowly compared to the rapid variation in the coil current, the airgap can be expressed as [17]:

$$x_g(t) = \left(\frac{\mu_0 N^2 A}{2v(t)}\right)\frac{di(t)}{dt} - \frac{l_c}{\mu_r} \tag{2.6}$$

From (2.6) it is clear that the airgap can be estimated from a direct measurement of the peak ripple current value. In DCM self-sensing the rotor position is therefore estimated from the

[3] If the spectrum of the position signal is situated at $f_x$ and the switching frequency of the amplifier is $f_s$, then modulated components will be found at $f_s$, $f_s \pm 2f_x$, $2f_s \pm f_x$, $2f_s \pm 3f_x$ etc. [36].

following equation [17]:

$$\begin{aligned} \hat{y}_y &= y_{linear} - y_{nonlinear} \\ &= \frac{1}{k_{DCM}} i_{\max} - \frac{1}{k_{DCM}} \left( k_2 \hat{B}^2 + k_1 \hat{B} + k_0 \right) \end{aligned} \tag{2.7}$$

where $y_{linear}$ is the uncompensated estimated position;
$y_{nonlinear}$ represents an empirically determined term that compensates the estimated position for nonlinear effects;
$i_{\max}$ denotes the measured value of the peak ripple current during one switching cycle;
$k_{DCM}$ represents a conversion constant between current and position;
$\hat{B}$ is an estimate for the magnetic flux density in the particular AMB stator pole;
$k_{0,1,2}$ are empirically determined polynomial coefficients.

The peak ripple current is deduced during the course of a single switching cycle $(T_{PA})$[4] of the raw coil current waveform in the following fashion:

$$i_{\max} = \max_{T_{PA}} \left( i(t) - \overline{i(t)} \right) \tag{2.8}$$

where the average coil current value over the whole switching period is denoted by $\overline{i(t)}$.

DCM self-sensing is completely described by (2.7) and (2.8) with the exception of duty cycle compensation. In [11] it is shown that the amplitude of the ripple current is a function of both the size of the airgap and the duty cycle of the power amplifier. This phenomenon is also known as *force feed-through* and is usually eliminated by making use of both the coil current and voltage waveforms in other amplitude modulation self-sensing techniques (e.g. [37] and [11]).

Alternatively, the dependency of the estimated position on the duty cycle can be removed by constraining the duty cycle to be exactly the same every time the ripple current is measured [17]. Obviously the twin demands of controlling the rotor position (which requires a variable duty cycle) and estimating the rotor position (which requires a constant duty cycle) can only be met through compromise. In DCM self-sensing the current ripple is measured every second switching cycle (during which the duty cycle is fixed at 50 %). Control is performed during the remaining alternate switching cycles. An example of the resulting coil current signal is shown in figure 2.6[5].

Niemann only implemented DCM self-sensing in the $y$-axis dimension of a 2-DOF AMB [17]. (The $x$-axis position of the rotor was measured with normal position sensors.) Consequently the simulation model for DCM self-sensing also only provides estimates for the $y$-axis position of the AMB rotor. Although the behaviour of the DCM self-sensing simulation model doesn't correlate exactly with the hardware implementation ([17]), it definitely does model the main characteristics of the hardware implementation.

[4] The switching period for a 30 kHz switching frequency amounts to 33.3 µs.
[5] The characteristic sawtooth waveform is caused by eddy current distortion.

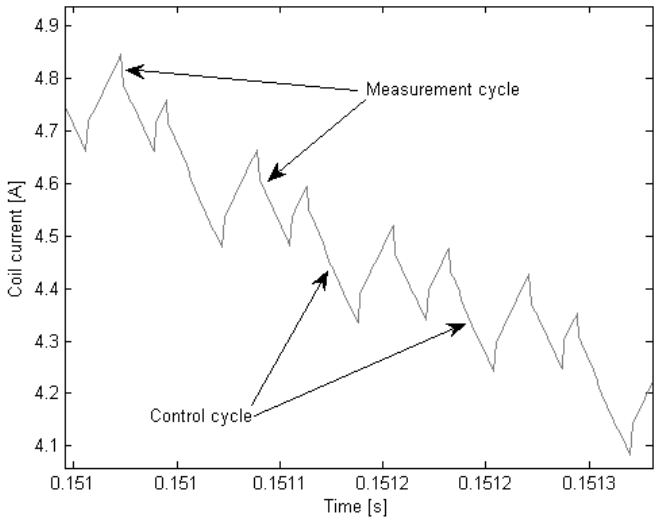


Figure 2.6: Typical coil current waveform showing measurement and control cycles

In most respects the self-sensing AMB is the same as the sensed AMB. The small differences between the self-sensing AMB and its sensed predecessor are highlighted in table 2.2. All of the results in the rest of this study were obtained by means of accurate simulation models for both the sensed and self-sensing AMBs summarised in tables 2.1 and 2.2.

## 2.2 System identification applied to AMBs

### 2.2.1 Motivation

Simulation models are useful for replicating the nonlinear behaviour of AMBs. Formal robustness analysis however requires accurate analytical models for the AMB and its components.

From figure 2.2 the main components of an AMB system are: a controller, power amplifier, AMB plant (consisting of the stator and rotor) and position sensors (or self-sensing module).

Table 2.2: Summary of the simulated selfsensing AMB

| Description | Value |
|---|---|
| Integral constant (position PID controller) | 700,000 |
| Proportional constant (position PID controller) | 20,000 |
| Derivative constant (position PID controller) | 38 |
| Proportional constant (power amplifier PI controller) | 0.7 |
| Integral constant (power amplifier PI controller) | 0.01 |
| Power amplifier switching frequency | 30 kHz |
| Lower bound on power amplifier duty cycle | 2 % |
| Upper bound on power amplifier duty cycle | 98 % |
| Mass of the point mass | 3.86 kg |

Inaccurate models for systems may result in either instability or loss in performance of the eventual control system [4]. Similarly, accurate robustness analysis requires that each of the constituent parts of an AMB be modelled accurately.

In section 2.1.1 it was determined that the magnetic force exerted by an AMB on its rotor is a nonlinear function of both the current flowing in the coils and the position of the rotor within the airgap. DCM self-sensing is similarly a nonlinear subsystem due to the peak-picking operation performed in (2.8). Furthermore, the requirement of fixing the duty cycle to 50 % on alternate switching cycles makes DCM self-sensing time-variant as well. The switching power amplifiers employed in AMBs are also nonlinear and time-variant. Although it is possible to model PWM generators with linear averaging state-space models [38], these LTI models are only valid for small excursions around the steady state. Accurate stability analysis of PWM systems require nonlinear and time-variant models combined with Lyapunov analysis [39]. The only component in the 2-DOF AMB system that it truly LTI is the PID controller.

In this study the stability margin is estimated by means of $\mu$-analysis. (This choice is motivated in section 2.3.) The fundamental prerequisite for $\mu$-analysis is that the system under scrutiny be modelled with an analytical LTI model (either a transfer function matrix or a state-space model). Consequently, each of the components of the AMB system has to be approximated as accurately as possible with LTI models.

It is important to ensure that the LTI model for the power amplifier has the capability to approximate the power amplifier's characteristic switching behaviour. Maslen *et al.* have found that the switching ripple current improves the robustness of amplitude modulation based self-sensing AMBs [13]. Consequently, any robustness analysis that ignores this critical feature is bound to deliver pessimistic assessments (e.g. [18]). In fact, this conclusion holds true for stability analyses of more general PWM systems [40].

Fortunately, it is possible for LTI black-box models obtained via system identification to closely approximate the oscillatory behaviour of switching power amplifiers if the order is chosen sufficiently high. This is in contrast with first principles analytical modelling that perforce make limiting assumptions to obtain LTI models [41]. System identification holds out the promise of delivering the best possible LTI models for nonlinear time variant systems that will still contain the dominant dynamics that ensure stable levitation in self-sensing AMBs.

Another advantage of system identification is that it doesn't have any trouble in modelling cross-coupling occurring in a system. This is a huge benefit since electromagnetic cross-coupling has a large effect on self-sensing implemented on heteropolar AMBs [42]. In contrast, electromagnetic cross-coupling is quite difficult to model from first principles due to the AMB plant being an underdetermined system.

All of these considerations make system identification the best option for obtaining LTI models for the various AMB subsystems.

### 2.2.2 Introduction to system identification

System identification is an empirical modelling approach "...where the model of a system or process is derived solely from experimental input/output messurements ..." [28]. Any modelling exercise is an iterative process and system identification is no exception on this rule. Armed with powerful numerical optimization algorithms, the task of the engineer in system identification reduces to the process of falsifying a multitude of candidate models [43]. The basic steps involved in obtaining a model by means of system identification are set out in the flowchart in figure 2.7 [44].

System identification begins with the design of a so-called optimal experiment. The objective of this experiment is to obtain input-output data of the system that is under investigation. The design of the data capturing experiment in turn entails defining the experimental conditions so that maximally informative data will be harvested [45]. Informative data captures the essential behaviour of the system and is able to distinguish between candidate models of varying quality [44]. Specific issues at stake and choices that have to be made during the experiment design step are:

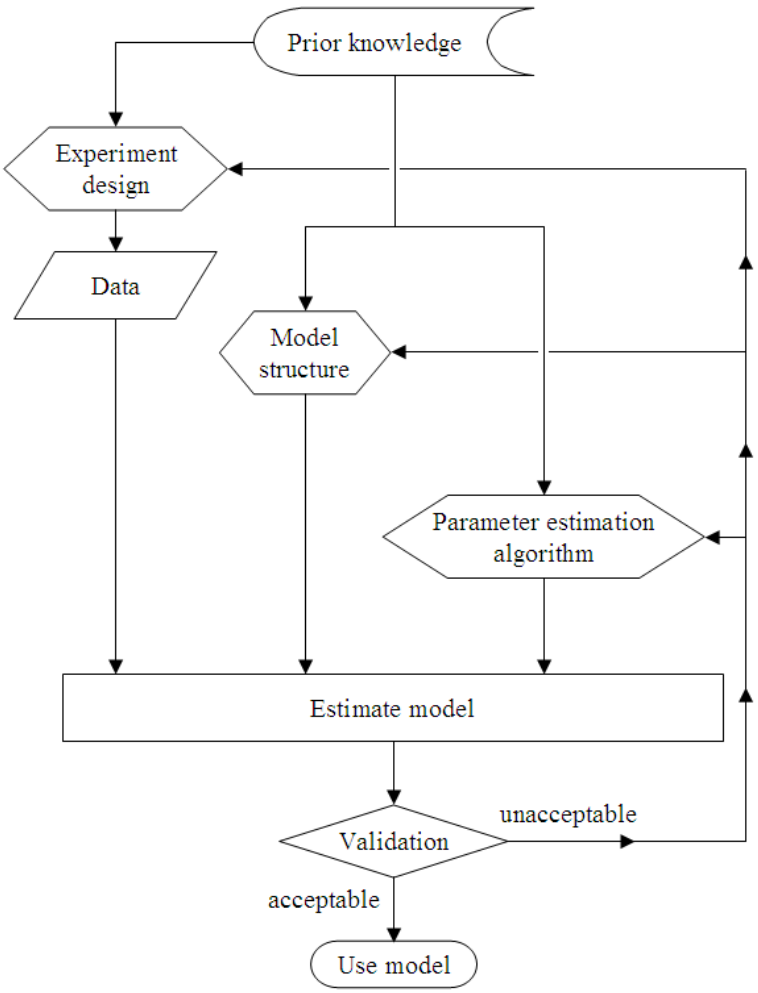


Figure 2.7: System identification as an iterative process

- Should the plant be operated in open-loop or closed-loop?
- Which inputs of the plant must be excited and which outputs have to be sampled?
- What is the best sampling frequency for the particular system?
- Define the nature and duration of the excitation signal with which the plant will be interrogated.

The second step of the system identification process involves choosing a suitable parameterized model structure. In black-box system identification the eventual model is a parameterized function of the current and delayed sample values of the input variable(s). By changing the number of adjustable parameters (the order of the model) as well as their specific values, the characteristics and behaviour of the model can be modified. More detail on this step will be given shortly (in section 2.2.3).

Once a specific parameterized model structure has been decided on, an appropriate parameter estimation algorithm has to be chosen. Parameter estimation algorithms are responsible for calculating the values of the model's parameters so that the model's response closely imitates the measured behaviour of the original system. Typically these algorithms are numerical optimization algorithms that seek to minimize some criterion or cost function defined on the data (e.g. least-squares minimization). Genetic algorithms can also be used in stead of classical parameter estimation algorithms [46].

Lastly, the candidate model has to be validated. The purpose of this step is to ascertain whether the candidate model is of sufficient quality for its intended purpose [44]. Validation entails testing the ability of the candidate model to duplicate the system's behaviour. Not only should the model's response closely correspond with that of the system on the data that was used for parameter estimation, but more importantly also on data that wasn't included in the estimation subset[6]. The candidate model can be evaluated on its ability to *simulate* the response of the system (when supplied with the same inputs) or its ability to *predict* the response of the system a few time steps in advance (in the case of an unstable system)[7].

Model validation requires objective measures of the quality of a candidate model. Possible measures are the coefficient of determination (which is discussed in section 3.1.3) and the model's residuals. The residuals of a model are defined as follows:

$$\epsilon(t) = y(t) - \hat{y}(t) \tag{2.9}$$

where $y(t)$ represents the measured output of the system, while $\hat{y}(t)$ denotes the output of the model.

Ideally, the residuals of a good model will be that part of the measured response which is impossible to simulate or predict (i.e. pure random noise). The residuals should therefore

[6]The data used for parameter estimation is known as the estimation subset, while the validation subset comprises another, separate set of data reserved for testing purposes only.

[7]A $k$-step-ahead predictor calculates the value of the output of the system $k$ time steps in advance from the current time step based on knowledge of the current state of the system as well as a history of its inputs up and to the present [44].

resemble white noise and be independent of the input signal [44]. Another criterion which should be taken into account when evaluating candidate models is the principle of parsimony [44]. This principle is also known as Ockham's razor and states that among competing models of equal quality the candidate with the lowest order should be chosen [29].

In the event of the candidate model being of insufficient quality, the analysist has the option of modifying any or all of the following aspects of the model:

- the experimental conditions under which data was captured;
- the model order and/or model structure; and
- the specific parameter estimation algorithm that was used.

### 2.2.3 Parameterized model structures

In the absence of any external disturbances or noise, an LTI system is completely described by its impulse response or its transfer function (in the frequency domain). Both the impulse response and transfer function of a practical LTI system can be empirically determined and then mathematically expressed as follows [44]:

$$y(t) = G(q)u(t) \tag{2.10}$$

where $u(t)$ and $y(t)$ represent the system input and output signals respectively and $G(q)$ is the so-called *transfer operator*. The transfer operator[8] of the system in (2.10) is defined as follows ([44] ):

$$G(q) = \sum_{k=1}^{\infty} g(k)q^{-k} \tag{2.11}$$

where the backward shift operator $q^{-1}$ is responsible for delaying the input signal by one sample period (i.e. $q^{-1}u(t) = u(t-1)$).

The impulse response of practical systems is causal and for all intents and purposes finite in duration. Consequently, the transfer operator of an LTI system can be conveniently summarized by means of a set of parameters. The LTI system can now be mathematically modelled with a *parameterized* model as follows:

$$y(t) = G\left(q, \boldsymbol{\theta}\right) u(t) = \sum_{k=1}^{N} \theta_k u(t-k) \tag{2.12}$$

The behaviour of the parameterized model in (2.12) is completely determined by the parameter vector:

$$\boldsymbol{\theta} = \begin{bmatrix} \theta_1 & \theta_2 & \cdots & \theta_N \end{bmatrix} \tag{2.13}$$

[8]The transfer operator is quite similar to the z-transform of the discrete-time impulse response $g(k)$, which is in turn defined as:

$$G(z) = \sum_{k=1}^{\infty} g(k)z^{-k}$$

.

The parameterized model in (2.12) is a specific example of the output error (OE) model structure[9] [44]. Different model structures are possible, depending on how the internal dynamics of the system are modelled. Other examples of families of model structures include: ARX (autoregressive with external inputs), ARMAX (autoregressive moving average with external inputs) and Box-Jenkins models. In e.g. ARX models, the system is modelled by the following general difference equation [44]:

$$y(t) + a_1 y(t-1) + \cdots + a_N y(t-N) = b_1 u(t-1) + \cdots + b_M u(t-M) \tag{2.14}$$

The parameterized transfer operator of an ARX model can therefore be defined as:

$$G(q, \boldsymbol{\theta}) = \frac{B(q)}{A(q)} = \frac{b_1 q^{-1} + \cdots + b_M q^{-M}}{1 + a_1 q^{-1} + \cdots + a_N q^{-N}} \tag{2.15}$$

with the following parameter vector:

$$\boldsymbol{\theta} = \begin{bmatrix} a_1 & a_2 & \cdots & a_N & b_1 & \cdots & b_M \end{bmatrix}$$

Parameter estimation is the process during which the parameters in the model's parameter vector are adjusted on the basis of observed input and output data in order that the model's response is as close as possible to the original observed system's response [44]. The data used during parameter estimation can be either in the time domain or in the frequency domain. Furthermore, the final parameterized models can be linear or nonlinear. One would also not be surprised by the existence of numerous different parameter estimation algorithms, each with its particular strengths, weaknesses and niche area. Clearly, the prospective user of system identification technology is confronted by a bewildering array of choices. With this in mind, the next section attempts to dichotomize the broad field of system identification in a few general approaches.

### 2.2.4 Classification of system identification techniques

The result of any classification process depends on the specific segregation measure used. Similarly, any overview of a diverse field of study (such as system identification) merely reflects a particular perspective on a complex subject. The dichotomy in figure 2.8 should therefore be viewed as merely one viewpoint on the topic[10].

First of all distinction can be made between system identification techniques that specialize on LTI models in exclusion to the more general class of nonlinear models. This is also the approach that was taken in this study, since $\mu$-analysis requires an LTI model of the system. Nonlinear systems can be identified by means of a variety of techniques including artificial

[9] In which no noise source is included.

[10] Note that only parametric system identification techniques are considered in this overview. Although nonparametric techniques such as the empirical transfer function estimate (ETFE) also belong to the broad class of empirical modelling techniques, the data reduction obtained by nonparametric techniques is much less than that of parameterized models. Nonparametric techniques are also unsuitable for $\mu$-analysis.

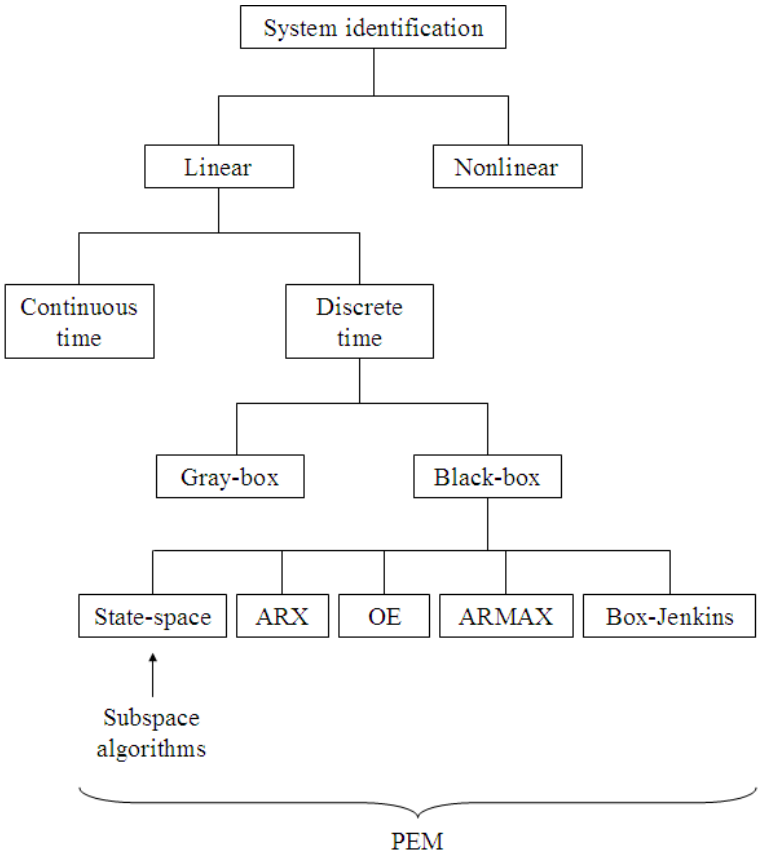


Figure 2.8: A bird's eye view on system identification

neural networks that are quite adept at duplicating any static or dynamic nonlinear input-output mapping [44]. By combining the learning capabilities of neural networks with the easily understandable rule-based structure of fuzzy logic models, neuro-fuzzy models are born. Neuro-fuzzy models can be estimated solely from data to result in transparent nonlinear models that not only closely reproduce the behaviour of the nonlinear system, but also give insight into the reasons for its behaviour [47]. Such models are known as grey-box models (which will be contrasted with black-box models shortly).

Within the confines of LTI system identification, the original system can be modelled either by means of continuous-time models ([48]) or discrete-time models ([44]). These models are typically expressed in terms of transfer functions in respectively the s-plane or the z-plane.

Continuous-time models are also known as frequency domain models and are obtained from discrete-time sampled data which has been transformed to the frequency domain via the fast Fourier transform [49]. Parameter estimation is typically done by means of a maximum likelihood algorithm [48] (in contrast with discrete-time system identification which often employs least-squares algorithms for parameter estimation). The use of maximum likelihood parameter estimation results in more accurate models that come at the cost of an increased computational burden [48].

Another disadvantage of discrete-time models is that they can only be accurate for frequencies

significantly lower than the Nyquist frequency [48]. This is due to the fact that discrete-time models approximate differentials with finite differences, which places an inherent limit on the accuracy of z-plane transfer functions. Unfortunately, currently available commercial software for frequency domain system identification is limited to SISO systems. In contrast, multivariable discrete-time models can be relatively easily obtained for selected model structures (e.g. state-space models and ARX models) [26].

As is the case with nonlinear system identification techniques, LTI discrete-time models can also be divided into black-box and grey-box models. Both are parameterized models. In black-box models the parameter values bear no relation to the physical system; they are merely a means to an end (namely to ensure an accurate input-output mapping) [44]. Grey-box models, in contrast, have a model structure which is derived from physical laws, but whose parameter values have to be obtained via parameter estimation. In grey-box models the adjustable parameters do have physical meaning [44].

In this study black-box system identification will be used for reasons already given in section 2.2.1. Black-box LTI models in turn can be further categorized on the basis of the functional structure of the models. Examples of different model structures include the well-known state-space representation, output-error (OE) structure (of (2.12)), ARX structure (of (2.14) and (2.15)), ARMAX and Box-Jenkins model structures [44]. The next chapter gives more details on which one of these model structures is best suited for modelling a 2-DOF AMB.

The model structure also influences the specific parameter estimation algorithm(s) that can be used to tune the model to mimic the system at hand. The well-known least-squares optimization algorithm forms part of the larger family of prediction-error method (PEM) parameter estimation algorithms. PEM algorithms are applicable to all of the black-box discrete-time model structures. Other approaches such as subspace algorithms (e.g. N4SID) can only be used for state-space models. Details on the advantages and disadvantages of PEM and subspace methods are discussed in chapter 3.

### 2.2.5 Closed-loop system identification

System identification can only deliver models if it is supplied with data of the inputs and outputs of the system to be modelled. AMBs are however inherently unstable, which poses a problem from a data collection viewpoint. The answer to this dilemma is to employ closed-loop system identification.

Closed-loop system identification entails operating a control system in closed-loop and building models for the component sub-systems from input-output data gleaned from the system's interconnections. This technique allows one to fit black-box models to the power amplifier, AMB plant and self-sensing module of an operating AMB system. Closed-loop system identification is not only useful for modelling unstable plants, but also in process control applications with severe cost implications associated with data gathering [50]. In the latter applications, it makes a lot of sense to slightly perturb an operating plant in order to identify a model for it rather than stopping production altogether for a few practice runs to gather data.

Unfortunately the primary advantage of negative feedback, namely that feedback reduces the closed-loop system's sensitivity for disturbances to the plant ([43]), complicates matters for system identification. The nett effect of feedback is therefore that the reduced sensitivity of the system results in less informative data for parameter estimation [44]. Special precautions have to be taken to ensure that the applied perturbation signals are still persistently exciting at the input of the plant (see section 3.3).

There are only three general approaches to closed-loop system identification namely: direct identification, indirect identification and joint input-output identification [44]. These approaches will now be briefly described for the simple closed-loop control system shown in figure 2.9. In this figure the signals $r(t)$ and $y(t)$ respectively denote the input and output of the closed-loop system, while $u(t)$ represents the actual input to the plant $(G_P(s))$. The controller is modelled with the transfer function $(G_C(s))$, while the output of the noise model $G_{noise}(s)$ represents the specific noise which impacts the plant. (The specific noise signal is merely a filtered version of white noise.)

Direct identification entails that the control system be operated in closed-loop while the system is subjected to a small perturbation applied anywhere in the loop. The desired subsystem in the loop can then be modelled by merely extracting data from its specific inputs and outputs [44]. If for instance the plant in figure 2.9 has to be modelled, it is only necessary to sample the signals $u(t)$ and $y(t)$ while the system is in operation. Direct identification doesn't require special parameter estimation algorithms. Neither is this approach dependent on the nature of the rest of the feedback system. Another advantage of direct identification is that it can model unstable plants (provided that the closed-loop system is stable). The only disadvantages of direct identification are that it requires a good noise model of the target subsystem [44] and that it also requires a high signal-to-noise ratio on the plant input [50].

Due to its simplicity and accuracy, direct identification is the approach used in this study. In contrast, the remaining two approaches are quite complicated with an increased risk of obtaining suboptimal models. They will therefore only be briefly introduced.

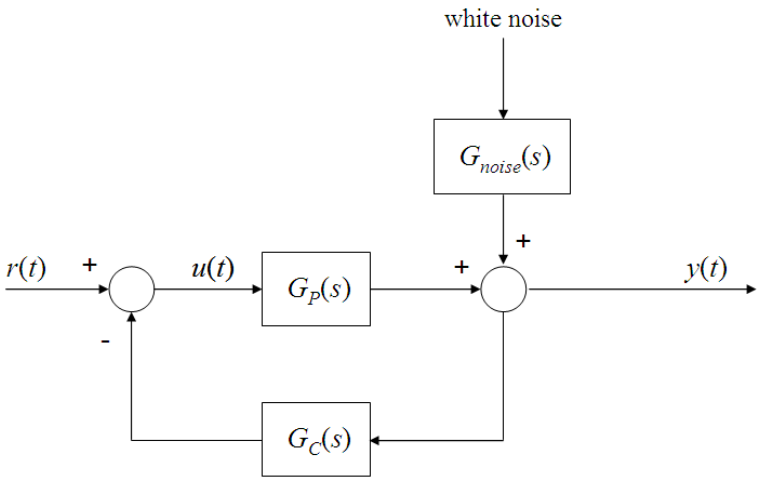


Figure 2.9: Block-diagram of a simple closed-loop system

Indirect identification is a two step process. First of all a black-box model is identified for the complete closed-loop system. (I.e. a model is identified on the basis of signals $r(t)$ and $y(t)$ in figure 2.9.) The second step entails that a model for the plant is mathematically derived from the closed-loop transfer function and the controller transfer function. Obviously, this approach requires detailed knowledge of the controller model. Any errors in the controller model will also result in an inaccurate plant model [44].

The joint input-output approach to closed-loop identification also entails mathematical manipulation. In this approach signals $y(t)$ and $u(t)$ are considered as outputs of a system driven by signals $r(t)$ and noise. Models for the controller and plant are then recovered from this joint model.

The last remaining system identification topic in this chapter is concerned with the perturbation signal with which the system is interrogated.

### 2.2.6 Persistent excitation

The parameters of a black-box model are determined from the input and output data of the subsystem of interest. These signals are in turn obtained by slightly perturbing the closed-loop system from its steady state values and recording the system's response. The excitation signal with which the system is perturbed is therefore arguably one of the most important aspects of successful system identification since this signal "...determines the nature and accuracy of the system characteristics that are identified ..." [51]. An excitation signal that gives rise to maximally informative input and output data is known as a persistently exciting signal. It is no small wonder that persistent excitation is regarded by some as an important precondition for successful system identification [41].

The system identification literature is full of vague descriptive terms for the excitation signal such as that it must be "rich". Basically such terms try to convey the message that the perturbation signal should expose all of the system's properties in order that the final identified model be an accurate representation of the original system's behaviour under all circumstances. The ideal excitation signal should therefore be a condensed compilation of all possible input signals that can be applied to the particular system.

In the frequency domain such a signal would be characterised by having a frequency content that is equally strong in all parts of the spectrum. One characteristic of persistently exciting signals is therefore that their power spectrum is flat over all frequencies within the system's bandwidth [41]. In fact, if the signal's power is low in a certain part of the spectrum, then the system's response in that part of the spectrum won't be accurately modelled [49].

A more formal definition of persistent excitation is that the *order* of a persistently exciting signal must be larger than the sum of the poles and zeros of the system to which it is applied [44]. (Where the order of a signal is defined as the number of peaks or spectral lines in its total spectrum encompassing both negative and positive frequencies [44].) Since the order of the system to be modelled is often an unknown quantity it therefore makes sense that the spectrum of the excitation signal should be as flat as possible.

Specific excitation signals are furthermore useful to highlight particular aspects of the system under scrutiny. Some signals for example can be employed to alternatively accentuate or disregard the effect of nonlinearities in the system's dynamics [49]. If the purpose of system identification is to fit an LTI model to a system, then the excitation signal's amplitude should be small enough to avoid exciting nonlinear behaviour, yet large enough to minimize the effect of noise [49].

The excitation signals commonly used in the literature can be classified into three broad categories, namely: random signals, periodic signals and non-periodic signals. Random signals include different forms of noise (e.g. white and pink noise) as well as pseudo-random binary sequences. White noise is per definition persistently exciting, but may induce nonlinear behaviour in the AMB (as discussed in the next chapter). Pink noise excitation signals sometimes give good results ([45]), but may hinder the identification of accurate time-invariant models (since pink noise itself is non-stationary over small time intervals). Pseudo-random binary signals are quite useful at masking nonlinear behaviour ([44]), but its high frequency content may also sometimes induce nonlinear behaviour in an AMB.

Non-periodic signals such as step signals have been used with success in both classical system identification ([52]) as well as system identification by means of genetic algorithms ([53]). Although at first glance step signals don't adhere to the requirements of persistent excitation, their spectra do contain high frequency components at sufficient power levels to result in accurate models. The only potential pitfall of these signals is that they have to be specified carefully to ensure that both the transient and steady-state behaviour of the target system is accurately modelled. (If for example the total response of the system consists mostly of transient behaviour, the final model will be biased towards accurate modelling of transient behaviour at the cost of large steady-state errors.)

Periodic excitation signals are only persistently exciting if they contain all of the frequencies all of the time. This excludes chirp signals and limits the possible periodic excitation signals to so-called multi-sines [44]. A multi-sine signal is merely a sum of sinusoids, each with a different frequency and phase.

When sinusoids are added together additive superposition may result in very large amplitude spikes at certain time instants (when all of the component sinusoids are in phase). It is therefore important to ensure that a multi-sine signal has a low crest factor (which is defined as the peak signal value to the signal's rms value [44]). The crest factor of multi-sines can be limited by either randomly adjusting the phases of the component sinusoids ([26]), or by means of Schroeder phases. The latter technique adjusts the phases of the component sinusoids deterministically on the basis of Woodward's theorem (which relates the distribution of instantaneous frequencies in an FM signal to its power spectrum) [54]. Multi-sines constructed by means of Schroeder phases are commonly known as Schroeder phased harmonic sequences.

The final choice of which excitation signal to use is also influenced by other considerations such as whether the eventual model should be LTI or not and specific aspects of AMB behaviour which have to be modelled. Consequently, a final decision on the optimimum excitation signal for this study is postponed to section 5.1.1.

Once the AMB has been modelled by means of system identification, its robustness has to be estimated by means of a robustness measure. This is the topic of the next section.

## 2.3 Robustness analysis

As mentioned in the previous chapter, the concept of robustness is always accompanied with a description or model of the specific uncertainties for which the system must be robust. There are various forms of uncertainty in a typical system (such as parametric and dynamic uncertainty) and also different paradigms with which these uncertainties can be modelled (e.g. probability theory and fuzzy logic). Parametric and dynamic uncertainty are defined in chapter 4. In short, parametric uncertainty is applicable when the system's model is accurate with the exception of a few parameters whose precise values aren't known. When the system's model is inaccurate due to unmodelled dynamics, dynamic uncertainty is the most appropriate avenue to describe this form of uncertainty.

Both parametric and dynamic uncertainty however have to be mathematically modelled. The different mathematical paradigms in which these uncertainties can be expressed include probability theory, fuzzy logic and norm-bounded uncertainties. Probability theory approaches uncertainty from the perspective of chance and unpredictable, random events [55]. Whether a specific event will occur or not is expressed in terms of a calculated probability and the behaviour of random variables is described by means of probability density functions. In contrast, fuzzy sets are more applicable to phenomena where the uncertainty is in the *nature* of the event or object [56]. Fuzziness describes non-random uncertainties in e.g. low-resolution and inaccurate sensors as well as uncertainties due to incomplete knowledge of a particular process [56]. In fuzzy logic uncertainty is modelled by means of fuzzy sets and their membership functions.

Robust control theory is however built on the notion of norm-bounded uncertainty [3]. This is a frequency domain concept where systems are modelled by means of transfer functions. The uncertainty surrounding a particular model can then elegantly be expressed by means of bounds on the norm of the model's transfer function (i.e. the gain of the model is bounded at each frequency). Phase information is ignored in this paradigm, since the phase of a system quickly becomes totally uncertain at higher frequencies. Norm-bounded uncertainties encompass a wide range of phenomena including noisy and deterministic disturbance inputs, inaccurate sensors, incomplete models and parametric uncertainty. Consequently this uncertainty paradigm is the best suited to model uncertainty in robustness analysis.

Robustness analysis is a three-step process which begins with the modelling of the nominal system (i.e. the system with all uncertainties ignored). The model of the system is only complete when the uncertainties surrounding it have also been modelled. Lastly, these models serve as input to a robustness estimation technique that estimates the stability margin of the nominal system for the modelled uncertainties.

Ideally the properties of the robustness estimation technique should match the characteristics of the system to be analysed. In practice this isn't always possible. AMBs are for example

nonlinear systems. Lyapunov analysis should therefore be the preferred robustness analysis technique.

Lyapunov analysis is a general stability theory that was developed to analyse the stability of nonlinear systems (as well as linear systems as a special case) [19]. The basic idea of Lyapunov analysis is that in a system with losses the total mechanical energy of the system is a scalar quantity that is proportional to the magnitude of the state vector. For a stable system the total mechanical energy will decrease until the system has settled in its nominal position. The total mechanical energy of unstable systems increases as time goes by. In Lyapunov analysis the system's "energy-level" is modelled by means of a so-called Lyapunov function. The properties of a system's Lyapunov function are therefore indicative of stability or instability. A clear advantage of Lyapunov-based robustness estimators is that they are applicable to nonlinear systems. This advantage is however offset by the difficulty in finding a suitable Lyapunov function (since Lyapunov theorems provide necessary, but not sufficient conditions for stability [19]).

It is however common practice to approximate a nonlinear system with a linear model over a subset of its total operating range. For this reason, linear robustness estimation techniques are also taken into consideration for the robustness analysis of AMB systems. As one could expect, there is a plethora of linear robustness estimation techniques in the literature. Only the most important few that are applicable to multivariable systems are summarized in this section.

The *de facto* standard robustness estimation technique in the AMB literature is currently the sensitivity function [18], [11], [9], [31] and [17]. This technique entails that the classical sensitivity function of the closed-loop system be measured. The peak value of the closed-loop sensitivity function is then used as an estimate of the smallest gain variation that would lead to instability[11] [22]. This measure is based on the same fundamental approach as the well-known SISO Nyquist criterion ([18]) and can easily be extended to MIMO systems ([25]). Another advantage of the sensitivity function is that it can be readily measured on hardware systems [22]. Furthermore, the peaks in the sensitivity function (which is a function of frequency) correspond to the critical frequencies of the AMB rotor [21]. Unfortunately, placing limits on the peak value of the sensitivity function only results in a necessary condition for stability which isn't sufficient to safely guarantee the robustness of AMB systems [22].

Probabilistic techniques are useful to not only model uncertainty, but also estimate the stability margin of a control system. One example from this family of techniques is the concept of stochastic robustness introduced by Stengel and Ray ([7] and [6]). In stochastic robustness the probability that all of a system's eigenvalues remain in the left-hand side of the s-plane is used as a scalar measure of the system's robustness. Monte Carlo[12] simulations are used to determine the probability of a system eigenvalue straying over to the right-hand side of the s-plane under the influence of pre-specified random perturbations of selected system parameters.

[11] A peak value of less than 8 dB corresponds to newly commissioned AMB systems. If the peak value is between 8 dB and 12 dB the AMB is fit for long-term use, while peak values between 12 and 14 dB indicate that the AMB should be taken out of continuous operation as soon as possible. Peaks above 14 dB are warning signs of imminent damage to the machine [9].

[12] Monte Carlo techniques entail random sampling from probability distributions and repetitive calculations. They can be used for a variety of purposes including numerical integration of high-dimensional problems, as well as numerical estimation of probability densities in complex systems [57].

This technique has the advantage of being easily applied to many different systems without requiring detailed knowledge on how the probability distributions of input variables to the system are distorted to become the probability distributions of the output variables. The accuracy of this technique can also be estimated by means of statistical confidence intervals. Monte Carlo techniques are however computationally expensive. An inherent limitation of the deductive approach taken by Monte Carlo simulations is that they can easily miss a potential destabilizing parameter combination [58]. (Monte Carlo techniques can only foster confidence in their results through copious repetitions.) Nonetheless, if a sufficient number of simulations have been done, Monte Carlo-based robustness estimation techniques deliver very accurate estimated stability margins.

Parametric uncertainty can be modelled as a nominal parameter value with a percentage deviation surrounding it. An equivalent representation is to model each parameter by means of a lower bound and an upper bound (much the same as the well-known concept of tolerances in engineering). Modelling parametric uncertainty in a parameter in terms of lower and upper bounds opens the door for using interval arithmetic to estimate the robustness of the system. Interval arithmetic entails that numbers be represented as intervals (akin to the well-known engineering concept of tolerances). The basic arithmetic operations (e.g. addition and multiplication) can also be modified to accomodate intervals rather than mere scalar numbers [59]. Interval arithmetic can then be used to calculate lower and upper bounds on the system performance (i.e. estimate the system's performance robustness) [60].

Robustness estimates based on interval arithmetic are non-conservative and quite intuitive [60]. Unfortunately, the computation time increases exponentially with the number of uncertain parameters [5]. Interval arithmetic is therefore only suitable for the simplest of problems. Interval arithmetic is also limited to the robustness analysis of parametric uncertainty and is unable to model the effect of dynamic uncertainty.

Another robustness analysis technique that is limited to parametric uncertainty in linear systems is based on Kharitonov's theorem [61]. This robustness measure entails evaluating the Routh-Hurwitz stability of four polynomials encompassing a hyper-rectangle of possible polynomials (representing the parametric uncertainty). Kharitonov's theorem assumes that coefficient perturbations are independent of each other. This assumption results in conservative robustness estimates. This disadvantage coupled with the limitation to parametric uncertainty places robustness estimators based on Kharitonov's theorem out of contention.

The effect that different parameter variations can have on a system can be assessed by means of the $\nu$-gap metric [22]. The $\nu$-gap metric characterises the "distance" between a nominal and perturbed open loop system in terms of a scalar value on the unity interval. The smaller the value, the closer the perturbed system is to the nominal system. This measure is a function of frequency and can be used to pinpoint specific frequency intervals that are cause for concern (i.e. where small parameter variations have a large effect on the system) [27]. Unfortunately, this robustness measure can't directly determine the stability margin of the system, since it only is a comparative measure.

The singular values of a MIMO model correspond to the gains of the different input-output channels through the system [25]. Consequently, the maximum singular value of a system can

be used as an estimate of the worst-case gain of the system in any situation. Various robustness estimation techniques have been based on singular value analysis (e.g. [62] and [21]). All of these techniques are quite conservative due to the manner in which uncertainties are modelled (namely so-called unstructured uncertainty) [25]. (The difference between unstructured and structured uncertainties is elucidated in chapter four.)

The conservatism of robustness measures based on singular values can be greatly reduced by modelling the parametric and dynamic uncertainties in terms of structured uncertainties (which basically entails that all uncertainties occuring in the system are arranged on the main diagonal of a block-diagonal matrix) [25]. The resultant singular values are known as structured singular values and the largest of them is known as $\mu$. Similar to the $\nu$-gap metric, $\mu$ is a function of frequency. This allows the analysist to identify certain regions of concern in the spectrum of the system [63]. This measure is quite convenient, since it entails a scalar-valued function of frequency that reflects the effect of as many parametric and dynamic uncertainties on the system stability as is required [64]. Calculating the values of $\mu$ is however quite computationally intensive (in fact, it is only possible to estimate lower and upper bounds for the values of $\mu$) [65]. Fortunately, commercial software is available to take this concern out of the hands of the analysist [26].

The ease of use of $\mu$-analysis software, combined with minimal conservatism and an inherent capability to model multivariable systems, makes $\mu$-analysis the method of choice for the analysis of the stability margin of 2-DOF AMBs.

## 2.4 Related work

This study employs system identification in order to model a 2-DOF self-sensing AMB. The resultant model(s) are in turn used to perform $\mu$-analysis to obtain an estimate of the stability margin of the AMB system. This study therefore lies at the intersection? of three fields of study, namely: self-sensing AMBs, system identification and robustness analysis (which explains the structure of this chapter thus far). Despite the fact that robustness analysis is one of the fundamental objectives of control systems and self-sensing is one of the few remaining research problems in AMBs, the literature on the topic of robustness analysis of self-sensing AMBs is quite sparse.

Kanemitsu *et al.* conducted a comparative study in which a few different robustness measures were applied to normal sensed AMBs [21]. In their study the gain- and phase margin (classical SISO stability margin measures) fared quite well. This experimental result contradicts conventional wisdom in the MIMO literature (which warns against the use of the gain- and phase margin on multivariable systems [3]). One possible reason for this surprising result is that Kanemitsu *et al.* used decentralized PID controllers in their experimental rig, since this still the most common form of controllers in AMB technology to date.

Other robustness analysis techniques that were used in [21] were: a measure based on the damping ratio of the natural vibration of the elastic rotor, the maximum singular value of the system's sensitivity function, as well as the peak value of the same sensitivity function. Of

these three, the damping ratio probed to be unsuitable as a measure of the stability margin, while the rest couldn't improve much on the gain-and phase margin.

The *de facto* standard for robustness estimation in the AMB literature however remains the sensitivity function ([11], [31], [17]). This state of affairs is due to the fact that the sensitivity function is proposed as a stability measure in the draft ISO standard for the evaluation of the stability of rotating machinery equipped with AMBs [9]. Acceptance of the draft ISO standard isn't unanimous in the AMB research community. In [22] it is argued that the peak value of the sensitivity function only gives a necessary (but not sufficient) condition for robust stability. Their theoretical arguments were also supported by practical examples of AMB suspended systems that met the criteria set out by the draft ISO standard yet became unstable due to modal variations or gyroscopic coupling.

The limitations in the proposed ISO standard uncovered by [22] have emboldened other researchers to use alternative MIMO robustness analysis techniques. The generalised Nyquist criterion has been successfully applied to assess the robustness of an $H_{infty}$-controlled vertical AMB system for variations in the shaft's rotational speed [66]. Drawbacks of the generalised Nyquist criterion are that it requires a visual interpretation of a Nyquist plot and that it doesn't directly estimate the stability *margin* of the system (it merely performs a stability check).

Tsai *et al.* also employed the Kharitonov stability theorem ([67][13]) as additional validation of the stability of their AMB system [66]. As mentioned in section 2.3, this technique is only suitable for parametric uncertainty in the system model and prone to conservatism.

The $\nu$-gap metric has also been applied to assess the robustness of AMB suspended systems. In section 2.3 one of the main limitations of the $\nu$-gap metric was identified, namely that it is only a relative measure useful for identifying the effect of uncertainty on a system. This was precisely how the $\nu$-gap metric was applied in [68]. It turns out that the $\nu$-gap metric is quite useful to determine the effect of negative feedback on the amplification or attenuation of different forms of uncertainty in an AMB system. Armed with the $\nu$-gap metric it is possible to determine which forms of uncertainty can be safely ignored and which have to be compensated for.

Despite the above mentioned advantages, the $\nu$-gap metric isn't suitable for explicit estimation of the stability margin of an AMB system. Of the available LTI MIMO robustness estimation techniques, $\mu$-analysis holds out the promise of delivering the least conservative estimates of the stability margin of an AMB system. Although $\mu$-synthesis has been applied to design controllers for AMB systems ([69] and [68]), $\mu$-analysis curiously has never been used to assess the robustness of AMBs (which provides additional motivation for its use in this study).

In the self-sensing literature robustness analysis techniques have played a pivotal role in the debate on the viability of self-sensing AMBs. After the development of state-estimator self-sensing AMBs, Kucera showed by means of a sensitivity analysis that such self-sensing AMBs are quite sensitive for parametric uncertainty [16]. Following this result, Morse *et al.* used the sensitivity function to prove that self-sensing in general has fundamental theoretical limits on its stability robustness [18]. These negative results were however soon contradicted by various

[13] Kharitonov's original work was published in Russian and only much later introduced to the English speak world by Barmish.

researchers (e.g. [11]) who showed that practical modulation based self-sensing AMBs can be almost as robust as sensed AMBs (according to the proposed ISO standard).

The apparent contradiction between the theory and practical results on the robustness of self-sensing AMBs was addressed by Maslen *et al.* [13]. They found that it is essential to include the switching ripple component on the coil current in the AMB model that is subjected to robustness analysis. In contrast with previous theoretical studies Maslen *et al.* modelled the self-sensing AMB by means of a linear periodic model[14]. To maintain consistency with the rest of the self-sensing AMB literature the robustness analysis in [13] was conducted by means of the sensitivity function. This result gave a theoretical basis for the success of practical self-sensing AMBs.

Another theoretical proof of the viability of self-sensing AMBs was provided by Maslen *et al.* [71]. Once again a linear periodic model was used to model the self-sensing AMB system. Lyapunov analysis was however employed to prove that switching ripple in the coil current is essential to obtain robust self-sensing. This contribution is of additional interest since parameter estimation was used to perform self-sensing and system identification was used to estimate the size of the AMB airgap.

System identification has been applied in various forms and for various motives to AMBs. The most basic application of system identification concepts is the use of parameter estimation algorithms to obtain values for parameters that can't be measured with conventional sensors. Examples of such parameters in AMBs are the damping and stiffness of the bearing (in particular the position- and current stiffness constants of (2.4)) that have been estimated by both discrete-time ([72]) and frequency domain system identification ([73]).

Frequency domain system identification has also been applied to obtain a single multivariable model for twin radial sensed AMBs with a flexible shaft [74]. Their identified model encapsulated the power amplifiers, both AMBs, as well as the rotor. (In fact everything except the controllers.) This MIMO model was obtained by means of a novel parameter estimation algorithm based on amongst other things singular value decomposition. Besides being limited to sensed AMBs, their model was also only valid for a non-rotating shaft[15].

Discrete-time system identification has been applied to a 1-DOF AMB with the purpose of modelling the nominal plant as well as its dynamic uncertainties [76]. Once again the "plant" contained the power amplifier, stator and point-mass. Parameter estimation was performed by means of recursive least squares that resulted in an ARMA model (which was in turn converted to a z-plane transfer function). The objective of the whole modelling process was to design an $H_\infty$ controller for the 1-DOF AMB.

The same research team has since extended their work to twin radial bearings with a rotating flexible rotor [77]. Once gain system identification was performed with controller synthesis in

[14] DeSmidt *et al.* also modelled an AMB system as a linear periodic system [70]. In their work they made use of Floquet theory (specifically the eigenvalues of the Floquet transition matrix) to analyse the robustness of the AMB system. Their work was however focussed on the potential destabilising effect of non-constant velocity flexible couplings in an AMB suspended segmented driveshaft system.

[15] Rotating shafts in heteropolar AMBs are exposed to eddy currents, which result in significant distortion of the measured current signals ([75]).

mind and consequently only the controller was excluded from the ”plant”. Similar work has been done for a stationary flexible shaft with the exception that homopolar AMBs were used and no uncertainty models derived [41].

System identification was furthermore employed in [78] with the aim of designing a controller by means of $\mu$-synthesis. The specific application entailed an AMB supported machine tool spindle. This work was no exception on the rest in that the identified AMB plant model included everything except the controller. Furthermore, the required uncertainty bounds were based on the designers' experience and not on physical measurements of the mismatch between the model and reality.

Although the basic idea (namely of performing $\mu$-analysis on the basis of models obtained via system identification) isn't new, it is the first time that it has been applied to self-sensing AMBs. The closest prior work in this general field was performed by Jun *et al.* [79]. Their work was however confined to SISO systems in the process control industry.

A related approach was followed in [80] where an AR-Markov model for the system was obtained by means of system identification. The resultant model was then converted to a state-space representation. The stability margin of the system is then estimated from the singular values of the A-matrix of the state-space model. Their work is however limited by the fact that it was only applied to SISO example problems in the process control industry as well as the fact that robustness anlyses performed on normal singular values are notoriously more conservative than $\mu$-analysis [25].

In contrast, this study is limited to a 2-DOF AMB. This work is however distinguished by the fact that *self-sensing* AMBs are modelled. The dependency of DCM self-sensing on an accurate representation of the ripple current in turn requires that the self-sensing, plant and power ampifier models be separated, which is another unique feature of this study.

## 2.5 Conclusion

This study is based on nonlinear simulation models of respectively a sensed and self-sensing 2-DOF AMB. These two bearings are summarized in tables 2.1 and 2.2. DCM self-sensing itself is modelled by means of (2.7) and (2.8).

System identification will be used to model the components of the nominal AMB system with LTI discrete-time black-box models. The choice of the specific parameterized model structure (state-space, OE, ARX, ARMAX or Box-Jenkins) is postponed until the next chapter (as well as the choice of the best parameter estimation algorithm). AMBs are inherently unstable which requires that closed-loop identification has to be used. Direct closed-loop identification is the method of choice due to its simplicity and accuracy.

$\mu$-analysis is currently one of the best robustness estimation techniques. It is widely applicable due to the general nature of norm-bounded uncertainty. In contrast with e.g. gain- and phase margin, $\mu$-analysis does take cross-coupling into account when estimating the stability margin of a multivariable system. Furthermore $\mu$-analysis is the least conservative of all robustness

estimation techniques based on singular value analysis. The only potential problem with $\mu$-analysis is that it proceeds from the assumption that the system is LTI. The validity of this assumption is one of the topics in the next chapter.

# CHAPTER 3

# System identification applied to AMBs

*"System identification is generally the art of mathematical modeling, given input-output measurements from a dynamical system." This definition by Matts Viberg ([81]) highlights the fact that the application of the theory of system identification to practical systems involves a fair amount of experience and insight into the specific problem at hand. This chapter describes all of the important issues that have to be taken into account when fitting a nominal LTI model to a 2-DOF self-sensing AMB by means of system identification. Special attention is given to ensure that the fundamental assumptions of LTI system identification are met (namely that the AMB is operated and analysed in a linear operating regimen). This has an impact on the choice of the excitation signal that is used to illuminate the system dynamics. The excitation signal can also be injected at different points in the control system. Factors that influence the choice of where to inject the excitation signal are also discussed in this chapter. Defining the structure of the model is another topic that is examined, especially choosing the right inputs and outputs for the different components in the loop. It is also important to use the best parameterized model structure to ensure that the eventual model's response is true to the original nonlinear system. Lastly, the chapter closes with a few hard-earned pieces of advice concerning the transformation of discrete-time models to continuous-time models. Using system identification to model dynamic uncertainties in the various system components of an AMB is however a topic that is postponed until chapter four.*

## 3.1 The boundaries of LTI models

### 3.1.1 Introduction

In the previous chapter, $\mu$-analysis was chosen as the preferred means with which to estimate the stability margin of self-sensing AMBs. Careful examination of the definition of the structured singular value reveals that an implicit assumption upon which $\mu$-analysis is based, is that the system under scrutiny is linear and time-invariant (LTI) (see e.g. [3]). Accurate robustness estimates can therefore only be obtained via $\mu$-analysis if the system is truly linear (in other

words, if a linearized model of the system is a sufficiently accurate representation of the real system). The requirement of linearity and time-invariance poses a bit of a problem, since it was also shown in the previous chapter that AMBs are inherently nonlinear.

Most systems are nonlinear to a certain degree and any linear approximation would only be valid over a small interval [82]. Anyone who has had practical experience with transistors or operational amplifiers would agree with this statement. Transistors are inherently nonlinear devices over their total operating range, but can be conveniently regarded as being linear for certain bias levels and ranges of input signals. This elementary example highlights the fact that the behaviour of a nonlinear system is to a large extent determined by the bias level and amplitude excursions of its input signals[1].

The linear operating domain of AMBs can be extended by operating them in differential driving mode [8]. Differential driving mode entails that the reference current supplied by the controller is added to and subtracted from a bias current. The resulting reference currents are amplified by two separate power amplifiers and eventual currents supplied to opposing electromagnets in the AMB stator. This has the effect of ensuring a linear force-current relationship.

Unfortunately, this linear approximation only holds for small excursions in the airgap between the rotor and stator of an AMB. In fact, a rotor deflection of only half the airgap may result in a 44 % deviation of the true magnetic force from its linearized version [83]. Nonlinear effects therefore still play a significant role in the total behaviour of an AMB.

The enduring presence of nonlinear dynamics in the behaviour of an AMB may cast some doubts on the suitability of $\mu$-analysis as a robustness estimator for AMB systems. This issue can however be approached from another perspective by investigating the specific circumstances under which $\mu$-analysis will still deliver accurate estimates of the stability margin for an AMB. The estimates obtained via $\mu$-analysis are only as good as the models for the nominal system and its expected uncertainties. When these models are obtained by means of system identification, the fundamental question is therefore how to synthesize appropriate excitation signals that are guaranteed to constrain the AMB's behaviour to within the LTI domain. (The consequence of using such excitation signals is that the resultant models are in a sense optimal LTI models for a system that didn't exhibit any nonlinearities whatsoever *during interrogation*.)

Per definition linear systems obey the well-known superposition principle [82]. Deciding whether a system is linear or not is theoretically quite easy (provided that an analytical model of the system is available). In practice however, any model is a simplified and imperfect abstraction of reality. Any conclusions made on the linearity of a system must take the mismatch between the model and reality into consideration[2]. Another complicating factor is that the boundary between linear and nonlinear behaviour is quite hazy (when the focus is only on so-called continuous nonlinearities[3]).

[1] In fact, the stability of a nonlinear system is determined by the system parameters, its initial conditions, as well as the specific input signals [82]. This is in contrast with linear systems, where the system stability is purely a function of the system's parameters.

[2] It can easily happen that an oversimplified model will erroneously predict that a system is linear.

[3] In contrast with *discontinuous* (or so-called "hard") nonlinearities, *continuous* nonlinear behaviour can be locally approximated by linear functions [19].

All of these diverse issues come to the fore when a nonlinear system has to be modelled by an LTI model obtained via system identification. Firstly, it has to be kept in mind that the system behaviour might be slightly nonlinear depending on the specific input signal used. Secondly, it is desireable to be able to decide whether a system behaves linearly or not, solely on the basis of measured input and output data.

A necessary prelude to system identification is the ability to measure the presence of nonlinear behaviour in a real system. Only then is it possible to choose or synthesize an excitation signal that will ensure that the system remains within the narrow confines of linear behaviour.

Basically the same holds for the equally well-known concept of time-invariance. A time-invariant system's parameters remain independent of time during the system's lifetime [84]. Time-invariance is reminiscent of the statistical concept of stationarity. A stationary process is defined as one whose statistical distribution function remains constant for all time [85]. Since practical control systems are always exposed to noise and subjected to disturbance signals, it is clear that a real-life system may be viewed as a statistical process. The time-variance of real systems may therefore be safely determined from their stationarity.

This seemingly trivial line of reasoning enables us to test a system for time-invariance by employing statistical tests for stationarity. Testing for wide-sense stationarity theoretically entails ascertaining that all of the statistical moments[4] of the process's distribution remain constant for all time. Most practical tests for stationarity settle for verifying that the first few moments don't exhibit any trends for a given data sample.

It is now possible to analyse the response of a system to a particular excitation signal and decide whether the system is LTI or not (for the operating range defined by the excitation signal). The following two sections will elaborate further on this topic by firstly describing a practical test for stationarity and secondly a few options on how to measure linearity.

### 3.1.2 Measuring time-invariance

Due to the ubiquitous presence of noise, it is futile to merely calculate the various moments of a process over short time windows and test whether they remain "constant" as time goes by. Numerous statistical tests are available that are sensitive for various forms of non-stationarity (e.g. trends and heteroscedasticity[5]). The ideal stationarity test is non-parametric[6] and based on the minimum of assumptions regarding underlying distributions in the data. One such test is the so-called run-test [87].

Applying the run-test to test whether a system is stationary or not, entails the following procedure:

[4]The first four statistical moments of a process are respectively the mean value, variance, skewness and kurtosis of the distribution function.

[5]Processes whose variance change over time are known as heteroscedastic. Such processes can be identified by means of e.g. the Glejser test [86].

[6]In other words independent of a user-defined parameter.

1. Divide the data into consecutive, non-overlapping segments. The number of segments ($n$) must be an even integer.

2. Calculate the value of a statistical moment for each segment in the data sequence. The result is that the data is reduced to $n$ "random" values. The question is now whether the specific realization of the underlying random variable can be regarded as being independently generated.

3. With this question in mind, the number of runs in the sequence of $n$ data values is counted. A run is defined as: "... a sequence of identical observations that is followed and preceded by a different observation or no observation at all." [87]. Figure 3.1 elucidates the concept of runs in the context of evaluating the values of a sequence of calculated statistical moments. In this figure a run is defined as a section of data points that remain either above or below the value of the same moment calculated over the whole data set. (I.e. a global estimate.)

4. Compare the number of runs with the bounds obtained from a table of the so-called "run distribution" [87]. This comparison basically entails that the variation in the data is compared to the variation of a known independently distributed variable. For the illustrative case of 60 segments and a significance level of 95 %, the lower and upper bounds for the number of runs are respectively 22 and 39. If the number of runs lies within this interval, the original data set can be regarded as being stationary, otherwise it is non-stationary.

A critical assumption that has to be met for valid application of the run-test is that the segment length is considerably longer than the fundamental period of the process under scrutiny. This assumption ensures that the sample[7] estimate of the particular statistical moment is consistent[8].

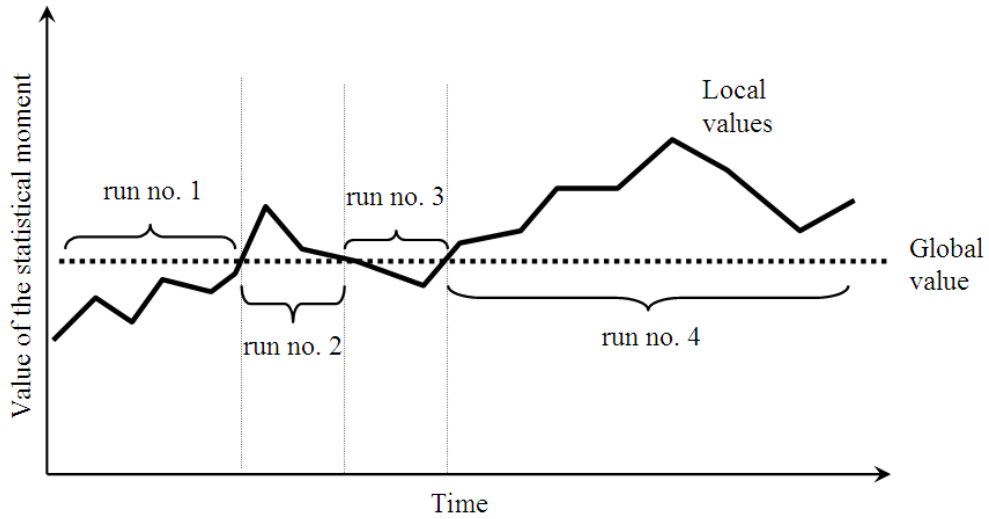


Figure 3.1: The concept of "runs" in data

[7]For the duration of the discussion on the run test, the usage of the word "sample" will conform to the standard meaning in the statistical literature.

[8]A statistical estimate is *consistent* if it converges to its theoretical value as the sample size approaches infinity [88].

For white noise (which is per definition stationary) Monte Carlo analysis has shown that the minimum segment size that will ensure consistent estimates of the first four statistical moments is approximately 1000 data points. In the case of a typical practical 2-DOF AMB with a flexible rotor, the first rigid mode (which corresponds to the dominant poles of the system) occurs approximately at 3,000 r/min (50 Hz) [30]. Consequently the data length required for an accurate run-test must be significantly longer than the period of the first critical mode (namely 20 milliseconds)[9].

The eventual purpose of data gathering is to model the 2-DOF AMB by means of system identification. It would therefore be wise to ensure that the length of the estimation subset results in optimal system identification. Successfull system identification requires that the total length of the estimation subset should be in the order of the dominant time constant of the system to be modelled [44]. Increasing the size of the estimation subset in disregard of this sage advice has a detrimental effect on the quality of the eventual models. (This guideline is especially valid if the models are estimated with a *prediction focus*, but more on this topic in section 3.6.)

Fundamentally the concept of stationarity implies that the distribution function of the data remains constant. As alluded to previously, a probability distribution can be described in terms of its statistical moments. The first four statistical moments are summarized in table 3.1. Also shown in table 3.1 are robust estimates of the various moments. The use of robust estimates of the statistical moments result in estimates that are insensitive to noise and especially outliers in the data. (In particular the estimates according to Bowley and Moors have been shown to be largely invariant for outliers in practical financial data [88].)

Table 3.1: Summary of the first four statistical moments

| Number | Moment | Property | Robust estimate |
|---|---|---|---|
| 1 | Mean | Centre point of the distribution. | Median |
| 2 | Variance | Width (spread) of the distribution. | Interquartile range[a] [55] |
| 3 | Skewness | Degree of symmetry about the distribution's centre. | Bowley coefficient of skewness [88] |
| 4 | Kurtosis | Relative contribution of the tails of the distribution. ("The degree of peakedness of a distribution" [59].) | Moors coefficient of kurtosis [88] |

[a] The interquartile range is defined as the difference between the 0.75 quantile and the 0.25 quantile of the data [55].

Non-stationary data comes in various incarnations ranging from data with mere trends, to data with seasonal variations and also heteroscedastic data. No single statistical moment is able to discriminate between stationary data and the wide variety of non-stationary processes. Consequently run tests are conducted using all four moments and a final decision reached via a simple majority vote between the recommendations of the four tests[10].

[9] An alternative viewpoint on this criterion is that it prevents so-called type I errors [55] (i.e. rejecting the null-hypothesis of stationarity for the alternative hypothesis of non-stationarity) because the short length of the data causes the fundamental period of the data to seem like a trend.

[10] Ties between the four recommendations are indicative of a sample that is too small, because the run-test is biased towards non-stationarity for samples of insufficient length.

Verification of the run-test is easy. Its performance on white noise and red noise[11] shows that it can successfully identify stationary and non-stationary processes respectively. Pink noise[12] (or $1/f$ noise), being halfway between white noise and red noise, is slightly problematic. Although Keshner unequivocally states that pink noise is nonstationary [91], the run-test may contradict this assertion given a sufficiently large sample of data. This slight ambiguity in the true nature of pink noise dictate against its use as an excitation signal for linear *time-invariant* system identification (even though some researchers have obtained surprisingly good results by means of *bandlimited* pink noise [45]).

### 3.1.3 Measuring linearity

Formal statistical tests for linearity abound, but they aren't always practical from an engineering perspective. The simpler approach taken in this study is inspired by the approach by Poggi and Portier [92] and can be called "model-based" linearity tests. In a nutshell, these tests involve fitting some kind of linear model to the measured data and then using the goodness of fit (modelling ability of the model to explain the observed data) as a measure of linearity. (After all, if a linear model can adequately explain the data, then the underlying process that generated the data must also be linear.) This linearity test therefore consists of two steps. Firstly a linear model is fitted to the observed inputs and outputs of the (non)linear system. Secondly, the quality of this model is assessed.

One option for a linear model for a multivariate system could be the following matrix equation,

$$\mathbf{y} = \mathbf{C}\mathbf{u} \tag{3.1}$$

where $\mathbf{u}$ is the vector of input variables and $\mathbf{y}$ represents the vector of output variables.

In (3.1) the matrix $\mathbf{C}$ represents a hyperplane in the input-output space of the multivariate system. A least-squares estimate for this matrix can easily be obtained via the Moore-Penrose pseudo-inverse [93] as follows:

$$\hat{\mathbf{C}}^T = \mathbf{U}^+\mathbf{Y} \tag{3.2}$$

where $\mathbf{U}$ is the matrix of inputs (in which the datapoints of each input variable are stored in a column vector) and $\mathbf{Y}$ is a similarly organized matrix of outputs and where the Moore-Penrose inverse is given by:

$$\mathbf{U}^+ = \left(\mathbf{U}^T\mathbf{U}\right)^{-1}\mathbf{U}^T \tag{3.3}$$

The problem with such a model is that it is only suitable for static mappings (e.g. the output equation of a state-space model). Any hope to apply this approach to model the input-output mapping of a dynamic model is futile. The reason for this can be easily seen by considering

[11] Also known as brown noise, this type of noise has a reddened spectrum and is related to Brownian movement, since its instantaneous values follow a random walk. Red noise is generated by a non-stationary process. Both white and red noise can be generalized into the class of $1/f^\gamma$ noise, [89], where $f$ refers to frequency and $\gamma$ is a positive real-valued parameter.

[12] Pink noise is defined as follows: "Pink noise ... has equal power in octave frequency bands or any constant intervals on a logarithmic frequency scale." [90].

the general LTI continuous-time state-space equation in (3.4) and (3.5). If a least-squares hyperplane is fitted to the input-output mapping of the system (in other words from the vector of input variable **u**, to the vector of output variables **y**), it totally disregards the mapping from the input variables to the state-variables in the state-equation (3.4). In other words, a single least-squares mapping is suitable for either the state-equation (3.4) or the output equation (3.5), but not both simultaneously. Since the internal state-variables of a dynamic model aren't in general readily available without an observer, the approach of (3.1) and (3.2) isn't useful.

$$\dot{\mathbf{x}} = \mathbf{A}\mathbf{x} + \mathbf{B}\mathbf{u} \tag{3.4}$$

$$\mathbf{y} = \mathbf{C}\mathbf{x} + \mathbf{D}\mathbf{u} \tag{3.5}$$

A much better approach to model MIMO dynamic systems is to use system identification to fit an LTI state-space model to observed input-output data of the system. The fidelity of the resultant model is then a measure of the degree to which the underlying system is linear or not. A drawback of this approach is the computational effort required to obtain such a model. Another more fundamental objection to this approach is that it combines the selection of suitable excitation signals and the eventual system identification process into a single step, thereby making troubleshooting in the event of poor model performance much more difficult. Nevertheless, this method has the advantage of being simple and easy to implement.

An essential component of the model-based linearity measure is the ability to quantify the fidelity of an identified model. For stable models, the so-called coefficient of determination (3.6) can be used [55]. This coefficient is a measure of the percentage variation in the data that can be explained by the model.

$$R^2 = \frac{\sum_{k=1}^{N}(y(k) - \bar{y})^2 - \sum_{k=1}^{N}(y(k) - \hat{y}(k))^2}{\sum_{k=1}^{N}(y(k) - \bar{y})^2} \tag{3.6}$$

Where $\bar{y}$ is the mean value of the measured outputs;
$y(k)$ is the $k^{\text{th}}$ datapoint of the measured output; and
$\hat{y}(k)$ is the $k^{\text{th}}$ datapoint of the model output.

The coefficient of determination can be applied to measure the fidelity of linear and nonlinear models. Its estimates are however only meaningful when there are considerably more datapoints than dimensions [94] (i.e. in an overdetermined problem). The measure in (3.6) is only suitable for SISO models, but can be easily generalized to multivariate systems by making use of vector norms as in (3.7).

$$\begin{aligned} R^2 &= \frac{\sum_{k=1}^{p} \|\mathbf{y}(k) - \bar{\mathbf{y}}\|^2 - \sum_{k=1}^{p} \|\mathbf{y}(\mathrm{k}) - \hat{\mathbf{y}}(\mathrm{k})\|^2}{\sum_{\mathrm{k}=1}^{\mathrm{p}} \|\mathbf{y}(\mathrm{k}) - \bar{\mathbf{y}}\|^2} \\ &= \frac{\sum_{k=1}^{p} \left[\sum_{i=1}^{m}(y_i(k) - \bar{y}_i)^2\right] - \sum_{k=1}^{p}\left[\sum_{i=1}^{m}(y_i(k) - \hat{y}_i(k))^2\right]}{\sum_{k=1}^{p} \left[\sum_{i=1}^{m}(y_i(k) - \bar{y}_i)^2\right]} \end{aligned} \tag{3.7}$$

Where $\bar{y}_i$ is the mean value of the $i^{\text{th}}$ measured output variable;
$y_i(k)$ is the $k^{\text{th}}$ datapoint of the $i^{\text{th}}$ measured output variable; and
$\hat{y}_i(k)$ is the $k^{\text{th}}$ datapoint of the $i^{\text{th}}$ output variable of the model.

One drawback of the coefficient of determination is however that its results are somewhat dependent on the specific input signal used (remember that a nonlinear system's output is quite sensitive to the specific inputs applied). Overfitted models (where the model order is much higher than warranted by the system dynamics) can also give a false sense of security. Both of these concerns can be addressed by using a so-called validation dataset (data that haven't been used in the estimation of the model) with which to evaluate the quality of the model [44].

A novel alternative measure of linearity is the *gain-based measure*. This measure is also model-based, and requires that an LTI model first be fitted to the data. It is based on the fundamental difference between linear and nonlinear systems, namely adherence to the superposition principle. Nonlinear systems don't conform to the superposition priciple because their input-output gain is (amongst other things) dependent on the amplitude of the input signal. Consequently, a difference in the estimated gain of a system and an LTI model for it, is indicative of the presence of nonlinearities. By comparing the relative gains of the system and its model for various input signals, it is possible to quickly determine whether the system has departed from a linear regimen. A convenient measure of the gain of a system or model over a certain time interval is the ratio of the spread of the output signal to the spread of the input signal (thereby making this measure suitable for stochastic excitation signals). Mathematically, the gain-based measure can be expressed as follows:

$$\gamma = \frac{\frac{\sigma\{y(t)\}}{\sigma\{r(t)\}}}{\frac{\sigma\{\hat{y}(t)\}}{\sigma\{r(t)\}}} = \frac{\sigma\{y(t)\}}{\sigma\{\hat{y}(t)\}} \tag{3.8}$$

where $\sigma\{y(t)\}$ is a measure of the spread of the measured output of the system;
$\sigma\{r(t)\}$ is a measure of the spread of the measured input of both the system and its model; and
$\sigma\{\hat{y}(t)\}$ is a measure of the spread of the output of the LTI model.

The gain-based measure is also useful for detecting any change in the instantaneous gain of a nonlinear system. This incarnation of the gain-based measure is even independent of any model fitted to the system and can be applied to only the measured system data. By estimating the gain of the nonlinear system over a small time interval by means of (3.9) and tracking the gain as time goes by (and various inputs are applied to the system), it is easy to see how the nonlinear system changes from setpoint to setpoint over its operating range.

$$\gamma = \frac{\sigma\{y\}}{\sigma\{u\}} \tag{3.9}$$

where $u$ is the input to the system and $y$ is the output of the system.

## 3.2 Nonlinearities in 2-DOF AMBs

### 3.2.1 The impact of different nonlinear mechanisms

The basic equation governing the relationship between the current applied to the single coil of a 1-DOF AMB, the position of the point-mass in the airgap and the electromagnetic force exerted on the mass was introduced in the previous chapter (equation (2.1)). From this model it is clear that the force is quadratically dependent on the current. At the same time there is an inverse quadratic relationship between the force and the position of the mass.

Through the use of differential driving mode both of these relationships can be linearized to an extent. Differential driving mode however doesn't give the analysist carte blanche to view an AMB as being purely linear over its whole operating range of positions and currents (as noted in [83]).

The extent of the nonlinear behaviour still present in a sensed 2-DOF AMB operating in differential driving mode is shown in figure 3.3. This figure shows the magnitude of the simulated *electromagnetic force* exerted on a point-mass in a 2-DOF AMB where the reference position was gradually changed in an outward spiral pattern[13] over a large part of the allowable operating range as shown in in figure 3.2. (The three-dimensional surface was obtained via linear interpolation between the datapoints obtained by the simulation.)

Clearly the AMB behaviour does slightly stray beyond the confines of a linear mapping between position and force. Nonetheless, a linear approximation for (2.1) ought to be sufficiently accurate for a number of control applications. (In fact, fitting a least-squares hyperplane through the observed data in figure 3.3 by means of the Moore-Penrose pseudo-inverse (3.2),

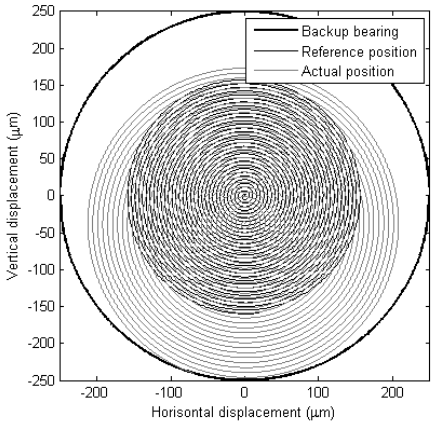


Figure 3.2: Input and output position of the AMB

[13]The continuous nature of a spiral pattern minimizes the occurrence of transient behaviour. The response in figure 3.2 also indicates that the AMB didn't exhibit any frequency-induced nonlinear behaviour (which will be elucidated shortly). The movement of the point mass is limited by the inner-diameter of the retainer bearings, which is 250 μm for the duration of this study. The influence of gravity on the AMB response is quite evident in the DC-offset between the commanded and actual rotor positions in figure 3.2.

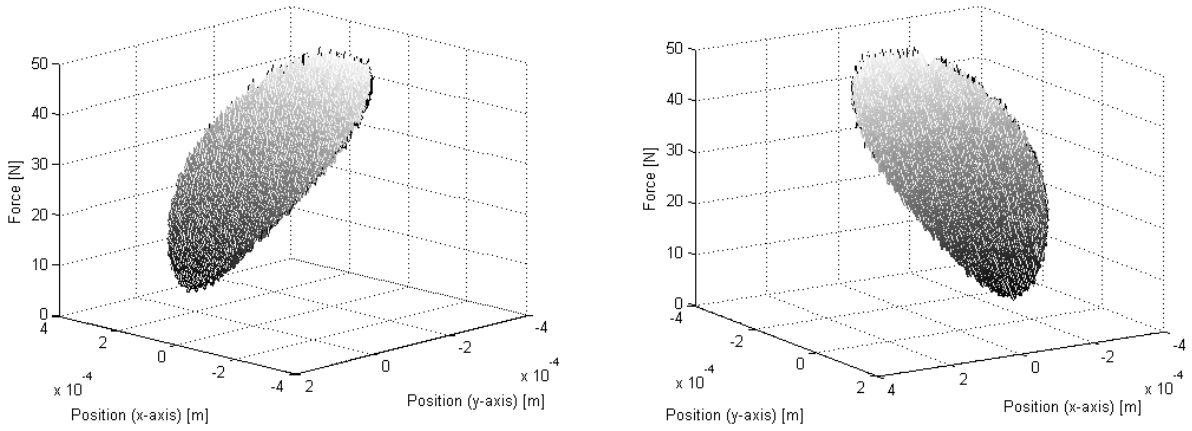


(a) (b)

Figure 3.3: Two viewpoints on the electromagnetic force as a function of rotor position

resulted in a model that could explain 96.26 % of the variability in the data according to (3.7).) Similar conclusions can be drawn from figure 3.4, which shows the effect of the currents in coil 1 and coil 2[14] on the *electromagnetic* force exerted on the point-mass. (In this case, a least-squares hyperplane could explain 96.59 % of the variability in the data.)

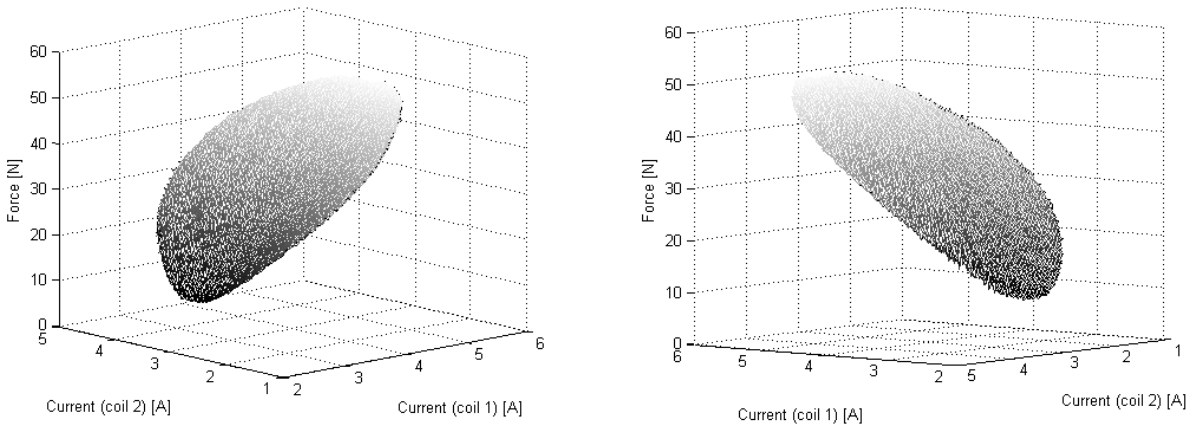


(a) (b)

Figure 3.4: Two viewpoints on the electromagnetic force as a function of the currents in coils 1 and 2

The other source of nonlinear behaviour in AMBs is the magnetic properties of the magnetic circuit and specifically the magnetic properties of the materials from which the AMB stator and rotor are manufactured. More specifically, the effects that come into play are saturation and hysteresis as well as leakage and fringing of the magnetic field.

Usually AMBs are designed in such a fashion that the greater part of their operating range

[14] As defined in figure 2.1.

is situated in the linear range of the hysteresis curve of the magnetic material from which it is constructed [8]. Saturation only rears its head when the permeability of the magnetic material wanders beyond this linear region. Consequently, the response of the AMB is only affected by saturation when the position of the point-mass embarks on large excursions from the centrepoint (i.e. movement closer to the back-up bearings). This statement is supported by simulations in which nonlinear magnetic properties of the stator material were alternatively included and excluded with little difference in the final system response. (As an example, figure 3.5(a) shows the simulated response of the AMB when hysteresis is included. The absolute difference between this response and the response when hysteresis is excluded from the simulation model is shown in figure 3.5(b). Clearly the effect of hysteresis on the behaviour of a sensed AMB is relatively insignificant.) Hysteresis and saturation therefore don't play a major part in influencing the response of a sensed AMB (during typical operation)[15].

The frequency content of the position signal of the rotor in the AMB also induces nonlinear behaviour in the AMB. This phenomenon is relatively unknown and entails that the rotor may suddenly reveal oscillatory behaviour or even delevitate if the rotor position is perturbed with a sufficiently high frequency disturbance signal.

Evidence of this phenomenon in the literature is sparse. Simulation results by Hegazy and Amer show that changing the amplitude of excitation signals (external disturbance forces) may induce chaotic behaviour[16] in the rotor [95]. These simulation results are supported by the experimental results of Jugo *et al.* [96]. They have shown that excessive vibrations (due

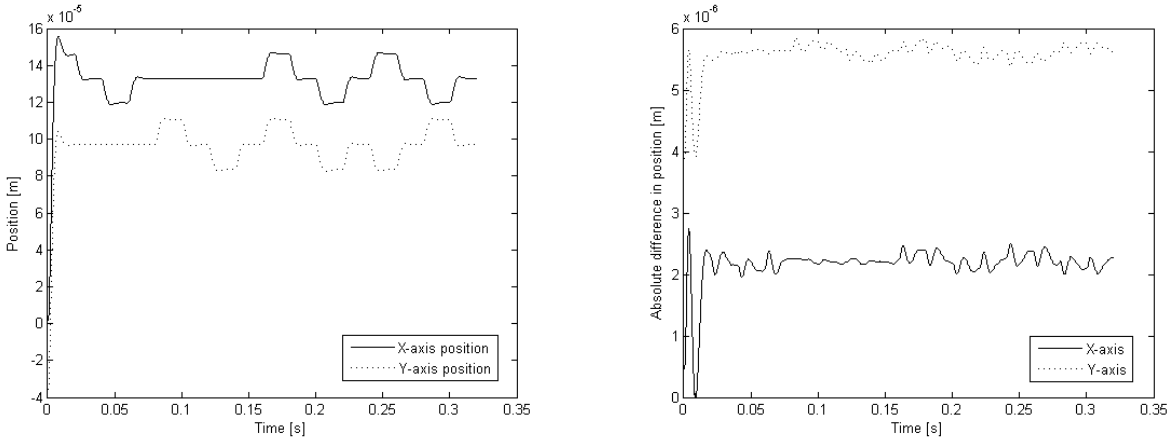


(a) Response with hysteresis included

(b) Absolute error due to the exclusion of hysteresis

Figure 3.5: The effect of the inclusion of hysteresis in the AMB simulation model

[15] At this point it must be stressed that this conclusion only holds for sensed AMBs. Self-sensing AMBs are very sensitive for saturation, since saturation directly influences the position information encoded in the coil currents due to the changing permeability of the magnetic material [35].

[16] *Chaotic* behaviour is a nonlinear phenomenon where the response of a nonlinear system is seemingly stochastic, yet repeatable if exactly the same initial conditions are used. This means that the response of a nonlinear system with chaotic tendencies is deterministic, yet extremely sensitive for the initial conditions under which the system was excited [19].

to mechanical resonance at certain rotational speeds) result in loss in the low-frequency gain of the AMB. (In other words, the magnetic force falls away if the rotor is vibrated at certain frequencies.) Their results also show that the magnetic force is a nonlinear function of position, current and frequency. Frequency induced nonlinearities may therefore occur if the shaft experiences excessive vibration due to rotordynamics, external disturbance forces impacting on the shaft or imprudently applied signals at the reference position (system input).

Accurate system identification however depends on persistent excitation which, in turn, is determined by the frequency content of the excitation signal. It is therefore vital to ensure that nonlinear behaviour isn't induced in the AMB by the very signal with which it is interrogated. With this in mind, the next section explores the topic of frequency induced nonlinear behaviour in more detail.

### 3.2.2 Frequency induced nonlinear behaviour

Figure 3.6 reveals the specific nonlinear behaviour induced by the frequency of the shaft position. This figure shows the simulated response of a 1-DOF sensed AMB for a reference position signal that consisted of a sine-wave frequency sweep at a constant amplitude. Also shown is the response of an LTI model[17] for the 1-DOF AMB to exactly the same signal. For low frequencies, the nonlinear system behaves like a typical low-pass LTI system in that its output is merely an attenuated and slightly delayed version of the input signal at a constant bias level. As the frequency of the input signal is gradually increased, the nonlinear system departs from LTI behaviour in that its bias level starts to drift away from its initial value. The latter behaviour is typical of linear affine systems. A further increase in the input frequency however results in an abrupt change in the behaviour of the nonlinear system: it enters a limit cycle whose frequency is much lower than that of the input signal. The frequency of these "oscillations" is also quite independent of the input signal. (In fact, this frequency has been measured and found to be approximately the same as that of the dominant pole of the closed-loop LTI model for the system[18].) Not shown in figure 3.6 is the consequence of a further increase in the frequency of the input signal, namely delevitation of the AMB.

From the above discussion it seems as if frequency induced nonlinear behaviour in AMBs can be classified into four regions, namely:

[17] This model was obtained via system identification, but the particulars are irrelevant at this stage of the discussion.

[18] For a double actuator 1-DOF AMB the frequency of the dominant AMB pole is given by the following equation, [32].

$$p_{1,2} = \pm\sqrt{2k_s/m}$$

In this equation the so-called position stiffness, $k_s$ of the AMB is given by:

$$k_s = \frac{-2\mu_0 N^2 i_0^2 A}{x_g^3}\cos(\theta)$$

For an AMB with a mass ($m$) of 5.378 kg, airgap ($x_g$) of 0.475 mm, a coil consisting of 80 turns ($N$) with a bias current ($i_0$) of 2.54 A, a pole face area ($A$) of 204.026 $\mu m^2$ and a pole face angle ($\theta$) of 22.5°; the frequency of the dominant pole is then 337.1 rad/s which translates to 53.6 Hz (which is approximately the frequency of the "oscillations" in figure 3.6).

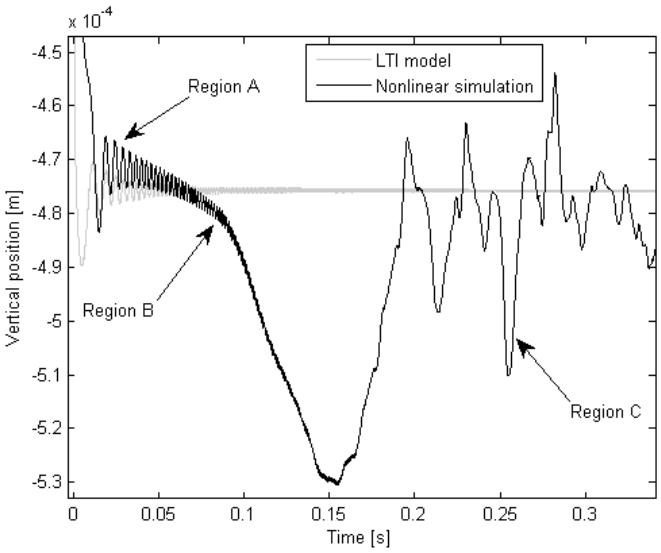


Figure 3.6: Response of a nonlinear 1-DOF AMB to a frequency sweep

- Region A: Pure LTI behaviour.
- Region B: Characterized by a drifting bias level, but otherwise similar to linear affine models.
- Region C: Nonlinear oscillations occuring at a much lower frequency than that of the input signal.
- Region D: Delevitation.

Up to this point, the response of a 1-DOF AMB has been used to introduce frequency-induced nonlinear behaviour. 2-DOF AMBs also exhibit this kind of behaviour, as can be seen from figure 3.7. Only the y-axis component of the rotor position is shown (since the desired behaviour is more pronounced in the vertical dimension due to gravity). Although the AMB response in this figure is a function of time, it has been plotted against the instantaneous frequency of the input signal to accentuate the relationship between the AMB response and frequency. The (admittedly fuzzy) boundaries between the various regions of behaviour have been determined via an algorithm which will be detailed in section 3.2.3.

It is important to ensure that the instantaneous frequency of the input signal changes gradually. This gradual change in the frequency of the input signal should also be slow enough to avoid transient behaviour dominating the waveform of the output signal. Abrupt changes in the frequency of the input signal will result in transient behaviour in the output signal, as can be seen clearly in figure 3.8(a) where the frequency of the input signal was increased in large increments of 99 Hz. By using smaller changes in the frequency of the input signal, the occurence of transients can be minimised (as can be seen in figure 3.8(b) where the frequency was increased in increments of 36 Hz).

The root cause of frequency-induced nonlinearities in AMB behaviour can best be explained by making use of the force equation (2.1) for a 1-DOF AMB. By collecting all constants in a single

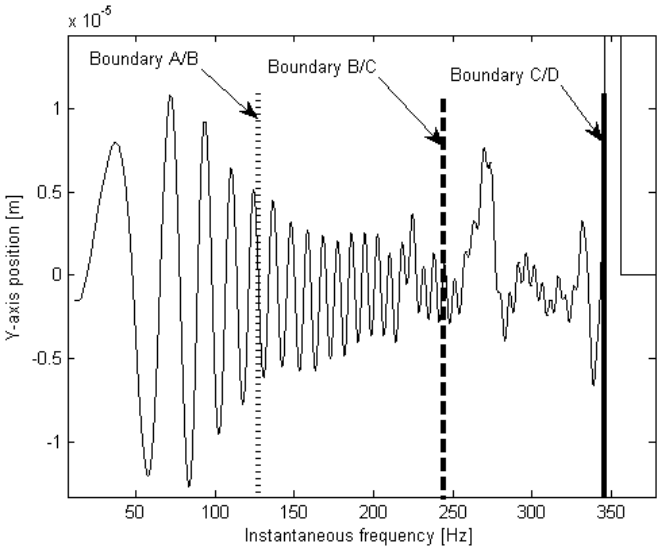


Figure 3.7: Response of a nonlinear 2-DOF AMB to a frequency sweep

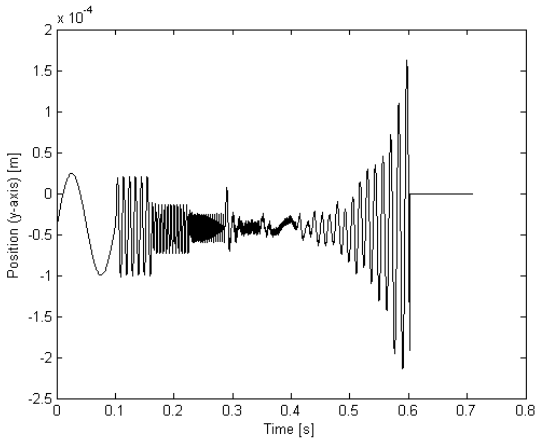


(a) 99 Hz frequency increments

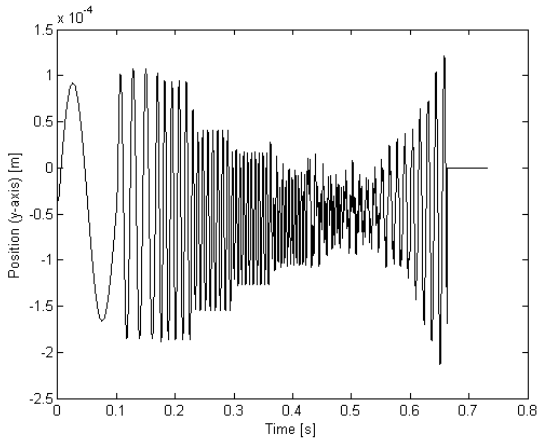


(b) 36 Hz frequency increments

Figure 3.8: Transient behaviour induced by abrupt changes in the frequency of the input signal

coefficient, $k$, the electromagnetic force exerted by a 1-DOF AMB can be modelled as follows (with all time-dependencies explicitly highlighted):

$$f_m(t) = k\frac{i^2(t)}{x_g^2(t)} \tag{3.10}$$

Taking the derivative of (3.10) with respect to time allows us to investigate the effect that *changes* in the position of the rotor can have on the force exerted by the AMB on the rotor. Application of the quotient rule of differentiation results in the following:

$$\frac{df_m(t)}{dt} = \frac{2ki(t)\frac{di(t)}{dt}x_g^2(t) - 2ki^2(t)x_g(t)\frac{dx_g(t)}{dt}}{x_g^4(t)} \tag{3.11}$$

Rearranging (3.11) with the aim of expressing the force of equation (3.10) in terms of the derivatives of position and current leads to:

$$f_m(t) = \frac{ki(t)\left(\frac{di(t)}{dt}\right)}{x_g(t)\left(\frac{dx_g(t)}{dt}\right)} - \frac{x_g(t)\left(\frac{df_m(t)}{dt}\right)}{2\left(\frac{dx_g(t)}{dt}\right)} \tag{3.12}$$

From (3.12) it is clear that the force exerted by the AMB is inversely proportional to the derivative of the position of the rotor. Sudden and large changes in the position of the rotor will therefore result in a commensurate loss in magnetic force applied to the rotor. Another conclusion stemming from (3.12) is that both the frequency and amplitude of the changes in the rotor position will lead to a reduction in the force. (The derivative of the position signal is after all not only determined by how quickly the input signal changes, but also by the amplitude of the change.)

### 3.2.3 Frequency-amplitude graph

The ultimate purpose of this discussion on the various forms of nonlinearity that plague AMBs, is to serve as guide for fitting accurate models via system identification. These models, in turn, are necessary ingredients for forming an estimate of the stability margin of the AMB by means of $\mu$-analysis. The latter analysis technique however assumes that the models of the nominal system and of the dynamic uncertainty are all LTI. Furthermore, it stands to reason that the most accurate LTI models will be fitted when the AMB is acting like an LTI system. The estimation data used for system identification should therefore be sampled when the AMB is exhibiting region A behaviour.

From the discussion in the previous section it was concluded that the combination of both the amplitude and frequency of the input signal[19] to an AMB system might induce various forms of nonlinear behaviour. It would be advantageous if the behaviour of an AMB for various combinations of frequencies and amplitudes of the input signal could be summarized in a

[19]The reference position required from the AMB (which is applied as the input signal in figure 2.2).

single graph. Such a tool would give an immediate indication of the expected fidelity of an LTI model for the AMB for different input signals[20].

Figure 3.9 presents the basic idea of a possible graphical AMB characterization tool. This graph is based on the response of an AMB to numerous frequency sweeps (of various combinations of the amplitude and maximum frequency reached during the sweep). By automatically determining the boundaries between the different regions of AMB behaviour, a clear pattern ought to emerge. From practical experience as well as the results in (3.12) it is reasonable to expect that the interval of frequencies for which the AMB will behave linearly will be much smaller for large amplitude position deviations than for smaller position deviations.

The conceptual graph in figure 3.9 can only be realized in practice if the boundaries between regions A, B, C and D can be automatically detected. Although these regions are defined rather hazily and the progression from one region to the next occurs gradually, it is possible to detect the boundaries between them on the basis of the observed system response. This can be done by clearly defining the onset of region B, C and D behaviour. Delevitation (region D) is easy to detect since it occurs when the radial position of the point mass exceeds the inner diameter of the retainer bearing (in this case 250 µm). Similarly, region B behaviour can be defined as the first occurence of a trend (in any direction) in the bias level of the AMB response. This leaves region C behaviour which can be defined as oscillations with a period that is significantly longer than the period of the input signal.

The complete algorithm with which a frequency-amplitude graph can be generated for an AMB can be summarized as follows:

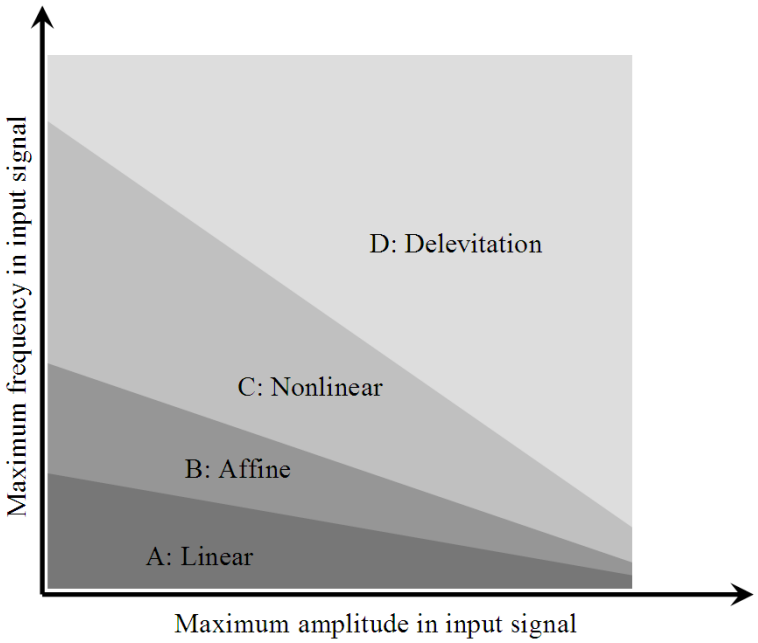


Figure 3.9: Conceptual frequency-amplitude graph of an AMB

[20]Remember that, in contrast with LTI systems, the response of nonlinear systems are dependent on the specific input signals.

1. Apply a frequency sweep with a certain amplitude and maximum frequency to the reference position input of the AMB and measure the position of the rotor for the duration of the sweep.

2. Calculate the median value of the measured $y$-axis rotor position signal. (This value will correspond to the bias value of the response of a fictional LTI model for the AMB.)

3. Identify all zero-crossings in the measured response. (Zero-crossings are defined by the measured rotor position signal falling from above its median value to below its median value.) The interval from one zero-crossing to the next consequently comprises a single "period"[21] of the AMB's response to the input sine-wave.

4. If the distance between consecutive zero-crossings in the AMB response increases significantly (e.g. it doubles) then it is an indication of the start of region C behaviour. (This is in contrast with the zero-crossings of the input signal, which are diminishing in duration as the instantaneous frequency of the input signal increases.)

5. Calculate the average value of the rotor position signal between successive zero-crossings. The resultant signal is a stepwise constant signal henceforth refered to as the short-time averaged signal.

6. If the difference in the gradient between successive "periods" of the short-time averaged signal exceeds some positive (or negative) constant ($\xi$) it signifies the start of a significant trend in the original response of the AMB and therefore the onset of region B behaviour. This constant ($\xi$) is the only user-defined constant in the algorithm.

7. Detect the instantaneous frequency at which delevitation occurs (if it occurs). If delevitation occurs at a particular frequency, the maximum frequency of the next sweep is reduced to this value.

8. Return to step 1 and repeat with an incrementally increased amplitude.

The choice of the parameter $\xi$ in the above mentioned algorithm is governed by the following two criteria:

- The boundaries in the final frequency-amplitude graph should resemble monotone decreasing functions of increasing amplitude. (This criterion is based on the fundamental axiom of inherent smoothness in the non-quantum domain of physical reality, which is frequently invoked in the proofs of mathematical theorems.)

- For each specific amplitude the different boundaries should be consistent with the definitions of the various regions of behaviour (e.g. the boundary between regions A and B can't exceed the boundary between regions B and C).

From numerous trials, it was found that a value of $\xi = 2 \times 10^{-8}$ most often satisfies both of these criteria.

[21] Obviously a chirp signal doesn't have a period, but the interval between successive zero-crossings does correspond to the period of a sine wave with the particular instantaneous frequency at that point in the sweep.

Frequency-amplitude graphs for both the sensed and self-sensing AMBs specified in sections 2.1.2 and 2.1.4 are shown in figures 3.10 and 3.11 respectively. The main difference between these two graphs is that the linear region of the self-sensing AMB is even more limited than that of the sensed AMB. This can be attributed to the lower bandwidth of self-sensing AMBs as well as the increased sensitivity of self-sensing for hysteresis and saturation. Both of these graphs indicate that AMBs have a surprisingly small range of linear operation (in terms of allowable amplitudes and the frequency content of the excitation signal). All of the nominal models obtained via system identification will be confined to region A behaviour in these graphs. Consequently, the nominal models are only valid over a small subset of the total operating range[22].

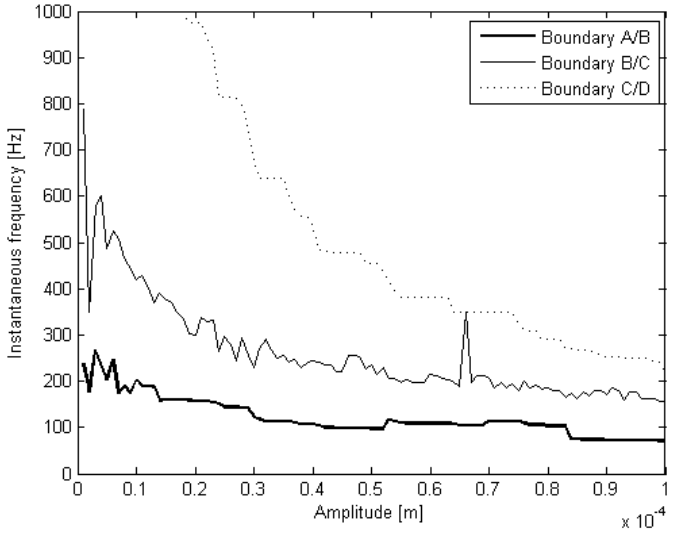


Figure 3.10: Frequency-amplitude graph for a sensed AMB

## 3.3 Injection points and measuring points

Applying system identification to AMBs is a challenging exercise due to the inherent instability of magnetic bearings. Since open-loop operation of an AMB is impossible, system identification must be performed while the AMB is in closed-loop operation. Of the closed-loop identification schemes discussed in the previous chapter, direct identification is the simplest.

Empirical models are however only as good as the data from which they are derived. In fact, in system identification, the nature and quality of the model that is eventually identified is to a large extent determined by the excitation signal used [43]. As mentioned in the previous chapter, the attribute required of excitation signals is persistent excitation. The main feature of a persistently exciting excitation signal is that its power spectrum must be as flat as possible

[22]The spiral pattern used in figure 3.2 for example has a frequency content limited to a maximum of 5 Hertz. From figure 3.10 one can therefore confidently assert that no frequency-induced nonlinear behaviour is present in the response of the AMB shown in figures 3.2, 3.3 and 3.4.

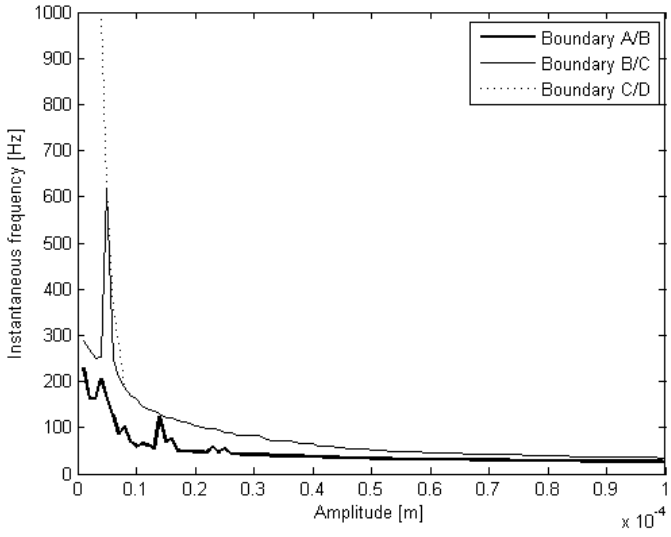


Figure 3.11: Frequency-amplitude graph for a self-sensing AMB

(within a specified frequency band) [41]. Alternatively put, the excitation signal must contain as many distinct frequencies as possible within a specified band [44].

Even though an excitation signal may conform to the standards of persistent excitation, the specific injection point at which it is applied may influence the extent to which the excitation signal is distorted before it arrives at the AMB input. So, when confronted with a closed-loop control system, the question arises where this optimal excitation signal must be applied in order to experience the least distortion. This issue can be settled by comparing expressions for the input signal eventually applied to the plant for the same excitation signal injected at different points in the control system.

Figure 3.12 is a block diagram of a generic SISO control system with various possible points where the excitation signal can be applied through additive perturbation. This control system consists of a controller, $G_C(s)$ in series with a plant, $G_P(s)$. The reference input signal is denoted by $r(t)$, while the error and plant input signals are respectively represented with $e(t)$ and $u(t)$. The output of the system is given by $y(t)$. All nominal signals (i.e. signals before being perturbed) are indicated with an overhead bar (e.g. $\bar{r}(t)$). The numbered points in figure 3.12 can serve as either injection points[23] or measurement points[24] (or both).

For the sake of illustration, let's assume that the objective of system identification in figure 3.12 is to obtain an empirical model for the plant, $G_P$. In the absence of any perturbation signals,

[23] An injection point is defined as the place where the excitation signal is added to the nominal value of the signal already present at that point.

[24] A measurement point is defined as the place where the input or output signals of a sub-system are recorded.

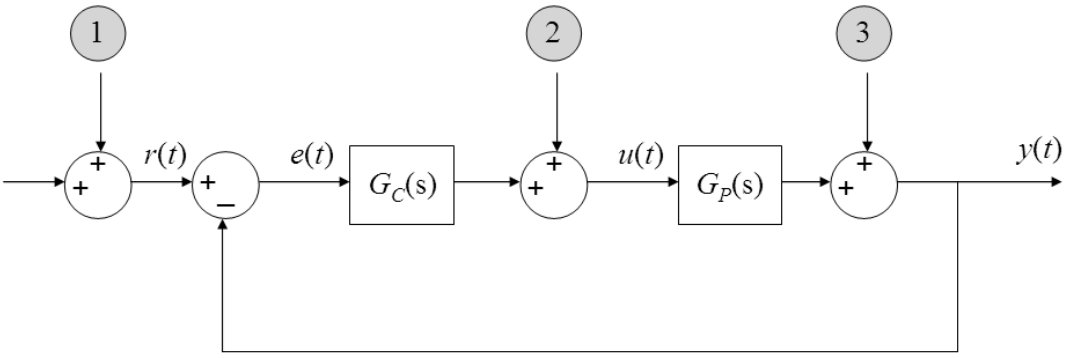


Figure 3.12: SISO closed-loop control system with different potential injection points

the input signal to the plant can be expressed as follows in the s-plane:

$$\begin{aligned} U(s) &= G_C(s)E(s) \\ &= G_C(s)[\bar{R}(s) - Y(s)] \\ &= G_C(s)\bar{R}(s) - G_C(s)G_P(s)U(s) \\ \therefore U(s) &= \frac{G_C(s)\bar{R}(s)}{1 + G_C(s)G_P(s)} \end{aligned} \tag{3.13}$$

This expression can be simplified by making use of the definition of the (SISO) sensitivity function [25], which is given in (3.14). The sensitivity function is defined as the transfer function from output (plant) disturbances to the output of the plant. It is typically a low-pass function and reflects how high frequency disturbances are rejected by the feedback loop.

$$S(s) = \frac{1}{1 + G_C(s)G_P(s)} \tag{3.14}$$

Substituting (3.14) into (3.13) results in (3.15). Under nominal conditions, the input to the plant can be modelled as the product of the controller transfer function and the sensitivity function and the original reference input signal. This means that (even under nominal conditions) the reference signal is filtered by the series combination of the controller and the sensitivity function.

$$U(s) = G_C(s)\bar{R}(s)S(s) \tag{3.15}$$

If the excitation signal is injected at point 1 in figure 3.12, the reference signal is given by $R(s) = \bar{R}(s) + \Xi(s)$ (where $\Xi(s)$ is the Laplace transform of the excitation signal). The measured input signal of the plant is therefore:

$$\begin{aligned} U(s) &= G_C(s)R(s)S(s) \\ &= G_C(s)\bar{R}(s)S(s) + G_C(s)S(s)\Xi(s) \end{aligned} \tag{3.16}$$

Applying the excitation signal $\Xi(s)$ at injection point 2 results in the following measured input

signal:

$$\begin{aligned} U(s) &= \bar{U}(s) + \Xi(s) \\ &= G_C(s)E(s) + \Xi(s) \\ &= G_C(s)[R(s) - G_P(s)U(s)] + \Xi(s) \\ \therefore U(s) &= \frac{G_C(s)R(s)}{1 + G_C(s)G_P(s)} + \frac{\Xi(s)}{1 + G_C(s)G_P(s)} \\ &= G_C(s)\bar{R}(s)S(s) + S(s)\Xi(s) \end{aligned} \tag{3.17}$$

Although injection point 3 seems counter-intuitive when the objective is to obtain a model for the plant, this injection point is often used for practical measurement of the sensitivity function[25]. If this point is used, the Laplace transform of the system output signal is $Y(s) = \bar{Y}(s) + \Xi(s)$ and the plant input can then be expressed as:

$$\begin{aligned} U(s) &= G_C(s)E(s) \\ &= G_C(s)[\bar{R}(s) - Y(s)] \\ &= G_C(s)\bar{R}(s) - G_C(s)G_P(s)U(s) - G_C(s)\Xi(s) \\ \therefore U(s) &= G_C(s)\bar{R}(s)S(s) - G_C(s)S(s)\Xi(s) \end{aligned} \tag{3.18}$$

Standard practice in system identification dictates that the measured input and output data is first detrended before proceeding with parameter estimation [44]. This means that the "steady state component" (namely the term: $G_C(s)\bar{R}(s)S(s)$) should be disregarded when comparing the various input signals obtained in (3.16), (3.17) and (3.18). The distortion experienced by the excitation signal when applied at the different injection points, can therefore be summarized as follows:

- Point 1: $G_C(s)S(s)\Xi(s)$
- Point 2: $S(s)\Xi(s)$
- Point 3: $-G_C(s)S(s)\Xi(s)$

Excitation signals injected at point 2 will therefore theoretically experience the least distortion from the three options investigated in figure 3.12. The poorest plant models will be obtained by using injection point 3, since the resultant estimation data will be contaminated by an additional 180° phase-shift in addition to the distortion introduced by the controller transfer function.

[25]This is however not the case for AMBs, since it is inherently impractical to apply a disturbance at point 3 (due to the non-contact nature of AMBs). As an alternative, the proposed standard for AMB stability recommends using point 1 to measure the closed-loop transfer function of the system [9]. For the configuration in figure 3.12 the sensitivity function can be obtained from the closed-loop transfer function via the following relationship: $S(s) = 1 - G_{CL}(s)$ (where $G_{CL}(s)$ represents the closed-loop transfer function).

## 3.4 Model structure: inputs and outputs

The main disadvantage of black-box modelling is that it gives limited insight into the internal dynamics of the real system that is being modelled. A single black-box model for a closed-loop control system gives the user no indication of the interaction between the various components in the system. In the context of robustness analysis, this implies that it is difficult to apportion blame to specific system components when the total closed-loop system is fragile (and only a single model for the whole system is available). The solution to this problem is more detailed modelling where individual components in the control system are also modelled via system identification. As soon as separate models for the main components in the loop are available, it is possible to assess the influence of each individual component on the total system stability margin.

As discussed in section 2.1, the main components in a 2-DOF self-sensing AMB are the controller, power amplifiers, AMB plant and self-sensing module. A simplified block-diagram of a 2-DOF self-sensing AMB is given in figure 3.13. The controller is generally known to quite a level of detail, since it is the product of a design process and typically implemented on some form of computer. In this study the controller consisted of two identical decoupled PID controllers, each responsible for the control of one axis of freedom. Movement of the rotor in the horizontal plane is determined by one controller, while the other controller only has influence on the vertical plane. The only form of uncertainty in the controller considered in this study[26] is the effect that parameter-changes in the proportional-, derivative- and integral coefficients can have on the system's stability margin.

The AMB plant consists of the coils of the electromagnets, the stator of the AMB as well as the mass which is levitated against gravity. For the eight-pole heteropolar AMB assembly shown in figure 2.1, this AMB model has four inputs (one for each electromagnet) and two outputs (namely the measured $x$-axis and $y$-axis position of the rotor). The AMB plant can therefore be modelled with a four-input, two-output black-box model. The outputs of the AMB plant also

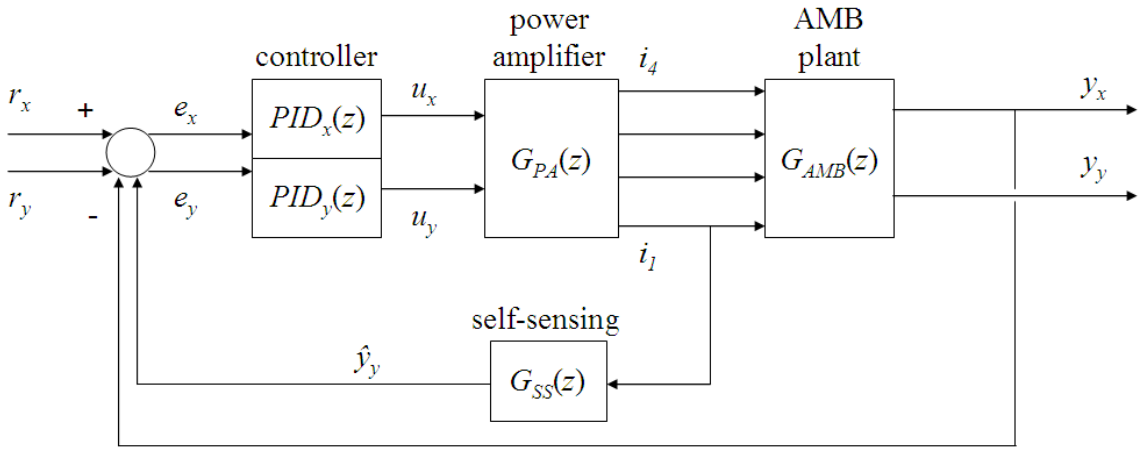


Figure 3.13: Blockdiagram of a 2-DOF self-sensing AMB showing the main system components

[26]Other factors that could also influence the system's stability are the cycle-time of the processor on which the controller is implemented, as well as finite wordlength effects.

form the outputs of the closed-loop system. Of these two outputs only the $x$-axis position is fed back to the controller, since self-sensing is employed to estimate the $y$-axis position.

DCM self-sensing (as implemented in [17]) only takes a single input (namely the current flowing in the top pair of coils) to form an estimate of the $y$-axis rotor position. A SISO black-box model would therefore be sufficient to model the existing DCM self-sensing system.

Modulation-based self-sensing techniques are based on the assumption that the coil currents contain information on the position of the rotor in the form of a small ripple component modulated on top of the normal control current. This assumption is obviously met in the real self-sensing system from which data is captured for system identification purposes. Whether this assumption is met by the LTI models obtained via system identification, is another story altogether. In other words, the LTI self-sensing model will only give accurate and useful estimates of the $y$-axis position if it receives an input signal (current) that contains position information. In contrast with what one would think, the weakest link in an LTI model for a self-sensing AMB isn't the self-sensing model, but rather the power amplifier model.

In a typical 8-pole heteropolar radial AMB, four power amplifiers are employed to supply currents to the four electromagnets arranged along the stator (see figure 2.1). Differential driving mode entails that the output of the $y$-axis controller is added to and subtracted from a bias current level to obtain the reference inputs for the power amplifiers that supply currents to the top and bottom electromagnets respectively. Similarly the $x$-axis controller output is added to and subtracted from the same bias current to give the inputs for the two power amplifiers responsible for the currents in electromagnets two and four (following the same notation as in figure 2.1). At first glance, it seems as if the power amplifier component in figure 3.13 could be satisfactorily modelled by a two-input, four-output model.

A two-input, four-output power amplifier model would be sufficient for a sensed AMB. In a self-sensing AMB however, such a power amplifier model would lead to delivation, because the power amplifier outputs don't contain any position information.

The fundamental principle upon which self-sensing is based is that the impedance of the coils (specifically their inductance) is a function of the airgap [31]. This means that a power amplifier's response is not only a function of the controller output, but also of the actual position of the mass within the airgap. (Such inputs, which aren't explicitly engineered into the control system may be referred to as *implicit inputs*.) To ensure that the outputs of the LTI power amplifier model contain position information, the LTI model should be an explicit function of all variables that have an effect on the real coil currents. This means that the LTI power amplifier model now accepts four inputs (namely two outputs from the controller and two position signals from the output of the AMB plant).

The improved block-diagram of the LTI self-sensing AMB is given in figure 3.14. This figure highlights one potential problem in the closed-loop system, namely the presence of algebraic loops. Algebraic loops occur when the output of a sub-system is directly fed back to its own input, making the output a function of itself [97]. Such loops can be clearly seen in the dependence of the LTI power amplifier model on the AMB output position. (Depending on the values in the respective state-space models of the power amplifier and AMB plant, it is a

distinct possibility that the output of the power amplifier might be a function of itself.) The presence of algebraic loops makes it much more difficult to obtain a closed-loop expression for the complete control system. They are unfortunately a necessary evil in order to obtain stable levitation for the LTI self-sensing AMB model.

Once the model structure has been finalized and data collected, the last step before parameter estimation is often detrending the data in order to remove all mean values from the data. Detrending is however inadvisable in self-sensing, since DCM self-sensing is sensitive for the bias current level in order to compensate for the nonlinearity due to hysteresis and saturation in the magnetic material of the AMB stator [17]. Detrending would result in loss of information on the necessary setpoint of the LTI self-sensing model, with subsequent (and inevitable) delevitation. The effect of detrending on the information content of the resulting LTI power amplifier models is illustrated in figure 3.15. In each of these figures the essential position information present in the nonlinear power amplifier output is compared with that of the LTI power amplifier model output. The next few paragraphs will aid in the interpretation of these figures.

Based on the discussion in section 2.1.3, the position of the rotor can be estimated by demodulating the spectral components of the coil current residing in the vicinity of the switching frequency. Demodulation of a specific AM modulated signal can be accomplished by isolating the switching frequency component with an appropriate bandpass filter (centered on 30 kHz in our case). Thereafter the absolute value of the filtered signal is calculated and then filtered by a lowpass filter (whose passband is limited to the time constants of the rotor, namely 1 kHz). If the original coil current was sampled from a real operating AMB system, the demodulated current signal would correspond exactly to the position signal of the rotor. This might not be the case for an LTI model of the power amplifier.

Figure 3.15 shows scatterplots of the output position as a function of the demodulated coil currents (collected during typical AMB operation). Ideally, there should be a linear relationship between these two variables (otherwise self-sensing would have been impossible). A strong

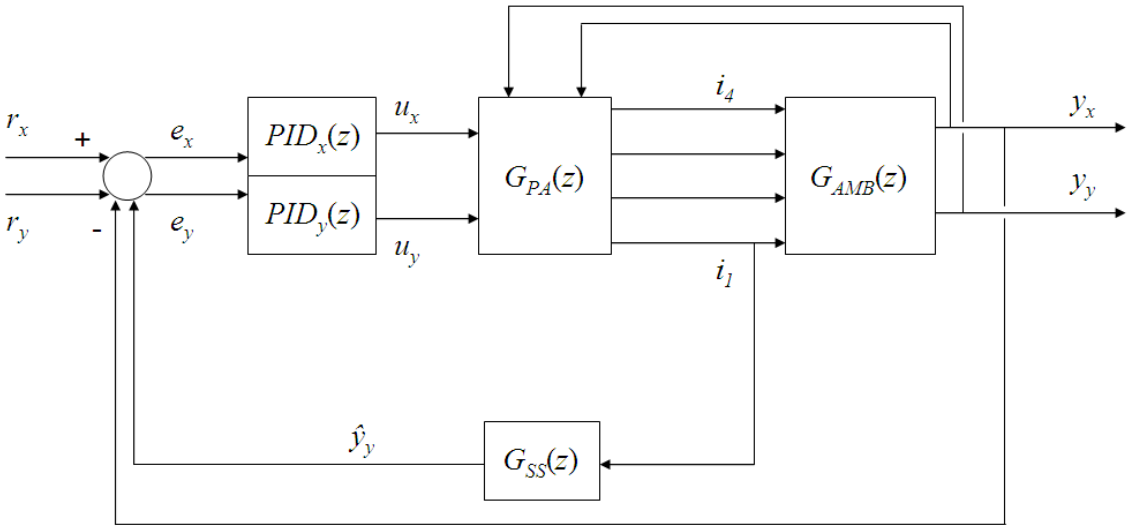


Figure 3.14: Detailed block-diagram of an LTI self-sensing AMB

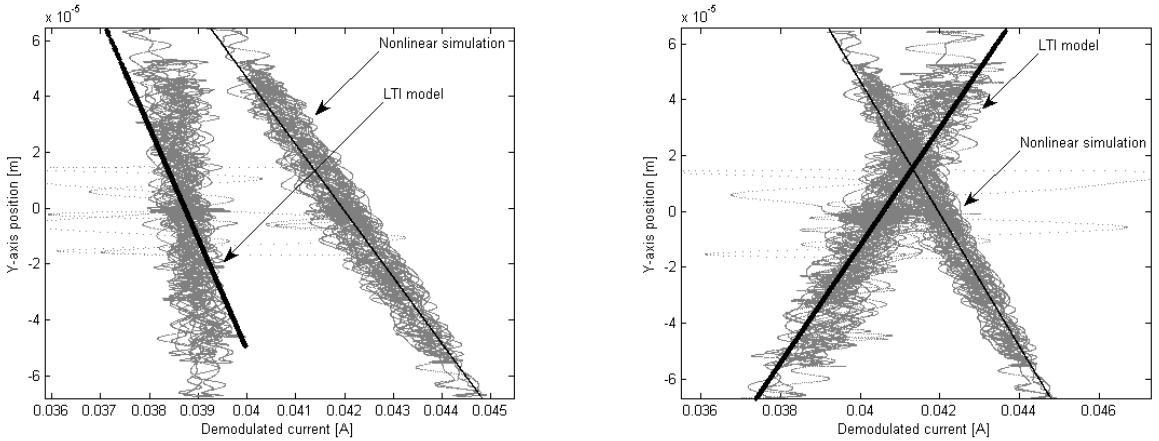


(a) Without detrending (b) After detrending

Figure 3.15: The effect of detrending on the position information content of the power amplifier output signal

linear relationship can be seen between the measured output position and demodulated coil current obtained from the *nonlinear AMB simulation* (shown in the left-hand and right-hand figures). Both figures also show scatterplots obtained in a similar fashion for the *LTI power amplifier model*. Least-squares lines have also been fitted through the respective scatterplots as an aide in comparing the nonlinear simulation with the LTI model[27]. The only difference between the two plots in figure 3.15 is that detrending was performed prior to the parameter estimation of the LTI model in the right-hand plot. By comparing the two plots in figure 3.15 it is obvious that detrending has a huge impact on the eventual information content of the output signal of the LTI power amplifier model. In fact, detrending changed the sign of the gradient of the linear relationship between demodulated current and position, thereby rendering the LTI power amplifier model useless for self-sensing purposes.

There are only two remaining issues that have to be addressed before system identification can be applied to obtain nominal models for the various components in a self-sensing AMB. Before parameter estimation can be performed, a specific model structure has to be chosen and before that can be done, the sampling period of the model has to be finalized.

## 3.5 Model structure: sampling frequency

This study wil make use of discrete-time system identification to obtain models for the self-sensing AMB. Prior to the application of a parameter estimation algorithm, it is necessary to choose the sampling frequency of the eventual models. This choice is however not as trivial as one would presume.

System identification works best if the sampling frequency is commensurate with the time

[27]The apparent discrepancy between the one least-squares line and its scatterplot in figure 3.15(a) is due outlier datapoints that have a disproportionate effect on the final fitting.

constants of the plant [44]. The lower bound on the sampling frequency is dictated by the Nyquist frequency (which is once again determined by the phenomena that we want to model). If the sampling frequency is chosen too high, numerical problems may arise during parameter estimation. Furthermore, the resultant model may contain too many high frequency dynamics and loose its focus on the important low frequency characteristics of the system. High sampling frequencies can also lead to nonminimum phase models [44]. The presence of right half plane zeros places fundamental limits on control in both SISO and MIMO systems [25] and complicates some stability analysis techniques [84]. Another problem that will arise if the sampling period is chosen injudiciously high is that the accuracy of the eventual robustness analysis based on the identified model may be compromised. This problem can be elucidated by studying the expressions for the theoretical z-plane plant poles of a simple second order model for an AMB[28], namely:

$$z = e^{\pm\sqrt{\frac{2k_s}{m}}T} \tag{3.19}$$

where $k_s$ once again represents the position stiffness, $m$ is the mass of the rotor and $T$ is the sampling period.

Clearly the poles start clustering around the (1,0) point on the perimeter of the unit circle in the z-plane as the sampling period approaches zero. This is undesirable for two reasons:

- It becomes more and more difficult to discern between different neigbouring poles as the sampling period is reduced.
- Any small errors in the pole positions are amplified by the transition from the z-plane to the s-plane (the topic of section 3.7.1). The resulting $\mu$-analysis will therefore be handicapped by erroneous nominal s-plane models.

Self-sensing AMBs are complex systems with many processes occuring on different time scales, making the choice of the sampling frequency even more difficult. At least two different time scales can be discerned in a typical AMB, namely the mechanical and electrical time scales [11]. The movement of the rotor is obviously on a much slower time scale (1 kHz or less) than the signal processing performed in the digital controller. In self-sensing systems these two time scales are typically separated by a factor of 10 or more. The electrical time scale in DCM self-sensing consists of the control cycle (performed at 10 kHz) and the self-sensing cycle. DCM self-sensing requires accurate measurements of the peak values of the modulated component present at the switching frequency of the power amplifiers (which is at 30 kHz). This means that the eventual identified models must have sampling frequencies higher than 60 kHz at least.

The original nonlinear simulation is however conducted at 1 MHz. A necessary precursor to parameter estimation is therefore that the sampled data be decimated (or downsampled) to the target sampling frequency (of the desired LTI models). Decimation involves two steps [98]. First, a low-pass filter is applied to avoid aliassing when the sampled signal is resampled at a slower tempo. Secondly, every $k^{\text{th}}$ sample of the original sampled sequence is selected to form a new signal. In this study the decimation factor ($n$) is limited to integers.

[28] These equations are derived in Appendix A.

Decimation does however introduce slight distortion in the downsampled signal. These spurious values are due to transient behaviour of the anti-alias filter at the beginning and end of the original signal. In order to avoid these errors influencing the models obtained during parameter estimation, it is necessary to discard any transients that were introduced during decimation. The number of spurious samples in question is very small (in the region of the order of the low-pass filter used for anti-aliassing). Consequently the loss in data is quite acceptable.

Another problem introduced by the anti-alias filter used in decimation is that practical filters lead to slight attenuation of higher frequency components in the decimated signal. This is especially troublesome if wide bandwidth excitation signals (e.g. white noise) were used to interrogate the AMB system. One solution to this problem is to rescale the decimated signal back to approximately its original distribution after downsampling has been performed. If $x$ represents the original sampled data before decimation, and $y$ is the data after downsampling, rescaling involves that each sample in $y(t)$ is replaced as follows:

$$y \leftarrow ((y - \bar{y}) \times \alpha) + \bar{x} \tag{3.20}$$

where $\bar{x}$ is the mean value of $x$, $\bar{y}$ is the mean value of $y$ and the scaling factor, $\alpha$ is defined as follows:

$$\alpha = \frac{\max(x) - \min(x)}{\max(y) - \min(y)} \tag{3.21}$$

The scaling constant in (3.21) is however quite sensitive to outliers. A more robust estimate of the spread of the data (that is also independent of the underlying distribution of the data) is the interquartile range (IQR), resulting in the following scaling constant:

$$\alpha = \frac{IQR(x)}{IQR(y)} \tag{3.22}$$

Now that all the problems surrounding decimation have been addressed, the issue stil remains: "what would the best sampling frequency be?" As a preliminary investigation into lowering the sampling frequency, table 3.2 compares a few possible sampling frequencies on the basis of the number of samples available for each period of the power amplifier. It is important that the peak values of the switching ripple on the current signal is correctly captured in the downsampled signal, since DCM self-sensing requires accurate measurements of this quantity. The number of samples devoted to each switching period is calculated by dividing the switching period (which is 33.3 $\mu$s) by the sampling period of the downsampled signal. Clearly the probability of missing the peak value of the current ripple in a switching period becomes larger as the sampling frequency of the decimated signal decreases.

The risk of consistently missing the peak value of the current ripple is dramatically increased if the sampling frequency is close to being an integer multiple of the switching frequency. One example of such a sampling frequency is 90.9 kHz. The position information content in the coil current of this signal is compared to that of the original 1 MHz signal in figure 3.16(a)[29]. A similar graph is shown in figure 3.16(b), but this time for a 83.3 kHz downsampled

[29]These figures were obtained in the same fashion as figure 3.15.

signal. In the latter graph the demodulated current of the downsampled signal is almost indistinguishable from the original signal. This is however not the case for a 90.9 kHz signal. The latter downsampled demodulated current has a slightly wider distribution, as well as a significant offset compared to the original (1 MHz) demodulated current. Another sampling frequency which is disqualified on the same grounds as 90.9 kHz is 66.6 kHz.

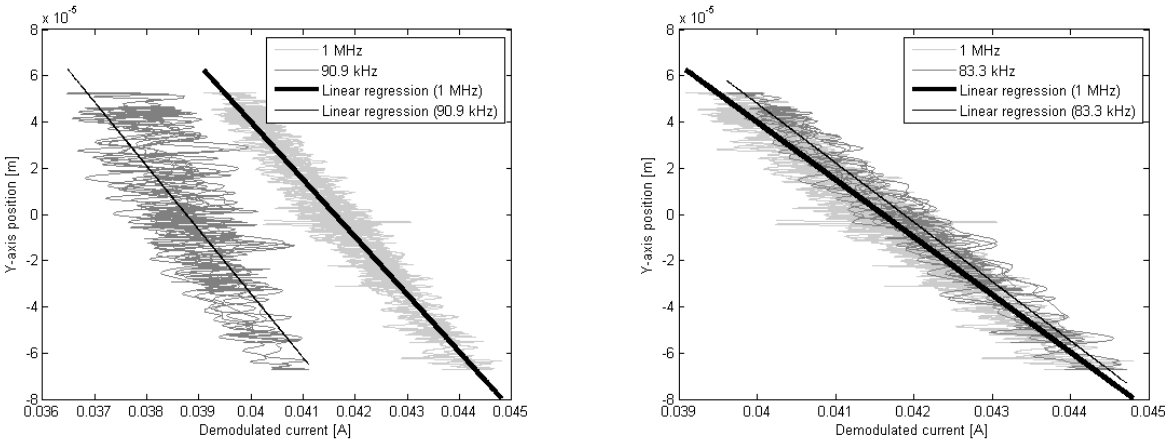


(a) (b)

Figure 3.16: The effect of decimation on the position information content of the power amplifier output signal

The final shortlist of potential sampling frequencies is therefore 71.4 kHz, 76.9 kHz and 83.3 kHz. All three sampling frequencies result in coil currents with essentially the same position information content as the original 1 MHz signal. In the interest of using a sampling frequency which is as low as possible, all LTI models are therefore fitted to data sampled at 71.4 kHz (where possible).

## 3.6 Model structure: parameterized structures

Once the number of inputs and outputs of a black-box model as well as its sampling frequency have been finalized, the next step is to choose a suitable parameterized model structure. This

Table 3.2: Implications of different sampling frequencies

| Decimation factor | Sampling frequency [kHz] | Sampling period [µs] | Number of samples per switching period |
|---|---|---|---|
| 10 | 100.0 | 10 | 3.33 |
| 11 | 90.9 | 11 | 3.03 |
| 12 | 83.3 | 12 | 2.78 |
| 13 | 76.9 | 13 | 2.56 |
| 14 | 71.4 | 14 | 2.38 |
| 15 | 66.7 | 15 | 2.22 |

choice has far reaching effects since an incorrect model structure contributes to the bias error of the model [44]. The two criteria that influence this choice are firstly the fact that most of the component sub-systems in the AMB control system are multivariable (see figure 3.14). Secondly, the model structure must have the capability to model both unstable and stable plants. (The AMB plant is after all inherently unstable and should therefore also be modelled as such.)

Various model structures are available with which MIMO systems can be modelled, including ARMAX and Box-Jenkins [44]. At present, Matlab's system identification toolbox[30] is limited to multivariable ARX and state-space model structures. Of these two, the state-space model structure is inherently an easier and more elegant framework to extend to multivariable problems, since it places the power of linear algebra at the disposal of the analysist. Some of the parameter estimation algorithms for state-space models (specifically subspace methods) are also better suited to MIMO systems [41].

AMBs are however inherently unstable. This implies that system identification will have to be performed on data obtained while the system is in closed-loop operation [77]. Apart from the difficulty in obtaining quality estimation data for the AMB plant, an added burden is that the eventual model of the AMB plant should also be unstable[31]. Fortunately, ARX models are suitable for direct closed-loop identification of unstable systems [50]. The primary drawback of ARX models is that they may exhibit a slight high-frequency bias if the sampling frequency is too large [44], which manifests itself in the form of very large transient responses.

It is however possible to obtain unstable state-space models via system identification provided that the correct weighting scheme of the residuals is used during parameter estimation. If the weighting function is calculated as the product of the spectrum of the input signal and the inverse of the estimated noise model, then unstable plant models may ensue, provided that the correct model order is chosen. This weighting scheme is known as a "prediction focus", because it basically entails minimizing the one-step ahead prediction error of the model [26]. The resultant models admittedly have a high-frequency bias, yet don't exhibit the same large transients as ARX models do.

The model structure of choice is therefore state-space models, since it is possible to estimate both stable and unstable models for multivariable systems with them.

A related issue to the model structure is the specific parameter estimation algorithm with which its parameters can be obtained. Broadly speaking, parameter estimation algorithms for state-space models can be dichotomized into two slightly overlapping families of algorithms, namely prediction error methods (PEM) and subspace methods [99]. Prediction error methods is a family of algorithms that aim to minimize the difference (or error) between the measured system response and the model's response by adjusting the parameter vector (2.13). This is typically achieved by minimizing a cost function (based on the model residuals) which is expressed as a function of the model parameters.

[30] In this study system identification is merely a means to an end and not the primary focus of the investigation, hence the use of Matlab's system identification toolbox.

[31] This condition doesn't hold for the power amplifier model.

Subspace methods are non-iterative algorithms that find the **A**, **B**, **C** and **D** matrices of a state-space model in two steps [99]. The first step entails estimating the state-vector from the observed data. This step makes it possible to solve the remainder of the parameter estimation problem via prediction error methods (e.g. least-squares methods)[32]

PEM algorithms lay claim to optimal solutions of the parameter vector (in terms of the cost function that was used). Unfortunately, this advantage comes at the cost of increased computation time. (PEM algorithms converge iteratively to the "optimal" solution.) In contrast, subspace methods are non-iterative and therefore extremely fast, with only a slight bias error in their final estimates of the parameter vector [99]. In fact, Favoreel *et al.* have found that subspace methods performed quite satisfactorily on a range of industrial identification problems compared to PEM [99]. In practical applications, subspace methods regularly provide the initial estimate from which PEM algorithms proceed to the final solution ([99] and [26]). This approach is also followed in this study.

## 3.7 Model conversions

As we will see in the next chapter, estimation of the stability margin via $\mu$-analysis involves numerous conversions of models from one form to another. Inevitably these conversions exact their toll in the form of potential errors that can be introduced in the analysis procedure. In this, the last section of this chapter, we'll briefly discuss the pitfalls surrounding two of these conversions.

### 3.7.1 Z-plane to s-plane conversion

The result of MIMO subspace system identification via Matlab's system identification toolbox is a discrete-time state-space model. Once LTI models for the nominal system and its dynamic uncertainties are available, $\mu$-analysis can be applied to obtain an estimate of the stability margin of the system. Although $\mu$-analysis can be directly applied to discrete-time models, this is rarely performed in practice due to numerical problems [25]. Instead, the *de facto* procedure in $\mu$-analysis is to convert the discrete-time model to an equivalent continuous-time model prior to calculating the values of $\mu$.

Conversion between the z-plane and s-plane is usually performed via the bilinear transformation, which is summarized by the following equation [97]:

$$z = \frac{1 + (T/2)s_w}{1 - (T/2)s_w} \tag{3.23}$$

where $T$ is the sampling period of the discrete-time model, $z$ is the z-plane complex-valued variable and $s_w$ represents the approximated s-plane variable.

The bilinear transformation is an example of a conformal mapping between the z-plane and s-plane. As hinted in the explanation of (3.23), the bilinear transformation is only an approx-

[32] This is the reason why [44] includes subspace methods into the greater family of prediction error methods.

imation[33] of the underlying relationship between the s-plane and z-plane. Per definition, the relationship between the s-plane and z-plane is governed by the following equation:

$$z = e^{sT} \tag{3.24}$$

According to (3.24), the whole of the left hand side of the s-plane is mapped into the inside of the unit circle on the z-plane, while the outside of the unit circle in the z-plane corresponds to the whole of the right hand side of the s-plane. This seemingly benign mapping places an enormous responsibility on the parameter estimation algorithm used in system identification, since small errors in z-plane pole and zero positions are magnified enormously during the mapping to the s-plane. Consequently, any errors incurred during parameter estimation of the original z-plane model are amplified in the subsequent s-plane model, leading to inaccurate robustness analyses.

To be more specific, small complex-valued perturbations from any point in the vicinity of the unit circle are amplified by approximately the sampling frequency during the mapping to the s-plane (see appendix B). This doesn't pose a problem for textbook control systems with slow sampling frequencies, but does become troublesome for the high sampling frequencies found in AMB systems. (In our case, any errors in the parameters of the identified z-plane model are magnified by a factor of more than 71,400 times in the eventual s-plane model.)

The results obtained in appendix B imply that the models obtained via discrete-time system identification have to be very accurate to avoid inaccurate robustness estimates. Another potential pitfall in the whole robustness analysis process is erroneous instability caused by conversions between state-space models and transfer function models. This problem is the topic of the next section.

### 3.7.2 State-space to transfer function conversion

In the robust control framework, dynamic uncertainty is modelled in terms of frequency responses (e.g. [3] and [25]). Frequency responses (whether measured or conjectured) are modelled most naturally by means of transfer functions (especially if the numerators and denominators of the transfer functions are factorised).

System identification of multivariable systems is however best accomplished when the systems are modelled in terms of state-space models. It would therefore seem as if the identified state-space models have to undergo two conversion steps before $\mu$-analysis can be conducted, namely: mapping to the s-plane, followed by conversion to transfer function matrix representation.

The conversion from a state-space model to its equivalent transfer function matrix model, is governed by (3.25) [84].

$$\boldsymbol{G}(s) = \mathbf{C}\left(s\mathbf{I} - \mathbf{A}\right)^{-1}\mathbf{B} + \mathbf{D} \tag{3.25}$$

[33] More specifically, the bilinear transformation is only accurate for frequencies below *one tenth* of the sampling frequency [97].

The presence of matrix inversion in (3.25) heralds the possibility of numerical problems during the conversion from state-space representation to transfer function representation. These numerical problems only become a problem for sensitive systems such as AMBs. In fact, it often occurs that a stable state-space model for a component in the AMB control system has an unstable transfer function representation. For this reason, $\mu$-analysis is best conducted with continuous-time state-space models in stead of transfer function models. (Obviously, this restriction will have repercussions in the modelling of dynamic uncertainty, as we'll see in the next chapter.)

## 3.8 Conclusion

A lot of ground has been covered in this chapter on the topic of system identification applied to self-sensing AMBs. The following list summarizes the most important conclusions made in the past chapter:

- Accurate LTI models for self-sensing AMBs will only be obtained if the excitation signal is stationary and doesn't induce any nonlinear behaviour in the AMB.
- A number of nonlinear mechanisms influence the response of a self-sensing AMB. Of these, frequency induced nonlinearities has the largest effect.
- Excitation signals should be injected as close as possible prior to the component of interest in the control system (to minimize distortion on the actual input to the component that has to be modelled).
- The minimum sampling frequency for the identified models in a self-sensing AMB is 71.4 kHz. In addition, the specific inputs and outputs of each of the main components of the closed-loop self-sensing AMB were finalized.
- Care has to be taken that the identified models are accurate, since any errors are magnified in the ensuing transformation to continuous-time models.
- State-space models will be used throughout the robustness analysis procedure in order to obtain accurate results.

CHAPTER 4

# Application of $\mu$-analysis to AMBs

*The aim of the previous chapter was to put everything in place so that system identification can be applied to obtain LTI models for the main components of self-sensing AMBs. The focus of the study as a whole is to estimate the stability robustness of self-sensing AMBs. As we know, a system is said to be robust if it is insensitive to all differences between the original model for the system and its eventual hardware implementation. Robustness analysis therefore requires more than a nominal model of the system; the unknown factors for which the system must be insensitive must also be modelled. This chapter fills in the remaining blank spaces in order to obtain an estimate of the stability margin of a self-sensing AMB. The chapter kicks-off with an overview of the whole $\mu$-analysis procedure. Thereafter, time is devoted to arguably the most important part of robustness analysis, namely modelling the specific uncertainty for which the system must be robust. The heart of the chapter is concerned with the issue of applying system identification to obtain the required uncertainty models, as well as how to validate those models. Finally, the problem of validation of the final stability margin estimates is addressed.*

## 4.1 Procedure for applying $\mu$-analysis to an AMB

The relationship between $\mu$-analysis and uncertainty modelling is akin to the chicken and egg situation; it is difficult to describe either one without detailed knowledge of the other. With this "dilemma" in mind, a brief introduction to uncertainty modelling in the robust control framework will now be given as preparation for the discussion on $\mu$-analysis.

When a system operates outside the laboratory, it is confronted with the ever present mismatch between the model of the system and the real manufactured system. The uncertainty surrounding model of the system can be modelled by means of two main classes of models, namely: parametric uncertainty and dynamic uncertainty [25]. When the model of the system is quite accurate with the exception of the precise values of a few of the model parameters, *parametric uncertainty* is the appropriate modelling technique. *Dynamic uncertainty* is appropriate when, aside from inaccurate parameters, the model can't explain all of the observed system behaviour

(also known as unmodelled dynamics). Since all models are simplified abstractions of reality, dynamic uncertainty can be found in almost every control system.

Both parametric and dynamic uncertainty can be elegantly modelled in the broader paradigm of norm-bounded uncertainty (referred to in section 2.3). Parametric uncertainty is expressed in a similar fashion to the well-known engineering concept of tolerances. If a certain parameter $\beta$ is known to be confined to the interval $[\beta_{min}, \beta_{max}]$, this uncertainty in the true value of $\beta$ can be modelled as follows, [25]:

$$\beta = \bar{\beta}\left(1 + r_\beta \Delta\right) \tag{4.1}$$

where $\bar{\beta}$ is the nominal (mean) value of $\beta$;
$\Delta$ is any real scalar subject to $|\Delta| \leq 1$; and
$r_\beta = \frac{\beta_{\max} - \beta_{\min}}{\beta_{\max} + \beta_{\min}}$

In (4.1) $\Delta$ represents a general norm-bounded uncertainty which is "customized" to the specific situation by the weight $r_\beta$.

Dynamic uncertainty can be elegantly modelled in the frequency domain by means of transfer functions. Typically, unmodelled dynamics correspond to neglected high-frequency behaviour [3]. This means that the original (or nominal) model may be quite accurate at lower frequencies, yet inaccurate at higher frequencies. Such frequency dependent uncertainties in a model can be expressed in a variety of different ways, one of which is known as additive uncertainty. Equation (4.2) is an example of dynamic uncertainty which has been modelled in terms of additive uncertainty [25].

$$G(s) = \bar{G}(s) + W(s)\Delta(s) \tag{4.2}$$

where $G(s)$ represents the measured (true) transfer function of the system, while $\bar{G}(s)$ denotes the nominal model of the system. Once again, $\Delta(s)$ represents a general norm-bounded uncertainty, which is scaled to the specific system and its nominal model by means of the weight transfer function $W(s)$. The norm-bounded uncertainty $\Delta(s)$ is any stable transfer function whose magnitude must be less than one for all frequencies (and no restrictions on its phase) [25], in other words:

$$\|\Delta(j\omega)\|_\infty \leq 1 \; \forall \; \omega \tag{4.3}$$

Both (4.1) and (4.2) are quite general models. The aim of any robustness analysis is however to assess the sensitivity of a *specific* system for a *particular* uncertainty (imprecise parameter value or unmodelled effect). In (4.1) and (4.2) this particular uncertainty is modelled by the scalar weight $(r_\beta)$ and the weight function $(W(s))$ respectively. The process by which these weights are given realistic values (in the context of the specific robustness analysis problem) is known as *uncertainty modelling*. Uncertainty modelling is the first step in $\mu$-analysis (assuming that the nominal model has been finalized).

An example of dynamic uncertainty in self-sensing AMBs is the unmodelled dynamics that will occur if DCM self-sensing is modelled by means of LTI system identification. As outlined in section 2.1.4, DCM self-sensing consists of two steps. First, the duty-cycle of the power amplifier is constrained to 50 %. Secondly, the peak value of the resultant current waveform

is measured and nonlinearly scaled to obtain an estimate of the rotor position. DCM self-sensing is consequently inherently nonlinear and time variant (non-autonomous). Judicious application of system identification will result in an LTI model for DCM self-sensing that can successfully interact with LTI models for the remaining AMB system components to obtain stable levitation (as we'll see in the next chapter). The performance of the LTI closed-loop model for a DCM self-sensing AMB (in terms of bandwidth) is however poorer than that of the original system indicating possible unmodelled dynamics in the self-sensing module.

Without delving too deeply into the different options for modelling dynamic uncertainty, we'll assume that the dynamic uncertainty in DCM self-sensing can be modelled with additive uncertainty (similar to (4.2)). An improved LTI model that attempts to model the behaviour of DCM self-sensing more accurately, is the following additive combination between the nominal LTI self-sensing model $\bar{G}_{SS}(s)$ and the LTI uncertainty weight function for self-sensing, $W_{SS}(s)$:

$$G_{SS}(s) = \bar{G}_{SS}(s) + W_{SS}(s)\Delta(s) \tag{4.4}$$

A block-diagram of the complete LTI closed-loop AMB system with dynamic uncertainty included in the self-sensing module is given in figure 4.1. The system depicted in this figure is merely the LTI closed-loop model of figure 3.14 in which additive uncertainty has been included [25].

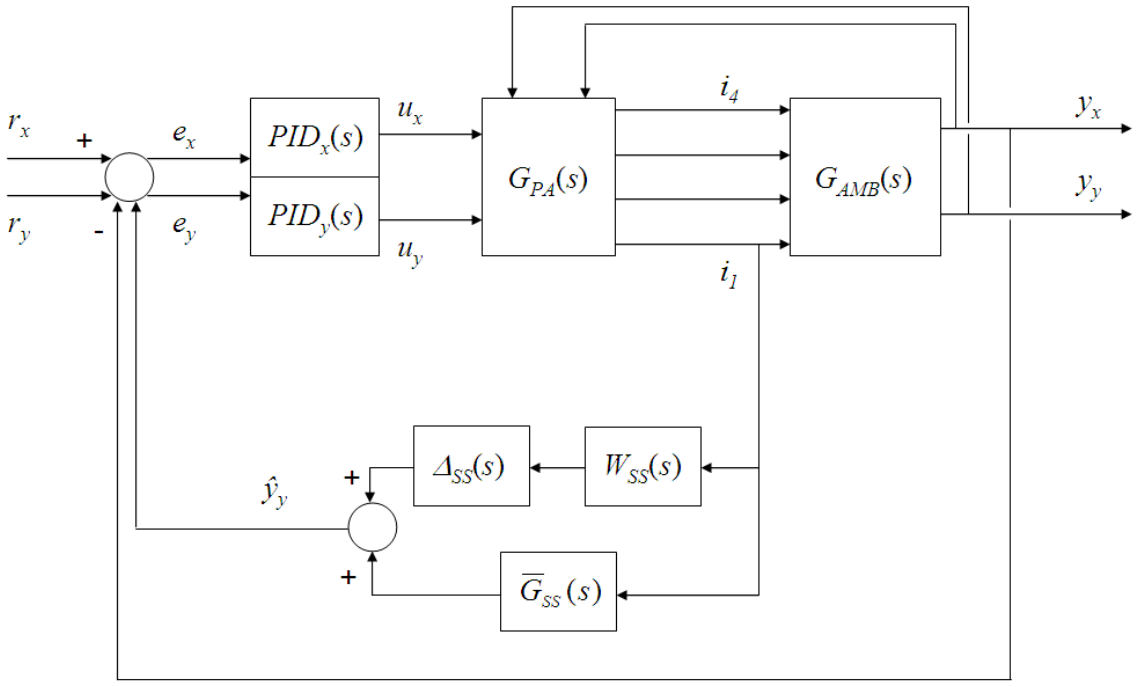


Figure 4.1: Block-diagram of an LTI self-sensing AMB with additive dynamic uncertainty in the self-sensing module

The next step in $\mu$-analysis entails rearranging the block-diagram to obtain the generalized form of figure 4.2 [25]. In this block-diagram the controller is represented by **K**, while the nominal model of the rest of the AMB system is collected in **P** (also known as the generalized

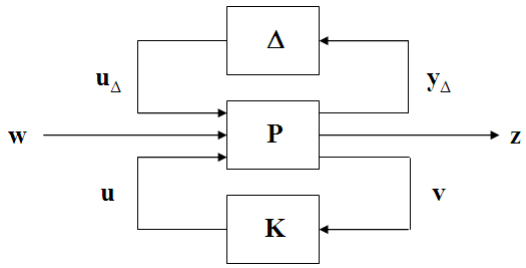


Figure 4.2: Generalized block diagram

plant). All modelled uncertainties in the original block-diagram (figure 4.1) are however segregated in $\mathbf{\Delta}$ in the form of a block-diagonal matrix of scalar weights and/or weight transfer functions representing all the individual parametric and dynamic uncertainties occuring in the system. All input signals to the original control system (namely the reference input, disturbances on the output of the plant, and measurement noise) are bundled together in the vector $\mathbf{w}$. The output signal $\mathbf{z}$, is usually defined as the normalized error of the system, namely the difference between the actual system output and the reference input (which is the desired or commanded system output) [25]. Mathematically, figure 4.2 can be represented as follows:

$$\begin{bmatrix} \mathbf{y}_\Delta \\ \mathbf{z} \\ \mathbf{v} \end{bmatrix} = \mathbf{P} \begin{bmatrix} \mathbf{u}_\Delta \\ \mathbf{w} \\ \mathbf{u} \end{bmatrix} \tag{4.5}$$

Rearranging the block-diagram in figure 4.1 to the generalized configuration of figure 4.2 results in the diagram of figure 4.3 (where the controller, generalized plant, and uncertainty matrix have been shaded). It is important to note that the uncertainty matrix $\mathbf{\Delta}$ only consists of norm-bounded general uncertainties (scalars or LTI transfer functions conforming to respectively $|\Delta_m| \leq 1$ and $\|\Delta_n(j\omega)\|_\infty \leq 1 \ \forall \ \omega$[1]). The uncertainty matrix therefore represents general uncertainties that can impact on different aspects of the nominal generalized plant. The degree to which the general uncertainties in $\mathbf{\Delta}$ actually influence the self-sensing AMB are determined by the weights (whether scalar weights or weight transfer functions). These weights are incorporated into the generalized plant $\mathbf{P}$, as can be seen in figure 4.3.

Robustness analysis is concerned with the stability margin of the *whole control system* for some unknown factor. This means that the controller $\mathbf{K}$ has to be incorporated into the generalized plant $\mathbf{P}$ so that the maximum singular value of the whole nominal system with a particular structured uncertainty model $\mathbf{\Delta}$ can be calculated. The controller can be combined with the generalized plant by means of a lower linear fractional transformation (LFT). If the generalized plant $\mathbf{P}$ in (4.5) is partitioned as in (4.6), then the lower LFT of the system is performed as in (4.7) [25] to obtain (4.8).

$$\begin{bmatrix} \begin{bmatrix} \mathbf{y}_\Delta \\ \mathbf{z} \end{bmatrix} \\ \mathbf{v} \end{bmatrix} = \begin{bmatrix} \mathbf{P}_{11} & \mathbf{P}_{12} \\ \mathbf{P}_{21} & \mathbf{P}_{22} \end{bmatrix} \begin{bmatrix} \begin{bmatrix} \mathbf{u}_\Delta \\ \mathbf{w} \end{bmatrix} \\ \mathbf{u} \end{bmatrix} \tag{4.6}$$

$$\mathbf{N} = \mathbf{P}_{11} + \mathbf{P}_{12}\mathbf{K}\left(\mathbf{I} - \mathbf{P}_{22}\mathbf{K}\right)^{-1}\mathbf{P}_{21} \tag{4.7}$$

[1] Where the subscripts $m$ and $n$ refer to the corresponding elements in the block-diagonal matrix.

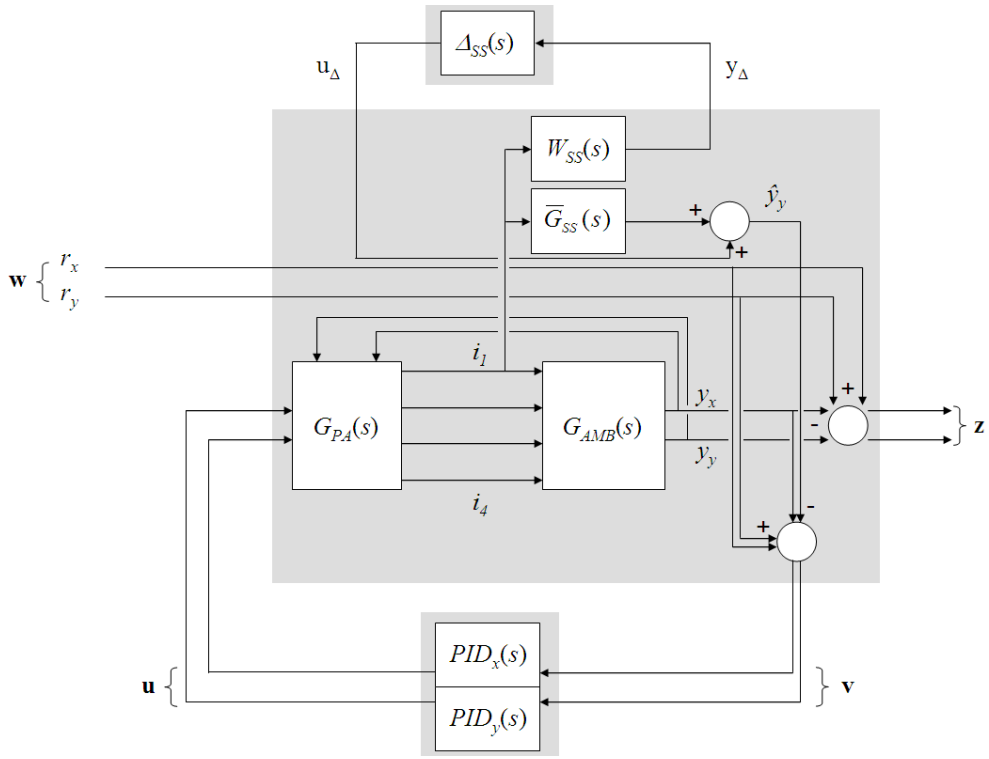


Figure 4.3: Detailed generalized block-diagram of a self-sensing AMB with dynamic uncertainty in the self-sensing module

$$\begin{bmatrix} \mathbf{y}_\Delta \\ \mathbf{z} \end{bmatrix} = \mathbf{N} \begin{bmatrix} \mathbf{u}_\Delta \\ \mathbf{w} \end{bmatrix} = \begin{bmatrix} \mathbf{N}_{11} & \mathbf{N}_{12} \\ \mathbf{N}_{21} & \mathbf{N}_{22} \end{bmatrix} \begin{bmatrix} \mathbf{u}_\Delta \\ \mathbf{w} \end{bmatrix} \tag{4.8}$$

By also partitioning the transfer function matrix $\mathbf{N}$ in (4.8), it is possible to obtain a closed-form expression for the output $\mathbf{z}$ in terms of the input $\mathbf{w}$ by means of an upper LFT. This is shown in (4.9) [25].

$$\mathbf{z} = \left( \mathbf{N}_{22} + \mathbf{N}_{21} \mathbf{\Delta} \left( \mathbf{I} - \mathbf{N}_{11} \mathbf{\Delta} \right)^{-1} \mathbf{N}_{12} \right) \mathbf{w} \tag{4.9}$$

If the nominal system is internally stable (i.e. if each of the components of the transfer function matrix $\mathbf{N}$ is internally stable), then the stability of the complete system[2] hinges on the feedback term $\left( \mathbf{I} - \mathbf{N}_{11} \mathbf{\Delta} \right)^{-1}$ [25]. Consequently, the robust stability of the complete system is determined by the stability of the $\mathbf{N}_{11}$ component of the $\mathbf{N}$ transfer function matrix.

The last step of $\mu$-analysis is therefore to isolate the $\mathbf{N}_{11}$ component and to determine its structured singular value. For a given complex matrix $\mathbf{N}_{11}$ and block-diagonal matrix $\mathbf{\Delta}$ (where the maximum singular value of each diagonal element in $\mathbf{\Delta}$ has an upper bound of one, i.e. $\sigma_{\max}\left(\Delta_n\right) \leq 1$), the structured singular value is defined as follows [25]:

$$\mu_{\mathbf{\Delta}} \left( \mathbf{N}_{11} \right) = \frac{1}{\min \left\{ k \middle| \det \left( \mathbf{I} - k \mathbf{N}_{11} \mathbf{\Delta} = 0 \right) \right\}} \tag{4.10}$$

[2] In other words, the nominal system as well as the modelled uncertainty.

(Where the subscript (Δ) accentuates the fact that the structured singular value is influenced by the structured uncertainty matrix $\mathbf{\Delta}$ in addition to the nominal model $\mathbf{N}_{11}$.)

Under the assumption that both the nominal closed-loop system and the uncertainty matrix are stable, the perturbed system[3] is stable if and only if the following condition holds [25]:

$$\mu_{\mathbf{\Delta}} \left( \mathbf{N}_{11} \left( j\omega \right) \right) \leq 1 \; \forall \; \omega \tag{4.11}$$

If the peak value of $\mu_{\mathbf{\Delta}}(j\omega)$[4] is less than one for all frequencies, then the difference between one and the aforementioned peak value reflects the stability margin of the system. In other words, if the maximum value of $\mu$ is less than one, it means that all possible perturbations to the nominal system within the confines of the uncertainty matrix $\mathbf{\Delta}$ will still be stable. In fact, even more uncertainty (represented by the difference between the maximum value of $\mu$ and one) will still not destabilize the nominal system. The stability margin estimated by $\mu$-analysis for parametric uncertainty in a benchmark SISO control system is compared to classical stability analysis techniques in appendix C.

Robustness analysis via $\mu$-analysis therefore rests on three pillars, namely: calculation of the structured singular value; modelling the nominal system; and modelling of the specific uncertainties (for which the system must be insensitive). Of these three, the first falls beyond the scope of this study (since there are a number of commercial algorithms available with which $\mu$ can be calculated). In this study, the nominal system is modelled via system identification (as discussed in the previous chapter). As we'll see shortly, system identification also plays a significant role in obtaining the system's uncertainty model (which is merely the weight functions in figure 4.3).

## 4.2 The centrality of the uncertainty model

In robustness analysis, the attention often falls primarily on the development of an analysis technique (e.g. $\mu$-analysis) as well as the derivation of an accurate nominal model. The more accurate a nominal model is (compared to reality), the less unmodelled factors may have an unexpected impact on the system when in operation. If it were possible to obtain a perfect model that exactly replicates the physical system, robustness analysis would be largely unnecessary (except as a tool with which to assess the impact of certain parameters on system stability or performance).

All models are however mathematical abstractions and are at best simplified and imperfect representations of reality. Consequently, imprecise model parameters and unmodelled dynamics are a fact of life in engineering.

Uncertainty however, doesn't imply a total lack of knowledge. The precise value of a parameter may be unknown, but more often than not its value is confined to a clearly defined interval. Similarly, unmodelled dynamics may defy exact description with the analytical tools at hand,

[3] The nominal system after being subjected to the modelled uncertainties.

[4] The structured singular value is also a function of frequency.

yet dynamic uncertainty rarely changes the fundamental characteristics of a system. Uncertainty itself can and must be modelled in order to obtain systems that can operate in real life. In fact, the fundamental concept of robustness is inextricably linked to the twin notions of a nominal model and the uncertainty surrounding it.

Robustness *analysis* is only half of the story. The lessons learnt and the recommendations made during robustness analysis of a system often gives guidance for the development of robust *controllers*. In the design of robust controllers, the objective is to obtain a controller that will guarantee a certain level of stability or performance irrespective of the well-defined uncertainties it will face in practice.

Robust controllers attain a measure of insensitivity for system uncertainties by sacrificing a fraction of the nominal system performance. It is an inescapable fact of life that high performance systems often aren't tolerant for small variations or uncertainties, while robust systems aren't as fast, efficient or as accurate as their finely tuned cousins. The conflicting demands of robustness and performance can't be simultaneously met without paying a price either way. This is known as the robustness-performance tradeoff [100]. The best solution to this dilemma is to model the bounds of the particular uncertainty as accurately as possible in order to limit the loss of performance, while at the same time instilling a measure of robustness to the system [101].

Similarly, the accuracy of an estimate of the stability margin of a particular system is influenced by the accuracy of both its nominal model and its uncertainty model. If the uncertainty surrounding the nominal model is ill-defined, the resultant robustness estimate will also be inaccurate. To prevent inaccurate robustness estimates, the uncertainty model must be realistic (and as simple as possible) [25].

## 4.3 Limitations of black-box models for uncertainty modelling

Self-sensing AMBs are nonlinear systems with complex dynamics that are difficult to model analytically from first principles. Uncertainties are therefore a fact of life in these systems. As mentioned previously, these uncertainties can be dichotomized into parametric uncertainties and dynamic uncertainties. Parametric uncertainty is a static imprecision surrounding the exact value of an individual parameter. Dynamic uncertainty on the other hand, arises due to neglected or incorrectly modelled behaviour in the system when compared to the real, measured system. As we'll see presently, not all of the uncertainties encountered in a self-sensing AMB system can be described within the empirical black-box modelling paradigm that is system identification.

Typical causes of parametric uncertainty in industrial systems are in the form of ageing components (and therefore drifting parameter values), environmental changes, calibration and manufacturing errors [102]. Inaccuracies in the AMB position sensors or a misallignment between the AMB centrepoints of the rotor and stator result in uncertainty in the exact size of the airgap (which may by exacerbated by thermal effects and manufacturing errors) [103].

Although a seemingly inconsequential error, misallignment may result in an increased negative stiffness and potential delevitation of the AMB [104].

Other examples of parametric uncertainties in AMBs include the various stiffness constants as well as the exact values of the modal frequencies of the rotor. The current and position stiffness constants of the linearised AMB model are essential in the design of a suitable controller for the AMB, yet in practice these constants are difficult to measure [105]. Imprecision may also surround the values of the natural frequencies of vibrational modes of the rotor in the case of a flexible rotor [69]. These modal frequencies may be modified further due to frequent reassembly of the AMB system, gyroscopic effects, as well as shrink fits that change with temperature and speed (with potential destabilizing results) [22].

In this study, the nominal model is obtained via system identification. The resulting black-box model is merely a parameterized state-space model that duplicates the input-output mapping of the AMB without giving any insight into the internal dynamics of the AMB. Consequently, none of the above mentioned parametric uncertainties and their effect on the AMB's stability margin can be investigated in this study. (An analytical model derived from first principles is the prerequisite to analyse the effect of parametric uncertainties on a system's robustness.)

System identification itself also contributes to parametric uncertainty in the final model. If the excitation signal with which the model is estimated isn't persistently exciting, or has a low signal to noise ratio, or the model order is too high; the final estimated parameter values in the model may be slightly uncertain [26]. This uncertainty manifests itself in the form of a small stochastic variability in each parameter value in the models obtained for different realizations of essentially the same excitation signal. Such errors may have a large impact on the eventual robustness estimates due to the amplification of errors during the transformation from the z-plane to the s-plane (see section 3.7.1).

In order to estimate the lower and upper bounds for the possible values of each parameter in the identified state-space model, it is necessary to estimate the covariance matrix of the parameter vector of the identified model. Unfortunately, no specific state-space model (with a free parameterization) is unique, since similarity transformations allow us to transform any state-space model to other equivalent models with different parameter values [84][5]. The infinite number of possible state-space models for a given estimation set makes it impossible to calculate the covariance matrix theoretically [44]. Our only recourse to estimate the covariance matrix would then be by means of Monte Carlo analysis (for a fixed model order fixed and parameter estimation procedure). The computational cost involved with this approach is however prohibitively high, since the estimated covariance matrix will only converge to the true value after numerous simulations of the nonlinear system response.

The above mentioned form of parametric uncertainty is only of concern if inferior excitation signals are used to gather the estimation subset. Under the assumption of a persistently exciting

[5]The exception is canonical state-space models, e.g. controllability canonical form. It is possible to directly estimate a state-space model in controllability canonical form by means of the system identification toolbox. The resulting models have a fixed structure and therefore it is also possible to calculate their covariance matrices theoretically. Due to the predominance of zero entries in their matrices, canonical models however have less modelling capability for a given order than models with a free parameterization.

excitation signal with a high signal to noise ratio, the PEM parameter estimation algorithm delivers optimal state-space models in a least-squares sense. Parametric uncertainty in the identified model parameters can therefore be avoided by careful synthesis of suitable excitation signals and collection of the required estimation data.

The only instance of parametric uncertainty that will be investigated in this study is parametric uncertainty in the coefficients of the PID controller in the AMB control system. It is possible to investigate the effect that these constants have on the stability margin of the AMB, because analytical models for the PID controller are readily available and can be easily connected with the black-box models for the other system components to form a closed-loop system model.

The PID controllers in practical AMB systems also exhibit dynamic uncertainties. Imprecision during the digital to analogue conversion process and finite wordlength effects contribute to adding noise (i.e. high frequency dynamics) to the system. In some instances, the occurence of these errors in practical implementations of robust controllers (e.g. $\mu$-synthesis controllers) can destabilize the whole control system [106]. These effects play a relatively minor part in the response of the PID controller, but become significant during the implementation of DCM self-sensing [17]. The dynamic uncertainty introduced by finite wordlength effects can be modelled alongside the dynamic uncertainty due to nonlinear behaviour in the self-sensing module by means of a single uncertainty weight function.

The dominant contributor towards dynamic uncertainty in self-sensing AMBs is the occurrence of nonlinear behaviour that can't be modelled in the LTI paradigm (and which is often exacerbated by an unwise choice of the model order of the LTI model). This form of dynamic uncertainty can be found in each of the main components of a self-sensing AMB system, namely the power amplifier, AMB plant and self-sensing module. As we'll shortly see, this form of uncertainty can be easily modelled in the presence of black-box nominal models and will therefore form the focus of the robustness analysis in this study.

In practice, disturbance forces acting in on the rotor of an AMB represent a frequent source of uncertainty in AMB systems. Examples include mass imbalances on the rotor of the AMB [105], as well as unpredictable forces experienced in AMB supported machining spindles [107]. From the perspective of a black-box model for the AMB plant, disturbance forces form part of the internal dynamics of the AMB. This is clearly illustrated in figure 4.4, which is the signal flow graph of a 1-DOF AMB in differential driving mode [32]. The dotted line represents the boundary of a black-box model for the AMB plant and the shaded arrow indicates the specific node where disturbance forces must be added to. Any change in the disturbance force is therefore reflected by a change in the input-output behaviour of the AMB plant.

The influence of disturbance forces on the robustness of an AMB can be assessed by modelling these forces by means of dynamic uncertainty. A model for this dynamic uncertainty can be obtained by comparing the frequency response of the measured system (including the disturbance force) with that of the nominal model for the system (without any disturbance forces). The resultant differences between the two frequency responses can be used to deduce a weight transfer function for the dynamic uncertainty due to the disturbance force.

Typical disturbance forces are large, repetitive forces with a narrow frequency band. (An

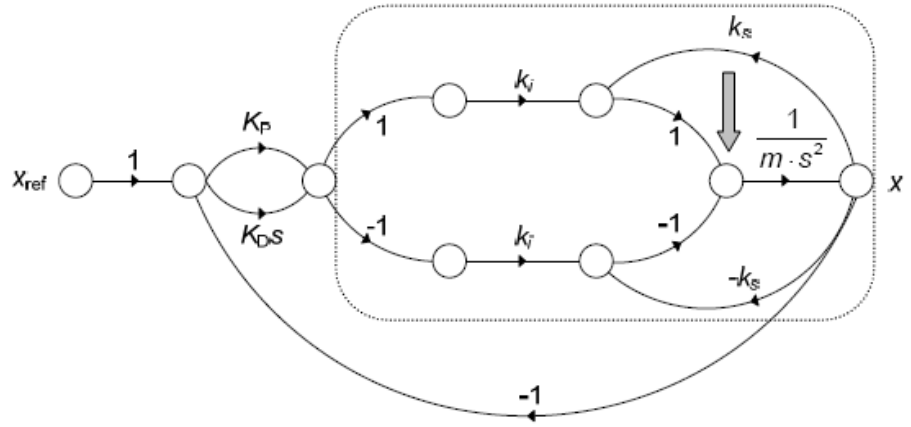


Figure 4.4: Signal flow graph of a 1-DOF AMB indicating where disturbance forces should be included

imbalance in the AMB rotor, for example, manifests itself in the form of a sinusoid with a frequency equal to the rotation frequency of the shaft.) In the spectral domain, such disturbance forces are represented by dirac delta functions at their respective frequencies [107]. Dirac delta functions in the frequency domain are difficult to duplicate accurately with rational transfer functions (each delta requires an impractical number of poles and zeros for a barely adequate representation). Consequently, the effects of disturbance forces also lie outside the focus of this study (due to the use of black-box models for the nominal system).

In summary, the use of system identification as a modelling tool dictates that the robustness analyses of this study is limited to the following two cases:

- parametric uncertainty in the PID controller coefficients;
- and dynamic uncertainty in the rest of the loop components due to nonlinear effects.

## 4.4 Modelling of dynamic uncertainty

Parametric uncertainty is completely described by the lower and upper bounds in (4.1). From (4.2) the dynamic uncertainty present in a particular subsystem is specified by means of the uncertainty weight transfer function $W(s)$. The remainder of this chapter is concerned with the modelling of dynamic uncertainty (i.e. finding the required weight functions) and establishing procedures with which those models can be validated.

### 4.4.1 Options for acquiring uncertainty weight functions

The purpose of the uncertainty weight function is to model the mismatch between the response of the real system and the response of a nominal model for the system [108]. The process of

modelling this mismatch often entails a two step process. Firstly, the "difference"[6] between the model and real system is measured empirically. Secondly, the measured differences are summarized by means of a simplified transfer function.

Bayard *et al.* followed this approach (as part of a design procedure for an $H_\infty$-controller) [109]. The disparity between the model and real system was measured in terms of the absolute difference between the magnitudes of the model's frequency response and the real system's measured frequency response. A low order transfer function was then fitted to the frequency residuals by means of a graphical technique. The latter step is the central weakness of their approach since human intervention always carries with it the risk of obtaining inconsistent and subjective results.

Sugie and Tanai eliminated this risk by defining a quadratic cost function on the basis of the measured frequency domain residuals. This paved the way for obtaining a weight function by means of iterative numerical optimization techniques that minimized the aforementioned cost function [108]. Another improvement introduced by Sugie and Tanai is that they used the $L_\infty$-norm as a measure of the spectral distance between the model and the real plant, thereby making it easier to incorporate the uncertainty weight function into the design process for robust controllers.

A more complicated approach was taken by Rivera *et al.* in which they modelled the uncertainty weight as consisting of a bias term and a variance term [110]. These terms were in turn estimated from the estimated power spectral densities of the following signals: the disturbance signal; the input signal; and the cross-spectrum of the input signal and output residuals. Their technique is however by their own admission prone to deliver quite conservative weight functions.

An attractive alternative for the numerical optimization step used by Sugie and Tanai is to employ genetic algorithms to obtain the best weight function from the measured residuals. Genetic algorithms are numerical optimization techniques inspired by the theory of natural selection through survival of the fittest proposed by Darwin [46]. In these algorithms an initial population of potential solutions (also known as chromosomes) to a well-defined problem are allowed to "compete" with each other. The performance of each potential solution is evaluated by means of a so-called fitness function (which is merely a problem-specific cost function that formulates the optimization problem as a minimization problem). After all the potential solutions have been evaluated, a subset of the best solutions is retained. A small percentage of these "survivors" are modified by introducing a small amount of noise into their chromosomes (e.g. the coefficients of the transfer functions are perturbed randomly). Another subset of the surviving solutions are allowed to combine with each other and form a new set of solutions. These two processes are commonly called mutation and crossover respectively. The whole process is repeated for many iterations (or "generations") until an optimal solution has been discovered.

Genetic algorithms have been successfully applied to obtain both the nominal model as well as the uncertainty weight function [46]. Typically the fitness function that is used consists of

[6] In the next section we'll see that there are various fundamental models to explain and quantitavely measure the mismatch between the nominal model and real system.

the sum of squared differences between the frequency response of the candidate model and the measured system. (The candidate models are coded in terms of the coefficients of their s-plane transfer function representations.) It is however also possible for genetic algorithms to identify s-plane transfer functions for the nominal model and uncertainty weight on the basis of discrete time-domain data [53]. Another advantage of genetic algorithms is that they can autonomously search for the best order of the functions that have to be identified [53].

On the down side, genetic algorithms are quite computationally expensive at each iteration, often taking many iterations to converge to an optimal solution [111]. Furthermore, the final results are heavily influenced by the specific crossover process employed [111]. Genetic algorithms are also very prone to getting stuck in local minima (since they don't have any formal guarantees of converging to the global optimal solution) [46]. This means that the domain over which the initial population is distributed often plays an unacceptably large role in the final solution that will be obtained. Yet another weakness of genetic algorithms is that the variability introduced during mutation and crossover (which is essential for the success of genetic algorithms) also introduces a fair amount of variability in the final solutions that are obtained. Consequently, the identified nominal model and weight function are themselves subject to an unacceptably high parametric uncertainty (in contrast to deterministic optimization methods such as classical system identification).

System identification itself is an option to fit the uncertainty weight function to the measured spectral residuals. One problem that has to be overcome with this approach is that the uncertainty weight functions in the robust control paradigm per definition don't have any phase information [3] and [25]. Alternatively, classical system identification can be used to fit a model on time-domain residuals of the nominal model and real system [105]. Unfortunately, this approach requires that the nominal model and real system have exactly the same input signal. This requirement is troublesome for AMBs since they are inherently unstable and have to be operated in closed-loop control systems[7].

Some researchers include an intermediate smoothing step between the calculation of the residuals and the fitting of a weight function. An example of this approach is the "confidence interval network" of Buckner, Choi and Gibson ([101] and [105]). In their work an artificial neural network[8] is employed to reduce the noisiness in the measured transfer functions. After measuring the frequency response function of both the nominal model and the real plant, the spectral residuals are calculated by taking the absolute difference between the two magnitude responses. These measurements are repeated numerous times to obtain sufficient training data for the neural network. By using a bilinear cost function, it is possible for the neural network to mimic the 99.9 % quantile of the training data (thereby training the network to be an overbound to the measured spectral residuals). If the size of the neural network (i.e. the number of neurons in its hidden layers) is kept sufficiently small, the output of the neural network will be

[7] The requirement of identical input signals for the nominal model and real plant is unnecessary for techniques based on frequency domain residuals.

[8] An artificial neural network is a collection of simple processing units (known as neurons) that are interconnected in a predefined manner. The strength of each connection is typically modified by a scalar weight. These weights determine the specific input-output mapping performed by the total network. The weights can also be modified by means of a so-called training algorithm (which basically boils down to an iterative nonlinear optimization algorithm) to enable the network to duplicate any nonlinear MIMO mapping.

a smoothened version of the original data. Finally, a low order rational function can be fitted to the smoothened data by means of system identification.

The main disadvantage of the above neural network based technique is the additional computational expense incurred by the neural network. As we'll see in section 4.4.3, it is possible to fit a smooth transfer function directly to the measured spectral residuals without resorting to computationally intensive intermediate smoothing steps.

### 4.4.2 Modelling the difference between the plant and its nominal model

Modelling of dynamic uncertainty consists of two steps. The first is to obtain an empirical transfer function estimate (ETFE) of the measured mismatch between the real plant and its nominal model. Once the ETFE of the uncertainty weight has been determined, all that remains is to fit a low order transfer function model to the data (which is the topic of section 4.4.3).

An observed deviation of the nominal model from the real system can be attributed to any number of possible causes. Unmodelled low frequency dynamics could for example give rise to a slight bias and phase error in the model's response. If however the root cause of the mismatch is a nonlinear mechanism impacting on the output signals of the otherwise linear system, the difference between the responses of the model and the real system would look entirely different. This example emphasizes the fact that modelling the mismatch between a real system and its nominal model is a bit more involved than merely calculating residuals. It is of cardinal importance to take the fundamental causative mechanism for the mismatch into account when measuring and modelling dynamic uncertainty.

In the robust control paradigm, the objective in uncertainty modelling is firstly to express the reality-model mismatch in terms of the nominal model $\bar{G}(s)$, a general norm bounded uncertainty $\Delta(s)$ and a specific weight function $W(s)$[9]. Secondly, to obtain a suitable transfer function $W(s)$ that will accurately describe the discrepancy between the real system $G(s)$ and its nominal model $\bar{G}(s)$.

Six different models for the model-reality mismatch that are used in the literature are shown in block-diagram form in figure 4.5. These models are examples of unstructured uncertainty models, since the norm bounded uncertainty function $\Delta(s)$ has no structure. (For MIMO systems it would have been a full complex perturbation matrix in contrast with the block-diagonal uncertainty matrix used in $\mu$-analysis.) Each of these six block-diagrams is an LTI model for the real system. Table 4.1 summarizes these models, their mathematical expressions, as well as possible examples where each would be applicable ([3] and [25]).

ETFEs of the mismatch between the real system and its nominal model can be obtained from the equations in table 4.1. These equations are based on frequency domain measurements of

[9]The exception to this general approach is the so-called coprime uncertainty description in which the nominal plant model is subjected to a left or right coprime factorization, which serves as basis for a model of the real system [3]. The coprime uncertainty model is useful for a generic uncertainty description in the absence of *a priori* information on the specific mechanism that gives rise to the mismatch between the model and the real system [25]. To prevent overly conservative robustness estimates, the uncertainty description must be realistic [25]. In the interest of accurate robustness estimation coprime factorization won't be investigated in this study.

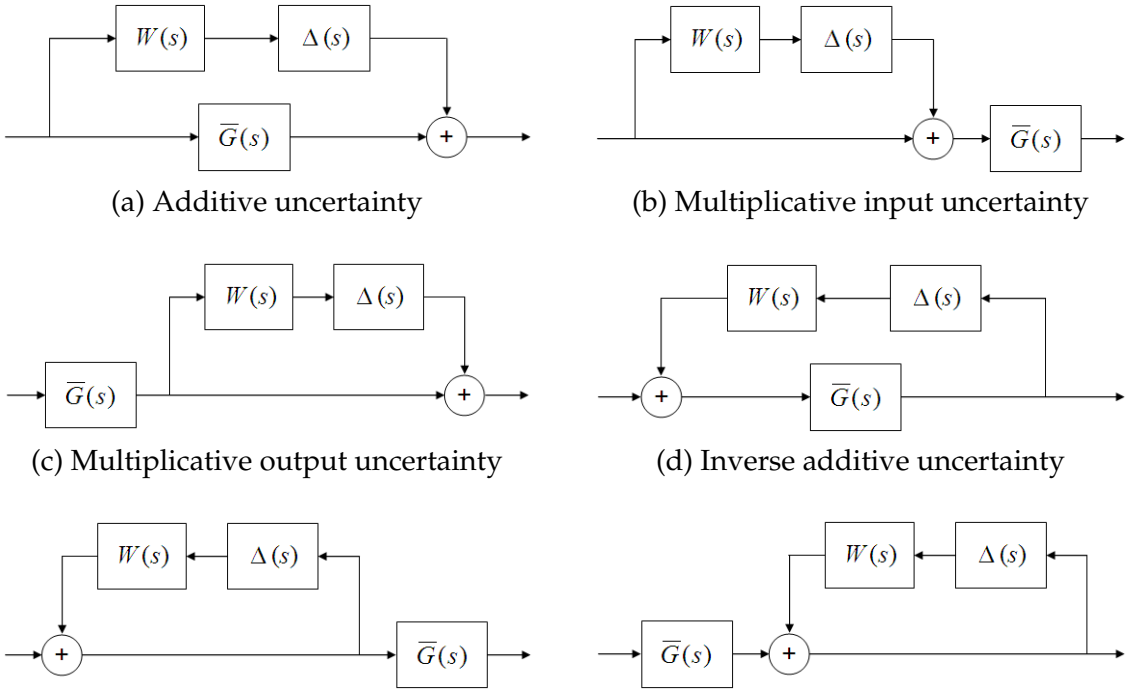


(a) Additive uncertainty

(b) Multiplicative input uncertainty

(c) Multiplicative output uncertainty

(d) Inverse additive uncertainty

(e) Inverse multiplicative input uncertainty

(f) Inverse multiplicative output uncertainty

Figure 4.5: Block-diagram models for the mismatch between a real system and its nominal model

the input and output signals of both the real system and its nominal model. The advantage of a frequency domain comparison between reality and the model is that it isn't necessary to use exactly the same input signal for the real system and its nominal model (in contrast with time domain residuals). This advantage is critical in AMBs since AMBs have to be operated in a closed-loop both in real life as well as in simulation (due to their inherent instability). Consequently, it will be highly unlikely that the input signals to both the real *AMB plant* and its nominal model will be exactly the same given the reality of small modelling errors in each of the LTI models comprising the closed-loop LTI model.

Table 4.1: Basic models for the mismatch between a real system and its nominal model

| Name | Possible cause | Mathematical model |
|---|---|---|
| Additive uncertainty | Unmodelled high-frequency dynamics<br>Additive plant errors<br>Uncertain nonminimum phase zeros[a] | $G(s) = \bar{G}(s) + W(s)\Delta(s)$ (4.12) |
| Multiplicative input uncertainty | Unmodelled high-frequency effects<br>Hammerstein systems[b]<br>Input errors<br>Uncertain nonminimum phase zeros | $G(s) = \bar{G}(s)\left(I + W(s)\Delta(s)\right)$ (4.13) |
| Multiplicative output uncertainty | Unmodelled high-frequency dynamics<br>Wiener systems[c]<br>Output errors<br>Uncertain nonminimum phase zeros | $G(s) = \left(I + W(s)\Delta(s)\right)\bar{G}(s)$ (4.14) |
| Inverse additive uncertainty | Low-frequency parametric errors<br>Uncertain unstable poles[d] | $G(s) = \bar{G}(s)\left(I - W(s)\Delta(s)\bar{G}(s)\right)^{-1}$ (4.15) |
| Inverse multiplicative input uncertainty | Low-frequency parametric errors<br>Uncertain unstable poles | $G(s) = \bar{G}(s)\left(I - W(s)\Delta(s)\right)^{-1}$ (4.16) |
| Inverse multiplicative output uncertainty | Low-frequency parametric errors<br>Uncertain unstable poles | $G(s) = \left(I - W(s)\Delta(s)\right)^{-1}\bar{G}(s)$ (4.17) |

[a] Zeros that occur outside the unit circle (for discrete-time models) or in the right hand side of the s-plane (for continuous-time models).

[b] A Hammerstein system is a nonlinear system which is modelled with a static nonlinearity at the input, followed by an LTI model [44].

[c] A Wiener system is a nonlinear system which is modelled by an LTI model followed with a static nonlinearity at the output [44]. Wiener systems can be modelled by means of output multiplicative uncertainty [112].

[d] Poles that occur outside the unit circle (for discrete-time models) or in the right hand side of the s-plane (for continuous-time models).

From the mathematical model for additive uncertainty in table 4.1, the ETFE of the uncertainty weight $W(s)$ can be calculated as follows:

$$\begin{aligned} W(s)\Delta(s) &= G(s) - \bar{G}(s) \\ &= \frac{Y(s)}{X(s)} - \frac{\bar{Y}(s)}{\bar{X}(s)} \end{aligned} \tag{4.18}$$

where the spectra of the input and output signals of the real system are represented by $X(s)$

and $Y(s)$ respectively. Similarly, the input and output spectra of the nominal model are given by $\bar{X}(s)$ and $\bar{Y}(s)$ respectively.

The general norm-bounded uncertainty $\Delta(s)$ is however constrained as follows: $\|\Delta(j\omega)\|_\infty \leq 1 \ \forall \ \omega$, where the $H_\infty$-norm is defined as follows for any proper and stable transfer function $G(s)$ [25]:

$$\|G(j\omega)\|_\infty = \sup_\omega |G(j\omega)| \tag{4.19}$$

Consequently, the ETFE of the uncertainty weight for additive uncertainty must conform to the following inequality:

$$|W(s)| \geq \left| \frac{Y(s)}{X(s)} - \frac{\bar{Y}(s)}{\bar{X}(s)} \right| \tag{4.20}$$

If there is reason to suspect that the real system can be accurately modelled as a Hammerstein system, multiplicative input uncertainty would be the appropriate model to represent the disparity between reality and the nominal LTI model. From table 4.1 the ETFE of the corresponding uncertainty weight can be calculated as follows (once again making use of the simplification: $|\Delta| \leq 1$):

$$|W(s)| \geq \left[\bar{G}(s)\right]^{-1} G(s) - I \tag{4.21}$$

Equation (4.21) requires the calculation of the inverse of the transfer function of the nominal model. The inverse of a SISO LTI system has the reciprocal frequency response of the original LTI system in order that the following relation holds: $G(s)G^{-1}(s) = 1$, [113]. If the transfer function of the nominal model is given by $\bar{G}(s) = \frac{\bar{Y}(s)}{\bar{X}(s)}$, then the inverse of the nominal is given by:

$$\left[\bar{G}(s)\right]^{-1} = \frac{\bar{X}(s)}{\bar{Y}(s)} \tag{4.22}$$

Finally, the uncertainty weight for multiplicative input uncertainty can be calculated as follows from measured spectra:

$$|W(s)| \geq \left| \frac{\bar{X}(s)}{\bar{Y}(s)} \frac{Y(s)}{X(s)} - I \right| \tag{4.23}$$

Similar derivations yield the equations for the uncertainty weights of the other four uncertainty models. These equations are summarized in table 4.2.

Table 4.2: Uncertainty weights for various uncertainty models

| Name | Uncertainty weight | |
|---|---|---|
| Multiplicative output uncertainty | $\|W(s)\| \geq \left\| \frac{Y(s)}{X(s)} \frac{\bar{X}(s)}{\bar{Y}(s)} - I \right\|$ | (4.24) |
| Inverse additive uncertainty | $\|W(s)\| \geq \left\| \frac{\bar{X}(s)}{\bar{Y}(s)} - \frac{X(s)}{Y(s)} \right\|$ | (4.25) |
| Inverse multiplicative input uncertainty | $\|W(s)\| \geq \left\| I - \frac{X(s)}{Y(s)} \frac{\bar{Y}(s)}{\bar{X}(s)} \right\|$ | (4.26) |
| Inverse multiplicative output uncertainty | $\|W(s)\| \geq \left\| I - \frac{\bar{Y}(s)}{\bar{X}(s)} \frac{X(s)}{Y(s)} \right\|$ | (4.27) |

The uncertainty weights in table 4.2 and (4.20) and (4.23) are only valid for SISO systems. In a 2-DOF self-sensing AMB the only SISO component is the self-sensing module, the rest of the components of the AMB system are all multivariable. How should the dynamic uncertainties in MIMO systems be represented?

The black-box nominal model for the AMB plant, for example, takes the four currents delivered by the power amplifiers as inputs and has the horizontal and vertical position of the shaft as its two outputs. In order to keep the order of the resultant models as low as possible, the state-space models delivered by system identification in this study have a free parameterization. Consequently, the state-space model of the AMB plant is capable of modelling the electromagnetic cross-coupling in the AMB stator (a process by which the top coil current for example has an influence on both the vertical and horizontal position of the AMB rotor). All of the interactions between the various inputs and outputs of the AMB plant will however be imperfectly modelled by an LTI state-space model and will therefore be subject to dynamic uncertainty. Once again, the issue now at stake is how to model and measure the dynamic uncertainty present in a multivariable plant.

Previously, it was concluded that the inherent instability of the AMB as well as the limitations of LTI modelling preclude the use of time domain residuals to measure the disparity between the real plant and its nominal model. Frequency domain measurements are much more suitable for AMB systems. Transfer functions are in turn the natural mathematical vehicle with which to represent the frequency response of the dynamic discrepancy between the model and reality. A transfer function matrix model of the dynamic uncertainty is therefore the preferred choice.

A transfer function matrix representation of the LTI nominal model of the AMB plant is given by:

$$\begin{bmatrix} Y_x(s) \\ Y_y(s) \end{bmatrix} = \begin{bmatrix} G_{AMB(x,1)}(s) & G_{AMB(x,2)}(s) & G_{AMB(x,3)}(s) & G_{AMB(x,4)}(s) \\ G_{AMB(y,1)}(s) & G_{AMB(y,2)}(s) & G_{AMB(y,3)}(s) & G_{AMB(y,4)}(s) \end{bmatrix} \begin{bmatrix} I_1(s) \\ I_2(s) \\ I_3(s) \\ I_4(s) \end{bmatrix} \tag{4.28}$$

where $Y_x(s)$ and $Y_y(s)$ represent the Laplace transforms of the horizontal and vertical shaft position signals; $I_n(s)$ is the Laplace transform of the $n^{\text{th}}$ current signal and $G_{AMB(n,m)}(s)$ represents the AMB plant transfer function from input $m$ through to output $n$.

Following the same general approach as in [114], each of the SISO transfer functions in the AMB plant transfer function matrix may be modelled in terms of a nominal model and an uncertainty weight which is combined via one of the six uncertainty models in table 4.1. If the underlying discrepancy between the nonlinear AMB plant and its LTI nominal model can be accurately described in terms of additive uncertainty, each of the SISO transfer functions in the transfer function matrix in (4.28) can be written as follows:

$$G_{AMB(n,m)}(s) = \bar{G}_{AMB(n,m)}(s) + W_{AMB(n,m)}(s)\Delta(s) \tag{4.29}$$

where $\bar{G}_{AMB(n,m)}(s)$ represents the nominal AMB plant transfer function from input $m$ through to output $n$ and $W_{AMB(n,m)}(s)$ is the corresponding uncertainty weight function.

By substituting (4.29) into (4.28) the complete MIMO model for additive dynamic uncertainty in the AMB plant model is given by (4.30). The primary advantage of this approach is that it

enables the analysist to measure the MIMO uncertainty piecemeal via SISO techniques from each individual input-output channel. Moreover, the uncertainty weight functions can then be collected in a single transfer function matrix separate from the nominal LTI model, as is shown in (4.30). Another potential advantage of this approach is that the number of possible uncertainty models in table 4.1 is reduced from six to four. (For SISO functions there is no difference between multiplicative input and output uncertainty models, just as there is no difference between inverse multiplicative input and output uncertainties [25].)

$$\begin{bmatrix} Y_x(s) \\ Y_y(s) \end{bmatrix} = \begin{bmatrix} \bar{G}_{AMB(x,1)}(s) & \bar{G}_{AMB(x,2)}(s) & \bar{G}_{AMB(x,3)}(s) & \bar{G}_{AMB(x,4)}(s) \\ \bar{G}_{AMB(y,1)}(s) & \bar{G}_{AMB(y,2)}(s) & \bar{G}_{AMB(y,3)}(s) & \bar{G}_{AMB(y,4)}(s) \end{bmatrix} \begin{bmatrix} I_1(s) \\ I_2(s) \\ I_3(s) \\ I_4(s) \end{bmatrix} + \begin{bmatrix} W_{AMB(x,1)}(s) & W_{AMB(x,2)}(s) & W_{AMB(x,3)}(s) & W_{AMB(x,4)}(s) \\ W_{AMB(y,1)}(s) & W_{AMB(y,2)}(s) & W_{AMB(y,3)}(s) & W_{AMB(y,4)}(s) \end{bmatrix} \times \mathbf{\Delta}_u(s) \begin{bmatrix} I_1(s) \\ I_2(s) \\ I_3(s) \\ I_4(s) \end{bmatrix} \tag{4.30}$$

where $\mathbf{\Delta}_u(s)$ is a $4 \times 4$ matrix of SISO norm bounded uncertainties (a so-called unstructured uncertainty matrix).

The separation between the MIMO nominal model and the uncertainty weight transfer function matrix in (4.30) is essential to obtain a stable generalized model (figure 4.2). With the nominal model and uncertainty weights separated from each other, it is possible for the nominal model to remain in state-space representation during the construction of the generalized model. In this fashion, potential instabilities that could occur due to the transformation from a state-space representation to a transfer function matrix model (see section 3.7.2) can be avoided.

Unfortunately, the segregation in (4.30) can't be duplicated with any of the other uncertainty models in table 4.1. This isn't a problem for the 2-DOF self-sensing AMB system, since not one of its component subsystems (controller, power amplifier, plant and self-sensing module) can be viewed as either a Wiener or Hammerstein system (thereby placing all of the multiplicative models out of contention). Consequently, the only suitable uncertainty model for the AMB system is additive uncertainty.

Accurate measurement of the uncertainty weights in (4.30) requires that only a single input signal be perturbed while the rest are kept constant. Unfortunately significant cross-coupling occurs in the AMB plant in addition to the fact that the inherent instability of the AMB requires closed-loop control. These two factors contribute to a situation where none of the inputs of the AMB plant can be kept constant at the whim of the analysist and each input influences all of the output signals to a greater or lesser degree. The best one can hope for is to excite each axis independently to minimize cross-talk between the input signals[10] [46].

[10]Take for example the situation where an excitation signal is injected in the current flowing in the top pair of coils in the AMB stator. Almost immediately a commensurate perturbation will occur in the current flowing in the bottom pair of coils (due to feedback). These two currents will result in a vertical perturbation in the position of

To summarize, the procedure for obtaining the ETFEs of the uncertainty weights up to this point is as follows:

1. Form a closed-loop LTI model for the AMB system consisting of nominal LTI state-space models for the controller, power amplifier, AMB plant and self-sensing module. (In general, these LTI models are based on measurements taken from a real AMB system. In this study, accurate nonlinear simulation models are used to generate the required data for system identification.) A block-diagram of this closed-loop model is shown in figure 3.14. A closed-loop LTI state-space model can be constructed from the state-space models of the constituent subsystems by algebraic manipulation (see e.g. [115]).

2. Apply the same position reference signal to both the nonlinear AMB simulation model and the closed-loop LTI model and simulate the responses of both models. The input and output signals of each of the major subsystems in the AMB system must be recorded during both of these simulations.

3. Calculate the ETFE of each (additive) SISO uncertainty weight in the weight transfer function matrix of (4.30) by means of (4.20). This will result in the measured uncertainty weights for dynamic uncertainty in the AMB plant. By a similar calculation the ETFEs of the uncertainty weights for additive dynamic uncertainty in the other subsystems (namely the power amplifier and self-sensing module) can also be obtained.

Step two in the above procedure requires that the specific input and output signals of each of the sub-systems in the closed-loop LTI model of the AMB be obtained. These signals can be obtained from the vector of state-variables of the closed-loop LTI state-space model. Recursion is commonly used to calculate the response (and state-variables) of a discrete-time state-space model for a specific input signal. The vector of state-variables of the closed-loop system is a mere concatenation of the state-vectors of the subsystem models. Consequently the state-variables of each subsystem can be extracted from the vector of closed-loop state-variables. Finally, the output of each subsystem can be calculated from the history of its state-variables by means of the subsystem's output equation (see (3.5)).

As a final example, figure 4.6 shows the frequency responses used to calculate one of the SISO uncertainty weights in (4.30). Figure 4.6(a) shows the measured frequency responses of the nonlinear AMB plant as well as an LTI model for it. These frequency responses were obtained by injecting a perturbation at point 2 (see figure 3.12) consisting of a bandlimited random-phase multi-sine signal. Clearly, the LTI model in this example is an imperfect representation of the nonlinear AMB plant. The additive uncertainty weight ETFE is shown in figure 4.6(b). This uncertainty weight corresponds to $W_{AMB(y,1)}(s)$ in (4.30) and was calculated via (4.20). This uncertainty weight ETFE reveals that the nominal LTI model struggles to accurately model the nonlinear AMB plant over the greater part of its dynamic range.

the AMB rotor, as well as a small perturbation in the horizontal position (due to electromagnetic cross-coupling). Finally, the latter horizontal movement of the AMB rotor will also result in a small change in the currents flowing in the left-hand and right-hand coils of the AMB stator (due to feedback).

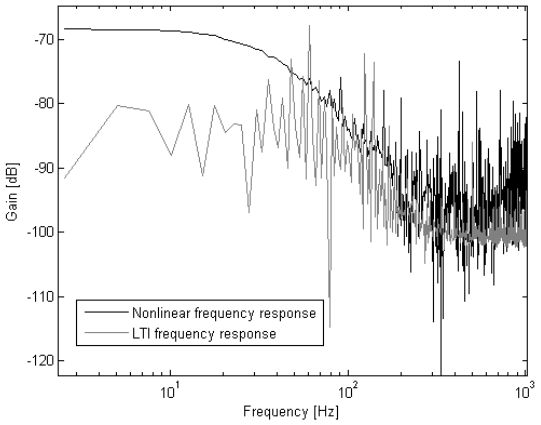


(a) Measured frequency responses

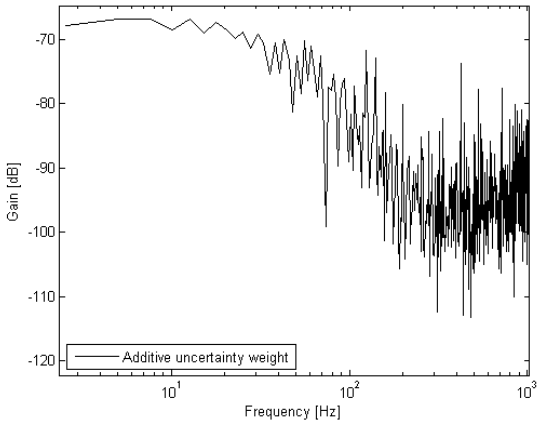


(b) Additive uncertainty weight ETFE

Figure 4.6: Example of additive uncertainty

### 4.4.3 Fitting a transfer function to an ETFE

As mentioned previously, modelling of dynamic uncertainty consists of two steps. The first is to obtain an empirical transfer function estimate (ETFE) of the measured mismatch between the real plant and its nominal model. An example of such an ETFE is given in figure 4.6(b). All that remains is to fit a low order transfer function model to the data. (These transfer function models are a prerequisite for $\mu$-analysis.)

The *de facto* practice in the literature is to fit a smooth function which acts as an upper bound to the measured frequency response [25], [105] and [109]. From figure 4.6(b) the problem at hand can therefore be generalized as fitting an s-plane transfer function of minimum order to form a supremum to a noisy, discretely sampled ETFE of the uncertainty weight. Potential solutions to this problem have to meet the following criteria:

- Speed. Robustness analysis via system identification and $\mu$-analysis is already computationally intensive without incurring unnecessary additional delays.
- Accuracy. Any fitted transfer function should be as true to the observed frequency response as possible. Differences between the observed ETFE and the fitted transfer function have a direct impact on the accuracy of the resultant robustness analysis.
- Repeatable results. Deterministic algorithms are preferable over algorithms that involve a certain element of unpredictability (e.g. genetic algorithms), since the accuracy of the eventual robustness analysis is also influenced by any additional uncertainty introduced during the modelling of the dynamic uncertainty.

Pseudo-least-squares algorithms have been developed to fit a transfer function to a measured gain frequency response (e.g. [116] and [26]), yet they aren't truly autonomous (and consequently not totally objective or consistent). This section details a novel algorithm which

solves this problem autonomously with the minimum of tunable parameters (that influence the performance of the algorithm).

As could be expected, the ETFE of the uncertainty weight is rather "noisy" or discontinuous. The task of the algorithm can be significantly alleviated by a preprocessing step during which the observed frequency response is smoothened. One simple solution to this problem is to identify a few peaks in the ETFE and connect them with low order curves. The result is a piecewise continuous curve that closely approximates the original ETFE, yet is much smoother. More specifically, this preprocessing procedure entails the following steps:

1. Convert the ETFE to a decibel scale (to facillitate the approximation of the measured Bode plot by first order functions, as we'll see later on).
2. Divide the frequency axis into a predefined number of intervals. The boundaries of these intervals are logarithmically spaced to reflect the logarithmic frequency axis of a Bode-plot (i.e. smaller intervals at lower frequencies and larger intervals for higher frequencies). In this fashion, the eventual piecewise continuous function will conform to the underlying philosophy of uncertainty modelling, namely that less is known about the plant as the frequency increases.
3. Define the first and last peaks in the piecewise continuous function as the first and last samples in the measured frequency response. This step helps to find the correct DC value for the Bode plot and also prevents the eventual uncertainty weight function from becoming an improper transfer function.
4. Find the highest peak in each interval. The result is unevenly spaced peaks that approximate the underlying shape of the ETFE.
5. Fit a straight line between each adjacent pair of peaks. Use these first order curves to calculate the values of the piecewise continuous curve between peaks. The result is a smooth alternative for the original noisy ETFE.

One of the few adjustable parameters in the whole algorithm is the number of peaks that have to be identified in the above mentioned preprocessing stage. As can be seen in figure 4.7, this parameter influences the smoothness and accuracy of the piecewise continuous upper bound to the original ETFE. A small number of peaks results in a low-order and very smooth transfer function, which is also quite inaccurate. On the other hand, a high number of peaks increases the risk of sharp changes in the upper bound which in turn requires a high order transfer function for the eventual uncertainty weight function. In this study, a balance was struck between the opposing imperatives of smoothness and accuracy by identifying twelve peaks in the observed ETFE.

The rest of the algorithm approaches the problem of fitting a transfer function to an observed frequency response[11] in the same manner as a human would. Once the DC gain of the Bode plot has been finalized, the Bode plot of the observed frequency response is inspected from low

[11] Remember that the observed ETFE has been replaced by the piecewise continuous upper bound determined during preprocessing.

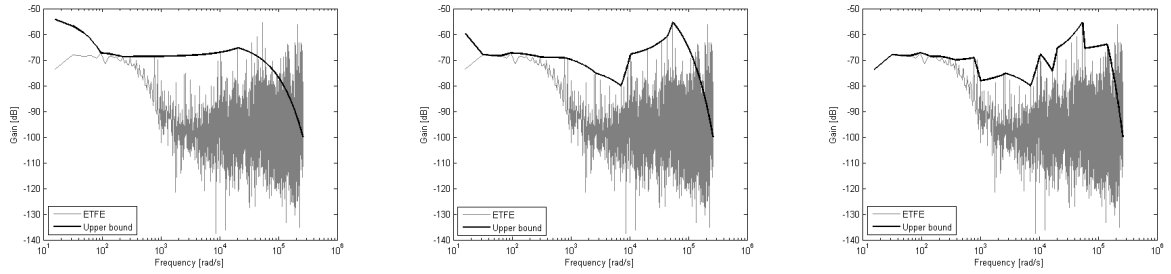


(a) 5 peaks (b) 12 peaks (c) 20 peaks

Figure 4.7: The effect of the number of peaks in the piecewise linear upper bound

frequencies to high frequencies. Zeros and poles are added in accordance with the well-known first order asymptotic approximations[12] for Bode plots (see e.g. [117]). This iterative procedure is continued until the deviation between the observed ETFE and the fitted function is below a predefined threshold.

More specifically, the algorithm proceeds as follows:

1. Initiate the transfer function with a DC gain (i.e. at this stage the fitted function consists only of a constant value for all frequencies). This DC gain is initially taken as the first value of the piecewise continuous upper bound.
2. Recalculate the Bode-plot of the present version of fitted function.
3. Inspect the Bode-plot of the fitted function and the Bode-plot of the piecewise linear upper bound at each discrete frequency value.
   (a) Ensure that the DC value of the piecewise upper bound is still the same as that of the present fitted function. (A previous iteration of this algorithm could have placed a pole or zero slightly above the current frequency. This would result in an erroneous DC value for the fitted function.)
   (b) Determine the difference between the Bode-plot of the upper bound and the Bode-plot of the fitted function as follows: $\epsilon(j\omega) = |y(j\omega)|_{dB} - |\hat{y}(j\omega)|_{dB}$. Where $\epsilon(j\omega)$ is the decibel difference between the gain of the upper bound ($|y(j\omega)|_{dB}$) and the gain of the fitted transfer function ($|\hat{y}(j\omega)|_{dB}$) at a specific frequency ($j\omega$).
   (c) Decide whether a pole or a zero has to be added to the present fitted transfer function.
      i. If the error is larger than a predefined positive threshold (expressed in decibels), the loop is stopped and a flag raised indicating that an additional zero is required in the vicinity of the current frequency.
      ii. If the error is smaller than a predefined negative threshold[13] (also measured in

[12] Currently the algorithm is limited to fitting real-valued poles and zeros to the observed data.

[13] The positive and negative thresholds don't have to have the same absolute value. The possibility of having differently sized positive and negative thresholds enables the user to fit conservative, average or optimistic transfer functions to the piecewise continuous function.

decibels), the loop is stopped and a flag raised indicating that an additional pole is required in the vicinity of the current frequency.

(d) Increment the frequency index and go back to step (b) unless a flag has been raised (signalling that a pole or zero has to be added) or the whole frequency response has been investigated without any error.

4. If an additional pole or zero is required (from the previous loop), include it in the fitted transfer function in the following manner:

   (a) Calculate the sum-of-squares error between the present fitted function and the upper bound (up and to the current frequency position in the spectrum).

   (b) Say (for example) that the current fitted transfer function can be expressed as follows[14]: $G_{old}(s) = \frac{K_{DC}(s-z_1)}{(s-p_1)}$ where $K_{DC}$ is the DC value of the function, then the new pole or zero ($p_2$ or $z_2$) is added in the following manner[15]:

      i. If a new zero has to be added: $G_{new}(s) = \frac{K_{DC}/z_2(s-z_1)(s-z_2)}{(s-p_1)}$

      ii. If a new pole has to be added: $G_{new}(s) = \frac{K_{DC}p_2(s-z_1)}{(s-p_1)(s-p_2)}$

   (c) Calculate the Bode-plot of the new fitted transfer function.

   (d) Calculate the sum-of-squares error between the new (proposed) fitted function and the upper bound (up and to the current frequency position in the spectrum).

   (e) If the sum-of-squares error for the new (proposed) fitted function is less than the sum-of-squares error for the previous fitted function, the proposed function is accepted and the frequency index is reset to the beginning (i.e. go back to step 2). Otherwise, the proposed modifications are rejected and the old fitted function is retained. In the latter case, the frequency index isn't reset and the search in step (b) continues[16].

5. The algorithm is terminated when the whole spectrum has been investigated.

As an example, figure 4.8 shows the results of the above mentioned algorithm when applied to one of the SISO uncertainty weight ETFEs in the AMB plant uncertainty model. A maximum of 3 dB deviation was allowed between the piecewise continuous upper bound and the fitted transfer function. Such stringent requirements however result in higher order transfer functions (48 zeros and 58 poles in this specific example). Despite the disadvantage of being

[14]Representing a transfer function in factorized form is more natural for the purposes of constructing a transfer function from first order asymptotic Bode-plot approximations. Another advantage of the factorized representation over the well-known rational function representation is that the latter is more prone to numerical errors in calculating the actual pole and zero positions [26].

[15]Take note that the new pole or zero is added at the previous frequency increment (and not the current frequency index where the loop has been stopped) and that the DC value of the fitted function is modified after the inclusion of the new pole or zero. These slight modifications attempt to compensate for the differences between the real Bode-plot and first order approximations to it (this algorithm is based on first order asymptotic Bode-plot approximations).

[16]The algorithm can be speeded up by borrowing the following concept from artificial neural network training algorithms [118]. In essence, this entails that the step-size of the search algorithm is gradually increased when little progress is made. In this algorithm, the frequency index is updated as follows: $k \leftarrow k + (n+1)$, where $n$ is the number of consecutive unsuccessfully proposed fitted functions.

a high order function, the fitted transfer function is still a smooth and accurate model of the measured dynamic uncertainty.

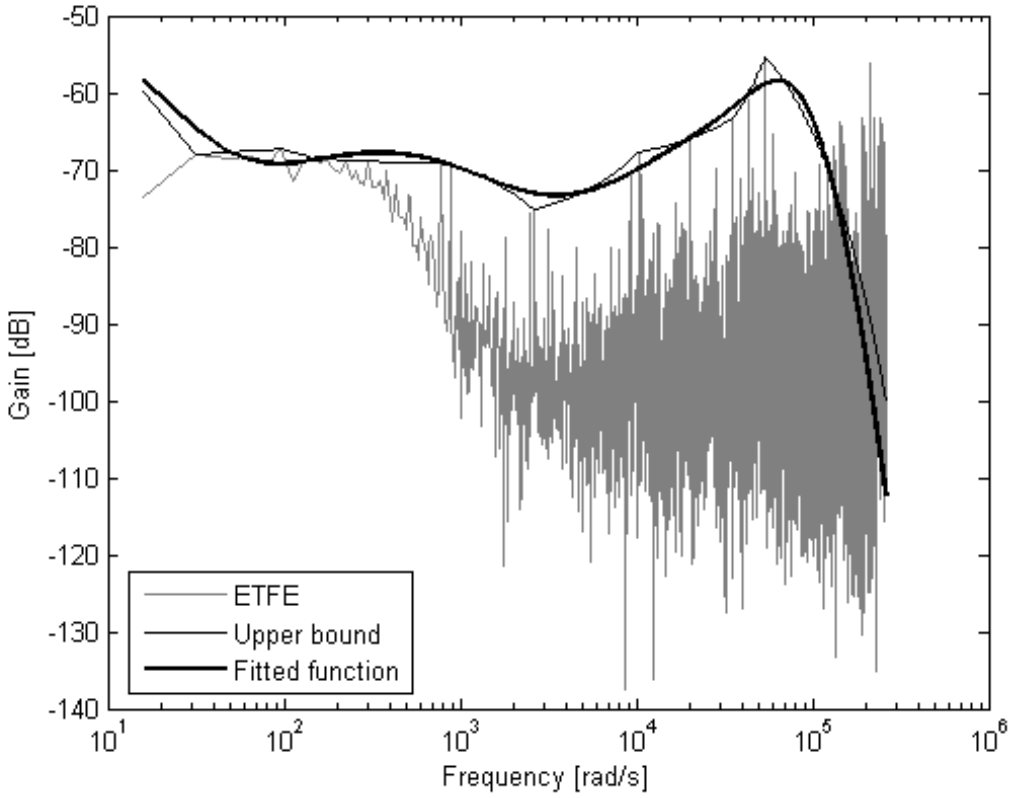


Figure 4.8: Fitting a transfer function to an ETFE

### 4.4.4 Validation of the uncertainty model

The last step in the uncertainty modelling process is to validate the uncertainty weight function which has been identified in the previous section. Roy Smith originally coined the term *model validation* as the process of finding out whether a particular model and unknown perturbation could account for observed input-output signals [119]. Fundamentally, the task of model validation is "...to assess whether the model is consistent with experimental observations" [120]. Validation of a model for dynamic uncertainty therefore basically entails assessing whether the uncertainty model is truly an accurate representation of the unmodelled effects in the original system as modelled by the nominal model. This important issue only very rarely receives attention in the literature.

Smith ([119]) broached the topic by asking the question: given a nominal model, uncertainty model , measured I/O data and an uncertain disturbance signal; is it possible that the observed data could have been generated by these models and the said disturbance signal? This specific model validation problem has been solved by Smith and his co-workers by means of singular value analysis (e.g. the so-called generalized $\mu$, [120]). Unfortunately this study is limited to

dynamic uncertainty and therefore the effect of disturbance forces falls beyond the scope of this study. Another objection to the approach of Smith *et al.* is that it is questionable whether using analysis techniques limited to the robust control paradigm would result in a validation test that is sufficiently critical of the uncertainty model (which is also confined to the robust control paradigm).

The $\nu$-gap metric has also been employed in the validation of uncertainty models [121]. As usual, the $\nu$-gap metric was used to estimate the distance between two models ([27]) and this formed the basis of a technique to estimate the validity of a model for parametric uncertainty. (More specifically, the $\nu$-gap was compared to the "optimal stability margin" of the system.) The prime objection against the $\nu$-gap metric is that it is only a relative measure and as such would be better suited to compare two different uncertainty models against each other, rather than to measure a model against objective reality.

Alternatively, the validity of the uncertainty model can be indirectly measured by means of the accuracy of the resultant $\mu$-analysis. (In other words an accurate stability margin would be indicative of a realistic uncertainty model.) This approach is similar to the validation procedure of Buckner *et al.* who assessed the validity of the uncertainty model via the performance of the resultant $H_\infty$ controller [101]. (This controller has been synthesized on the basis of the said uncertainty model.) Once again, this approach is limited to the confines of LTI systems. This approach also only gives an indirect measure of the quality of the uncertainty model.

The tack that will be taken in this study is loosely based on some of the ideas in [119] and [101]. Essentially, an uncertainty model would be valid if it could be used along with the nominal model to duplicate the behaviour of the nonlinear system[17]. In other words, a new LTI closed-loop system model is synthesized from the nominal models identified during system identification, as well as the uncertainty weighting functions fitted by means of the algorithm in section 4.4.3. (The norm-bounded uncertainty, $\Delta(s)$, which usually accompanies the uncertainty weight, is now taken as the all-pass function.) An example of such an LTI closed-loop model is given in figure 4.9 for the case of dynamic uncertainty in the self-sensing module. (This figure is obtained from figure 4.1.) The response of the resultant LTI model can then be calculated for any particular input signal. By comparing the response of the new closed-loop LTI model (known as the *augmented* model in this study) with the corresponding response of the nonlinear system, it is possible to qualitatively and quantitatively measure the accuracy of the uncertainty model.

The main drawback of a simulation based approach to model validation is that it is philosophically impossible to validate a model through simulation studies. At most, simulation studies can invalidate a model, or otherwise foster increasing confidence in the model as more and more successful simulations are conducted. This weakness should however be seen in context, since Smith *et al.*'s mathematically rigorous approach is by their own admission also only a model invalidation technique [119].

The overarching concern with the proposed model (in)validation scheme is that the mismatch

[17]The residuals of a model are defined quite similar to additive uncertainty, namely: $\epsilon(t) = y(t) - \hat{y}(t)$, where $y(t)$ is the original system and $\hat{y}(t)$ is a model for the system [44]. If both the original system and its model are LTI, the response of the original system can be perfectly reconstructed from its model and the model's residuals.

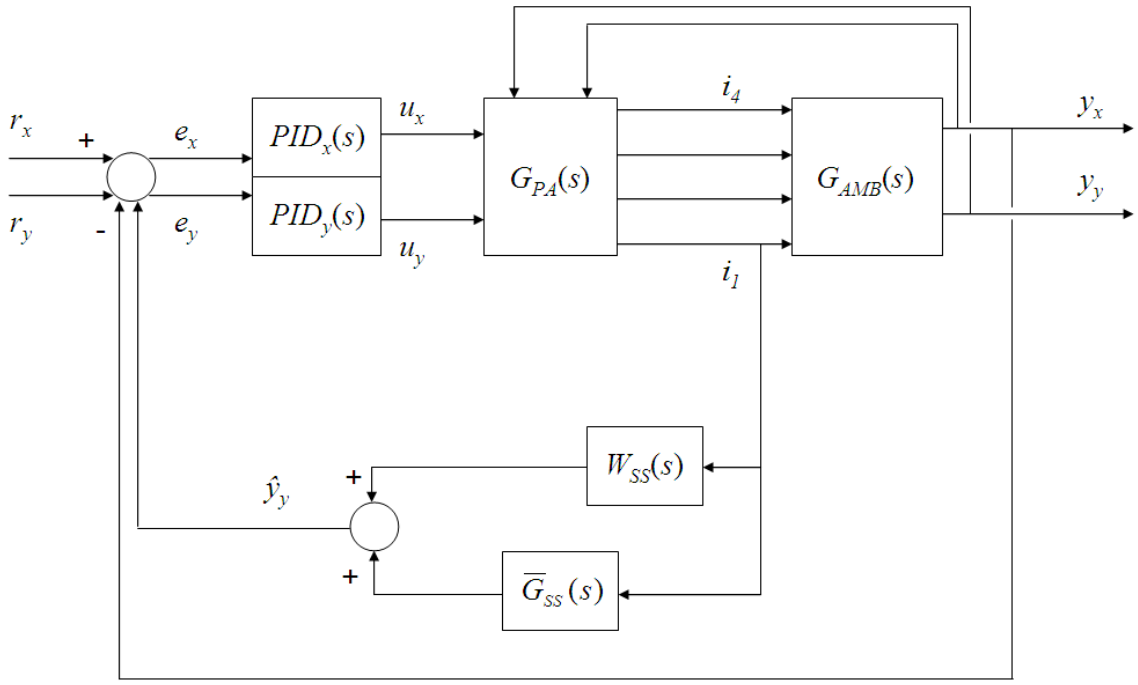


Figure 4.9: Augmented model for self-sensing with additive dynamic uncertainty

between a nonlinear system and its LTI model can't necessarily be modelled by means of adding another LTI model to the nominal LTI model. Consequently, both the additive uncertainty model, as well as its validation procedure might be unsuitable for nonlinear AMB systems. This concern can be addressed by purposefully including input signals during the model validation phase that will excite nonlinear behaviour in the AMB (and possibly highlight deficiencies in the LTI uncertainty model).

## 4.5 Validation of $\mu$-analysis

Validation of the final stability margin estimated via $\mu$-analysis is by and large similar to the validation of the uncertainty model upon which the $\mu$-analysis is based, but with a slight difference in accent. In the validation of $\mu$-analysis the focus is on verifying the accuracy of the *stability margin* estimated by $\mu$-analysis. The stability margin of a system is defined in chapter one as "...the minimum perturbation that will destabilize [the system]". Consequently, validation of the stability margin (predicted by $\mu$-analysis) depends on the specific perturbation that is under the spotlight. This study focusses on two specific forms of uncertainty, namely: parametric uncertainty in the controller coefficients, and dynamic uncertainty due to unmodelled effects in the identified models for the major AMB subsystems[18].

In the case of parametric uncertainty, the stability margin predicted by $\mu$-analysis can be validated in a two-pronged fashion. First, a Monte Carlo analysis of the LTI closed-loop model is conducted during which the probability of instability is calculated. (This probability

[18]The power amplifier, AMB plant model and self-sensing module.

is merely the frequency of delevitations during the whole Monte Carlo analysis.) The Monte Carlo analysis entails numerous random perturbations of the controller coefficients[19]. Each perturbation is followed by a simulation of the response of the LTI closed-loop system for a particular input signal. Delevitation per definition occurs when the rotor position exceeds the inner diameter of the retainer bearing. This specific Monte Carlo analysis is however limited by the fact that the AMB system is represented by an LTI model. Nonetheless, this validation procedure is useful to identify possible conservatism in the results of $\mu$-analysis.

Secondly, a nonlinear Monte Carlo simulation is conducted to ascertain the true effect of the parametric uncertainty on the stability robustness of the AMB system. The only difference between the nonlinear Monte Carlo simulation and its predecessor is that the AMB system is now represented by a nonlinear simulation model. The nonlinear Monte Carlo simulation is consequently time consuming, but delivers an accurate estimate of the probability of delevitation for the modelled parametric uncertainty in the controller coefficients. This probability then serves as an objective benchmark for the stability margin estimated by $\mu$-analysis. Furthermore, the nonlinear Monte Carlo simulation is also valuable to highlight the limitations of LTI modelling (as we'll see in the next chapter).

The situation is slightly different for dynamic uncertainty. Although Monte Carlo simulations of the LTI closed-loop system with additive uncertainty (e.g. figure 4.1) is in principle possible, the presence of algebraic loops makes it difficult in practice. The stability margin predicted by $\mu$-analysis will therefore have to be validated by means of stability checks done on the augmented closed-loop model (e.g. figure 4.9) which has been exposed to signals that excite different forms of nonlinear behaviour in the system. Obviously these stability checks are compared to similar stability checks performed on the original nonlinear AMB system.

The complete validation procedure for dynamic uncertainty in any of the AMB subsystems consists of the following steps:

1. Choose a specific amplitude for the test signal that will be injected at point 1 (figure 3.12) of both the augmented model as well as the nonlinear simulation model of the AMB. The final test signal will be a sine-wave frequency sweep with a maximum frequency determined from the AMB's frequency-amplitude graph (either figure 3.10 or figure 3.11). (The validity of the additive uncertainty models will be tested by means of frequency induced nonlinearities.)
2. Use the frequency-amplitude graph in the previous step to specify the bandwidth of another excitation signal. This additional signal will be used to obtain uncertainty weight functions for dynamic additive uncertainty (via the procedure in sections 4.4.2 and 4.4.3). The excitation signal will be a random phase multi-sine signal whose bandwidth encompasses any of the regions of AMB behaviour (A,B or C) in the frequency-amplitude graph, depending on the specific focus of the robustness analysis at hand.
3. Estimate the stability margin by means of $\mu$-analysis.
4. Apply a sine-sweep test signal to both the augmented model and the original nonlinear simulation model. By comparing the responses of the two models, it is possible to assess

[19]The random perturbations are obtained from a uniform probability distribution.

the validity of the LTI uncertainty model. The specific frequency at which delevitation occurs is also a convenient measure of the stability margin of both the augmented model and the nonlinear simulation. The stability margin predicted by $\mu$-analysis will be indirectly validated if both the augmented model and the nonlinear simulation model delevitate at similar frequencies.

## 4.6 Conclusion

The main conclusions of this chapter are:

- The mismatch between the nominal model and the nonlinear system can only be modelled by means of additive uncertainty. (Due to limitations imposed by black-box nominal models and numerical problems associated with the transformation between state-space models and transfer function models.)
- The inherent instability of the AMB requires that the additive uncertainty weights be estimated in the frequency domain.
- A novel algorithm was presented with which a transfer function can be fitted to an ETFE of the uncertainty weight.
- Procedures were outlined with which the model for dynamic uncertainty and the estimated stability margins can be validated.

Everything is now in place to obtain estimates of the stability margin of a 2-DOF self-sensing AMB for the following uncertainties:

- perturbations in the controller coefficients;
- and dynamic uncertainty due to unmodelled effects in either the power amplifier, AMB plant model, or self-sensing module.

# CHAPTER 5

# Putting it all together

*This chapter describes the application of μ-analysis to estimate the stability margin of the self-sensing AMB due to dynamic uncertainty and parametric uncertainty in the controller coefficients. The results presented in this chapter were obtained by means of nonlinear simulation models for both a sensed and self-sensing AMB. To avoid a build-up of uncertainties and consequent inaccurate robustness analyses, each form of uncertainty is individually investigated. A prerequisite for these robustness analyses is an accurate nominal LTI model for the self-sensing AMB and its major subsystems. LTI models for the various components in the control system can be found as soon as suitable excitation signals have been generated. The frequency-amplitude graph introduced in chapter 3 is ideally suited to analyse different potential excitation signals and choose the most suitable one.*

## 5.1 Nominal models

### 5.1.1 Optimal experiment design

Detailed robustness analysis of the 2-DOF self-sensing AMB entails that separate nominal models have to be fitted to the power amplifier, AMB plant and self-sensing module shown in figure 3.14. According to the flowchart in figure 2.7 application of system identification begins with the collection of maximally informative data that completely describes the real system's response.

As mentioned previously, the unstable nature of AMBs dictate that the self-sensing AMB be operated in closed-loop. An excitation signal is injected at point 2 to minimize any distortion on the excitation signal by subsystems in the loop (see figure 3.12). For the self-sensing AMB injection point 2 is defined as the output of the PID controller (i.e. prior to the implementation of differential driving mode). Estimation data for each subsystem can then be obtained by sampling the relevant input and output signals in the closed-loop system. (This whole process is known as direct closed-loop identification.)

The nature of the excitation signal has a profound impact on the quality of the models that are obtained during the subsequent parameter estimation phase. With respect to its length, the duration of the excitation signal should be commensurate with the dominant time constants of the AMB [44]. Equally important is that the spectral content of the excitation signal should be specified in accordance with the frequency-amplitude graph of the specific AMB (see figures 3.10 and 3.11). This practice ensures persistent excitation and also constrains the AMBs behaviour to remain within the LTI domain.

The utility of the frequency-amplitude graph becomes evident when it is used as a tool to evaluate potential excitation signals. Take for example the frequency-amplitude graph of a sensed 2-DOF AMB (figure 3.10). (This graph is merely used for illustrative purposes.) The effect that a particular excitation signal will have on the AMB's behaviour can be predicted by superimposing the spectral content of the excitation signal onto the vertical axis of the frequency-amplitude graph. In this way it is possible to see in advance whether a particular signal will induce region B or C behaviour in the AMB. This has been done for the case of white noise in figure 5.1(a)[1]. The excitation signal has a standard deviation of 1000 μm and has been injected at point 1. The superimposed spectrum clearly shows the characteristic flat spectrum of white noise. Furthermore, it is also evident that this excitation signal contains significant components in region B and C (at the specified amplitude). Consequently, it should come as no surprise that this excitation signal does induce nonlinear behaviour in the AMB.

In order to ensure LTI operation of the AMB, the frequency-amplitude graph advises that the spectral composition of the excitation signals should be biased toward low-frequency components rather than high frequency components. Pink noise (being $1/f$ noise) conforms to this general guideline. As figure 5.1(b) however shows, the high frequency content of this pink noise signal[2] is sufficient to induce region C behaviour in the AMB.

What is required is an excitation signal whose spectral content can be constrained to be within a narrow band. Examples of such signals are random phase multi-sine signals and rectangular waves. As figure 5.1(c) shows, the boundaries of the spectrum of a chirp signal can be defined quite clearly. The spectral content of random phase multi-sine signals can be controlled equally well. Rectangular waves are also ideal excitation signals for LTI system identification, since their spectrum falls away rapidly for increasing frequencies. If the amplitude of the rectangular wave is specified prudently, the AMB will remain within its LTI operating domain (see figure 5.1(d)).

As mentioned previously, the excitation signal is injected at point 2 in order to limit the distortion caused by negative feedback and the individual loop components. It would therefore be more appropriate to choose potential excitation signals by means of a frequency-amplitude graph determined with injection point 2 as input. (I.e. a frequency-amplitude graph in which

[1] Strictly speaking, the spectrum superimposed in figure 5.1(a) represents the frequency content of a bandlimited white noise sequence. In practical digital control systems the requirements of the sampling theorem dictate that any theoretical white noise sequence has to be limited to the Nyquist frequency to ensure that the random samples of the sampled noise sequence remain uncorrelated [122]. The specific spectrum shown in figure 5.1(a) was obtained by sampling a white noise process at a sampling frequency of 10 kHz for the duration of ten seconds.

[2] This spectrum also represents a bandlimited pink noise spectrum due to sampling. The specific spectrum was obtained by sampling a pink noise process with a standard deviation of 350 μm at 10 kHz for a duration of 1.8 seconds.

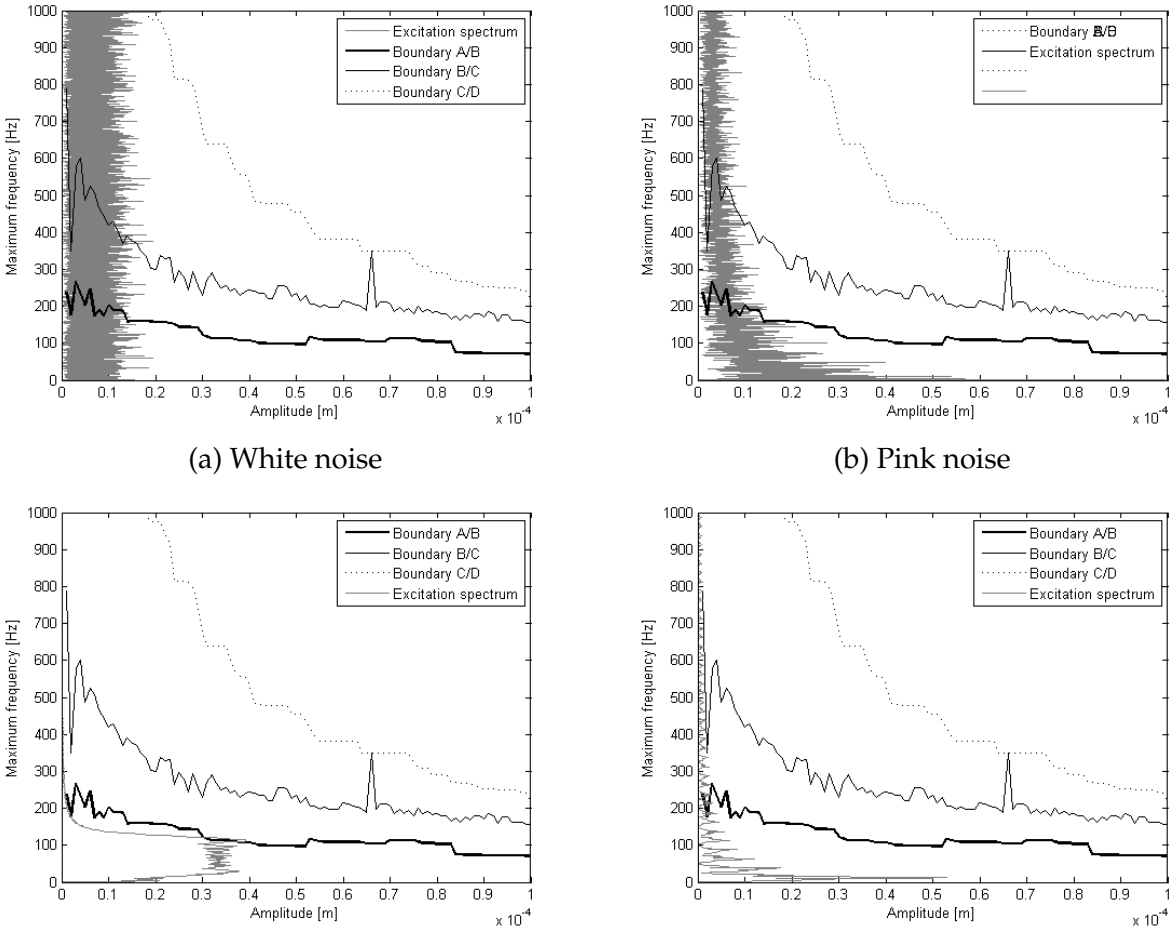


(a) White noise

(b) Pink noise

(c) Sine sweep from 10 Hz to 70 Hz

(d) Rectangular pulses

Figure 5.1: Evaluation of potential excitation signals

frequency sweeps are applied at point 2.) The resulting graph for a self-sensing 2-DOF AMB is shown in figure 5.2.

From figure 5.2 it seems that (for larger amplitude signals) the excitation signal's spectral content is limited to 46 Hz or less in order to maintain LTI operation. (In order to keep the length of the estimation signal within practical bounds, multi-sine signals are generated with a specific minimum frequency as well. For the problem at hand, this lower bound is typically chosen as 5 Hz.) Alternatively, a rectangular wave can still be used without inducing nonlinear behaviour in the AMB.

A potential objection to the above mentioned use of the frequency-amplitude graph is that nonlinear systems don't obey the superposition principle. Linear systems are defined by the fact that they exhibit superposition. If a linear system is confronted with an input signal consisting of more than one frequency component, its response will contain only those frequency components (with different amplitudes and phases). Nonlinear systems, on the other hand, are characterised by subharmonic generation, where the output spectrum contains components at

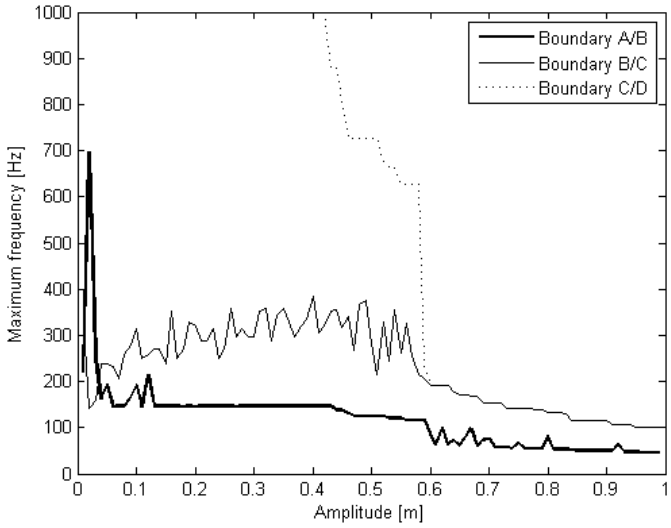


Figure 5.2: Frequency-amplitude graph for a self-sensing AMB perturbed at injection point 2

frequencies that are linear combinations of the input spectral components' frequencies[3] [82].

Subharmonic generation is however avoided in the AMB provided that it remains in region A operation. In the absence of frequency induced nonlinear behaviour, a 2-DOF AMB can be accurately modelled by means of LTI models. In section 3.2.1 it is shown that linear models can explain at least 96 % of the AMB behaviour due to position and/or current variations (see figures 3.3 and 3.4). Furthermore, it is also shown in section 3.2.1 that hysteresis and saturation have a neglegible impact on the behaviour of a sensed AMB (see figure 3.5).

If a process can be accurately modelled by means of an LTI model, it is safe to assume that the process is predominantly linear. This is true of an AMB constrained to operate in region A of the frequency-amplitude graph. Figure 5.3 shows the response of a ninth order LTI model fitted to a sensed 2-DOF AMB. (In this instance the model was estimated on the first half of the nonlinear response data.) Clearly, the LTI model can accurately describe the behaviour of the nonlinear AMB (with the exception of a bias-error on the $y$-axis response, which can be easily solved by adding a suitable bias value).

Further evidence that multi-sine excitation signals may be safely applied to an AMB operating in region A is given by the fact that subharmonic generation is only evident in AMBs that are operating beyond region A (i.e. regions B and/or C). Figure 5.4(a) shows the output spectrum of a sensed AMB in response to two simultaneous sinusoids being applied at its input (with frequencies of respectively 30 Hz and 50 Hz). According to figure 3.10 the AMB ought to behave like a linear system, which it does (as is testified to by the absence of subharmonic components in its output spectrum). When the same AMB is however confronted with an 80 Hz sinusoid, as well as a 100 Hz sinusoid in its input signal, then subharmonic components are visible in the AMB's output spectrum[4]. This result makes sense since the bandwidth of the

[3] In other words, if two frequencies $f_1$ and $f_2$ are present in the input signal, then the output signal contains components at the following frequencies $af_1 \pm bf_2$, where $a$ and $b$ are arbitrary integers.

[4] Both of the output spectra in figure 5.4 reflect the frequency content of the AMB's $y$-axis response.

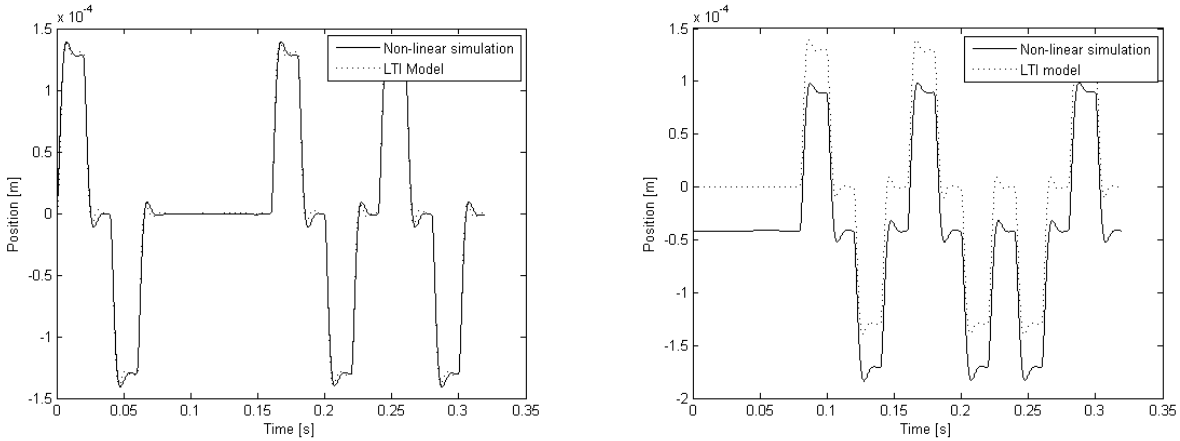


(a) X-axis response (b) Y-axis response

Figure 5.3: An accurate model for a sensed AMB

input signal forced the AMB into region B operation (according to figure 3.10).

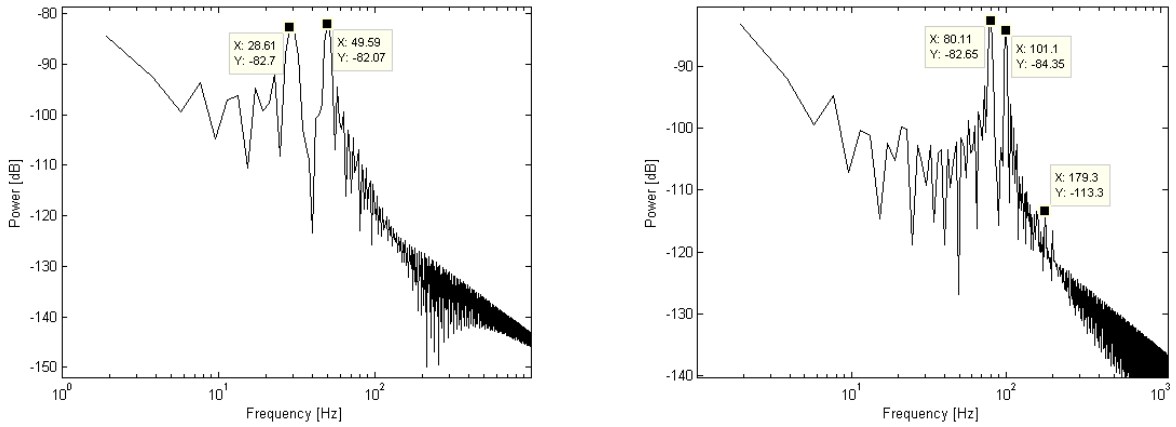


(a) Region A operation (b) Region B operation

Figure 5.4: Subharmonic generation in an AMB as a function of the bandwidth of the input signal

Another consideration that has to be kept in mind (while designing a system identification experiment) is that it often is better to apply excitation signals independently to the different inputs of a MIMO system [46]. In the case of the 2-DOF AMB this implies that perturbations be applied consecutively, but separately to the horizontal and vertical dimensions of the bearing[5]. Such excitation signals however run the risk of becoming too long leading to suboptimal model identification.

Optimal experiment design for self-sensing AMB identification to a large extent reduces to designing an excitation signal that conforms to all of the following criteria:

[5]This doesn't mean that the effect of cross-coupling is being overlooked. In fact, the cross-talk within the AMB stator is actually highlighted in this approach.

- Its spectral content should be limited to the band from 5 Hz to 46 Hz.
- Total duration must be in the order of the dominant time constants of the system.
- The point-mass should traverse as much of the airgap as possible.
- Horizontal and vertical dimensions have to be excited separately.

One excitation signal that meets all of the above requirements is a rectangular wave applied out of phase to the $x$- and $y$-axes with the result that the point mass is moved in a square pattern through the airgap. The resultant movement of the point-mass is shown in figure 5.5.

The last step before parameter estimation can be done is to reduce the sampling frequency of the data (as discussed in section 3.5). Obviously, the choice of the decimation factor has a huge impact on both the size of the estimation subset, as well as the accuracy with which the peak ripple current is represented in the data (as reflected in table 3.2). A shortlist of potential sampling frequencies was compiled in chapter three, namely: 71.4 kHz, 76.9 kHz and 83.3 kHz. Of these three options, the 83.3 kHz data captures the peak ripple currents most accurately and therefore also results in the best identified models. In the interest of accurate robustness analysis the final sampling frequency of the data should be 83.3 kHz.

### 5.1.2 Results of parameter estimation

During the parameter estimation phase of system identification, different candidate state-space models are fitted by means of subspace algorithms (e.g. N4SID). At this stage, the only parameter over which the user has control is the order of the model that is to be fitted. Once a number of candidate models of different orders for the three subsystems in the AMB have been fitted, the analysist has to select a combination of models that will accurately replicate the original nonlinear self-sensing AMB. The following general guidelines can be followed in the selection process.

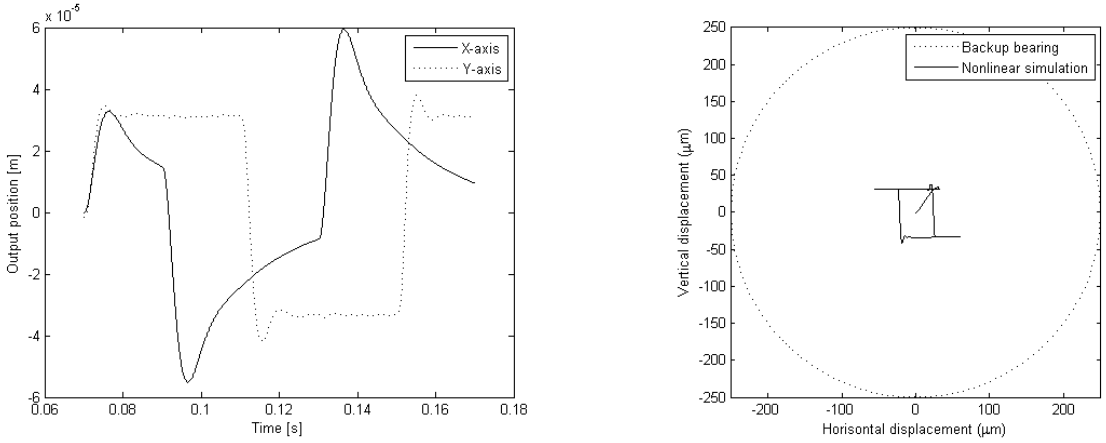


(a) Response as a function of time (b) Orbital plot

Figure 5.5: Response of the nonlinear self-sensing AMB simulation to the final excitation signal

- **AMB plant** Ensure that the models are fitted with a prediction focus in order that they are unstable. The residuals of the candidate models should resemble white noise and be decorrelated with any input signals.
- **Self-sensing** This model should also be estimated with a prediction focus, since the mapping from coil currents to $y$-axis position is fundamentally similar to that of the AMB plant (i.e. unstable). It is especially important that the models for the self-sensing module should be of low order.
- **Power amplifier** In contrast with the previous two models, the model of the power amplifier has to be stable and therefore should be estimated with a simulation focus. It is important that the output currents of this model should contain accurate position information (for the purposes of self-sensing). The graph in figure 3.15 is a useful tool in this regard.

After the final combination of subsystem models has been selected, it is validated by means of the simulation performance of the resultant closed-loop system of LTI models. The closed-loop simulation performance can be qualitatively assessed by means of a visual comparison between the response of the nonlinear simulation and the LTI closed-loop model for the same input signal. Alternatively, the closed-loop simulation performance can be quantitatively evaluated by means of the coefficient of determination in (3.7).

Finally, the subsystem models are re-estimated by means of PEM. Experience confirms the results of [99], namely that the quality of models obtained via N4SID and PEM are virtually indistinguishable from each other. As an example the closed-loop simulation performance of the LTI system obtained via N4SID is 99.93 % and -8.46 % on the $x$- and $y$-axes respectively[6]. The performance of the LTI system obtained via PEM is almost the same, namely: 99.92 % and -8.17 %. These specific simulation results are shown in figure 5.8. Clearly, the $y$-axis response of the closed-loop model is quite poor.

The final nominal closed-loop LTI model of the 2-DOF self-sensing AMB of this study consisted of the following components: a $9^{\text{th}}$ order AMB plant model; a $7^{\text{th}}$ order power amplifier model and a $3^{\text{rd}}$ order model for DCM self-sensing. Appendix D contains the matrices of these state-space models.

The validity of the identified nominal models can be assessed by calculating the LTI closed-loop system's simulation performance for system input signals different from the estimation data [44]. Parameter estimation was performed on rectangular pulses injected at point 2 to obtain the response in figure 5.5. The first validation test will therefore be on the same signal injected with a different amplitude at point 1. Figure 5.6 shows the responses of both the original nonlinear simulation as well as the closed-loop LTI model. Once again the $x$-axis performance of the LTI model is quite impressive (93.76 %), while the $y$-axis performance of 50.76 % is much less so. Clearly the identified self-sensing model is at fault, drastically reducing the bandwidth and fidelity of the total closed-loop system. Poor performance of LTI models for nonlinear systems

[6] Although it may seem odd, the negative simulation performance on the $y$-axis response is in keeping with the definition of this measure (see (3.7)). Negative values merely indicate a large discrepancy between the model and the measured value.

containing ”hard” nonlinearities such as the maximum-operator used in DCM self-sensing is however to be expected.

As the shape and amplitude of the test signal draw further and further away from the estimation data, one would expect a degradation in the performance of the LTI closed-loop model. The extent to which this degradation is delayed gives an indication of the generalization ability of the model. (I.e. an accurate model for a system will duplicate the original system's response even for inputs not present in the estimation subset.) In the case of the closed-loop LTI model for the 2-DOF self-sensing AMB, the model's performance degrades rapidly for previously unknown input signals. The poor generalization ability of the LTI closed-loop system model is clearly visible in figures 5.7 and 5.8.

Figure 5.7 shows the responses of the nonlinear simulation and the closed-loop LTI model for another sequence of rectangular waves (this time centered at the origin of the airgap). This signal has approximately the same amplitude levels as the estimation data, but its shape is slightly different. The simulation performance of the LTI model on this signal is respectively 90.79 % and 24.00 % on the $x$- and $y$-axes.

The input signal applied to the nonlinear simulation and LTI model in figure 5.8 consists of a random phase multi-sine constrained to frequencies between 5 Hz and 46 Hz and limited to a maximum amplitude of 100 µm. Once again the poor $y$-axis performance is quite obvious. (The simulation performance of the LTI model in this instance is: 99.93 % and -8.46 %.) Although the performance of the LTI closed-loop model isn't inspiring, it should be seen in the context of LTI techniques used to model a nonlinear process. Discrepancies are therefore to be expected.

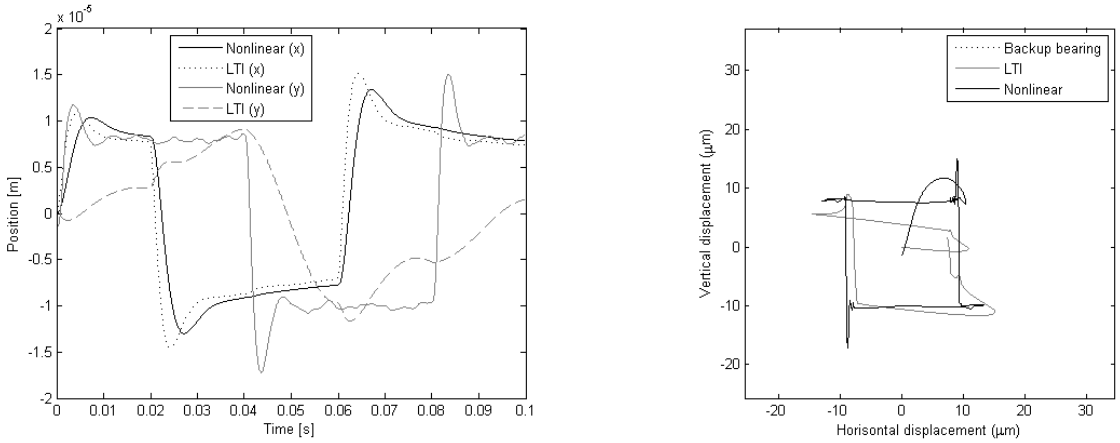


(a) Response as a function of time

(b) Orbital plot

Figure 5.6: Performance of the nominal LTI closed-loop model on data similar to the estimation subset

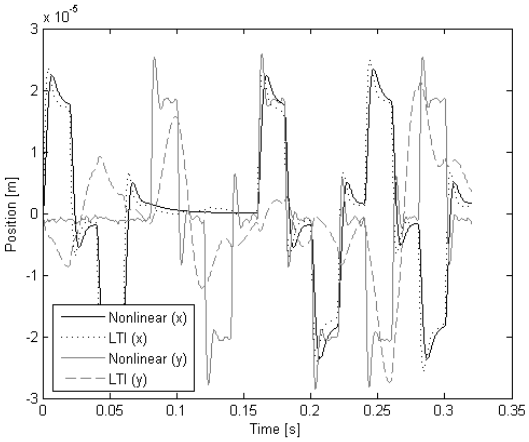


(a) Response as a function of time

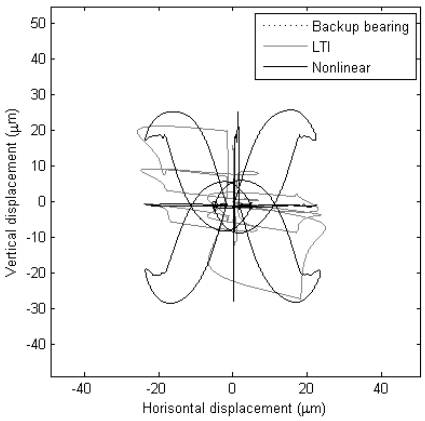


(b) Orbital plot

Figure 5.7: Performance of the nominal LTI closed-loop model on a rectangular wave

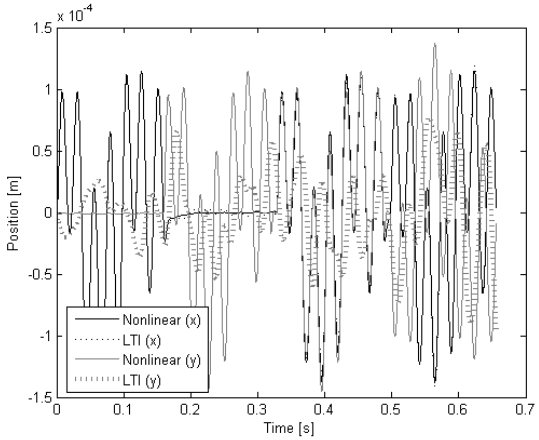


(a) Response as a function of time

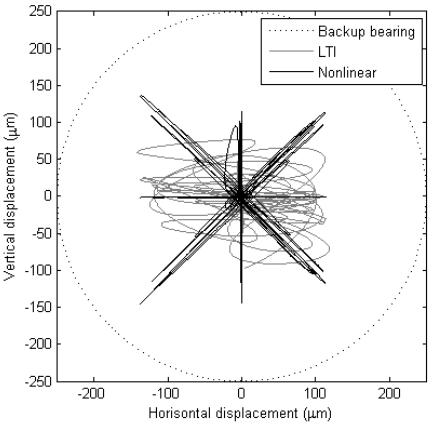


(b) Orbital plot

Figure 5.8: Performance of the nominal LTI closed-loop model on a random phase multi-sine signal

## 5.2 Robustness analysis for parametric uncertainty in the controller

The 2-DOF self-sensing AMB is controlled by means of two decoupled PID controllers (i.e. two identical PID controllers are applied independently to the $x$-axis and $y$-axis). Three coefficients consequently determine the characteristics of the controller and eventually of the whole system. These coefficients are respectively the proportional $(K_P)$, integral $(K_I)$ and derivative coefficients $(K_D)$.

Parametric uncertainty is the ideal vehicle for determining the stability robustness of the self-sensing AMB for variations in these PID controller parameters. The procedure for performing $\mu$-analysis for parametric uncertainty is the same as for dynamic uncertainty (see section 4.1). First of all the specific uncertainty in each of the three controller parameters is modelled by means of (4.1). Secondly, the closed-loop system must be rearranged to the generalized configuration of figure 4.2. In this instance the $\mathbf{\Delta}$ matrix is a $3 \times 3$ diagonal matrix with the modelled uncertainty for the three coefficients on its main diagonal. The values of $\mu$ are lastly calculated according to the rest of the procedure outlined in section 4.1.

The effect of variability in each of the controller coefficients on the system's stability margin will now be discussed in turn. In all of these analyses the frequency axis over which the values of $\mu$ are calculated is divided into 1,000 increments. (A fine frequency grid is especially important when real-valued parametric uncertainty has to be analysed, since the resultant $\mu$-plot often contains narrow peaks that can be easily missed with a coarse frequency gridding [24].)

### 5.2.1 Perturbation in $K_D$

If a variation of 80 % is allowed in the value of $K_D$, while the other two are kept relatively constant[7], $\mu$-analysis estimates that the control system will remain robustly stable. This can be seen from figure 5.9. The peak value of $\mu$ in figure 5.9 is 0.93 which indicates that $K_D$ may be perturbed by slightly more than 80 % without destabilizing the system.

All of the peaks in figure 5.9 represent dynamics of the closed-loop system that is influenced by $K_D$. The low-frequency peak (situated at 2.57 Hz) corresponds to the natural frequency of the specific self-sensing AMB. Constructive superposition occuring at this resonant frequency results in a system gain which is higher than at the surrounding frequencies. This resonant gain is obviously influenced by the controller coefficients, which explains its presence in various degrees in every $\mu$-plot in this section.

The frequency position of the other peaks in the $\mu$-plots for parametric uncertainty in the controller coefficients, is a function of the coefficients themselves. This can be explained by taking the analogy of calculating the closed-loop poles of a simple SISO control system consisting of a controller $(G_C(s))$ and plant $(G_P(s))$ in the forward path with unity feedback. The closed-loop transfer function of this system is the well-known expression:

$$G_{CL}(s) = \frac{G_P(s)}{1 + G_P(s)G_C(s)} \tag{5.1}$$

[7] "Constant" is regarded as a maximum of 0.1 % variation in the particular coefficient's value.

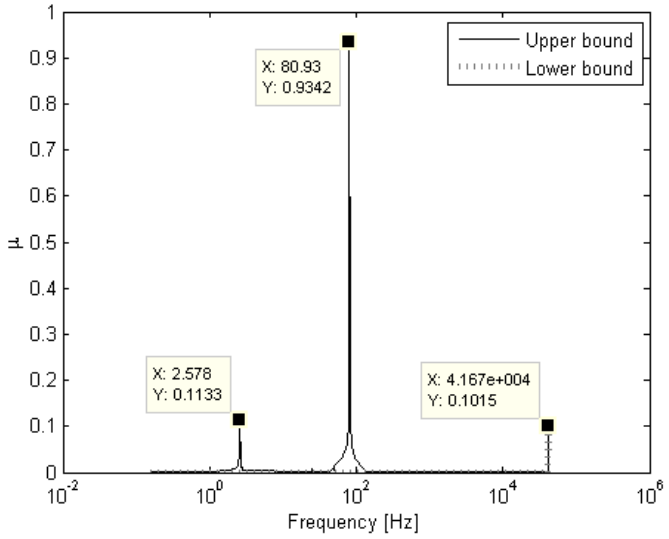


Figure 5.9: $\mu$-plot for variation in $K_D$

Clearly the closed-loop poles of the system are determined by both the poles and zeros of the controller and plant. Some of the closed-loop poles of the system are therefore functions of some of the controller coefficients. In a similar fashion each PID coefficient has an effect on the system gain at different specific frequencies. This effect is made visible by means of singular value analysis in e.g. $\mu$-plots.

The numerical properties of $\mu$-analysis performed on real-valued parametric uncertainty can be improved by introducing a small complex-valued perturbation in each real-valued parameter. This complex-valued dithering of the modelled uncertainty results in a smoother $\mu$-plot without changing the estimated stability margin. Figure 5.10 shows the results when a 5 % complex-valued perturbation was introduced in each of the controller coefficients. Clearly, dithering doesn't change the estimated stability margin of the system, but does improve the calculated lower bound of $\mu$.

As outlined in section 4.5 the stability margin estimated by $\mu$-analysis is validated by calculating the probability of instability by means of Monte Carlo simulations. First of all, a Monte Carlo study was performed on the nominal LTI closed-loop model. This study consisted of 100 simulations of the closed-loop response of the LTI model for randomly perturbed controller coefficients (within their modelled ranges). The input signal used during these simulations was a random-phase multi-sine signal whose upper and lower frequencies were respectively 5 Hz and 46 Hz. This signal was applied with a 90° phase shift between the $x$- and $y$-axes (as can be seen from figure 5.11).

The second stage of validation consisted of a similar Monte Carlo study conducted on the original nonlinear simulation. These nonlinear simulations are quite computationally expensive which explains why the Monte Carlo study is limited to only 100 trials[8]. Such a small number of trials doesn't invoke much confidence in the calculated probability of instability. It does

[8] A hunderd repetitions of the nonlinear simulation model for the input signal in figure 5.11 equates to approximately two days' worth of computer-time on a standard PC.

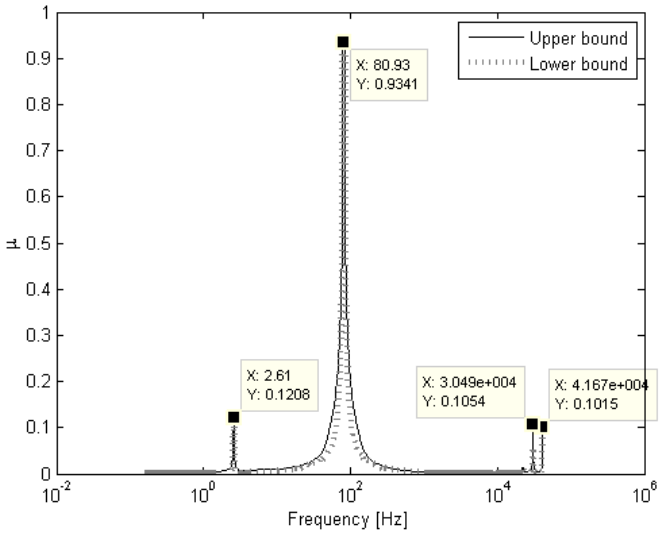


Figure 5.10: $\mu$-plot for variation in $K_D$ (with 5 % added complex dithering)

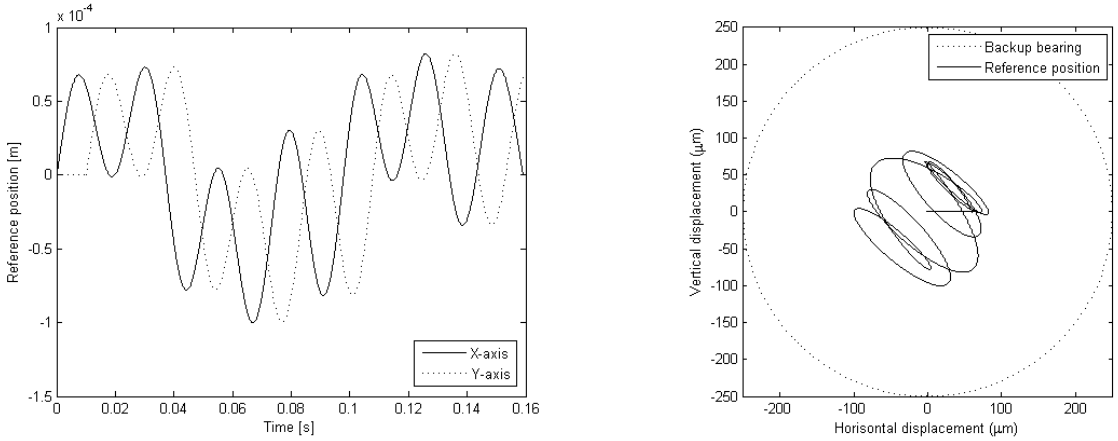


(a) Response as a function of time (b) Orbital plot

Figure 5.11: Multi-sine test signal used during Monte Carlo validation of $\mu$-analysis

however provide an approximate benchmark for the stability margin estimated by $\mu$-analysis.

For the test signal in figure 5.11 the LTI Monte Carlo study revealed an 85 % probability of instability. In other words, if the LTI closed-loop model is subjected to a variability of 80 % in the value of $K_D$ while $K_P$ and $K_I$ remain constant, the AMB has a probability of 85 % to delevitate. This surprising result contradicts the estimated stability margin of $\mu$-analysis, which shows that $\mu$-analysis is clearly overoptimistic in its assessment of the robustness of the AMB. This conclusion is borne out by the nonlinear Monte Carlo study, which showed that the original nonlinear system has a 51 % probability of delevitating if exposed to the same uncertainty. (The difference between the two linear and nonlinear Monte Carlo studies is due to modelling errors in the LTI model as well as the effect of the fundamental assumption of linearity.)

The self-sensing AMB is at heart a nonlinear system. Its response is therefore dependent on the specific input signal. This means that the results of the above mentioned validation procedure are also influenced by the specific test signal which is used. Unfortunately it seems as if the signal in figure 5.11 is a gentle signal which doesn't place much demand on the nonlinear simulation model. A more stringent test would be to use the signal used for figure 5.7[9]. In this instance the measured probability of instability for both the LTI and nonlinear Monte Carlo studies is 100 %. A 2-DOF self-sensing AMB is therefore very fragile for variations in $K_D$ if certain input signals are used.

This exposes a flaw in the Monte Carlo based validation procedure, namely a lack of generality, since its conclusions are not only dependent on the number of trial performed, but also on the specific test signal.

### 5.2.2 Perturbation in $K_P$

The stability margin for variation in the proportional coefficient is calculated in a similar fashion as the previous analysis. According to $\mu$-analysis the maximum percentage deviation in the value of $K_P$ is 19 % (see figure 5.12(a)). (The other two controller coefficients were held "constant" with a maximum perturbation of 0.1 %.) Dithering these parametric uncertainties with a 5 % complex-valued perturbation only improved the aesthetic appearance of the lower bound of $\mu$ as can be seen in figure 5.12(b). Comparing the $\mu$-plots of $K_D$ and $K_P$ shows that (with the exception of the natural frequency) the two coefficients result in different "resonant frequencies".

Once again the stability margin estimated by $\mu$-analysis is contradicted by the LTI Monte Carlo simulation. For the same modelled uncertainty the probability of instability of the LTI closed-loop model is 100 %, while the probability of instability of the nonlinear simulation model is 0 %. (Both of these probabilities were estimated on the test signal of 5.11.)

[9] The sharp transitions in this signal create much more opportunity for frequency induced nonlinearities to crop up.

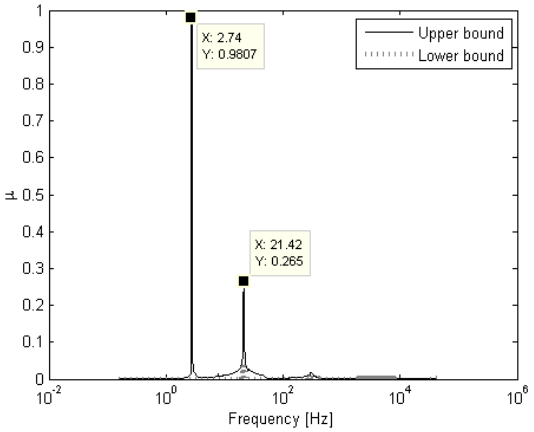


(a) Real-valued uncertainties

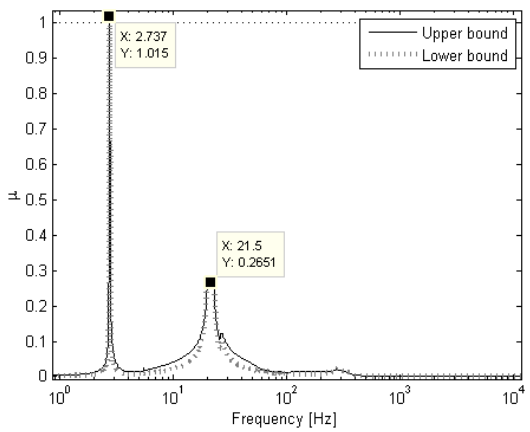


(b) Complex-valued dithering

Figure 5.12: $\mu$-plots for variation in $K_P$

### 5.2.3 Perturbation in $K_I$

Similar results were obtained if uncertainty is allowed in the value of $K_I$ while the other coefficients are kept constant. It seems that, compared to the other coefficients, the self-sensing AMB is most sensitive for deviations in the integral coefficient. Robust stability is only guaranteed for a maximum perturbation of 10 % in the value of $K_I$ according to $\mu$-analysis. Another interesting conclusion from the $\mu$-plot for $K_I$ (figure 5.13) is that this coefficient primarily impacts the worst-case gain of the AMB at the natural frequency of the AMB.

Compared to Monte Carlo simulations performed for the modelled uncertainty, $\mu$-analysis is once again over-optimistic. The estimated probability of instability for the modelled uncertainty on the closed-loop LTI model is 100 % (on the test signal of 5.11). Similarly the probability

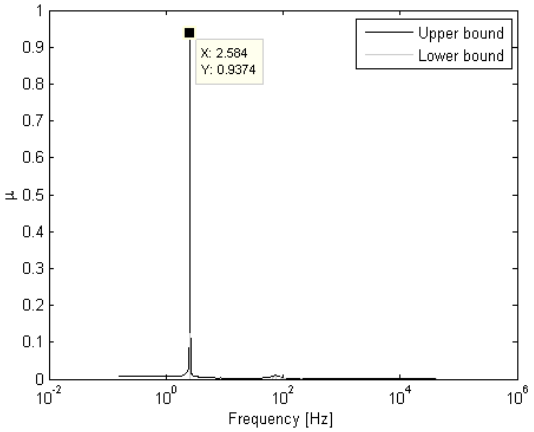


(a) Real-valued uncertainties

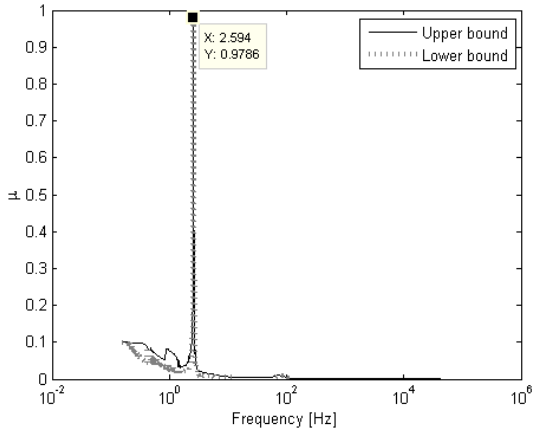


(b) Complex-valued dithering

Figure 5.13: $\mu$-plots for variation in $K_I$

of instability estimated via nonlinear Monte Carlo simulations is 40 %.

### 5.2.4 Sensed AMB

The same robustness analysis procedure was applied to the PD controller of a sensed AMB. System identification was used to fit a model for the AMB plant (which in this instance consisted of everything in the loop except the PD controller). The results of the eventual $\mu$-analyses and Monte Carlo simulations are summarized in table 5.1. Figure 5.14 shows the $\mu$-plots for 80 % uncertainty in respectively $K_P$ and $K_D$ (with the other coefficient being held constant at 0.1 % deviation). These results underscore the over-optimism of $\mu$-analysis when applied to parametric uncertainty in the AMB controller coefficients. A last conclusion that can be made from all of the robustness analyses conducted on the controllers of the sensed and self-sensing AMBs is that the sensed AMB is much more robust for deviations in the controller coefficients than the self-sensing AMB.

Table 5.1: Robustness analysis for controller parametric uncertainty in the sensed AMB

| Deviation in $K_P$ [%] | Deviation in $K_D$ [%] | Peak value of $\mu$ | Probability of instability (LTI) [%] | Probability of instability (nonlinear) [%] |
|---|---|---|---|---|
| 80.0 | 0.1 | 0.34 | 12 | 37 |
| 0.1 | 80.0 | 0.56 | 11 | 33 |

## 5.3 Robustness analysis for dynamic uncertainty in the AMB plant

Estimating the stability margin of a system for dynamic uncertainty in one of its sub-systems by means of $\mu$-analysis is accomplished by the following four-step procedure:

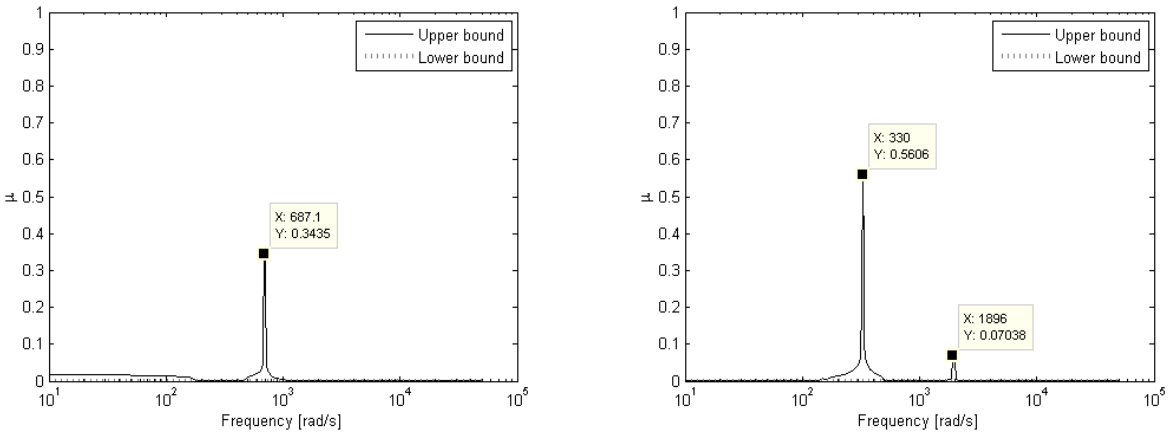


(a) 80 % deviation in $K_P$ (b) 80 % deviation in $K_D$

Figure 5.14: $\mu$-plots for parametric uncertainty in the sensed AMB

1. Obtain nominal LTI models for the subsystems and combine these models to form a closed-loop LTI model.
2. Determine the ETFE of the uncertainty weight for additive dynamic uncertainty (via the procedure on page 87).
3. Use the algorithm in section 4.4.3 to fit a transfer function to each uncertainty weight ETFE.
4. Calculate the values of $\mu$ as a function of frequency according to the procedure outlined in 4.1.

The AMB plant model takes the four coil currents as inputs and gives the x-axis and y-axis positions of the point-mass as its outputs. Dynamic additive uncertainty in this instance is modelled by means of eight SISO uncertainty weight functions, each connecting a specific input variable to a specific output variable according to the same general scheme as in figure 4.5(a).

In classical system identification the quality of the resultant nominal model is determined by the excitation signal with which the estimation data was obtained. Similarly, the quality of the ETFEs for the uncertainty weights is influenced by the specific excitation signal with which the AMB plant was interrogated. This signal consists of a random phase multi-sine applied separately to the $x$- and $y$-axes. The frequency content of the excitation signal is determined by the expected behaviour of the AMB (whether confined to region A, or encompassing more than one region in figure 3.11).

### 5.3.1 Dynamic uncertainty encompassing region A behaviour

The excitation signal is responsible for exposing the system's expected behaviour. If it is assumed that the AMB is operated solely in its linear domain, a suitable excitation signal would be the previously mentioned random-phase multi-sine signal with an amplitude of 100 μm and a spectral content limited to the band of 5 Hz to 26 Hz. The responses of the nonlinear simulation model and identified LTI model to this signal are shown in figure 5.15.

From the excitation signal in figure 5.15, the uncertainty weight ETFEs and bounding functions shown in figures 5.16, 5.17, 5.18 and 5.19 have been identified. Three graphs are shown in each of these figures. Firstly the raw ETFE of the particular uncertainty weight is shown. Secondly, the transfer function which has been fitted to this ETFE is also plotted. Due to the conservatism of $\mu$-analysis, the modelled dynamic uncertainty (i.e. the fitted weight transfer functions) often result in erroneous stability margins. It is therefore necessary to reduce the overall gain of the identified uncertainty weights by a certain scaling factor in order to obtain meaningful results. In essence the scaling of the measured uncertainty weights boils down to a reduction in the modelled uncertainty. For the specific case of dynamic uncertainty in the AMB plant, the identified uncertainty weights have to be scaled by a factor of 0.0013. The extent of this reduction in the uncertainty is made visible in these figures by lastly also plotting the scaled uncertainty weight function.

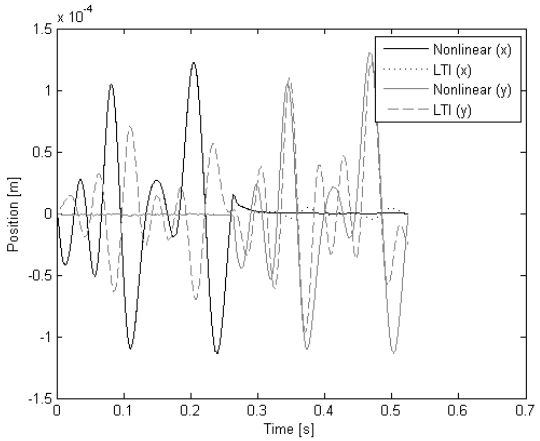


(a) Response as a function of time

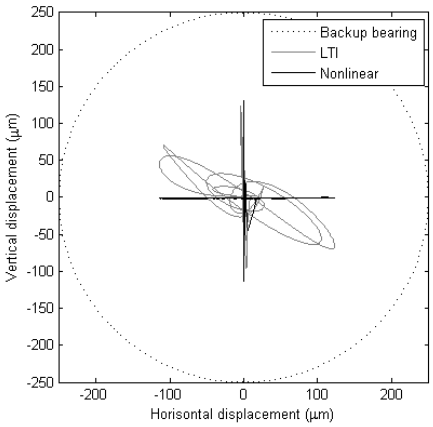


(b) Orbital plot

Figure 5.15: Multi-sine excitation signal used during the modelling of uncertainty weights

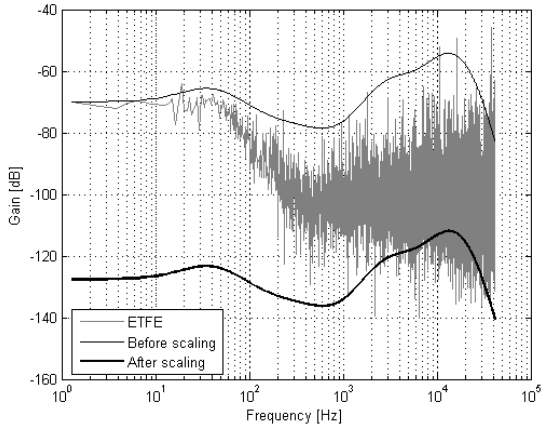


(a) Weight from current 1 to $x$-axis

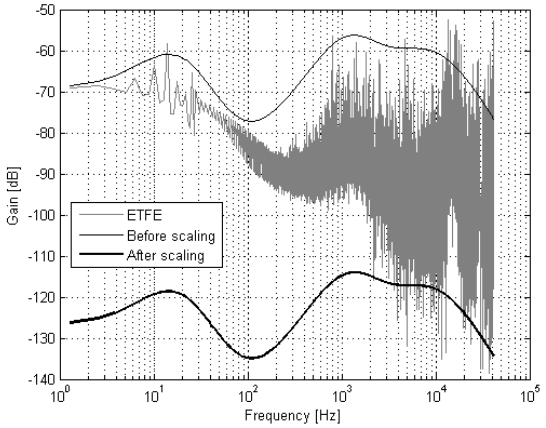


(b) Weight from current 2 to $x$-axis

Figure 5.16: Uncertainty weight ETFEs and bounding functions for dynamic additive uncertainty in the AMB plant (1)

Finally, $\mu$-analysis can be performed culminating in the $\mu$-plot of figure 5.20. The peaks in this plot correspond to the critical frequency of the AMB as well as the peaks occuring in the identified uncertainty weight functions (see figures 5.16, 5.17, 5.18 and 5.19). Since the highest peak in the $\mu$-plot is still smaller than 1, $\mu$-analysis predicts that the (LTI) closed-loop system will remain robustly stable for the modelled uncertainty.

In essence, this stability margin pertains to the nominal LTI model for the AMB and not the actual AMB itself[10]. The fact that the original identified weight functions had to be reduced, furthermore indicates that the nominal LTI model won't be able to withstand dynamic uncertainty commensurate with the mismatch between the LTI model and the nonlinear reality. This

[10] $\mu$-analysis was performed on the nominal LTI model of the AMB as well as the LTI uncertainty model.

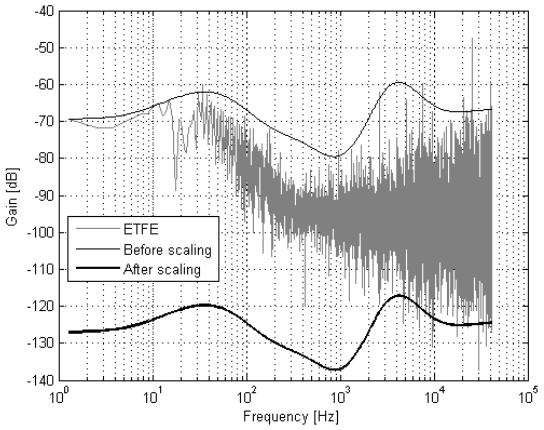


(a) Weight from current 3 to $x$-axis

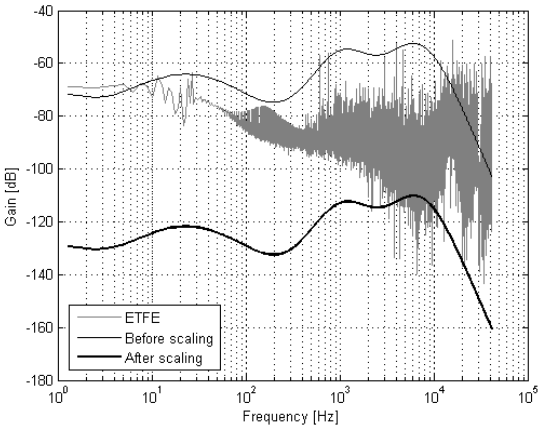


(b) Weight from current 4 to $x$-axis

Figure 5.17: Uncertainty weight ETFEs and bounding functions for dynamic additive uncertainty in the AMB plant (2)

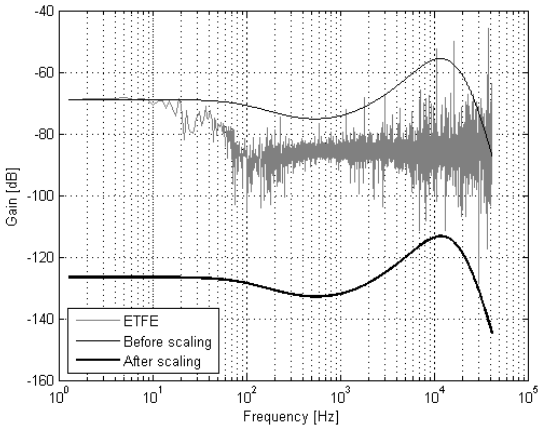


(a) Weight from current 1 to $y$-axis

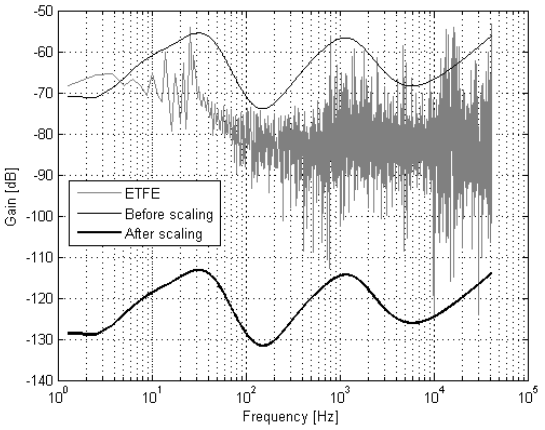


(b) Weight from current 2 to $y$-axis

Figure 5.18: Uncertainty weight ETFEs and bounding functions for dynamic additive uncertainty in the AMB plant (3)

is a clear indication of the limits of both LTI modelling and LTI robustness analysis techniques (such as $\mu$-analysis).

The LTI models fitted to the AMB system are however still *models of the system*. Any robustness analyses conducted on these models will therefore give rise to recommendations that are still of use for the original nonlinear system. One such recommendation stems from a comparison of the $\mu$-plots for parametric uncertainty in the $K_P$ coefficient of the controller and for dynamic uncertainty in the AMB plant (respectively figures 5.12 and 5.20). It is clear from these two figures that the AMB is very sensitive for perturbations at approximately 2.7 Hz and 25 Hz. By carefully optimizing the $K_P$ coefficient of the controller the impact of dynamic uncertainty in the AMB plant at these frequencies can be reduced. The other peaks in figure 5.20 are

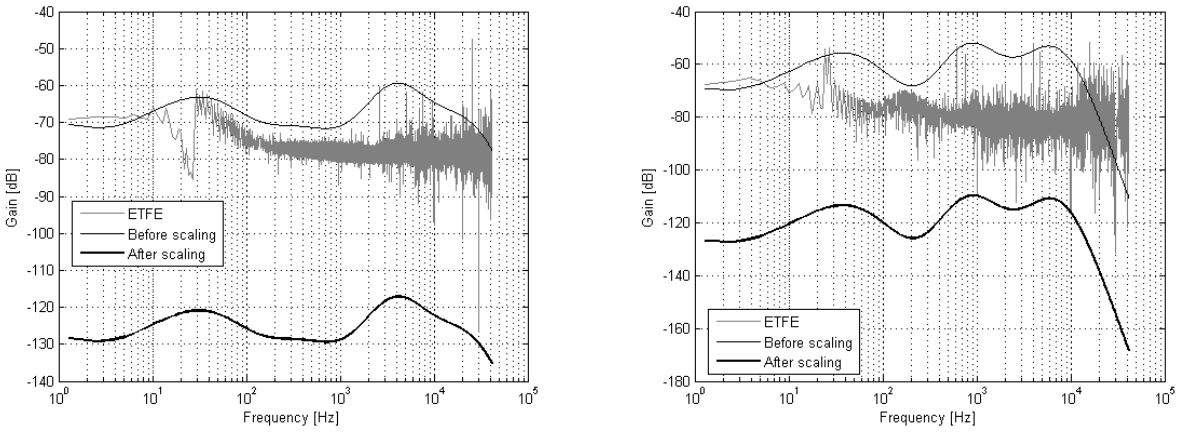


(a) Weight from current 3 to $y$-axis

(b) Weight from current 4 to $y$-axis

Figure 5.19: Uncertainty weight ETFEs and bounding functions for dynamic additive uncertainty in the AMB plant (4)

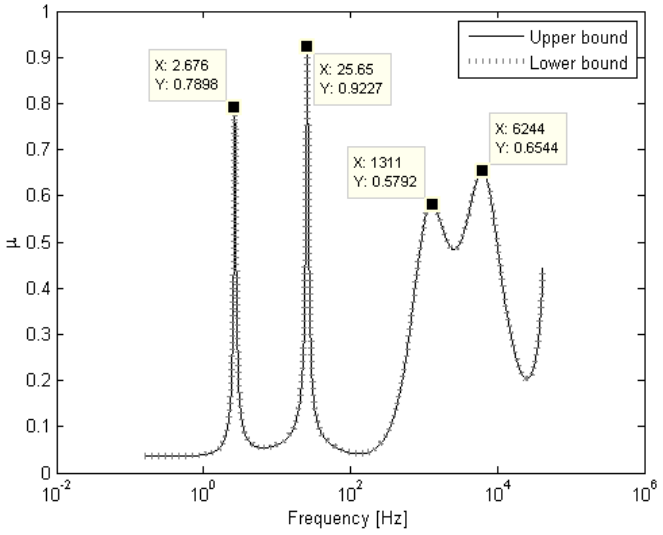


Figure 5.20: $\mu$-plot for dynamic uncertainty in the AMB plant (region A operation)

primarily due to unmodelled nonlinear effects. These effects are primarily high-frequency phenomena and can be neutralized by incorporating a low-pass filter in the forward path of the control system. In this manner the stability margin of the AMB can be further improved if the consequent loss in bandwidth is acceptable.

According to the validation procedure outlined in section 4.5 the results of $\mu$-analysis can be validated by applying a sinewave frequency sweep to both the nominal LTI model and the augmented LTI model[11]. A comparison of the resulting responses with the response of the nonlinear simulation model (to the same input signal) gives an indication of the validity of the uncertainty model.

To date, the nominal LTI models were estimated on rectangular waves, while the uncertainty weight functions were obtained on 100 µm amplitude multi-sine signals with a bandwidth of 5 Hz to 26 Hz. The response of the nominal closed-loop LTI model to a 99 µm amplitude sine sweep stretching from 11 Hz to 34 Hz is shown in figure 5.21. Once again the $x$-axis response of the model is quite satisfactory, which can't be said of the $y$-axis response. The poor $y$-axis response is due to an inadequate model for DCM self-sensing. Another shortcoming of the nominal model is that it couldn't predict the delevitation that occurs at approximately 0.18 seconds in the sine sweep.

The augmented model immediately delevitates when confronted with the sine sweep. In fact, the augmented model could only correctly respond to the sine sweep if the modelled uncertainty was scaled by a factor of $1 \times 10^{-6}$, which indicates substantial conservatism in the uncertainty model. The augmented model does however correctly predict instability if the frequency of the sweep is too high (as can be seen in figure 5.22).

Although the nominal LTI models are quite accurate (as is testified to by the very small gains of the ETFEs of the uncertainty weights), the uncertainty model is inadequate. The fundamental

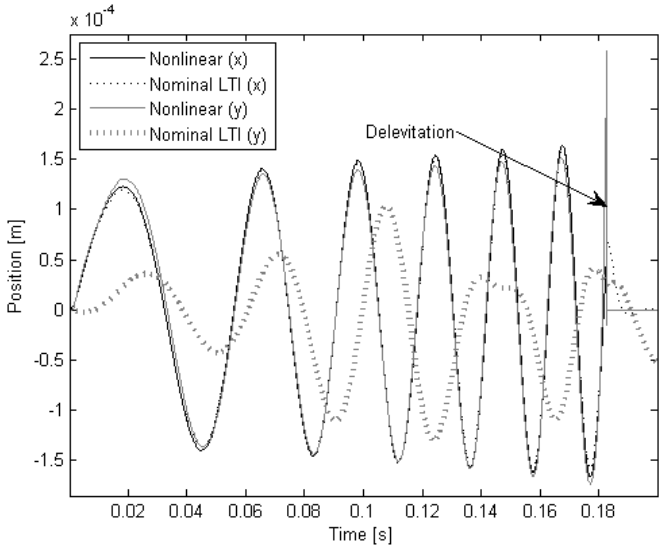


Figure 5.21: Response of the nominal closed-loop LTI model to a sine sweep

[11]The augmented model consists of the nominal LTI model and the identified uncertainty weight functions.

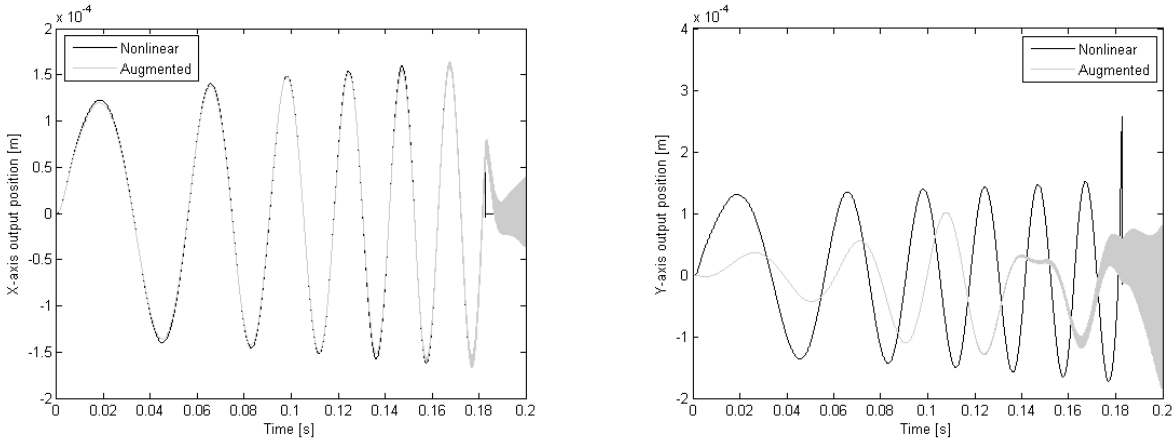


(a) $x$-axis response (b) $y$-axis response

Figure 5.22: Response of the augmented LTI model to a sine sweep

approach in norm-bounded uncertainty seems to be at fault, since there is no guarantee that a combination of LTI models can accurately model nonlinear dynamics.

### 5.3.2 Dynamic uncertainty encompassing regions A, B and C behaviour

The robustness analysis of the previous section was limited to region A behaviour. In other words, the only nonlinearities which were included in the uncertainty model were due to hysteresis and the nonlinear current-position-force relationship. Frequency induced nonlinearity didn't contribute anything to the dynamic uncertainty in the previous $\mu$-analysis.

The ability of norm-bounded additive uncertainty to correctly model frequency induced nonlinearity should be investigated since dynamic uncertainty includes all forms of unmodelled dynamics. A particular robustness analysis technique is after all only useful if it is accurate for a wide range of uncertainties that can impact the system. This section therefore contains the results of $\mu$-analysis applied to a self-sensing AMB exhibiting region A, B and C behaviour.

From the frequency-amplitude graph in figure 3.11 the desired behaviour can be elicited from the self-sensing AMB by exposing it to an input signal with an amplitude of 7 µm whose spectral content stretches from 5 Hz to 280 Hz. Such a signal can be easily synthesized in the form of a random-phase multi-sine similar to figure 5.15. The specific uncertainty weights that model the mismatch between the nonlinear system and the nominal LTI closed-loop model are shown in appendix E. The measured uncertainty weights once again had to be scaled to obtain useful results. In this instance the scaling factor is 0.0012.

The resultant $\mu$-plot is given in figure 5.23. As could be expected, this $\mu$-plot is similar to the $\mu$-plot obtained for the AMB constrained to region A behaviour. By comparing the weight functions and $\mu$-plots of this section with those of the previous section, it is clear that a $\mu$-plot is largely a function of the uncertainty weights. If the uncertainty weights are incapable of modelling a particular form of unmodelled dynamics $\mu$-analysis will be blind for that particular

uncertainty. This seems to be the case with frequency induced nonlinear behaviour, since the $\mu$-plot in figure 5.23 makes no mention of the destabilizing effect of frequency components above 280 Hz.

The inability of the LTI uncertainty weights to model the effect of frequency induced nonlinearity is further borne out by the response of the nominal LTI closed-loop to a 7 µm amplitude frequency sweep stretching from 11 Hz to 285 Hz. As can be seen from figure 5.24 the nominal system doesn't delevitate at 280 Hz. The small bandwidth of the DCM self-sensing model is also evident in this figure.

The augmented model is similarly incapable of modelling region B and C behaviour (see figure 5.25). The responses in figure 5.25 could only be obtained by scaling the uncertainty weights to very small levels. (The scaling factor is $1.5 \times 10^{-6}$.) Although the augmented model does become unstable for higher frequencies, the onset of delevitation is much more gradual than what occurs in the nonlinear AMB. All of these results confirm that LTI uncertainty models aren't suitable for modelling unmodelled dynamics due to nonlinear effects.

## 5.4 Robustness analysis for dynamic uncertainty in the self-sensing module

Without sensors active suspension in AMBs is impossible. The self-sensing algorithm is therefore in many respects the weakest link in a self-sensing AMB. Unfortunately, the self-sensing algorithm is situated in the feedback path of the closed-loop system. This means that closed-loop control won't be able to reduce the sensitivity of the closed-loop system for variations in the self-sensing algorithm. (In contrast, negative feedback is able to reduce the

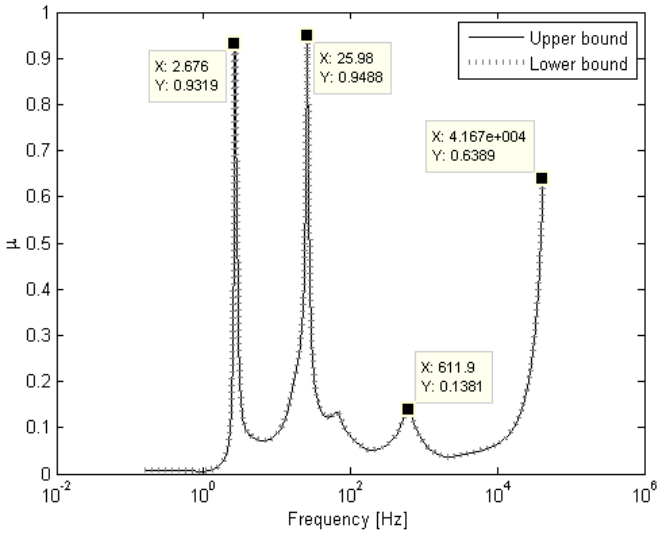


Figure 5.23: $\mu$-plot for dynamic uncertainty in the AMB plant exhibiting frequency induced nonlinear behaviour

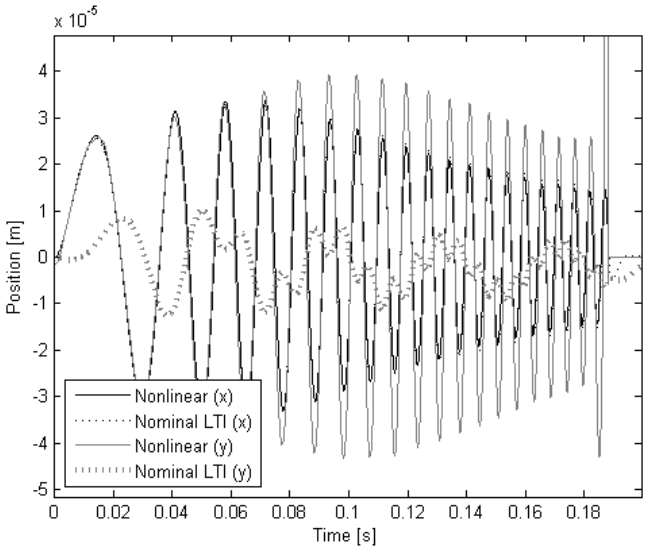


Figure 5.24: Response of the nominal closed-loop LTI model to high frequency input signals

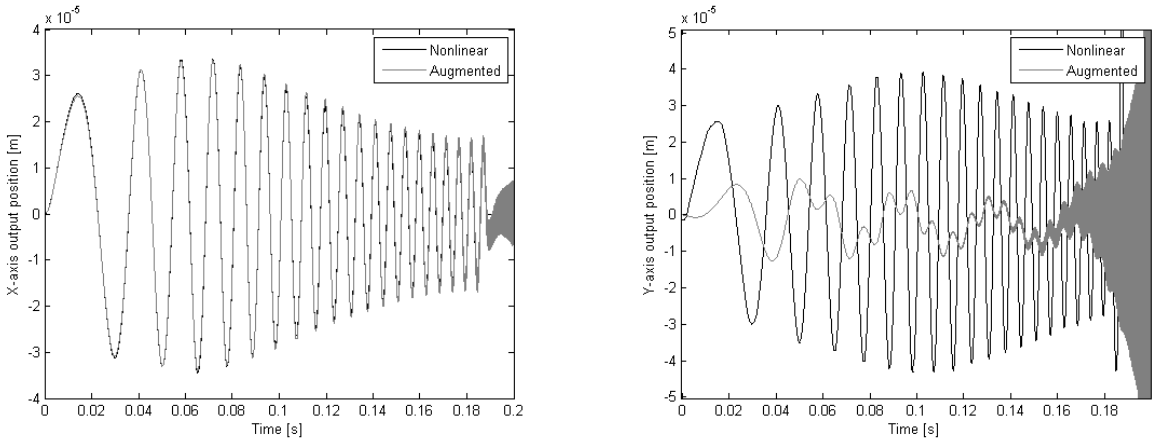


(a) $x$-axis response (b) $y$-axis response

Figure 5.25: Response of the augmented LTI model to high frequency input signals

impact of variability in components in the forward path on the closed-loop system response.)

The effect of dynamic uncertainty occuring in the self-sensing module on the closed-loop system's stability margin can be assessed in the same manner as the robustness analyses in section 5.3.1. First of all a random-phase multi-sine signal (with an amplitude of 100 μm and frequency content stretching from 5 Hz to 26 Hz) is applied to the system input. From this excitation signal the additive uncertainty weight in figure 5.26 is estimated. According to the modelled uncertainty, the nominal LTI self-sensing model's primary shortcoming is its high-frequency behaviour. Nonetheless, the generally low gain levels of the uncertainty weight are indicative of a relatively accurate LTI model for the self-sensing module. (Provided that the fundamental assumption of linearity isn't violated by frequency induced nonlinearities.)

Unfortunately the conservatism of $\mu$-analysis requires that the fitted uncertainty weight function be scaled down by a factor of 0.0012. This reduction in the modelled uncertainty is also reflected in figure 5.26. The resultant $\mu$-plot is shown in figure 5.27. Even though a 2 Hz component isn't visible in the uncertainty weight in figure 5.26, this component is the dominant factor in the $\mu$-plot. From the $\mu$-plot we can deduce that the closed-loop system's stability margin for dynamic uncertainty in the self-sensing module is dominated by an extreme sensitivity for the critical frequency of the AMB plant. The robustness of a self-sensing AMB for general dynamic uncertainty can therefore be improved by better control at this frequency.

The LTI uncertainty model is however totally unsuited to analyse the effect of nonlinear phenomena on the stability margin of the self-sensing AMB. This is once again proved by applying a 99 μm amplitude frequency sweep signal stretching from 11 Hz to 50 Hz at the system input. Neither the nominal LTI closed-loop model, nor the augmented model could correctly predict delevitation (as can be seen in figure 5.28).

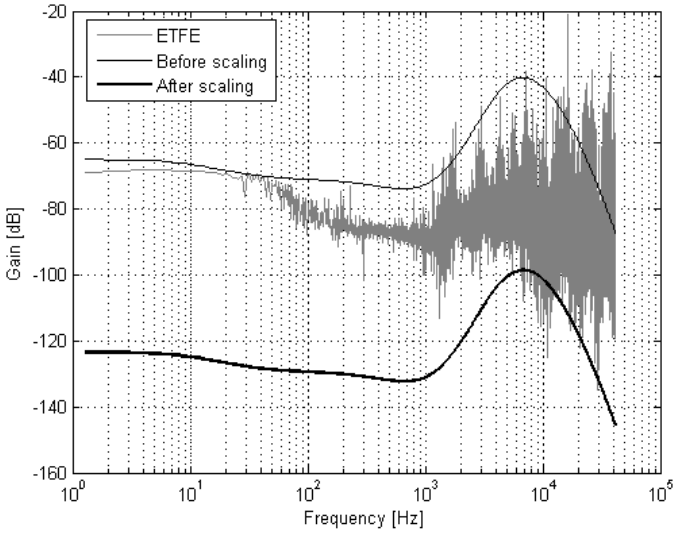


Figure 5.26: Uncertainty weight ETFE and bounding function for dynamic additive uncertainty in the self-sensing module

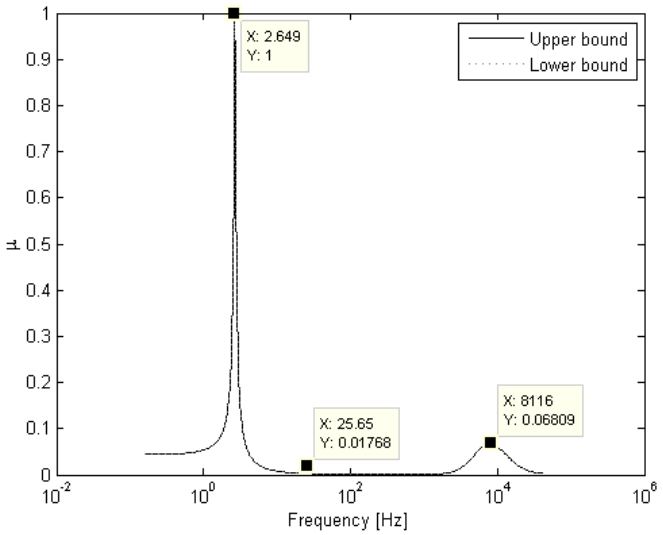


Figure 5.27: $\mu$-plot for dynamic uncertainty in the self-sensing module

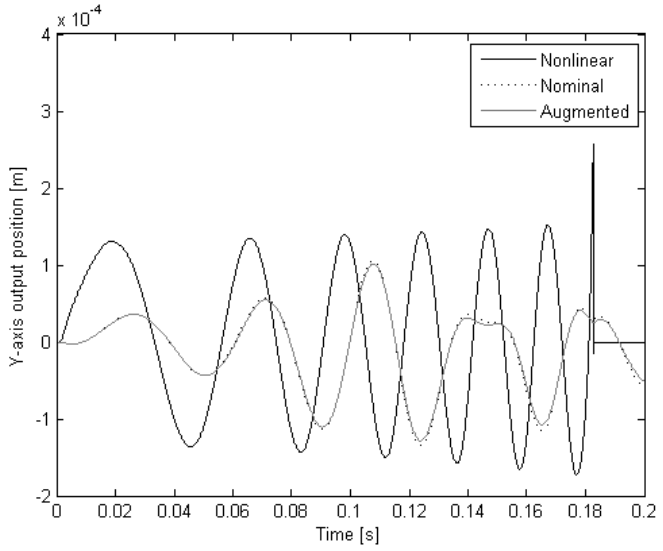


Figure 5.28: Responses to a frequency sweep

## 5.5 Conclusion

The frequency-amplitude graph has shown its true worth as a tool with which potential excitation signals can be evaluated. Furthermore, this graph is also useful to specify the frequency content and amplitude of excitation signals that are guaranteed to elicit a particular response from the AMB system.

Optimal nominal LTI models for the power amplifier, AMB plant and self-sensing module were identified in this chapter. These models collectively resulted in a stable LTI closed-loop model (although the $y$-axis performance has much room for improvement).

Both parametric uncertainties and dynamic uncertainties in selected loop components were analysed. During these analyses it was discovered that the LTI uncertainty model is unsuitable for modelling dynamic uncertainty that arises due to unmodelled nonlinear effects.

# CHAPTER 6

# When all is said and done

*This last chapter summarizes all of the results and conclusions scattered throughout the thesis. Closing arguments are made in support of the stated contributions of this study and recommendations are made for further investigations on this topic.*

## 6.1 Summary of results

The frequency-amplitude graph introduced in chapter 3 turned out to be quite useful. It gives a concise view on the frequency induced nonlinearity exhibited by an AMB. Furthermore, it can be used to evaluate potential excitation signals whether they are suitable for LTI system identification. Other excitation signals can also be synthesized via this graph with precise qualities that will excite specific behaviour in the AMB (e.g. region C behaviour to the exclusion of all else).

The main disadvantage of the black-box modelling approach taken in this study is that it precludes robustness analysis for parametric uncertainty in the AMB plant. This study is therefore limited to robustness analysis for dynamic uncertainty in the AMB plant and self-sensing module, as well as for parametric uncertainty in the PID controller.

Closed-loop system identification has to be used for AMBs due to their inherent instability. Other subsystems in the loop do however cause distortion on any excitation signal injected into the closed-loop system. This distortion can be minimized by injecting the excitation signal as closely as possible to the input of the subsystem that has to be modelled (section 3.3). Another consequence of the inherent instability of AMBs, is that dynamic uncertainty in any of the AMB subsystems can only be modelled by means of additive uncertainty (as discussed on page 86).

Discrete-time subspace system identification is useful for identifying multivariable state-space models. It is important to ensure that the identified model is as close to optimal as possible. As seen in sections 3.7.1 and 3.7.2, any imperfections are amplified greatly by the transformation

of the model to the s-plane, as well as transformations between model structures (e.g. between state-space and transfer function models).

Guidelines are given in section 5.1.2 to aid in the selection of appropriate models for the various subsystems in a self-sensing AMB. These guidelines enable the analysist to obtain LTI nominal models for the power amplifier, AMB plant and self-sensing module. The eventual closed-loop LTI nominal model has an excellent simulation performance on the $x$-axis movement of the point-mass (see e.g. figure 5.6). Unfortunately, the $y$-axis response of the LTI closed-loop model leaves much to be desired. The poor $y$-axis performance of the LTI closed-loop model is caused by inaccuracies of the LTI model for the self-sensing module (as discussed on page 104). System identification *per se* isn't at fault for the poor fidelity of the self-sensing model. The root cause of the self-sensing model's inaccuracy is the fact that DCM self-sensing makes use of discontinuous nonlinear operations which can't be satisfactorily approximated by linear models.

Self-sensing AMBs are more sensitive for variations in the controller coefficients than sensed AMBs. This conclusion is based on $\mu$-analyses conducted on nominal closed-loop LTI models for both a self-sensing AMB, as well as a sensed AMB (figures 5.9 to 5.14). These robustness analyses involved real-valued parametric uncertainties in the controller model. The resultant $\mu$-plots therefore contain very narrow and sharp peaks. Consequently the stability margins that are estimated from such $\mu$-plots are heavily influenced by the density of the frequency gridding used during $\mu$-analysis. (Complex-valued dithering of the parametric uncertainties couldn't improve this situation significantly.)

The three coefficients of a PID controller have differing effects on the system's stability margin. According to $\mu$-analysis $K_D$ can be perturbed by 80 % of its nominal value before destabilizing the AMB. By comparison $K_P$ and $K_I$ are allowed much less leeway, since $\mu$-analysis predicts that their respective maximum perturbations are only 19 % and 10 %. These recommendations should be viewed as rough guidelines only, since Monte Carlo simulations have shown these estimated stability margins by $\mu$-analysis to be over-optimistic.

Monte Carlo simulations were used in section 5.2 to validate the stability margins predicted by $\mu$-analysis for parametric uncertainty in the controller. These simulations are useful to estimate the true probability of instability of the system for the modelled uncertainty. In all instances, the stability margin calculated by means of Monte Carlo simulations were much more conservative than $\mu$-analysis (see e.g. table 5.1). The discrepancy between $\mu$-analysis and the LTI Monte Carlo simulations can be ascribed to the use of maximum singular values to estimate the stability margin in the case of $\mu$-analysis. The difference between the estimates obtained by $\mu$-analysis and the nonlinear Monte Carlo simulations is due to the fundamental assumption of linearity upon which $\mu$-analysis is built.

Calculating the probability of instability by means of Monte Carlo simulations has the disadvantage of being very time consuming (results may literally take days' worth of computation time on a standard desktop microcomputer). A final caveat on the use of nonlinear Monte Carlo simulations is that the results are quite sensitive to the particular input signals that are applied to the AMB system. (The characteristics of nonlinear systems are influenced by their specific inputs.) Consequently, Monte Carlo analyses are only suited for the *invalidation* of the

results of $\mu$-analysis.

The shape of the final $\mu$-plot obtained by $\mu$-analysis is influenced by critical frequencies in the system, as well as the shapes of the identified uncertainty weight functions which form the uncertainty model. This can be seen by comparing the shapes of the identified uncertainty weight functions in figures 5.16 to 5.19 with the shape of the eventual $\mu$-plot in figure 5.20. Consequently it is very important that the uncertainty weights be accurately measured and modelled by means of low-order[1] transfer functions. A novel algorithm was developed in section 4.4.3 to fit a transfer function to an ETFE of an uncertainty weight. This algorithm is however suboptimal and sometimes fails to converge to a satisfactory function.

When applied to dynamic uncertainty in the AMB plant or self-sensing module, $\mu$-analysis proved itself to be somewhat conservative. According to $\mu$-analysis the self-sensing AMB is very sensitive for dynamic uncertainties in either the AMB plant or the self-sensing module (see e.g. sections 5.3.1 and 5.4). The fundamental issue at stake is however the validity of modelling a mismatch between a *nonlinear* system and an *LTI* nominal model by means of *another LTI* model (the uncertainty model). An example of this problem is the inability of $\mu$-analysis to predict delevitation due to frequency induced nonlinearities in the AMB (e.g. in figures 5.24 and 5.28). Since the augmented model couldn't correctly model region B and C behaviour, the prime cause of the problem lies at the door of the LTI uncertainty weight.

Nonetheless, the $\mu$-plots obtained for dynamic uncertainty in the AMB are quite useful to identify specific frequencies where the system is especially fragile. Based on these $\mu$-plots it is possible to make detailed recommendations to improve the stability margin of the system (e.g. in section 5.4).

## 6.2 Contributions of this study

Most of the work that have been done on self-sensing AMBs are concerned with the development of functioning self-sensing algorithms. The robustness of self-sensing AMBs is either addressed in general terms (to prove of disprove the fundamental concept of self-sensing, e.g. [18] and [13]) or as a general parting shot at the end of a study with a totally different focus (e.g. [11], [31] and [17]). Typically the stability robustness of self-sensing AMBs is estimated by means of the sensitivity function in accordance with the proposed ISO standard [9].

To the best of my knowledge, this study is the first application of $\mu$-analysis to self-sensing AMBs in general and DCM self-sensing in particular. During this process two fundamental limitations of $\mu$-analysis were uncovered.

- The first is that $\mu$-analysis can only be as accurate as the uncertainty model upon which it is based. It is therefore of cardinal importance that the uncertainty weights be modelled acccurately. Modelling uncertainty by means of norm-bounded transfer functions has its uses, but it is not a suitable modelling paradigm for all underlying causes of uncertainty.

[1] Low-order transfer functions aren't essential, but such functions tend to result in less numerical difficulties during the subsequent stages of $\mu$-analysis.

Norm-bounded uncertainty certainly is not the silver bullet of uncertainty modelling that it is often proclaimed to be.

- The second limitation of $\mu$-analysis is that it is limited to LTI systems. This restriction also stems from the use of norm-bounded uncertainty models. LTI uncertainty weights are simply incapable of accurately modelling the mismatch between a nonlinear system and its LTI nominal model.

Although system identification was merely a means to an end in this study, the development of a black-box model for a self-sensing AMB by means of system identification also constitutes a contribution. The resultant model definitely isn't picture perfect, but does give insight into some of the interactions occuring inside a self-sensing AMB.

The last contribution of this study is also the most useful, namely a new perspective on the boundary between linear and nonlinear behaviour in AMBs. Through the use of the frequency-amplitude graph introduced in chapter three, it is possible to predict when a particular AMB will be operating in a linear domain and for which input signals it will be behaving nonlinearly. The frequency-amplitude graph is furthermore invaluable in choosing (or synthesizing) suitable excitation signals for black-box modelling of AMBs.

## 6.3 Recommendations for further work

Self-sensing AMBs are nonlinear multivariable systems. This thesis has shown that a linearization approach to the robustness analysis of this system isn't sufficient. Accurate robustness analysis requires accurate models of the nominal system and the expected uncertainty. A good model for robustness analysis purposes must mimic all aspects of the true system's behaviour: the good, the bad, and the ugly. Not only should the model replicate the system in well-behaved cases, but also when the system is teetering on the edge of instability.

Further work should therefore be done on the development of an analytical nonlinear model for a self-sensing AMB. Obviously an accurate nonlinear nominal model will only be complete with a nonlinear uncertainty description. One possibility would be to generalize the basic concept of norm-bounded uncertainty modelling to the world of nonlinear state-space models.

Armed with improved models for the self-sensing AMB, robustness analysis can then be performed via Lyapunov techniques. This proposed approach places a heavier mathematical burden on the shoulders of the analysist, but holds out the promise of delivering much more accurate and insightful robustness analyses.

# APPENDIX A

## Theoretical z-plane plant model of a 1-DOF AMB

The objective of this appendix is to outline the derivation of the z-plane transfer function of the plant of a 1-DOF AMB operated in differential driving mode. This derivation will embark from the following signal flow graph for a linearized [1] 1-DOF AMB control system [32].

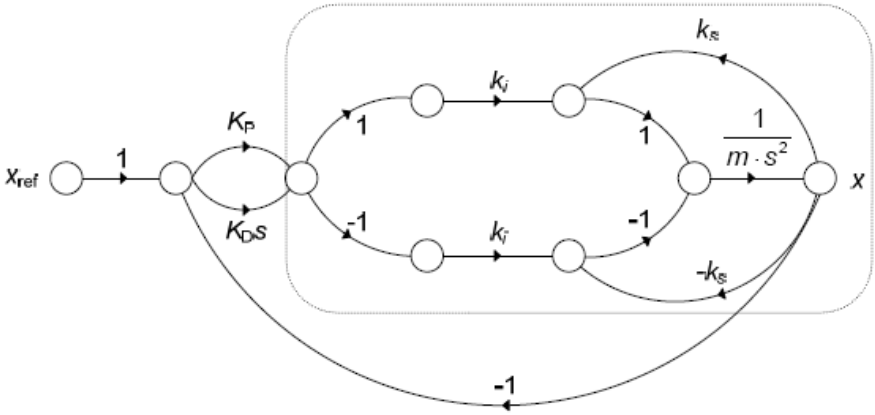


Figure A.1: Signal flow graph of a 1-DOF AMB in differential driving mode (with permission from [32])

Following the same decomposition procedure as in [84] the following controllability canonical

[1] Linearization is accomplished and improved by means of differential driving mode discussed in section 2.1.1.

form state-space model is obtained for the plant of the AMB (which is encircled in figure A.1).

$$\begin{aligned}
\dot{\mathbf{x}}(t) &= \mathbf{A}\mathbf{x}(t) + \mathbf{B}u(t) \\
y(t) &= \mathbf{C}\mathbf{x}(t) + Du(t) \\
\dot{\mathbf{x}}(t) &= \begin{bmatrix} 0 & 1 \\ \frac{2k_s}{m} & 0 \end{bmatrix} \mathbf{x}(t) + \begin{bmatrix} 0 \\ \frac{2k_i}{m} \end{bmatrix} u(t) \\
y(t) &= \begin{bmatrix} 1 & 0 \end{bmatrix} \mathbf{x}(t)
\end{aligned} \tag{A.1}$$

From (A.1) the equivalent s-plane transfer function of the AMB plant can be obtained as follows [84]:

$$\begin{aligned}
G(s) &= \mathbf{C}\left(s\mathbf{I} - \mathbf{A}\right)^{-1}\mathbf{B} + D \\
&= \frac{2k_i}{ms^2 - 2k_s}
\end{aligned} \tag{A.2}$$

From [117] and [97] the corresponding z-plane transfer function of the AMB plant is given by:

$$G(z) = \mathcal{Z}\left\{\frac{1 - e^{-sT}}{s} G(s)\right\} \tag{A.3}$$

Substituting (A.2) into (A.3) and making use of the relation: $z = e^{sT}$ results in:

$$\begin{aligned}
G(z) &= \left(1 - z^{-1}\right)\mathcal{Z}\left\{\frac{2k_i}{s(ms^2 - 2k_s)}\right\} \\
&= \frac{z-1}{z}\mathcal{Z}\left\{\frac{2k_i}{s(ms^2 - 2k_s)}\right\} \\
&= \left(\frac{z-1}{z}\right)\left(\frac{2k_i}{m}\right)\mathcal{Z}\left\{\frac{1}{s\left(s^2 - \frac{2k_s}{m}\right)}\right\}
\end{aligned} \tag{A.4}$$

where the linearity property of the z-transform was employed in the last step.

Factorizing the denominator inside the z-transform in (A.4) leads to:

$$G(z) = \left(\frac{z-1}{z}\right)\left(\frac{2k_i}{m}\right)\mathcal{Z}\left\{\frac{1}{s\left(s - \sqrt{\frac{2k_s}{m}}\right)\left(s + \sqrt{\frac{2k_s}{m}}\right)}\right\} \tag{A.5}$$

Now the following z-transform pair can be used:

$$\frac{1}{s(s+a)(s+b)} \leftrightarrow \frac{(Az+B)z}{(z - e^{-aT})(z - e^{-bT})(z-1)} \tag{A.6}$$

with $A = \frac{b\left(1-e^{-aT}\right) - a\left(1-e^{-bT}\right)}{ab(b-a)}$ and $B = \frac{ae^{-aT}\left(1-e^{-bT}\right) - be^{-bT}\left(1-e^{-aT}\right)}{ab(b-a)}$

Substituting the relevant constants into (A.6) and simplifying with amongst other things the following definition: $\cosh(\theta) = \frac{e^{\theta}+e^{-\theta}}{2}$, the following z-plane transfer function of the AMB plant is obtained:

$$G(z) = \left(\frac{k_i}{k_s}\right)\left[\cosh\left(\sqrt{\frac{2k_s}{m}}T\right) - 1\right]\frac{z+1}{\left(z - e^{\sqrt{\frac{2k_s}{m}}T}\right)\left(z - e^{-\sqrt{\frac{2k_s}{m}}T}\right)} \tag{A.7}$$

The theoretical z-plane poles of the plant of a 1-DOF AMB in differential driving mode are therefore:

$$z = e^{\pm\sqrt{\frac{2k_s}{m}}T} \tag{A.8}$$

APPENDIX B

# Inherent dangers in the conversion from the z-plane to the s-plane

During the transformation of a discrete-time transfer function to its continuous-time equivalent, small complex-valued perturbations from any point in the vicinity of the unit circle are amplified by approximately the sampling frequency during the mapping to the s-plane. This point will now be thoroughly expounded by a first order analysis followed by a numerical verification.

Related work has been done in [123] where the focus is firstly on finding the range of sampling frequencies over which the Tustin transformation is accurate and secondly on representing a sampled-data control system with an approximate continuous-time equivalent system. The analysis in this appendix is however concerned with the fundamental mapping from the z-plane to the s-plane without modelling a first-order sample-and-hold circuit by means of the Padé approximation. Furthermore, the focus in this appendix is on estimating the amplification of errors in the identified z-plane transfer function during the transformation to the s-plane.

## B.1 Theoretical analysis

Say that a complex-valued point[1] in the z-plane has the value $z_0 \in \mathcal{C}$. This point can represent a pole or a zero of the discrete-time model or merely a parameter value in its state-space representation. Applying a small complex-valued perturbation ($\delta_z \in \mathcal{C}$) to this point results in another point, namely $z_0 + \delta_z$.

The question now is by how much the perturbation is amplified during the transformation to the s-plane. Equation (3.24) describes the mapping from the s-plane to the z-plane. The inverse transformation is given by:

$$s = \frac{1}{T} \ln(z) \tag{B.1}$$

[1] The poles and zeros of the identified z-plane transfer function are complex-valued.

By applying the inverse mapping in (B.1) to the original and perturbed z-plane points individually, the size of the perturbation in the s-plane can be calculated as follows:

$$\begin{aligned} |e(s)| &= \left| \frac{1}{T} \ln(z_0 + \delta_z) - \frac{1}{T} \ln(z_0) \right| \\ &= \frac{1}{T} |\ln(z_0 + \delta_z) - \ln(z_0)| \end{aligned} \tag{B.2}$$

where $e(s)$ represents the size of the resulting perturbation in the s-plane.

Due to the nonlinear nature of (B.1) the magnification of any perturbations in z-plane pole or zero positions during the mapping to the s-plane depends on where poles or zeros were originally situated. In this first order analysis, the z-plane will be divided into three nonoverlapping regions, namely:

- strictly inside the unit circle ($|z| < 1$);
- nearby the perimeter of the unit circle ($|z| \approx 1$);
- and strictly outside the unit circle ($|z| > 1$).

For points strictly inside the unit circle, the size of the s-plane perturbation is:

$$\begin{aligned} |e(s)| &= \frac{1}{T} \left| \ln\left( \frac{z_0 + \delta_z}{z_0} \right) \right| \\ &= \frac{1}{T} \left| \ln\left( 1 + \frac{\delta_z}{z_0} \right) \right| \end{aligned} \tag{B.3}$$

Inside the unit circle, the following relation holds: $\left| \frac{\delta_z}{z_0} \right| < 1$. Consequently, (B.3) can be simplified by making use of the Taylor series expansion in (B.4) and thereafter only retaining first order terms to obtain (B.5).

$$\ln(1 + z) = z - \frac{z^2}{2} + \frac{z^3}{3} - \cdots \tag{B.4}$$

$$\begin{aligned} |e(s)| &= \frac{1}{T} \left| \left( \frac{\delta_z}{z_0} \right) - \frac{(\delta_z / z_0)^2}{2} + \frac{(\delta_z / z_0)^3}{3} - \cdots \right| \\ &\approx \frac{1}{T} \left| \frac{\delta_z}{z_0} \right| \end{aligned} \tag{B.5}$$

From (B.5) it becomes clear that during the mapping from the z-plane to the s-plane, any perturbations inside the unit circle amplified by the sampling frequency as well as the factor $1/z_0$.

For points very near to the perimeter of the unit circle, the following Taylor series expansion holds:

$$\ln(z) = z - 1 - \frac{(z-1)^2}{2} + \frac{(z-1)^3}{3} - \cdots \tag{B.6}$$

By making use of a first order approximation to the series in (B.6), the size of the corresponding s-plane perturbation can be calculated from (B.2) as follows:

$$\begin{aligned} |e(s)| &= \frac{1}{T}\left|\ln\left(z_0+\delta_z\right)-\ln\left(z_0\right)\right| \\ &\approx \frac{1}{T}\left|\left(1+\delta_z\right)-\frac{\left(1+\delta_z\right)^2}{2}\cdots-\left(z_0\right)+1+\frac{\left(z_0-1\right)^2}{2}-\cdots\right| \\ &\approx \frac{1}{T}\left|\delta_z-z_0+1\right| \\ &\approx \frac{1}{T}\left|\delta_z\right| \end{aligned} \tag{B.7}$$

Any errors in pole or zero positions that are very near to the unit circle in the z-plane are therefore magnified by a factor approximately equal to the sampling frequency during the mapping to the s-plane.

The remainder of the z-plane consists of all points strictly outside the unit circle. The further a nominal point is from the unit circle, the greater the disparity between its magnitude and the size of the perturbation to it becomes (i.e. $|z_0| \gg |\delta_z|$). This means that the amplification factor of z-plane errors during the transformation to the s-plane tapers off to nothing as the nominal points move further and further away from the unit circle, as can be seen in (B.8)

$$\begin{aligned} |e(s)| &= \frac{1}{T}\left|\ln\left(z_0+\delta_z\right)-\ln\left(z_0\right)\right| \\ &\approx \frac{1}{T}\left|\ln\left(z_0\right)-\ln\left(z_0\right)\right| \\ &= 0 \end{aligned} \tag{B.8}$$

The amplification of perturbations in the z-plane over to the s-plane is therefore primarily a problem for poles or zeros in the vicinity of the unit circle.

## B.2 Numerical verification

This analysis can be verified by numerical calculation. By making the following substitutions $z_0 = a_0 + jb_0$ and $\delta_z = \delta + j\epsilon$, the amplification of perturbations during the transformation from the z-plane to the s-plane is given by (B.9) which was used to generate figure B.1.

$$\begin{aligned} \frac{|e(s)|}{|\delta_z|} &= \frac{\frac{1}{T}\left|\ln\left(z_0+\delta_z\right)-\ln\left(z_0\right)\right|}{|\delta_z|} \\ &= \frac{1}{T}\frac{\sqrt{\left\{\ln\left(\frac{\sqrt{a_0^2+b_0^2}}{\sqrt{\left(a_0+\delta\right)^2+\left(b_0+\epsilon\right)^2}}\right)\right\}^2+\left\{\tan^{-1}\left(\frac{b_0}{a_0}\right)-\tan^{-1}\left(\frac{b_0+\epsilon}{a_0+\delta}\right)\right\}^2}}{\sqrt{\delta^2+\epsilon^2}} \end{aligned} \tag{B.9}$$

Figure B.1 shows the amplification of small perturbations at different points in the z-plane if those perturbed points were to be transformed to the s-plane. (This figure was generated for

a sampling frequency of 20 kHz.) Each point in the subset of the z-plane shown in figure B.1 was surrounded by a small grid of points representing potential perturbations to the original nominal point. By making use of (B.9) the amplification of each error in the small grid was computed. The median value of (B.9) was finally taken for all points in the small grid surrounding the nominal point to obtain a representative "amplification" for that nominal point. This procedure was then repeated for all nominal points in the presented subset of the z-plane. Clearly, perturbations inside the unit circle are amplified by significantly more than the sampling frequency (20 kHz), while the amplification factor does drop below the sampling frequency outside the unit circle.

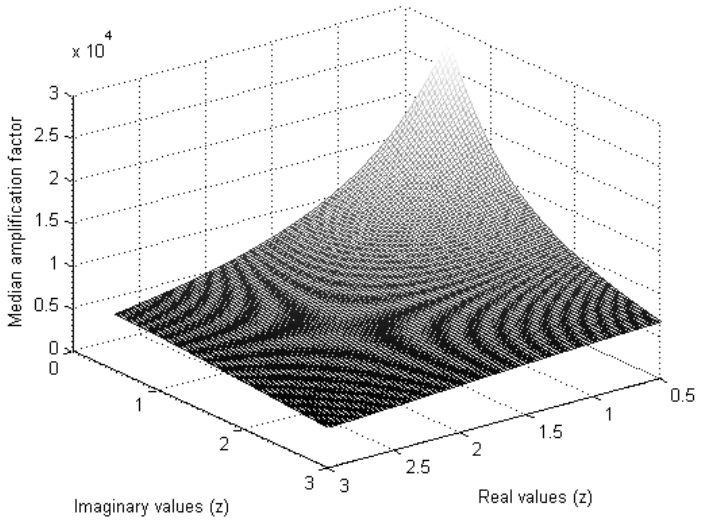


Figure B.1: Amplification of errors during the mapping from the z-plane to the s-plane

# APPENDIX C

# Benchmark $\mu$-analysis problem

Section 4.1 gives a summary of the main steps involved in performing $\mu$-analysis on a closed-loop control system subject to dynamic uncertainty. Exactly the same procedure is followed in the event of parametric uncertainty, with the exception that the parametric uncertainty is modelled by means of (4.1) rather than (4.2). In this appendix the results of $\mu$-analysis are compared to a few classical stability analysis techniques in order to verify the accuracy of $\mu$-analysis and to develop an intuition for the results obtained by $\mu$-analysis. Throughout this study Matlab® functions were used to perform the system manipulations and numerical calculations outlined in section 4.1. This appendix will therefore only report on the results obtained with these functions.

The benchmark problem posed in this appendix is the same as example problem 6.4 in [97]. This problem entails stability analysis of the control system shown in figure C.1.

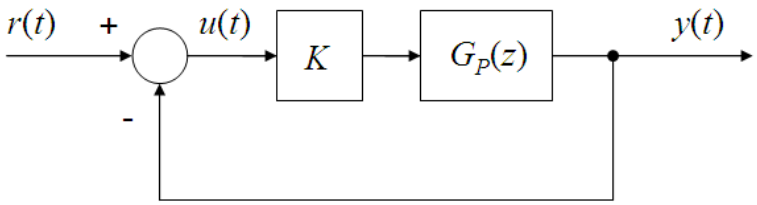


Figure C.1: Block diagram of the benchmark control system

The SISO unity feedback control system of figure C.1 has a sampling period of 1 second and an adjustable gain $K$. The plant transfer function is given by:

$$G_P(z) = \frac{0.368z + 0.264}{z^2 - 1.368z + 0.368} \tag{C.1}$$

The adjustable gain $K$ is reminiscent of root locus design. An adjustable gain can also be viewed as a parametric uncertainty. The possible destabilising effect of the parametric uncertainty in

the value of $K$ can therefore be analysed by means of the root locus technique. In [97] the interval of gains that resulted in a stable system were calculated to be $0 < K < 2.39$. Figure C.2 gives a graphical representation of the movement of the closed-loop system poles as a function of the changing value of $K$. If the value of $K$ is close to 2.39 the system becomes marginally stable with an oscillation frequency of approximately 1.3 rad/s.

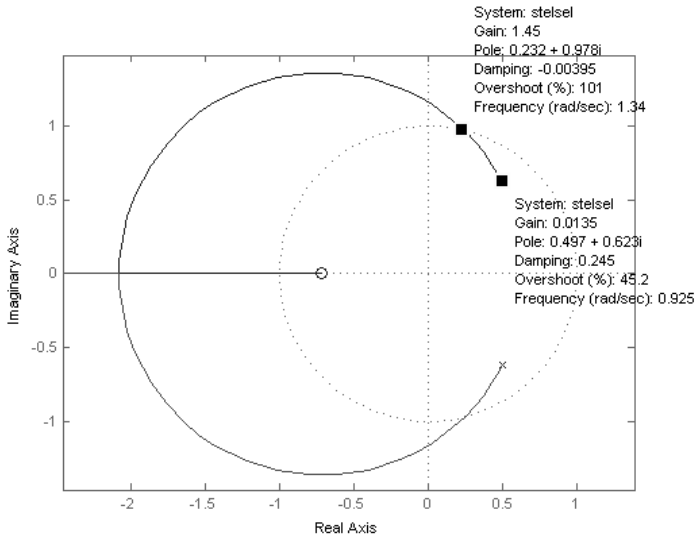


Figure C.2: Root locus of the benchmark control system

By fixing the gain $(K)$ at a constant value (e.g. $K = 1$), a stability check can be performed by means of the well-known Nyquist criterion. As figure C.3 shows, the system is indeed stable for $K = 1$ (which correlates with the estimated stability margin provided by the root locus in figure C.2). This figure exposes a drawback of the Nyquist criterion, namely that it can't elegantly estimate the stability margin of a control system (different values for $K$ have to be represented by separate Nyquist plots).

For a fixed value of $K$, the stability margin of the system can be easily computed by means of the gain margin and phase margin of the system. Figure C.4 shows the gain margin and phase margin of the control system for $K = 1$. Clearly, the system will remain stable for a further (small) increase in the value of $K$. Furthermore, the gain margin predicts potential stability problems at a frequency of roughly 1.3 rad/s (subject to the value of the gain $K$).

As mentioned previously, variation in the gain $K$ can be modelled by means of real-valued parametric uncertainty in the robust control paradigm. In order to avoid potential numerical difficulties, it is best to perform $\mu$-analysis on a continuous-time model of the system [25]. By making use of the bilinear transform, the equivalent $s$-plane transfer function of the plant $G_P$ is given by (C.2) (where the gain $K$ has been included in the transfer function as a parameter).

$$G_P(s) \simeq -\frac{1}{2}K\frac{3s^2 + 132s - 316}{171s^2 + 158s} \tag{C.2}$$

Unfortunately real-valued parametric uncertainties may sometimes result in ill-conditioned

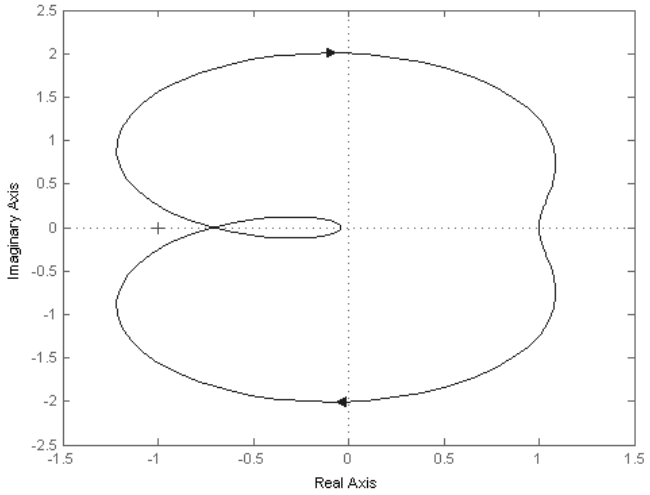


Figure C.3: Nyquist plot of the benchmark control system

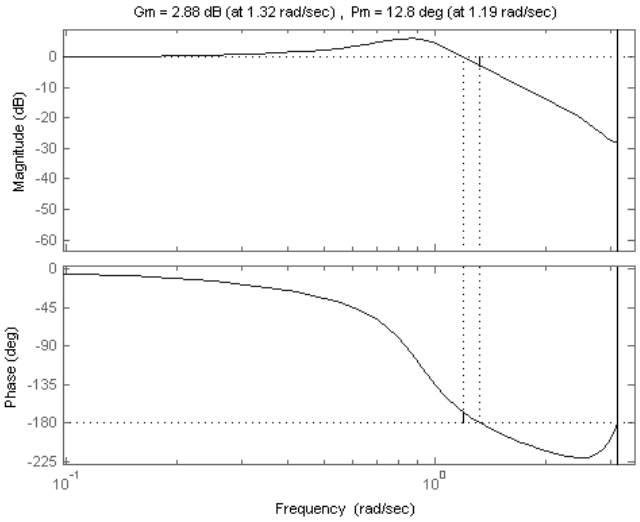


Figure C.4: Gain and phase margin of the benchmark control system

numerical calculations of the value of the structured singular value. This problem can be circumvented by adding a small complex-valued uncertainty to the original real-valued uncertainty [27]. The resultant $\mu$-analysis can be summarised by figure C.5. This plot was obtained for values of $K$ in the interval $0 < K < 2.39$. The fact that the peak value of the $\mu$-plot is quite close to one signifies that the system will remain stable for any variation in $K$ within the specified interval. This result correlates quite well with the recommendation of the root locus. Furthermore, the frequency value of the peak of the $\mu$-plot also corresponds with the problematic frequencies identified in the root locus technique as well as the gain margin. (Small differences in the frequencies can be ascribed to a coarse frequency gridding which has been used in all of the analyses.)

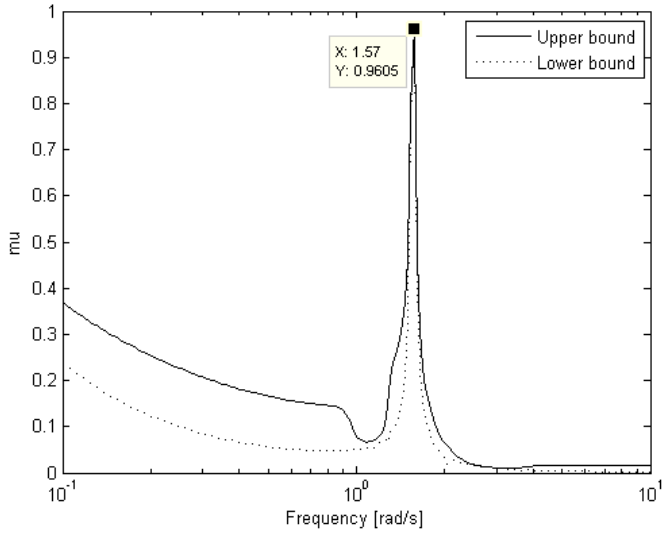


Figure C.5: $\mu$-plot of the benchmark control system

APPENDIX D

# Nominal state-space models

The procedure with which LTI models are fitted to the three subsystems of a self-sensing AMB (namely: the power amplifier, AMB plant and self-sensing module) is outlined in section 5.1. Each model is a state-space model of the following general form:

$$\begin{aligned} \dot{\mathbf{x}} &= \mathbf{A}\mathbf{x} + \mathbf{B}\mathbf{u} \\ \mathbf{y} &= \mathbf{C}\mathbf{x} \end{aligned} \tag{D.1}$$

The specific matrices of the nominal models identified in chapter 5 are now given. The presence of large off-diagonal elements in the A-matrices of the power amplifier model and the AMB plant model signify that cross-coupling between the various input variables is modelled.

## D.1 Power amplifier

$$\mathbf{A} = \begin{bmatrix} 0.9967 & 0.014907 & 0.063572 & -0.025849 & -0.053415 & -0.0060272 & -0.013227 \\ 0.061459 & 0.75918 & -0.26818 & -0.21383 & -0.028798 & -0.18119 & 0.25439 \\ 0.048897 & -0.23984 & 0.17915 & 0.16133 & 0.41442 & -0.35244 & 0.15053 \\ 0.051685 & -0.19816 & -0.18862 & -0.27644 & -1.6389 & -0.62368 & -0.95577 \\ 0.082348 & -0.22812 & -0.71286 & 0.21499 & -0.38769 & 0.41458 & -0.16431 \\ -0.17046 & 0.45596 & 1.776 & 0.092923 & -0.2711 & -1.3877 & 0.54156 \\ -0.10118 & 0.15469 & -0.30074 & -0.13405 & -1.204 & -0.38629 & -0.51816 \end{bmatrix}$$

$$\mathbf{B} = \begin{bmatrix} -0.0083307 & -0.017104 & -13.968 & 989.64 \\ 0.88898 & 0.68051 & -11403 & -55355 \\ 2.177 & 2.1078 & -51322 & -1.8093 \times 10^5 \\ 0.22432 & -0.66204 & 26627 & 1.2203 \times 10^5 \\ 1.371 & 0.81707 & -32942 & -1.5561 \times 10^5 \\ -0.75645 & 2.5602 & -54025 & -2.8737 \times 10^5 \end{bmatrix} \tag{D.2}$$

$$\mathbf{C} = \begin{bmatrix} 15.404 & -0.33503 & 0.26667 & -0.11872 & 1.4712 & 0.27622 & 0.3951 \\ 13.246 & 0.17154 & 0.014974 & 0.053698 & 1.6175 & 0.32253 & 0.4703 \\ 10.878 & -0.20064 & 0.026399 & -0.021151 & 1.6968 & 0.29006 & 0.42366 \\ 13.179 & -0.67857 & 0.12463 & -0.19253 & 1.6498 & 0.29499 & 0.37646 \end{bmatrix} \tag{D.3}$$

## D.2 Self-sensing module

$$\mathbf{A} = \begin{bmatrix} 1.0006 & -0.022387 & -0.0018327 \\ -0.00068562 & -0.50759 & 0.89581 \\ 0.014627 & 0.49353 & 0.43191 \end{bmatrix}$$

$$\mathbf{B} = \begin{bmatrix} 4.5249 \times 10^{-5} \\ -0.00078258 \\ 0.0012698 \end{bmatrix}$$

$$\mathbf{C} = \begin{bmatrix} 0.0029167 & -7.7461 \times 10^{-5} & -0.00018733 \end{bmatrix}$$

## D.3 AMB plant

$$\mathbf{A} = \begin{bmatrix} 0.9997 & -0.00072688 & -0.0030993 & -1.6341 \times 10^{-5} & 4.4034 \times 10^{-6} & 2.0215 \times 10^{-6} & -6.9205 \times 10^{-6} & -1.9531 \times 10^{-6} & 6.2381 \times 10^{-7} \\ 0.00048924 & 0.99991 & -0.00062241 & 0.0025949 & 7.5373 \times 10^{-6} & -2.7385 \times 10^{-5} & 1.7999 \times 10^{-6} & -1.9265 \times 10^{-6} & -3.209 \times 10^{-6} \\ -0.003791 & 5.9781 \times 10^{-5} & 1.0005 & -0.00061593 & -0.00021814 & 2.5603 \times 10^{-5} & -4.441 \times 10^{-5} & -2.3217 \times 10^{-6} & 1.2867 \times -6 \\ -0.00084234 & 0.0047525 & 0.00069939 & 0.99998 & -5.5885 \times 10^{-5} & 3.8098 \times 10^{-5} & -2.4551 \times 10^{-6} & -0.00033399 & -3.678 \times 10^{-5} \\ 0.016046 & 0.00090875 & 0.020014 & -0.0024269 & 0.67311 & -0.37213 & 0.56345 & 0.019288 & 0.038538 \\ -0.0032073 & -0.0015124 & 0.0054778 & 0.00055722 & 0.23824 & -0.6566 & -0.7182 & -0.00091101 & 0.038498 \\ -7.3277 \times 10^{-5} & -0.0023892 & -0.0037711 & 0.0029417 & 0.6711 & 0.64379 & -0.36 & -0.042854 & -0.082189 \\ 0.00067528 & -0.010194 & -0.00095521 & 0.014166 & 0.0072982 & 0.0050287 & -0.013219 & 0.97926 & -0.0073895 \\ 0.0014674 & 0.0026626 & -5.1977 \times 10^{-5} & -0.003845 & -0.0025748 & 0.0019844 & -0.0032891 & 0.11189 & -0.579 \end{bmatrix}$$

$$\mathbf{B} = \begin{bmatrix} -1.0032 \times 10^{-6} & -1.9566 \times 10^{-6} & 5.7646 \times 10^{-7} & 2.0761 \times 10^{-6} \\ -3.541 \times 10^{-6} & 2.6085 \times 10^{-6} & 3.8431 \times 10^{-6} & -3.6232 \times 10^{-6} \\ 2.1445 \times -6 & 0.00021938 & -6.8416 \times -6 & -0.00021567 \\ -0.00025321 & 1.2891 \times 10^{-5} & 0.00019087 & -1.5329 \times 10^{-5} \\ 0.012313 & -0.039612 & -0.018519 & 0.045822 \\ -0.052403 & 0.13896 & 0.060185 & -0.15212 \\ -0.034146 & 0.093635 & 0.046202 & -0.10619 \\ -0.0076712 & 0.0039162 & -0.0034112 & -0.0022743 \\ -0.57766 & 0.27638 & 0.76026 & -0.51897 \end{bmatrix}$$

$$\mathbf{C} = \begin{bmatrix} -0.0015516 & -1.2778 \times 10^{-5} & -1.2143 \times 10^{-5} & 7.3256 \times 10^{-6} & 3.5709 \times 10^{-8} & -6.0473 \times 10^{-10} & 2.3508 \times 10^{-8} & 8.8073 \times 10^{-9} & -1.1738 \times 10^{-9} \\ 0.00033211 & -0.0020703 & -2.6737 \times 10^{-6} & 7.4282 \times 10^{-6} & -5.2795 \times 10^{-7} & 5.5182 \times 10^{-8} & -2.5304 \times 10^{-7} & 1.4464 \times 10^{-8} & 5.5575 \times 10^{-9} \end{bmatrix}$$

# APPENDIX E

# Uncertainty weights for the AMB plant operated in regions A to C

This appendix contains the uncertainty weights that model the mismatch between a nominal LTI model for the AMB plant and the real plant that is exhibiting frequency induced nonlinear behaviour. The weights shown in this appendix were measured on a self-sensing AMB that was subjected to a random-phase multi-sine input signal similar to figure 5.15. More specifically, the excitation signal's amplitude was 7 μm, while its spectral content was limited to the bandwidth stretching from 5 Hz to 280 Hz. In contrast with other analyses in this study, the weight transfer functions were fitted by means of the Matlab function "drawmag" (due to convergence problems in the algorithm outlined in section 4.4.3).

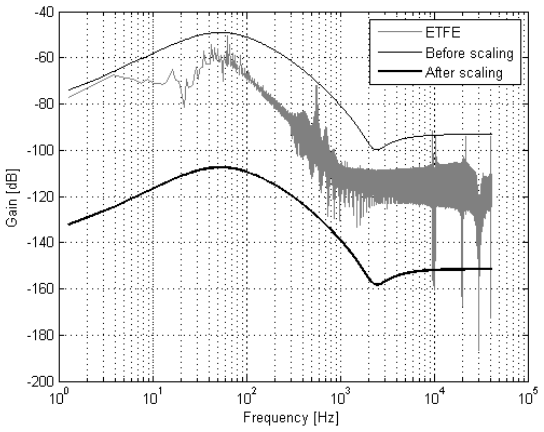


(a) Weight from current 1 to $x$-axis

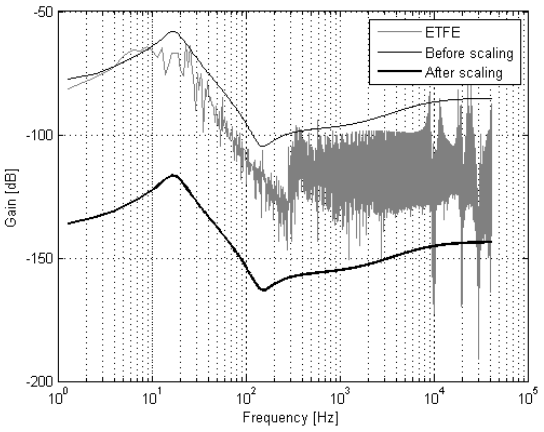


(b) Weight from current 2 to $x$-axis

Figure E.1: Uncertainty weight ETFEs and bounding functions for dynamic additive uncertainty in the AMB plant (1)

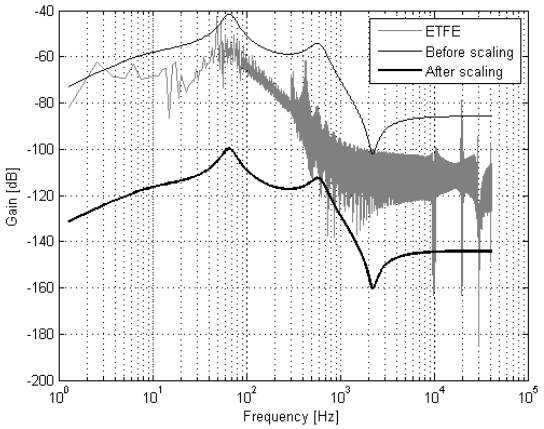


(a) Weight from current 3 to $x$-axis

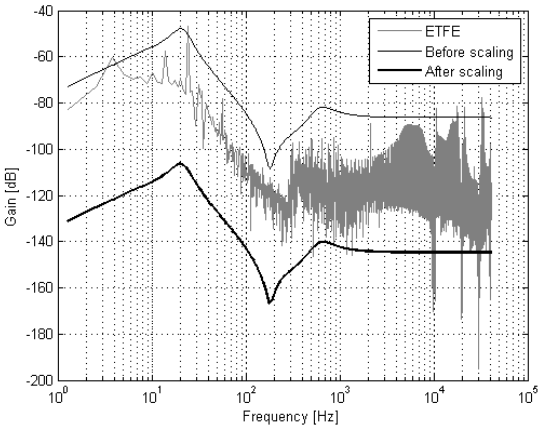


(b) Weight from current 4 to $x$-axis

Figure E.2: Uncertainty weight ETFEs and bounding functions for dynamic additive uncertainty in the AMB plant (2)

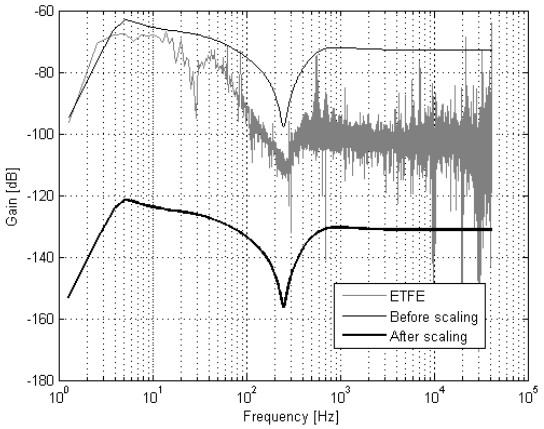


(a) Weight from current 1 to $y$-axis

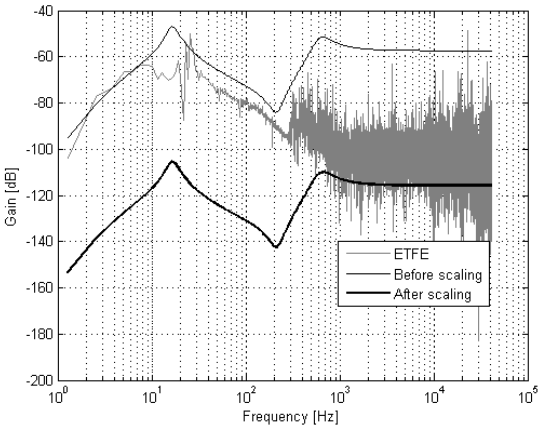


(b) Weight from current 2 to $y$-axis

Figure E.3: Uncertainty weight ETFEs and bounding functions for dynamic additive uncertainty in the AMB plant (3)

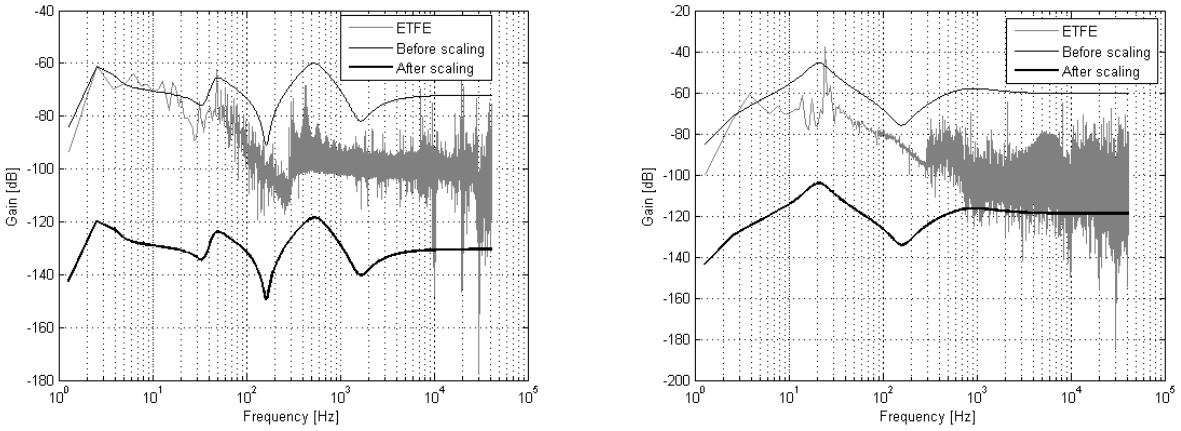


(a) Weight from current 3 to $y$-axis

(b) Weight from current 4 to $y$-axis

Figure E.4: Uncertainty weight ETFEs and bounding functions for dynamic additive uncertainty in the AMB plant (4)

# REFERENCES


[1] F. Doyle III, R. Gunawan, N. Bagheri, H. Mirsky, and T. To, "Circadian rhythm: A natural, robust, multi-scale control system," *Computers and Chemical Engineering*, vol. 30, p. 17001711, 2006.

[2] *The Holy Bible: New International Version*. The International Bible Society, 1984.

[3] K. Zhou, J. Doyle, and K. Glover, *Robust and optimal control*. Upper Saddle River, NJ: Prentice Hall, 1996.

[4] P. Banerjee and S. Shah, "The role of signal processing methods in the robust design of predictive control," *Automatica*, vol. 31, no. 5, pp. 681–695, 1995.

[5] S. Malan, M. Milanese, and M. Taragna, "Robust analysis and design of control systems using interval arithmetic," *Automatica*, vol. 33, pp. 1363–1372, 1997.

[6] L. Ray and R. Stengel, "A Monte Carlo approach to the analysis of control system robustness," *Automatica*, vol. 29, pp. 229–236, 1993.

[7] R. Stengel and L. Ray, "Stochastic robustness of linear time-invariant control systems," *IEEE Transactions on Automatic Control*, vol. 36, pp. 82–87, January 1991.

[8] G. Schweitzer, H. Bleuler, and A. Traxler, *Active Magnetic Bearings: Basics, Properties and Applications of Active Magnetic Bearings*. Zürich: Authors Reprint, 2003.

[9] "1st ISO/CD 14839-3 "Mechanical vibration vibration of rotating machinery equipped with active magenetic bearings part 3: Evaluation of stability margin"," International Organization for Standardization, Committee draft standard ISO/TC 108 / SC 2, October 2003.

[10] R. Larsonneur, "Short lecture course: Modeling and analysis of dynamic mechanical systems with a special focus on rotordynamics and active magnetic bearing (AMB) systems," Mecos Traxler AG, 8404 Winterthur, Switzerland, Tech. Rep., 2006. [Online]. Available: http://www.mecos.com/

[11] A. Schammass, "A self-sensing active magnetic bearing: modulation approach," Ph.D. dissertation, EPFL, Switzerland, 2003.

[12] B. Hanson and M. Levesley, "Self-sensing applications for electromagnetic actuators," *Sensors and Actuators A*, vol. 116, pp. 345–351, 2004.

[13] E. Maslen, D. Montie, and T. Iwasaki, "Robustness limitations in self-sensing magnetic bearings," *Journal of dynamic systems, measurement, and control*, vol. 128, pp. 197–203, June 2006.

[14] E. Maslen, "Magnetic bearing sensors," in *Short course on magnetic bearings*, 1997.

[15] D. Vischer and H. Bleuler, "Self-sensing active magnetic levitation," *IEEE Transactions on Magnetics*, vol. 29, no. 2, pp. 1276–1281, March 1993.

[16] L. Kucera, "Robustness of self-sensing magnetic bearing," in *Proceedings of MAG'97: Industrial conference and exhibition on magnetic bearings*. Alexandria, VA: Technomic, 1997, pp. 261–270.

[17] A. Niemann, "Self-sensing algorithms for active magnetic bearings," Ph.D. dissertation, North-West University, 2008.

[18] N. Morse, R. Smith, B. Paden, and J. Antaki, "Position sensed and self-sensing magnetic bearing configurations and associated robustness limitations," in *Proceedings of the 37th IEEE conference on decision and control*, December 1998, pp. 2599–2604.

[19] J.-J. E. Slotine and W. Li, *Applied nonlinear control*. Englewood Cliffs, NJ: Prentice-Hall, 1991.

[20] J. Blight, R. Dailey, and D. Gangsaas, "Practical control law design for aircraft using multivariable techniques," *International Journal of Control*, vol. 59, pp. 93–137, 1994.

[21] Y. Kanemitsu, X.-B. Yong, S. Kijimoto, and K. Matsuda, "Comparison of stability criteria for rotor levitated by active magnetic bearing," in *Proceedings of the 10th International Symposium on Magnetic Bearings*, Martigny, Switzerland, 2006.

[22] G. Li, E. H. Maslen, and P. Allaire, "A note on ISO AMB stability margin," in *Proceedings of the 10th International Symposium on Magnetic Bearings*, Martigny, Switzerland, 2006.

[23] *The pocket Oxford dictionary of current English*, 4th ed. Ely House, London: Oxford University Press, 1966.

[24] G. Ferreres and J.-M. Biannic, "Reliable computation of the robustness margin for a flexible aircraft," *Control Engineering Practice*, vol. 19, pp. 1267–1278, 2001.

[25] S. Skogestad and I. Postlethwaite, *Multivariable feedback control: analysis and design*, 2nd ed. Chichester, UK: John Wiley & Sons, 2005.

[26] *Matlab*, R2008a ed., The MathWorks.

[27] S. Gatley, D. Bates, M. Hayes, and I. Postlethwaite, "Robustness analysis of an integrated flight and propulsion control system using $\mu$ and the $\nu$-gapmetric," *Control Engineering Practice*, vol. 10, pp. 261–275, 2002.

[28] D. Coca, "Review of results and perspectives of nonlinear process identification from experimental data," *Advances in Space Research*, vol. 32, pp. 337–345, 2003.

[29] H. Gauch jr., *Scientific Method in Practice*. Cambridge University Press, 2003.

[30] E. Ranft, "The development of a flexible rotor active magnetic bearing system," Master's thesis, North-West University (Potchefstroom Campus), 2005.

[31] ——, "An improved model for self-sensing heteropolar active magnetic bearings," Ph.D. dissertation, North-West University (Potchefstroom campus), 2007.

[32] S. Myburgh, "The development of a fully suspended AMB system for a high-speed flywheel application," Master's thesis, North-West University, 2007.

[33] E. Maslen, "Power amplifiers," in *Short course on magnetic bearings*, 1997.

[34] D. Meeker, E. Maslen, and M. Noh, "An augmented circuit model for magnetic bearings including eddy currents, fringing, and leakage," *IEEE Transactions on Magnetics*, vol. 32, no. 4, pp. 3219–3227, July 1996.

[35] E. Maslen, "Self-sensing for active magnetic bearings: overview and status," in *Proceedings of the tenth international symposium on magnetic bearings*, Martigny, Switzerland, August 21-23 2006.

[36] W. Leach Jr., *Introduction to Electroacoustics and Audio Amplifier Design*, 2nd ed. Kendall Hunt, 2001.

[37] M. Noh, "Self sensing magnetic bearings driven by switching power amplifier," Ph.D. dissertation, University of Virginia, 1996.

[38] N. Mohan, T. Undeland, and W. Robbins, *Power Electronics: Converters, Applications, and Design*, 3rd ed. Hoboken, NJ: John Wiley & Sons, 2003.

[39] L. Hou and A. Michel, "Stability analysis of pulse-width-modulated feedback systems," *Automatica*, vol. 37, pp. 1335–1349, 2001.

[40] H. Kojori, J. Lavers, and S. Dewan, "A critical assessment of the continuous-system approximate methods for the stability analysis of a sampled data system," *IEEE Transactions on Power Electronics*, vol. 8, no. 1, pp. 76–84, January 1993.

[41] Y. Cho, S. Srinavasan, J.-H. Oh, and H. Kim, "Modelling and system identification of active magnetic bearing systems," *Mathematical and Computer Modelling of Dynamical Systems*, vol. 13, no. 2, pp. 125–142, April 2007.

[42] N. Skricka and R. Markert, "Influence of cross-axis sensitivity and coordinate coupling on self-sensing," in *Proceedings of 6th International Symposium on Magnetic Suspension Technology*, Turin, Italy, October 2001, pp. 179–184.

[43] H. Hjalmarsson, "From experiment design to closed-loop control," *Automatica*, vol. 41, pp. 393–438, 2005.

[44] L. Ljung, *System identification: theory for the user*, 2nd ed. Upper Saddle River, NJ: Prentice Hall, 1999.

[45] C. Rojas, J. Welsh, G. Goodwin, and A. Feuer, "Robust optimal experiment design for system identification," *Automatica*, vol. 43, pp. 993–1008, 2007.

[46] K. Tan and Y. Li, "Evolutionary $L_\infty$ identification and model reduction for robust control," *Proceedings of the Institution of Mechanical Engineers. Part I: Journal of Systems and Control Engineering*, vol. 214, pp. 231–237, 2000.

[47] R. Babuška and H. Verbruggen, "Neuro-fuzzy methods for nonlinear system identification," *Annual Reviews in Control*, vol. 27, pp. 73–85, 2003.

[48] J. Schoukens and R. Pintelon, *Identification of linear systems: a practical guideline to accurate modeling*. Oxford: Pergamon press, 1991.

[49] K. Godfrey, A. Tan, H. Barker, and B. Chong, "A survey of readily accessible perturbation signals for system identification in the frequency domain," *Control Engineering Practice*, vol. 13, pp. 1391–1402, 2005.

[50] P. Van Den Hof, "Closed-loop issues in system identification," *Annual reviews in control*, vol. 22, pp. 173–186, 1998.

[51] R. Hildebrand and G. Solari, "Identification for control: Optimal input intended to identify a minimum variance controller," *Automatica*, vol. 43, pp. 758–767, 2007.

[52] S. Ahmed, B. Huang, and S. Shah, "Novel identification method from step response," *Control Engineering Practice*, vol. 15, pp. 545–556, 2007.

[53] M. Iwasaki, M. Miwa, and N. Matsui, "Ga-based evolutionary identification algorithm for unknown structured mechatronic systems," *IEEE Transactions on Industrial Electronics*, vol. 52, no. 1, pp. 300–305, February 2005.

[54] M. Schroeder, "Synthesis of low-peak-factor signals and binary sequences with low autocorrelation," *IEEE Transactions on Information Theory*, vol. 16, no. 1, pp. 85–89, 1970.

[55] S. Vardeman, *Statistics for engineering problem solving*. Boston: PWS, 1994.

[56] T. Ross, *Fuzzy logic with engineering applications*. New York: McGraw-Hill, 1995.

[57] C. Robert and G. Casella, *Monte Carlo statistical methods*, 2nd ed. New York: Springer-Verlag, 2004.

[58] P. Menon, D. Bates, and I. Postlethwaite, "Nonlinear robustness analysis of flight control laws for highly augmented aircraft," *Control Engineering Practice*, vol. 15, no. 6, pp. 655–662, June 2007.

[59] [Online]. Available: http://mathworld.wolfram.com/Kurtosis.html

[60] S. Chen, M. Song, and Y. Chen, "Robustness analysis of responses of vibration control structures with uncertain parameters using interval algorithm," *Structural Safety*, vol. 29, pp. 94–111, 2007.

[61] B. Barmish, "A generalization of Kharitonovs four polynomial concept for robust stability problems with linearly dependent coefficient perturbations," *IEEE transactions on automatic control*, vol. 34, no. 2, pp. 157–165, February 1989.

[62] C. Marsh and H. Wei, "Robustness bounds for systems with parametric uncertainty," *Automatica*, vol. 32, no. 10, pp. 1447–1453, 1996.

[63] E. Laroche and D. Knittel, "An improved linear fractional model for robustness analysis of a winding system," *Control Engineering Practice*, vol. 13, pp. 659–666, 2005.

[64] E. Laroche, Y. Bonnassieux, H. Abou-Kandil, and J.-P. Louis, "Controller design and robustness analysis for induction machine-based positioning system," *Control Engineering Practice*, vol. 12, pp. 757–767, 2004.

[65] G. Ferreres and V. Fromion, "Computation of the robustness margin with the skewed $\mu$ tool," *Systems & Control Letters*, vol. 32, pp. 193–202, 1997.

[66] N.-C. Tsai, C.-H. Kuo, and R.-M. Lee, "Regulation on radial position deviation for vertical amb systems," *Mechanical Systems and Signal Processing*, vol. 21, pp. 2777–2793, 2007.

[67] B. Barmish, "Invariance of the strict hurwitz property for polynomials with perturbed coefficients," *IEEE transactions on automatic control*, vol. 29, no. 10, pp. 935–936, October 1984.

[68] G. Li, "Robust stabilization of rotor-active magnetic bearing systems," Ph.D. dissertation, University of Virginia, 2007.

[69] A. Lanzon and P. Tsiotras, "A combined application of $H_\infty$ loop shaping and $\mu$-synthesis to control high-speed flywheels," *IEEE Transactions on control systems technology*, vol. 13, no. 5, pp. 766–777, September 2005.

[70] H. DeSmidt, K. Wang, E. Smith, and A. Provenza, "On the robust stability of segmented driveshafts with active magnetic bearing control," *Journal of Vibration and Control*, vol. 11, pp. 317–329, 2005.

[71] E. Maslen, T. Iwasaki, and R. Mahmoodian, "Formal parameter estimation for self-sensing," in *Proceedings of the tenth international symposium on magnetic bearings*, Martigny, Switzerland, August 21-23 2006.

[72] S.-J. Kim and C.-W. Lee, "On-line identification of current and position stiffnesses by lms algorithm in active magnetic bearing system equipped with force transducers,," *Mechanical Systems and Signal Processing*, vol. 13, no. 5, pp. 681–690, 1999.

[73] T. Lim and S. Cheng, "Parameter estimation and statistical analysis on frequency-dependent active control forces," *Mechanical Systems and Signal Processing*, vol. 21, pp. 2112–2124, 2007.

[74] C. Gähler, M. Mohler, and R. Herzog, "Multivariable identification of active magnetic bearing systems," *JSME international journal. Series C, Mechanical systems, machine elements and manufacturing*, vol. 40, no. 4, pp. 584–592, 1997.

[75] R. Prins, M. Kasarda, and S. Prins, "A system identification technique using bias current perturbation for determining the effective rotor origin of active magnetic bearings," *Journal of Vibration and Acoustics, Transactions of the ASME*, vol. 129, pp. 317–322, 2007.

[76] N. Gibson, H. Choi, and G. Buckner, "$h_\infty$ control of active magnetic bearings using artificial neural network identification of uncertainty," in *2003 IEEE International Conference on Systems, Man and Cybernetics*, vol. 2, Washington D.C., 2003, pp. 1449–1456.

[77] H. Choi, G. Buckner, and N. Gibson, "Neural robust control of a high-speed flexible rotor supported on active magnetic bearings," in *Proceedings of the 2006 American Control Conference*, Minneapolis, Minnesota, June 2006, pp. 3679–3684.

[78] J. Sawicki, E. Maslen, and K. Bischof, "Amb controller design for a machining spindle using $\mu$-synthesis," in *Proceedings of the tenth international symposium on magnetic bearings*, Martigny, Switzerland, August 21-23 2006.

[79] K. Jun, D. Rivera, E. Elisante, and V. Sater, "A computer-aided design tool for robustness analysis and control-relevant identification of horizon predictive control with application to a binary distillation column," *Journal of Process Control*, vol. 6, no. 2/3, pp. 177–186, 1996.

[80] M. Kamrunnahar, D. Fisher, and B. Huang, "Performance assessment and robustness analysis using an armarkov approach," *Journal of Process Control*, vol. 14, pp. 915–925, 2004.

[81] M. Viberg, "Subspace-based methods for the identification of linear time-invariant systems," *Automatica*, vol. 31, no. 12, pp. 1835–1851, 1995.

[82] S. Shinners, *Modern control system theory and design*. New York: John Wiley & Sons, 1992.

[83] N. Skricka and R. Markert, "Improvements in the integration of active magnetic bearings," *Control Engineering Practice*, vol. 10, pp. 917–922, 2002.

[84] B. Kuo, *Automatic Control Systems*, 7th ed. Englewood Cliffs, NJ: Prentice Hall, 1995.

[85] W. Fuller, *Introduction to statistical time series*, 2nd ed. New York: Wiley Interscience, 1996.

[86] M. Furno, "The glejser test and the median regression," *Sankhyā : The Indian Journal of Statistics*, vol. 67, pp. 335–358, 2005.

[87] J. Bendat and A. Piersol, *Random data: analysis and measurement procedures*. New York: Wiley-Interscience, 1971.

[88] T.-H. Kim and H. White, "On more robust estimation of skewness and kurtosis," *Finance Research Letters*, vol. 1, p. 5673, 2004.

[89] J. Halley and W. Kunin, "Extinction risk and the 1/f family of noise models," *Theoretical Population Biology*, vol. 56, pp. 215–230, 1999.

[90] M. Schroeder, *Fractals, chaos, power laws: Minutes from an infinite paradise*. New York: Freeman, 1991.

[91] M. Keshner, "1/f noise," *Proceedings of the IEEE*, vol. 70, no. 3, pp. 212–218, March 1982.

[92] J.-M. Poggi and B. Portier, "Asymptotic local test for linearity in adaptive control," *Statistics & Probability Letters*, vol. 55, pp. 9–17, 2001.

[93] A. Ben-Israel and T. Greville, *Generalized inverses: theory and applications*. New-York: John Wiley & Sons, 1974.

[94] B. Flury and H. Riedwyl, *Multivariate statistics: a practical approach*. London: Chapman and Hall, 1988.

[95] U. Hegazy and Y. Amer, "A time-varying stiffness rotor-active magnetic bearings system under parametric excitation," *Proc. IMechE Part C: J. Mechanical Engineering Science*, vol. 222, pp. 447–458, 2008.

[96] J. Jugo, I. Lizarraga, and I. Arredondo, "Nonlinear modelling and analysis of active magnetic bearing systems in the harmonic domain: a case study," *IET Control Theory Applications*, vol. 2, no. 1, pp. 61–71, 2008.

[97] C. Phillips and H. Nagle, *Digital control system analysis and design*. Englewood Cliffs, NJ: Prentice Hall, 1995.

[98] E. Ifeachor and B. Jervis, *Digital signal processing: a practical approach*. Harlow, England: Addison-Wesley, 1993.

[99] W. Favoreel, B. De Moor, and P. Van Overschee, "Subspace state space system identification for industrial processes," *Journal of Process Control*, vol. 10, pp. 149–155, 2000.

[100] J. F. A. Nooraii and J. A. Romagnoli, "Robustness analysis and control of a pilot-scale distillation column," *Computers chem. Engng*, vol. 21, no. 7, pp. 703–717, 1997.

[101] H. Buckner, G.D. Choi and N. Gibson, "Estimating model uncertainty using confidence interval networks: applications to robust control," *Transactions of the ASME: Journal of dynamic systems, measurement, and control*, vol. 128, pp. 626–635, September 2006.

[102] E. Yaz, "Deterministic and stochastic robustness measures for discrete systems," *IEEE Transactions on Automatic Control*, vol. 33, no. 10, pp. 952–955, October 1988.

[103] M. Kasarda, J. Marshall, and R. Prins, "Active magnetic bearing based force measurement using the multi-point technique," *Mechanics Research Communications*, vol. 34, p. 4453, 2007.

[104] A.-H. Abulrub, M. Sahinkaya, C. Burrows, and P. Keogh, "Robustness of recursive autotuning strategy in flexible rotor and magnetic bearing systems," in *11th International symposium on magnetic bearings*, Nara, Japan, August 2008.

[105] B. Lu, H. Choi, G. Buckner, and K. Tammi, "Linear parameter-varying techniques for control of a magnetic bearing system," *Control Engineering Practice*, vol. 16, pp. 1161–1172, 2008.

[106] Z. Duan, L. Huang, and L. Wang, "Robustness analysis and synthesis of siso systems under both plant and controller perturbations," *Systems & Control Letters*, vol. 42, pp. 201–216, 2001.

[107] S. Auchet, P. Chevrier, M. Lacour, and P. Lipinski, "A new method of cutting force measurement based on command voltages of active electro-magnetic bearings," *International Journal of Machine Tools and Manufacture*, vol. 14, pp. 1441–1449, November 2004.

[108] T. Sugie and Y. Tanai, "$L_\infty$ identification in the frequency domain based on the set-membership approach," in *Proceedings of the 34th conference on decision & control*, New Orleans, LA, December 1995, pp. 3016–3021.

[109] D. Bayard, Y. Yam, and E. Mettler, "A criterion for joint optimization of identification and robust control," *IEEE Transactions on Automatic Control*, vol. 37, no. 7, pp. 986–991, July 1992.

[110] D. Rivera, J. Pollard, and C. Garca, "Control-relevant prefiltering: a systematic design approach and case study," *IEEE Transactions on Automatic Control*, vol. 37, no. 7, pp. 964–974, July 1992.

[111] S. Hwang and R. He, "Improving real-parameter genetic algorithm with simulated annealing for engineering problems," *Advances in Engineering Software*, vol. 37, pp. 406–418, 2006.

[112] J. Böling, K. Häggblom, and R. Nyström, "Multivariable uncertainty estimation based on multi-model output matching," *Journal of Process Control*, vol. 14, pp. 293–304, 2004.

[113] J. Proakis and D. Manolakis, *Digital signal processing: principles, algorithms, and applications*, 3rd ed. Upper Saddle River, NJ: Prentice-Hall, 1996.

[114] I. Craig and I. MacLeod, "Specification framework for robust control of a run-of-mine ore milling circuit," *Control Engineering Practice*, vol. 3, no. 5, pp. 621–630, 1995.

[115] J. Layton, *Multivariable Control Theory*. Stevenage, UK: Peter Peregrinus, 1976.

[116] P. Lopes dos Santos and J. Martins de Carvalho, "Automatic transfer function synthesis from a bode plot," in *Proceedings of the 29th Conference on Decision and Control*, Honolulu, Hawaii, December 1990, pp. 1093–1098.

[117] R. Dorf and R. Bishop, *Modern control systems*, 7th ed. Reading, MA: Addison-Wesley, 1995.

[118] C. Bishop, *Neural networks for pattern recognition*. USA: Oxford university press, 1996.

[119] R. Smith, "Model validation for robust control: an experimental process control application," *Automatica*, vol. 31, no. 11, pp. 1637–1647, 1995.

[120] R. Smith and G. Dullerud, "Continuous-time control model validation using finite experimental data," *IEEE Transactions on Automatic Control*, vol. 41, no. 8, pp. 1094–1105, August 1996.

[121] M. Gevers, X. Bombois, B. Codrons, G. Scorletti, and B. Anderson, "Model validation for control and controller validation in a prediction error identification frameworkpart ii: illustrations," *Automatica*, vol. 39, pp. 417–427, 2003.

[122] R. Brown and P. Hwang, *Introduction to random signals and applied Kalman filtering*, 2nd ed. New York: John Wiley & Sons, 1992.

[123] J. D'Azzo and C. Houpis, *Linear control system analysis and design: conventional and modern*, 4th ed. New York, NJ: McGraw-Hill, 1995.